




# MASPEX-Europa: The Europa Clipper Neutral Gas Mass Spectrometer Investigation

J.H. Waite Jr.<sup>1,2</sup>  · J.L. Burch<sup>3</sup> · T.G. Brockwell<sup>3</sup> · D.T. Young<sup>3</sup> · G.P. Miller<sup>3</sup> · S.C. Persyn<sup>3</sup> · J.M. Stone<sup>3</sup> · P. Wilson IV<sup>3</sup> · K.E. Miller<sup>3</sup> · C.R. Glein<sup>3</sup> · R.S. Perryman<sup>3</sup> · M.A. McGrath<sup>4</sup> · S.J. Bolton<sup>3</sup> · W.B. McKinnon<sup>5</sup> · O. Mousis<sup>6</sup> · M.A. Sephton<sup>7</sup> · E.L. Shock<sup>8</sup> · M. Choukroun<sup>9</sup> · B.D. Teolis<sup>3</sup> · D.Y. Wyrick<sup>3</sup> · M.Y. Zolotov<sup>8</sup> · C. Ray<sup>3,10</sup> · A.L. Magoncelli<sup>11</sup> · R.R. Raffanti<sup>12</sup> · R.L. Thorpe<sup>3</sup> · A. Bouquet<sup>6</sup> · T.L. Salter<sup>7</sup> · K.J. Robinson<sup>8</sup> · C. Urdiales<sup>3</sup> · Y.D. Tyler<sup>3</sup> · G.J. Dirks<sup>3</sup> · C.R. Beebe<sup>3</sup> · D.A. Fugett<sup>9</sup> · J.A. Alexander<sup>3</sup> · J.J. Hanley<sup>3</sup> · Z.A. Moorhead-Rosenberg<sup>3</sup> · K.A. Franke<sup>3</sup> · K.S. Pickens<sup>3</sup> · R.J. Focia<sup>3</sup> · B.A. Magee<sup>3</sup> · P.J. Hoeper<sup>3</sup> · D.P. Aaron<sup>3</sup> · S.L. Thompson<sup>3</sup> · K.B. Persson<sup>3</sup> · R.C. Blase<sup>3</sup> · G.F. Dunn<sup>3</sup> · R.L. Killough<sup>3</sup> · A. De Los Santos<sup>3</sup> · R.J. Rickerson<sup>3</sup> · O.H.W. Siegmund<sup>13</sup>

Received: 6 September 2023 / Accepted: 7 March 2024 / Published online: 2 April 2024  
© The Author(s) 2024

## Abstract

The MAss Spectrometer for Planetary EXploration (MASPEX) is a high-mass-resolution, high-sensitivity, multi-bounce time-of-flight mass spectrometer (MBTOF) capable of measuring minor species with abundances of sub-parts-per-million in Europa's sputter-produced and radiolytically modified exosphere and in its oceanic plumes. The goal of the MASPEX-Europa investigation is to determine, through in-situ measurement of the exosphere and plume composition, whether the conditions for habitability exist or have existed on Europa. As conventionally defined, based on our knowledge of Earth life, the three fundamental conditions for habitability are: (1) the presence of liquid water; (2) the presence of organic compounds and the biogenic elements CHNOPS; and (3) a source of energy available for metabolic processes, which for Europa will most probably be chemosynthetic rather than photosynthetic. Condition (1) is already established by previous indirect (magnetic field) measurements, while MASPEX will contribute directly to the evaluation of condition (2) through highly specific compositional measurements in the European exosphere and plumes. The composition measurements will also contribute to the test of condition (3) through disequilibrium states of chemical reactions. Thus, the primary goal of MASPEX for Europa Clipper is to assess the habitability of Europa and specifically of its interior ocean. MASPEX has been developed successfully, and its calibration has demonstrated that it meets its specified requirements for sensitivity, dynamic range, and mass resolution. This paper reports the development of the MASPEX scientific investigation, the instrument, its performance, and calibration.

**Keywords** Space-based high-resolution mass spectrometry · NASA Clipper Mission · Habitability · Galilean Moons

---

Europa Clipper: A Mission to Explore Ocean World Habitability  
Edited by Haje Korth, Bonnie J. Buratti and David Senske

---

Extended author information available on the last page of the article

## 1 Introduction

Europa's tenuous exosphere is produced by energetic-particle sputtering and radiolysis of the surface, with a contribution from sublimation of water ice (Johnson et al. 2009; Vorburger and Wurz 2018). Possible sporadically active plumes (Roth et al. 2014; Sparks et al. 2017; Jia et al. 2018; Paganini et al. 2020; Vorburger and Wurz 2021) may introduce oceanic material into the exosphere and onto the surface, while tectonism and effusive cryovolcanism may transport material from the deeper interior to the surface (e.g., Collins and Nimmo 2009; Prockter and Patterson 2009), where it can be sputtered or sublimed into the exosphere. The exosphere and any plume(s) represent potentially rich sources of information about the composition of Europa's ice crust and its interior, which may provide insights into the transformation of Europa's composition through processes that occurred early in its history as well as its recent past, and those that may be occurring today. Such processes include radiolysis of surface materials, surface-ocean exchange, local warming of the ice shell, decomposition of gas hydrates in ice, degassing of oceanic water through fissures, water-rock interaction, silicate volcanism, thermal evolution of organic matter beneath the ocean, and possible biological activity. Of particular importance is the prospect of hydrothermal activity at the interface between the ocean of Europa and its rocky mantle - as on Earth, hydrothermal systems (Lowell and DuBose 2005) may be both a potential source of metabolic energy for chemosynthetic microorganisms and a factory for the abiotic production of organic compounds (Shock and Schulte 1998; Amend et al. 2011; Shock et al. 2013; McDermott et al. 2015).

Two of the determinants of habitability can be posed as questions to which the answer is yes or no: is there liquid water? Are there organic compounds? It is straightforward to make the corresponding measurements that answer these questions. This is not the case for evaluating the forms and abundances of energy. To answer the question of available energy, multiple measurements combined with modeling are required. We began the evaluation process by assuming photosynthesis is extremely unlikely at Europa; so, the energy sources of greatest interest are all chemical reactions. Therefore, our goal is to examine the extent to which reactions have occurred. This is done by combining analytical abundance data for reactants and products with thermodynamic and kinetic calculations and laboratory investigations to yield the quantity of available energy. To reach this goal, the most essential determinations are the relative abundances of compounds. If the ratios indicate equilibrium with respect to reactions among those compounds, then there is no energy available. If the ratios indicate disequilibrium (away from equilibrium) states, then the forms and abundances of energy can be quantified. Therefore, determining whether Europa is, or ever was, habitable necessarily requires measurement and identification of many chemical compounds.

Using Cassini's mass spectrometry measurements at Enceladus as a point of reference, the Ion Neutral Mass Spectrometer (INMS) team was able to use measurements of H<sub>2</sub>, CO<sub>2</sub>, and CH<sub>4</sub> gases exsolved from Enceladus' ocean to demonstrate that there was ample chemical energy to support a methanogenic microbial metabolism (Waite et al. 2017). Additional modeling demonstrated that other metabolisms similar to those found in the Earth's ocean could use additional chemical energy (Ray et al. 2021). However, in the case of Europa, atmospheric measurements of the potential for a methanogenic pathway that include the abundances of H<sub>2</sub>, CH<sub>4</sub>, and CO<sub>2</sub> will likely be obscured by the high level of radiolytically produced H<sub>2</sub> from the surface ice that is also found in abundance in the atmosphere. However, alternative measurement pathways are available for identifying chemical energy in the Europa system using minor and trace organic compounds, which leads to a requirement on the mass resolution and the sensitivity of the measurements. Once more we can turn to

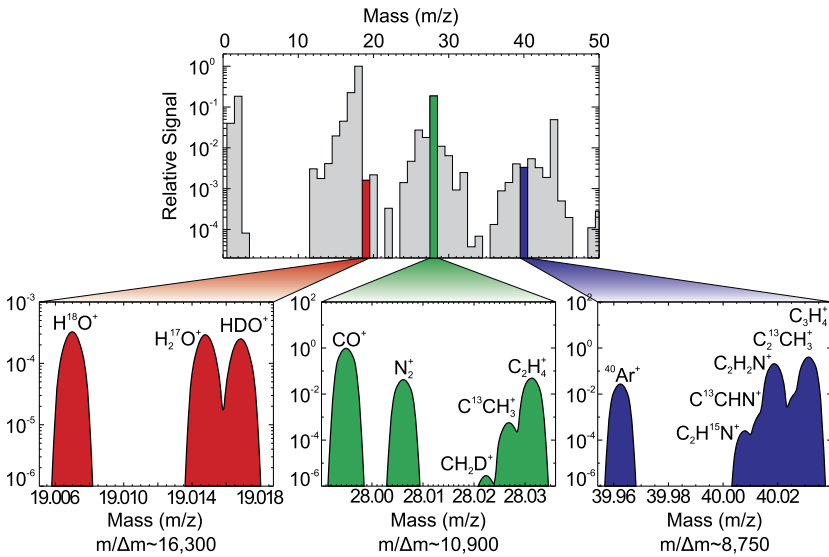


**Fig. 1** Upper panel shows Cassini INMS spectrum from Enceladus at unit mass resolution. The lower panels show simulations of potential species ion peaks convolved within each unit mass channel of the Cassini INMS spectrum, and how they may be observed and resolved with MASPEX. A dynamic range of  $\sim 10^6$  and mass resolution on the order of 17,000 ( $m/\Delta m$ ) at 10% valley is necessary to settle the most important current questions about the composition of Enceladus' plume as a model for Europa plumes: 1) direct measurement of all  $\text{H}_2\text{O}$  isotopes, 2) determination of C, N, O content via numerous ion separations (e.g.,  $[\text{N}_2^+, \text{CO}^+, \text{C}_2\text{H}_4^+]$  at 28 u,  $[\text{C}_2\text{H}_2\text{N}^+, \text{C}_3\text{H}_4^+]$  at 40 u, etc.), and 3) determination of noble gases such as  $^{40}\text{Ar}$  in the presence of near isobaric organic interferences

the Cassini INMS measurements at Enceladus to determine those requirements. Magee and Waite Jr (2017) have shown that clear evidence of organic compounds can be obtained if one is able to probe gas volume mixing ratios in the range from one part per thousand to one part per million, thereby setting the MASPEX sensitivity requirement. On the other hand, INMS did not have the mass resolution to properly identify the organics encountered and had to rely on extensive spectral deconvolution to reach somewhat ambiguous conclusions. However, these ambiguities serve as a guide for setting the mass resolution requirement for MASPEX as illustrated in Fig. 1. We set as a mission goal, the ability to determine the C, H, O, N, and S containing organic compounds less than 200 u (unified atomic mass units), which amounts to a mass resolution of 17,000 ( $m/\Delta m$ ) using the 10% valley definition. MASPEX, as delivered to Europa Clipper, can reach this goal, even though the mission level requirement for mass resolution is 4275 ( $m/\Delta m$ , 10% valley).

## 2 Science Objectives

MASPEX-Europa is an integral part of the Europa Clipper mission, making high-mass-resolution, high-sensitivity measurements of neutral gases in Europa's exosphere and within plumes. These measurements are designed to address three objectives:

1. Determine the distribution of major volatiles and key organic compounds in Europa's tenuous exosphere and their association with geological features,

2. Determine the relative abundances of key volatile compounds to constrain the chemical conditions of the European ocean, and
3. Search for potential biosignatures in the European environment.

MASPEX Objective 1 (MO1) is focused on advancing our understanding of Europa's atmosphere, geology (Daubar et al. 2024), and habitability (Vance et al. 2023). Data from MASPEX Objective 2 (MO2) will provide critical insights into Europa's interior (Roberts et al. 2023), geochemistry, and habitability (Vance et al. 2023). Both objectives are strongly linked to the Level-1 and Level-2 science requirements of the Europa Clipper mission. MASPEX is complementary with the SURface Dust Analyzer (SUDA), the Europa UltraViolet Spectrograph (Europa-UVS), and the Mapping Imaging Spectrometer for Europa (MISE) investigations.

MO1 contributes to Europa Clipper's goal of creating global composition maps via the spatial association of volatile abundances with surface features, especially potential organic materials and gas-releasing minerals that can constrain subsurface geochemistry and habitability. In addition, MO1 is important to the mission's goal of characterizing the atmospheric composition from globally distributed MASPEX measurements of major volatiles and key organic compounds. Such measurements can reveal outgassing sources based on heterogeneities in the atmosphere. MO2 leverages Europa Clipper's goal of searching for plumes, and if they are found, will seek indicators of ocean geochemical processes relevant to habitability by combining relative fluxes of endogenous plume gases with geochemical modeling. Both objectives represent a logical progression from the current state of the literature on Europa (see below), as well as being inspired and informed by past experience of linking mass spectrometry to surface or subsurface processes at Enceladus and other icy satellites in the Saturn system (Waite Jr et al. 2006; Glein et al. 2008; Waite Jr et al. 2009; Teolis et al. 2010; Bouquet et al. 2015; Glein et al. 2015; Teolis and Waite 2016; Teolis et al. 2017a; Waite et al. 2017; Postberg et al. 2018; Glein and Waite 2020; Ray et al. 2021; Hao et al. 2022). MASPEX Objective 3 is a more ambitious goal that seeks to identify known Earth-like biosignatures to directly assess the potential existence of microbes. Such a goal will stretch the dynamic range of the MASPEX measurements, but since it can easily be incorporated into the science measurement plan, exploring this goal in an unknown environment is quite reasonable.

## 2.1 Motivation and Details of MASPEX Objective 1

Europa's surface is predominantly water ice, with an admixture of non-ice material thought to consist primarily of hydrated magnesium and sodium sulfate and/or hydrated sulfuric acid (Carlson et al. 2009; Dalton et al. 2012; Brown and Hand 2013). Sodium chloride has been inferred by detection of a 450 nm absorption feature that is indicative of NaCl (Trumbo et al. 2019). Other than H<sub>2</sub>O, the only molecular species that have been definitively detected on the surface are SO<sub>2</sub>, CO<sub>2</sub>, H<sub>2</sub>O<sub>2</sub>, and O<sub>2</sub> (Carlson et al. 2009; Villanueva et al. 2023). Trace amounts of Na and K have been detected in Europa's exosphere, consistent with the presence of sodium and potassium salts on the surface. Chlorine and SO<sub>2</sub> may be present as well (Brown 2001; Cassidy et al. 2009, and references therein). Organic compounds have not been detected on the surface of Europa but would have been present in the rocky and icy materials from which it accreted. Many formation scenarios advocate for the accretion of Europa from solids originating from the giant planets' formation region (Mousis and Gautier 2004; Ronnet et al. 2018; Ronnet and Johansen 2020), implying that the organic-rich composition of comets (Goesmann et al. 2015; Altwegg et al. 2017) or alternatively



carbonaceous chondrites (Reynard and Sotin 2023), can be considered as a proxy for the primordial composition of the Galilean moons' building blocks.

The first two objectives of the MASPEX-Europa investigation are, through measurement of the sputter or radiolytically produced exosphere and possible plumes, to extend our knowledge of Europa's surface composition and its relation to the interior ocean, with particular emphasis on detecting the presence of organic compounds. The sputter-produced exosphere may contain both parent organic and inorganic molecules, and products of radiolysis such as  $\text{CH}_4$ ,  $\text{C}_2\text{H}_X$ ,  $\text{CO}$ ,  $\text{CO}_2$ ,  $\text{CH}_3\text{OH}$ ,  $\text{HCN}$ , and  $\text{H}_2\text{O}_2$  (Teolis et al. 2017c). Although the only chemical species inferred in the plume is  $\text{H}_2\text{O}$  (Roth et al. 2014; Paganini et al. 2020), it may be expected that European plumes, like that at Enceladus (Waite Jr et al. 2009; Waite et al. 2017; Postberg et al. 2018; Khawaja et al. 2019), will contain numerous minor and trace species, including organic compounds.

The degree to which the composition of the surface reflects the composition and chemistry of the interior and ocean is not known, although exchange of material between the surface and the interior is thought to be likely and apparent from the high degree of geological rifts and associated dark coloration of its surface. Europa's global- and regional-scale fault systems may provide communication pathways between the interior, the surface, and the exosphere (e.g., Tobie et al. 2010). The close association of sulfate and other non-ice materials with Europa's younger ridges (Carlson et al. 2009; Dalton et al. 2012) suggests that fluid and/or volatile flow along faults and fractures may have transmitted subsurface fluids to the surface in the past, and suggests a potential source for recent activity as well, i.e., plumes (e.g., Prockter et al. 2010; Sohl et al. 2010). Younger regions such as Thera and Thrace Macula may represent areas of active diapirism and/or partial melt and/or brine infiltration, with the potential for cryovolcanism and plume formation (e.g., Greeley et al. 2004; Schmidt et al. 2011). The ultimate form of surface-interior exchange of volatiles is represented by plume emissions (Roth et al. 2014; Sparks et al. 2017; Jia et al. 2018; Paganini et al. 2020).

MASPEX will inventory major and minor species in Europa's exosphere and plumes with unprecedented sensitivity and mass resolution during multiple flybys over different regions and terrain types. In addition to the most abundant species (e.g.,  $\text{H}_2\text{O}$ ,  $\text{H}_2$ ,  $\text{O}_2$ ,  $\text{CO}_2$ ), the most likely sputtered (Johnson et al. 2009) and/or plume-derived (Waite Jr et al. 2009; Magee and Waite Jr 2017) organic compounds (e.g.,  $\text{CH}_4$ ,  $\text{C}_2\text{H}_2$ ,  $\text{C}_2\text{H}_4$ ,  $\text{C}_2\text{H}_6$ ,  $\text{HCN}$ , and  $\text{CH}_3\text{OH}$ ) will be measured, thus providing the first definitive detection of organic compounds and nitriles on Europa if they are present. Because no conclusive spectroscopic detection of any N-bearing molecule on Europa has been made (Carlson et al. 2009), a measurement of this critical biogenic element as  $\text{N}_2$ ,  $\text{NH}_3$ , or organic N in the exosphere or a plume (as at Enceladus Waite et al. (2017)) will also be significant for assessing habitability.

Modeling the formation and maintenance of Europa's largely sputtered atmosphere and its expected variance has been a major objective of the MASPEX science team (Teolis et al. 2017b,c). Our models demonstrate that a European plume source, if present, may produce a global exosphere with complex spatial structure and temporal variability in its density and composition (see Sect. 3.2). The MASPEX science team has investigated this interaction using a water-source plume containing multiple organic and nitrile species introduced into a Monte Carlo exosphere model (see Fig. 2), taking account of the effect of Europa's gravity in returning plume ejecta to the surface, and the subsequent spreading of adsorbed and exospheric material by thermal desorption and re-sputtering across the entire body. We considered sputtered, radiolytic and potential plume sources, together with surface adsorption, regolith diffusion, cold trapping, and re-sputtering of adsorbed materials, and examined the spatial distribution and temporal evolution of the exospheric density and composition.

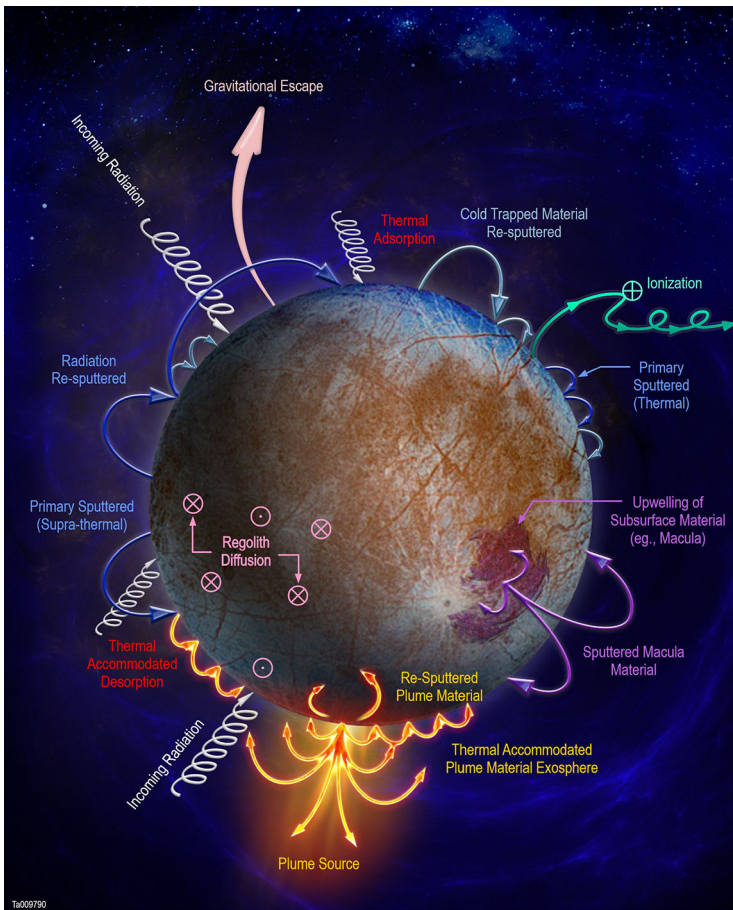


**Fig. 2** A complex set of processes controls the composition of Europa's exosphere. By determining the spatial and temporal variability of numerous exospheric chemical species, MASPEX will provide new constraints on how these processes work and are connected, as well as the potential to discover currently unrecognized processes (Teolis et al. 2017c)

While the mere detection of organics is of fundamental importance for the question of habitability, it is of equal importance to determine their source, whether Europa's interior or the icy surface. Volatiles detected in a plume may originate in the ocean of Europa or a subsurface lake (e.g., Postberg et al. 2011; Vorburger and Wurz 2021), although release of volatiles from a subsurface clathrate reservoir must also be considered, e.g., Kieffer et al. (2006). If the source is the surface, then knowledge of the terrain type and the relative timescales of radiologic and sputter modification compared to volatile resurfacing is important and is highly dependent on surface location. The plasma electron and energetic particle fluxes depend on the surface position relative to the direction of plasma sheet impingement (Paranicas et al. 2000). There is also location-specific surface modification by diurnally varying volatiles such as water and from seepage of resurfacing volatiles from regions of chaos that are below present levels of detection. This provides a complex geological network of radiolysis/sputtering modification versus volatile resurfacing timescales that are present on the surface, and that must be evaluated for assessing the significance of the detection.

Detection over an impact site, for example, could indicate exogenic origin, while volatiles detected over disrupted terrain may represent material from the ocean or other subsurface water reservoir that may have been deposited relatively recently on the surface through cryovolcanism (Carlson et al. 2009) and have experienced less radiolytic processing than older terrain types.

Correlation of MASPEX measurements with any plumes or disrupted terrain will help constrain past and present material exchange between the European ocean, ice shell, and the surface. The detection of noble gases would be an indicator of the delivery of recent plume or ocean waters to the surface and of the possible contributions of chemical compounds trapped in clathrates (Bouquet et al. 2019).

Argon-40, a decay product of potassium-40, is a critically important tracer of geological vigor and interior-surface exchange. Potassium has been detected in Europa's exosphere (Brown 2001; Johnson et al. 2002, 2009). Potassium salts are soluble in water, consistent with the K-chlorides and -carbonates in Enceladus plume particles (Postberg et al. 2009). Decay of  $^{40}\text{K}$ , coupled with degassing or venting on Europa, could release measurable  $^{40}\text{Ar}$  into the exosphere. Substantial  $^{40}\text{Ar}$  has been detected in Titan's atmosphere (Waite et al. 2005a; Niemann et al. 2010), and in the thinner Martian atmosphere, e.g., Mahaffy et al. (2013). Utilizing cryotrapping at Europa, our detection threshold for a one second integration is  $\sim 1$  ppm. Cryotrapping over multiple flybys would increase the signal-to-noise ratio to enable detection if ocean-sourced plumes contain sub-ppm levels of  $^{40}\text{Ar}$ . Sputtering of surface salts derived from ocean waters rich in K (Zolotov and Kargel 2009) may be another source of exospheric  $^{40}\text{Ar}$ . In-situ mass spectrometry offers the most sensitive search possible for  $^{40}\text{Ar}$  at Europa.

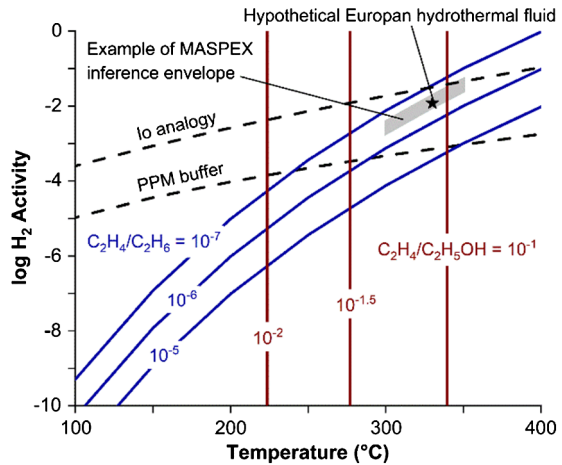
## 2.2 Motivation and Details of MASPEX Objective 2

Questions of habitability and selection of potential sites for a future Europa lander (Hand et al. 2022) require measurement and consideration in the context of multiple chemical compounds. Maximizing the variety of well-characterized abundances and isotopic compositions will reveal the complex history of geochemical transformations on Europa driven by external magnetospheric influences and internal geophysical and geologic processes. Plume volatiles extracted from an internal ocean provide the most direct means of using composition to infer the chemistry of the ocean, but surface retention of degassed volatiles also provides valuable information when considered within the context of radiolytic and thermal modification.

If there are organic compounds on the surface of Europa, inferences about their source and significance can be drawn from radiolytic products detected in the exosphere. Organic compounds subjected to irradiation produce organic solids dominated by polycyclic aromatic hydrocarbons. Irradiation produces progressively higher molecular weight organic networks as polymerization proceeds, increased aromatic/aliphatic ratios as aromatization continues, and increasing  $^{13}\text{C}$  contents as the more reactive  $^{12}\text{C}$  atoms are expelled, see Court et al. (2006). The presence of  $\text{H}_2\text{O}$  during radiolysis allows oxidation reactions involving  $\text{O}_2$ ,  $\text{H}_2\text{O}_2$ , and hydroxyl radicals (Carlson et al. 2009).

Internal hydrothermal activity can lead to oxidation and dehydration of organic compounds. The possibility for high-temperature water-rock reactions (either now or in the past) (Moore and Hussmann 2009; Běhounková et al. 2021) also means that there may be conditions where abundances of organic compounds are under thermodynamic control. This means that the relative abundances of such compounds can be used as indicators of whether their reactions occurred in the colder overlying ocean or in hydrothermal systems. For example, equilibrium ratios of alcohols to alkenes that are indicative of dehydration reactions

**Fig. 3** MASPEX can provide evidence of hydrothermal conditions that feed into Europa's potential habitability. Thermodynamic calculations shown here were performed using SUPCRT92 (Shock and Helgeson 1990; Johnson et al. 1992; Plyasunov and Shock 2001) for a subsurface pressure of 2000 bar on Europa



vary systematically with temperature, allowing measurements of these classes of organic compounds to be used as geothermometers (Bockisch et al. 2018). In addition, ratios of alkanes, indicative of oxidation or reduction reactions, can reveal the temperatures at which those reactions occurred (Shock et al. 2013). Ratios of alkanes to alkenes that are representative of hydrogenation reactions can be used to assess whether oxidation states imposed by specific mineral assemblages exerted influence over the organic compounds (Helgeson et al. 1993; Cruse and Seewald 2006), providing evidence for rock-hosted hydrothermal circulation (Fig. 3).

The blue curves show redox-temperature conditions that reflect the indicated molar ratio of ethene-to-ethane. Here, the redox state is represented by the activity of  $H_2$  (unitless), which is related to the molal concentration of  $H_2$ . The burgundy lines show how the molar ratio of ethene-to-ethanol can be interpreted in terms of temperature of the last equilibration. Redox conditions in Europa's rocky interior are unknown, but the dashed curves represent an attempt to define plausible limits. The reduced endmember corresponds to an equivalent oxidation state of rocks and magma on Io that sets the redox speciation of observed volcanic gases (Zolotov and Fegley 2000). The oxidized endmember (PPM = Pyrrhotite-Pyrite-Magnetite) is consistent with the redox state of basalt-hosted submarine hydrothermal systems on Earth (Shock 1990). As an example, the asterisk designates a case with a temperature of 330 °C and an  $H_2$  concentration of 12 millimolal. The corresponding equilibrium ratios of ethene/ethanol and ethene/ethane are  $8.5 \times 10^{-2}$  and  $3.1 \times 10^{-7}$ , respectively. A 30% uncertainty in the abundances of ethane, ethene, and ethanol measured by MASPEX would lead to inferred conditions within the gray area, with temperature constrained to 299–351 °C and  $H_2$  concentration constrained to 2 to 59 millimolal. With additional determinations of redox- and/or temperature-sensitive ratios of other volatiles, these ranges can be decreased by elucidating smaller sections of the parameter space where consistency with equilibrium is maintained within a larger set of reactions.

Redox (oxidation) states in the ocean and in subjacent rocks play a major role in habitability. The only thing we know for sure is that the outer surface of Europa is highly oxidized due to radiolysis caused by intense Jovian magnetospheric ion and electron bombardment. The existence of possible redox couples determines the nature and productivity of potential subsurface life; that is, the energy available to support maintenance, growth, and reproduction (Nealson 1997; Jakosky and Shock 1998; Hand et al. 2009), but we do not know the oxidation state of the ocean and rocky mantle below. If material can get from the surface to

the ocean, which is surely true in some sense and over some time scales (Hand et al. 2007), given the geologic youth of the surface and the evidence for crustal spreading and even subduction (Kattenhorn and Prockter 2014) then the ocean will slowly oxidize (as the Earth's ocean did at the end of the Archean (Lyons et al. 2014)). Determining the relative ratios of redox-sensitive compounds (C, N, and S species) in the ocean is the key to determining oxidation state (Shock and McKinnon 1993).

MASPEX will measure abundances of multiple H, C, N, and S species. Potential measurements of D/H,  $^{13}\text{C}/^{12}\text{C}$ ,  $^{15}\text{N}/^{14}\text{N}$  and O isotopes could, in addition, constrain the origin of these chemical compounds and/or provide solar system context (McKeegan et al. 2011; Mumma and Charnley 2011; Alexander et al. 2012; Cleaves et al. 2014). For example, measurements of D/H in  $\text{H}_2\text{O}$  and other H-bearing volatiles would allow disentangling different pre-formation and post-formation evolutionary scenarios (Ronnet et al. 2017; Bierson and Nimmo 2020; Mousis et al. 2023) that led to the current ice-to-rock ratio of Europa. Sampling of the  $^{15}\text{N}/^{14}\text{N}$  ratio in Europa's exosphere and its comparison with values measured in Jupiter, Saturn, Titan, and comets would shed light on the nature of the main reservoir from which N-bearing materials (Glein 2023) were delivered to this moon. MASPEX offers unprecedented detection capabilities for  $\text{N}_2$ ,  $\text{NH}_3$ , HCN, and more complex N compounds that may exist in the ocean.  $\text{N}_2$  is the expected product of a high-temperature oxidation of original N species (Matson et al. 2007; Miller et al. 2019), but because of its low solubility is expected to escape over time. Detection of  $\text{N}_2$  in a plume may indicate geologically recent oxidation of N-containing species in the interior. The ratios of reduced and oxidized N compounds (e.g.,  $\text{NH}_3/\text{N}_2$ ) in a plume can constrain the redox state of the ocean and degree of redox equilibration (e.g., Glein et al. 2008) provided other redox pairs and compounds can be measured.

Europa's ocean water could be rich in C-containing species, consistent with the detection of  $\text{CO}_2$  in reddish, disrupted surface areas (Hansen and McCord 2008). Inorganic C-containing species could be predominately bicarbonate and carbonate ( $\text{HCO}_3^-$ ,  $\text{CO}_3^{2-}$ ), though near-surface decompression of ocean water would lead to exsolution of  $\text{CO}_2$  gas (Daswani et al. 2021). In the ocean, inorganic and organic C species could coexist metastably owing to slow kinetic rates of redox reactions.  $\text{H}_2$ ,  $\text{CH}_4$ , and organic species could coexist with oceanic sulfate in particular, providing energy for putative sulfate-reducing organisms (Zolotov and Shock 2004). MASPEX will determine the key  $\text{CH}_4/\text{CO}_2$  ratio, or set strict limits, in any plumes. Concentration ratios (e.g.,  $\text{NH}_3/\text{N}_2$ ,  $\text{CH}_4/\text{CO}_2$ ,  $\text{C}_1/\text{C}_2/\text{C}_3$ , aliphatic/aromatic,  $\text{H}_2/\text{H}_2\text{O}$ ) will indicate temperature, pH, redox conditions, and extent of hydrothermal reactions that involve organic compounds. Thermodynamic calculations based on these measurements will also be used to quantify deviation from chemical equilibrium (McCollom and Shock 1997; Lu et al. 2021).

MASPEX measurements will quantify sources of chemical energy available for organisms that use  $\text{H}_2$  as electron donor (e.g., methanogens and sulfate reducers) that could live in the ocean-rock system (McCollom 1999; Zolotov and Shock 2004). For example, the amount of free energy for methanogens can be evaluated from the reaction  $\text{CO}_2 + 4\text{H}_2 \rightarrow \text{CH}_4 + 2\text{H}_2\text{O}$ , if all of these species are measured (Waite et al. 2017). Absence or extreme paucity of  $\text{H}_2$  in plume gases would indicate oxidized systems or a lack of active water-rock interactions (past  $\text{H}_2$  should have escaped) and limited sources of free energy to support life. A low  $\text{H}_2/\text{H}_2\text{O}$  ratio ( $<10^{-7}$ ) would be consistent with an oxidized sulfate-bearing ocean, while higher ratios ( $>10^{-7}$ ) would characterize a NaCl-type ocean without sulfates, assuming thermodynamic equilibrium (Zolotov and Kargel 2009). Detection of  $\text{H}_2\text{S}$  would be a direct indicator of a sulfidic rather than a sulfate-rich ocean (Zolotov 2008). If plume or other endogenic sources of  $\text{H}_2$  do not supply sufficiently large fluxes of  $\text{H}_2$ , then any  $\text{H}_2$  signal detected by MASPEX may be swamped by the surface radiolytic flux of  $\text{H}_2$ . In this case,



ratios of other redox-sensitive species would be needed to constrain the H<sub>2</sub> concentration in subsurface fluids.

### 2.3 Motivation and Details of MASPEX Objective 3

Finally, independent of the source of organics, MASPEX will search for suggestions of biology. Non-biological organic matter, such as that preserved in carbonaceous chondrites, is generally characterized by complete structural diversity (Sephton 2002, 2014). The number of isomers that can be produced by non-biological processes increases exponentially with the number of carbon atoms. For instance, ten carbon alkanes can have over 70 isomers while 20 carbon alkanes could have over 350,000 isomers (Sephton et al. 2018). In contrast, when organic synthesis is directed by biological enzymes, all the carbon atoms can be used to produce a single organic isomer. Biological origins of organic compounds are most obvious when both specificity and complexity are evident as noted by Summons et al. (2008), “Another characteristic of living things, also likely to be pervasive, is that an enormous diversity of large molecules are built from a relatively small subset of universal precursors. These include the four bases of DNA, 20 amino acids of proteins and two kinds of lipid building blocks.”. For example, a range of extremophile Archaea and Bacteria have been analyzed and the laboratory data converted to MASPEX-type signals (Salter et al. 2022). Molecules characteristic of protein, carbohydrate and lipid structures were detected and the characteristic fragmentation patterns corresponding to these different biological structures were identified (see Sect. 3.1.2). Protein pyrolysis fragments included phenols, nitrogen heterocycles, and cyclic dipeptides. Oxygen heterocycles, such as furans, were detected from carbohydrates. These data reveal how mass spectrometry on Europa Clipper can aid in the identification of the presence of life, by looking for characteristic microbial fingerprints that are similar to those from simple Earthly organisms. In addition, natural fatty acids on Earth occur as a set of even numbered carbon compounds (C<sub>4</sub>, C<sub>6</sub>, etc.). The directed nature of biological synthesis is readily detectable by mass spectra fragmentation patterns (Peters et al. 2004). A mass spectrometer with the mass range and resolution of MASPEX is by far the best instrument to characterize the organic molecule suite in any ocean water that may be vented to space above Europa.

## 3 Description of the Investigation

The MASPEX is a mass spectrometry investigation building on science returns from the Cassini-Huygens Ion Neutral Mass Spectrometer that made measurements of gas and grain composition deep inside the plumes of Enceladus (see for example, Waite et al. 2017; Postberg et al. 2018). MASPEX presents the opportunity to investigate the composition of the interior ocean of an icy moon in the outer solar system with much greater capabilities, enabling a unique and unprecedented class of astrobiological investigations (Schenk et al. 2018). The path forward for exploring the habitability of icy moons is through the identification of simple volatiles and organic compounds critical to determining the key characteristics of the European ocean’s oxidation state, hydrothermal characteristics, and pH. This information allows exploration of potential metabolisms that could tap the chemical energy of the ocean environment. Furthermore, MASPEX’s improvements in mass resolution over earlier instruments will greatly aid in the unique identification of organic compounds, especially the identification of oxygen, nitrogen, and sulfur-bearing organics, which are crucial to correctly identifying the ratios of relevant organic compounds that must be accurately quantified (see

Sect. 2.2 and Fig. 3). The low relative abundance of these compounds (<1%) originating from the outgassed surface and interior material put many of these compounds below the threshold for remote detection, thus requiring in situ measurements using mass spectrometry that can determine mixing ratios approaching parts per million. As discussed in Sect. 2, this was the backdrop for formulating the investigation.

MASPEX has two overarching science requirements: 1) cover the mass range from 1 to 500  $m/z$  (mass-to-charge ratio) at a minimum mass resolution of 4275 (10% valley), and 2) obtain high mass resolution spectra with adequate signal-to-noise for several key compounds of interest at mixing ratios of 1 part in 6000, requiring a dynamic range  $\geq 6000$ . Atmospheric modeling (Sect. 3.2) has been used to translate MASPEX science requirements into an operating scheme (Sect. 8.5.1) that satisfies the constraints on time and spatial resolution. In practice the latter requires a five-second spectral sampling cadence such that the spacecraft traveling at 5 km/s over the European surface allows MASPEX to measure spectra at closest approach at an altitude of 25 km, with a spatial resolution equal to the altitude of closest approach. Modeling also indicates that the longest co-addition of spectra needed to provide adequate signal-to-noise in the spectral segments containing the key trace species is one second. We simulated the dynamic range associated with a flyby (Sect. 6.3.1) and went on to discuss the sensitivity of a single extraction in Sect. 6.3.2.

The two distinguishing features of MASPEX are its exceptionally high mass resolution and sensitivity. This performance is accomplished using a novel ion optical design based on multi-bounce time-of-flight mass spectrometry, a storage-type ion source, and an external cryotrap. These elements of the MASPEX system are introduced in the remainder of this section and discussed in detail in Sects. 5 and 6.

High mass resolution relies on a multi-bounce time-of-flight (MBTOF) mass spectrometer comprised of two co-axial electrostatic mirrors facing each other in a 'reflectron' configuration. Ions bounce between the two reflectrons while remaining focused in time and space. In the MASPEX design, ions can 'bounce' as many as several hundred times, yielding times-of-flight up to several milliseconds. Because mass resolution is proportional to time-of-flight (TOF), resolutions over 100,000 can be attained. The reflectron technique was first applied in the laboratory by Ionov and Mamyrin (1953) and Mamyrin et al. (1973). It was then developed for space science applications on Giotto by Kissel et al. (1986) and on Rosetta by Balsiger et al. (2007). Significant later improvements by roughly an order of magnitude have been made by the MASPEX team (Young 2006; Young and Waite Jr 2007; Brockwell et al. 2016).

The MASPEX optical design leads to exceptionally high mass resolution since  $m/\Delta m = t/2\Delta t$  and  $t$  can be extended for an arbitrarily long period of time (resolution is also equivalent to  $l/2\Delta l$ ). MASPEX can also operate at relatively low resolution in a straight-through (i.e., without bouncing) configuration using the 50-cm long MBTOF ion optics tube. When operated in the multi-bounce mode, ions are focused into tight isochronous packets with flight times that can reach over one millisecond. (Fig. 47), approaching flight distances of roughly one kilometer for protons. Furthermore, with tight focusing, and the fact that resolution is  $\sim m/\Delta m$ , mass resolution increases with mass up to  $\sim 500 m/z$ , further contributing to high resolution capabilities (Fig. 49). As a result, MBTOF can reach resolutions over 25,000 at full-width half-maximum of the mass peaks. This was demonstrated during calibration (Sect. 6.4.2), and is more than sufficient to measure the substitution of the hetero atoms O, N, and S in organic molecules in the mass range up to 50 u. (Note that by convention we will use mass to charge ( $m/z$ ) when discussing ions and ion optics, and u when discussing chemical compounds, reactions or identifications.)

The electron ionization source design is not only important in determining mass resolution, but its ion storage capabilities also lead to high sensitivity that is important for

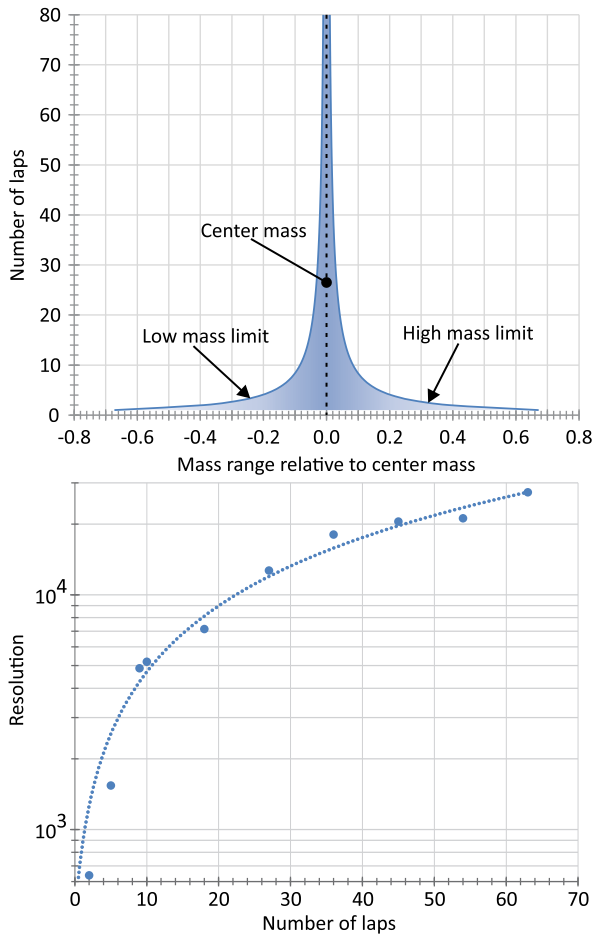


producing high dynamic range (Sect. 6.3.1). The ion source high voltage switching system operates at 1 kHz allowing a trade between dynamic range and temporal resolution. However, the key to the high dynamic range of the instrument lies in its ability to cryotrap gas samples on a sintered stainless-steel collector and retain it for analysis later, after the flyby data have been analyzed. The large quantity of gas in the cryotrap results in pressures in the instrument higher than the peak pressure seen during the flyby. This produces larger signals from the sample that can be equated to an increase in effective sensitivity, though the base source sensitivity is unchanged. The larger sample from the cryotrap enables the instrument to reach its maximum dynamic range. The other advantage of trapping gas during a flyby and analyzing the sample a few days later, is that it allows time to examine flyby mass spectra and optimize the instrument programming for the following cryotrap analysis. The flyby data are combined into a single spectrum that is downlinked right after the flyby. With this information, appropriate mass resolution can be applied to interesting portions of the spectrum, and the number of source extractions for selected mass ranges of low abundance compounds of interest can be increased. This process is referred to as ‘feedforward’ analysis and is discussed in detail in Sects. 3.3 and 8 covering operations.

The MBTOF measurement technique brings with it several technical and operational challenges that must be properly dealt with. As the number of ion bounces increases, “race-tracking”, or overlapping ion trajectories and times-of-flight, can occur between the lightest (fastest) and heaviest (slowest) ions in the extracted packet. An ion that completes a bounce off the back and front reflectrons in succession is said to have completed one “lap” (see Sect. 5.4.3). This requires the total mass range to be reduced by selectively raising and lowering reflectron voltages to keep the selected ions on the same total pathlength. Mass resolution and mass range are therefore linked – achieving a particular mass resolution fixes the mass range at a specific value, and vice versa. From a technical point of view, raising and lowering of the reflectron’s mirror potentials is not instantaneous, which creates some distortion of the mass spectrum near the time when the mass spectrum is cut. This inevitably leads to a few spurious masses continuing to appear in the spectrum. To identify this phenomena and deal with the issue we use a technique that alternates between  $n$  laps of ions through the flight tube, and  $n + 1$  laps. The mass spectra of interest shift in a predictable way within the spectrum, but the ‘errant’ mass peaks will appear to randomly shift or disappear. By operating the instrument in the  $n$  and  $n + 1$  lap mode the errant masses can be identified and dealt with during data analysis. The overall approach requires operational decisions that trade mass resolution for spectral range covered. The higher the required mass resolution the larger the number of laps, which results in a decreasing mass range over which the instrument can maintain ions on the same lap. Figure 4 illustrates the operational tradeoff in which a full mass range spectrum is constructed by combining segments covering different mass ranges at different resolutions. These must be selected in advance of a flyby based on the science requirements.

This leads to the important scientific question driving the MBTOF design: what mass resolution is required? This issue has already been discussed (Sect. 1) in the general scientific context of separating hydrocarbons from oxygen-bearing organics, and from nitrogen- or sulfur-bearing organic compounds. It is important to choose the minimum mass resolution needed to satisfy measurement requirements (in our case  $4275 \text{ m}/\Delta\text{m}$  at 10% valley). This choice gives the widest mass range, and thus the most efficient use of the time spent in the spatial sampling region, resulting in more ion source extractions over the mass segment of interest and thus increased dynamic range. The key to the choice of mass resolution is in understanding and deciding on the potential compounds that might lead to spectral interferences as discussed above. Thus, our operating approach relies heavily on modeling and,

**Fig. 4** The mass resolution / mass range trade-off. Top panel: The variation of MASPEX mass range with number of laps. The zero point on the  $x$  axis in the upper panel represents the center mass ( $m_c$ ) of the spectrum. The high and low mass limits may be calculated from  $limit = m_c + m_c \times R$ , where  $R$  is the value read from the  $x$ -axis at the desired number of laps. Bottom panel: The variation of mass resolution with the number of laps for 44  $m/z$  ions. Data redrawn from (Brockwell et al. 2016)



in particular, on previous measurements, to simulate the operation and determine the mass resolution needed to overcome any interferences. This is confounded by the unknown European atmospheric environment and can be exacerbated by molecular contamination from both internal and external sources.

Concerns about contamination will be operationally mitigated by three long (8 hour plus) contamination measurement campaigns in the appropriate target environment. These will fully measure and characterize the contaminant molecules – the levels of which are not high enough to interfere with the most abundant target volatiles but are abundant enough to threaten the identification of minor and trace compounds. Mitigation is particularly important, since ratios of minor and trace compounds, as discussed in Sect. 2, are key to some of the most important science goals of the MASPEX investigation.

### 3.1 Science Inputs and Examples

The three key science goals of the MASPEX instrument are to constrain the properties and composition of Europa’s interior and ocean to determine whether habitable environments exist there, and to search for direct biosignatures of life. While there are other chemical

and physical processes that we also want to explore on Europa, we began the process of gathering comparison data using these goals, and specifically three examples:

1. Major volatiles, which can be used as tracers for properties of the interior and which we expect to be present in larger abundances in Europa's atmosphere and/or plumes,
2. Organics, which can also be used as tracers for the properties of the interior and which we expect to be present in lower abundances, and
3. Biosignatures of microbial life, and specifically analogs of species like *Halomonas halodentrificans*, which thrive in cold, salty water on Earth and are likely the lowest abundance compounds of measurement interest.

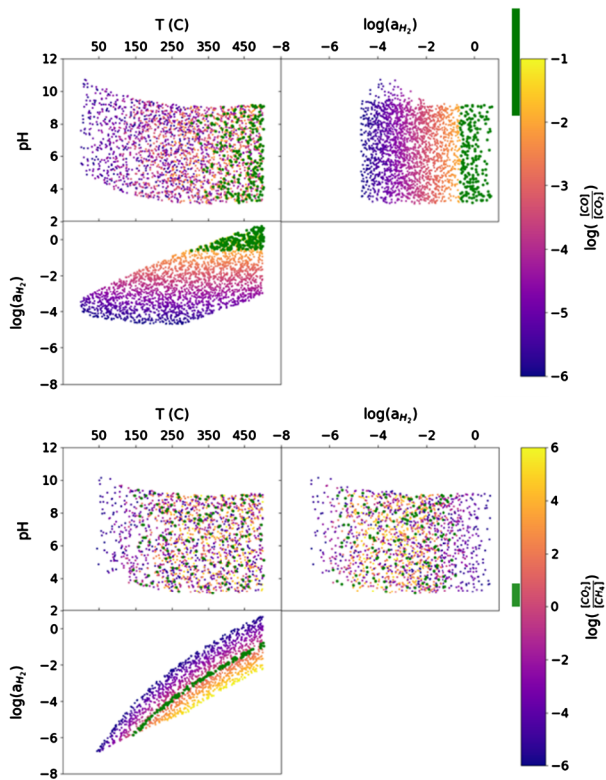
### 3.1.1 Tracing Geochemistry with Volatiles and Organic Compounds

The first two examples are complementary and represent similar science goals. The guiding scientific idea behind these two goals is that the properties of Europa's interior, including oxidation state, pH, temperature, and pressure, determine the forms and abundances of chemical species produced, if temperatures are sufficiently high and/or durations are sufficiently long such that thermodynamic equilibrium can be achieved. We also note that these thresholds can be vastly different among reaction classes. Some reactions equilibrate virtually instantaneously in superheated water while others may require millions or billions of years to reach steady state. By modeling the equilibrium speciation of major volatiles and organic reactions across a broad range of parameters, and calculating chemical compound ratios across this parameter space, we can determine which ratios best constrain different pairs or sets of parameters. When a given volatile or organic compound is measured with MASPEX, the feedforward science decision making process (see Sect. 8.4) can determine which parameters set the abundance of that species, and which additional species should be measured to calculate an abundance ratio that further constrains those same parameters.

An example of how sets of ratios of major volatiles can be used to constrain interior properties is provided here. Modeled  $\text{CO}/\text{CO}_2$  and  $\text{CO}_2/\text{CH}_4$  abundance ratios are shown as functions of interior temperature, oxidation state, and pH, with constrained values from the Enceladus plume overplotted in green for demonstration (Fig. 5). Both ratios provide tight constraints on temperature and oxidation state – when used together they can provide an even tighter constraint on these properties or reveal disparities that may be telling of other processes occurring. For Enceladus, the constraints do not agree and instead reveal two possible solutions within the parameter space. The discrepancy could be due to a number of chemical processes and/or measurement complications. With MASPEX, we can measure many more ratios to target these internal properties – the more compound ratios that can be compared, the more tightly the system can be constrained, and the greater the likelihood of untangling processes that cause apparent deviation from a single equilibrium state.

The minor and trace organic compounds that will be included in the measurement framework will work similarly. Since these chemical compounds will likely be present in much lower abundances than the major volatiles, our strategy is to search for major volatiles in the flyby data, determine which interior properties we could constrain using them, then search for pairs or sets of organics that further constrain those same properties in the cryotrapped dataset. The organic compounds also come with additional complications that turn out to be advantageous – the more complex the molecule (e.g., longer carbon chains, multiple functional groups), the more possible reactions and, therefore, the more geochemical parameters of interest that affect compound abundances. An example is shown for ethanol and its potential reaction products in Fig. 6 based on the framework described in Robinson et al.

**Fig. 5** Predicted equilibrium ratios for CO/CO<sub>2</sub> (top panels) and CO<sub>2</sub>/CH<sub>4</sub> (bottom panels) across 3000 different hydrothermal models. Each model has a temperature, oxidation state (log aH<sub>2</sub>), and pH value randomly chosen within wide bounds derived from present knowledge of Europa and other solar system analogs (Earth, Enceladus, and carbonaceous chondrites); the color of each dot shows the value of the predicted equilibrium ratio as indicated on the color bar. Green dots indicate areas of the parameter space consistent with the range of ratios observed in the Enceladus plume (green bar next to the color scale), demonstrating how observations can be used with these types of models to constrain the parameter space or reveal inconsistencies between measurements



(2023). While equilibrium abundances among ethanol, ethoxyethane, and ethene are controlled purely by temperature (T) and pressure (P, red boxes), reaction product distributions of ethane, ethyl acetate, and ethylamine depend additionally on oxidation state (aH<sub>2</sub>, blue box) and pH (yellow box). The accompanying plot shows how hypothetical measurements of ethene and ethanol could be compared with existing thermodynamic data to constrain the temperature and pressure at which the species equilibrated, at hydrothermal conditions in this example. All of the branching reaction pathways could theoretically occur and equilibrate within Europa (Xu et al. 1991; Seewald 1994, 2001; Robinson et al. 2020; Yoshida et al. 2021; Robinson et al. 2023; Yoshida et al. 2023), and therefore represent multiple pathways that could be taken in the science decision making process (see example decision tree in Fig. 6), depending on which pairs or sets of compounds are initially measured. Beyond this example with two-carbon organic species, a vast network of reactions that could influence decision making will need to be considered.

### 3.1.2 Biosignatures

Although we can search for fragments of many microbes based on the work of Vance et al. (2007); Salter et al. (2022), a good first example is *H. halodentrificans*, which thrives in cold, salty water similar to the expected Europa environment. The fragments associated with this microbe can be grouped into different categories, outlined in Table 1. The challenge with this science goal is simply to determine whether these complex and often high mass fragments belong to life or are abiotic in origin. This must be demonstrated statistically – therefore

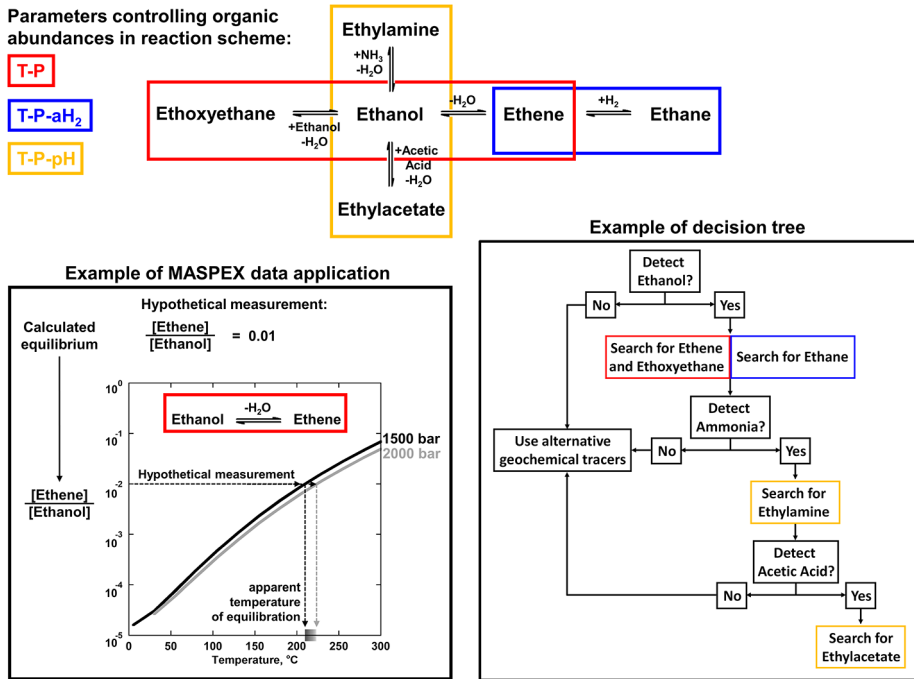


**Fig. 6** An example of geochemical tracers to target and the application of hypothetical MASPEX measurements in the feedforward science decision-making tool if different sets of two-carbon organic species are measured. According to the figure (from Shock and Helgeson 1990), a dynamic range of 6000 would allow detection of ethene/ethanol ratios consistent with hydrothermal activity greater than approximately 100 °C. An error in the ratio measurement of ±30% (for a sample that came from 100 °C) would result in error bars of approximately ±10 °C (an interpretation that the sample equilibrated at approximately 90-110 °C)

the more fragments in the table that can be measured and the better their abundances constrained, the more reliably they can be traced back to these experimental spectra.

### 3.2 Relationship of MASPEX Data to Ocean Composition

The three science goals identified in Sect. 3.1 form the basis of the MASPEX science investigation. Achievement of these goals requires the measurement of the source materials that drive the science in their environment. MASPEX, however, measures the composition of the atmosphere of Europa, and the materials present there are far removed from their sources.

The most direct sampling of the ocean would be MASPEX flying through a plume sourced from the ocean. However, even if a plume were present, the majority of MASPEX sampling will be over the surface of Europa where the presence of ocean materials will involve multiple different transport mechanisms and timescales that vary with local geology (Fig. 2). The surface materials will have had many opportunities for change in both composition and in chemistry as a result of their transport and surface exposure. Material in younger terrain is expected to retain more of the materials from the interior while older terrain materials will show the results of extensive radiolysis.

Beyond the effects of Europa’s environment on the measurements, there are also changes that occur to the sample because of sample collection and ionization that must also be considered in the interpretation of the data. We consider the key factors that will change the

**Table 1** Mass fragments associated with *H. halodentrificans* (Salter et al. 2022)

Compound type	Fragment ions ( <i>m/z</i> )	Possible origin	References
<i>Major components</i>			
Alkylbenzenes e.g., toluene, styrene, ethylbenzene (aromatic hydrocarbons)	65, 78, 91, 104, 106	Protein, peptides, amino acids	Stankiewicz et al. (1997)
Oxygen containing heterocycles (furans) e.g., Methyl-furan, dimethyl-furan, furfural, maltol	53, 69, 81, 82, 95, 96, 98, 109, 110, 126	Carbohydrates	Schrödter and Baltes (1991)
Nitrogen containing heterocycles e.g., Indole, benzyl nitrile, pyrrole	63, 66, 67, 79, 80, 90, 93, 94, 117, 130, 131	Proteins, amino acids	Stankiewicz et al. (1997); Zhu et al. (2016)
Phenols e.g., phenol, methylphenol	66, 77, 79, 94, 107, 108, 122	Protein, peptides, amino acids	Chiavari and Galletti (1992)
Cyclic dipeptides (2,5-Diketopiperazines)	70, 86, 125, 153, 154, 168, 194, 208, 244	Peptides, proteins	Smith et al. (1988); Fabbri et al. (2012)
<i>Minor components</i>			
Alkanes	57, 71, 85, 99, 113, 127, etc.	Lipids	Schwarzbauer and Jovančićević (2020)
Fatty acids e.g., C16:0 acid	60, 73, 97, 129, 157, 171, 185, 199, 213, 241, 256, 284	Lipids	DeLuca et al. (1990)
Anhydrosugars	57, 60, 69, 73, 85, 98, 115, 144	Carbohydrates	van Der Kaaden et al. (1983); Kebelmann et al. (2013)
Phytol fragments	68, 82, 95, 109, 123, etc.	Chlorophyll	Kebelmann et al. (2013)
Alkylamides	59, 72	Reactions between lipid and protein	Kebelmann et al. (2013)
Alkyl nitriles	57, 97, 110, 124, 138	Reactions between lipid and protein	Chiavari et al. (1998)

ocean materials prior to measurement to be the effects of radiolysis, the effects of hypervelocity sampling, and the effects of electron ionization, all of which result in fragmentation of the original molecules into smaller moieties. Each factor is discussed in more depth in the next section. Fragmentation, however, is only one aspect of providing context for the measured compound. The atmospheric structure, geological relevance, and the effect of transport processes must also be considered and are in part provided by the other investigations on board the spacecraft.

### 3.2.1 Fragmentation Due to Physicochemical Effects

There are three sources of molecular fragmentation that must be considered in interpreting the data from the MASPEX instrument aboard Europa Clipper: 1) energetic particle bombardment of the molecules contained in the surface ice, 2) impact-induced fragmentation, and 3) fragmentation from electron ionization in the ion source.

1. Radiolytic or sputtering processes by energetic ions and electrons can also fragment molecules of interest (Johnson et al. 1984). Many authors have studied how energetic particle impact processes in the harsh environment of Europa can modify molecules contained in the icy regolith, see for example, Plainaki et al. (2012). The MASPEX team has two members, A. Bouquet of Laboratory D' Astrophysique De Marseille and M. Sephton of Imperial College London, that are actively leading programs to characterize energetic particle impacts on molecules of relevance to the MASPEX investigation. Other outside contributions are expected as well.
2. Impact-induced fragmentation can also result when a molecule impacts the surface of the MASPEX thermalizing antechamber at speeds on the order 5 km/s. Studies of these types of processes have been addressed through laboratory studies of hypervelocity impacts (Bowden et al. 2009) and through molecular modeling (Jaramillo-Botero et al. 2012). On the one hand the results of the most recent laboratory studies by New et al. (2021) indicate that speeds above 3 km/s can affect the surface capture and surface dissociation of molecules and are a function of the particle size. On the other hand, numerical simulations by Jaramillo-Botero et al. (2012) indicate that molecular fragmentation due to hypervelocity impacts must be taken into account even at the relatively modest encounter velocities of  $\sim 5$  km/s. Dissociative adsorption and dissociative scattering are likely to appear by 6 km/s. Therefore, the effects of the spacecraft velocity with respect to the Europa atmosphere are highly relevant and are being presently studied by the MASPEX team. The MASPEX team also welcomes contributions from inside and outside the Clipper project.
3. The ion source uses 15 to 150 eV electrons (command selectable) to create ions by the removal of an electron. This process leaves the molecule with excess energy, and it is common for molecules to break bonds within themselves to lose this energy, resulting in smaller ionized species called fragment ions. Fragmentation from ionization begins at a discrete energy specific to the molecule (the "appearance energy") and becomes more significant as the energy increases. The range of fragment ions and their relative abundances are characteristic of the parent compound and can provide a means to identify the presence of the parent in the sample. Generally, an energy of 70 eV is used when recording fragmentation patterns, enabling comparison of data across multiple instruments. There are commercially available libraries of fragmentation patterns that can be used to identify compounds in a spectrum, and MASPEX will make use of these data. Small variations in the abundance of each fragment occur between instruments, so it will be necessary to gather our own calibration data to enable accurate quantitation of each compound. The engineering model of MASPEX will be used to gather this information during Europa Clipper's cruise to Jupiter.

### 3.2.2 Answering Science Goals with MASPEX Results

Answering the three key science goals of MASPEX requires that we use the results from MASPEX measurements suitably transformed to represent the composition in the ocean. If we consider the pathway from the source material to the observed material, we can consider the change as a transform (or a series of transforms) that describe how the process(es) they have undergone have changed them. For example, the hydrogen and oxygen signals measured by MASPEX are the product of a transform attributable to the radiolysis of water and another transform that describes how their mixing fractions change with the transport from the surface to MASPEX through the atmosphere.

There are many possible transforms that will be needed to convert from the signal observed at MASPEX into the signal of source materials at their origin and, as discussed



above, there are plans in place to gather key information while Europa Clipper is in transit to Jupiter. Additional transformations will be based on the physics of the process, for example, the changes due to the atmospheric structure will be determined through atmospheric modeling (Teolis et al. 2017c).

The details of each transform from these and other sources will be stored in the ground data system and will be used to transform the MASPEX-observed data into source data to enable interpretation of the science. This statement glosses over the complexities of the transformation and in reality, multiple transformations will be possible. This spread of possibilities will be reduced by incorporating other knowledge about the sample, such as the geological age of the terrain, comparison with other MASPEX measurements, and through measurements from the other instruments on the spacecraft.

### 3.3 Optimization of Science Return - the Feedforward Process

All missions plan to maximize science return from their instrument operations, and this also applies to the MASPEX instrument on Europa Clipper. The harsh radiation environment at Europa prompted plans to analyze cryotrap samples around apojoove, where the signal contribution from radiation would be minimized and allow measurement of the least abundant species in the sample. The interval between the flyby and the cryotrap analysis presents an opportunity to refine cryotrap operations based on data taken during the flyby.

The flyby data is primarily used to determine the temporal and spatial structure of the major components of the atmosphere. To achieve this objective, mass resolution and dynamic range are constrained to maintain a 5 s cadence of measurements (representing a ~25 km-long ground track). The cryosample allows analysis of trace components integrated over intervals longer than the 5 s cycle. However, analysis time is not unconstrained as the fragmentation of molecules in the ion source adds further complications to the data, limiting the total analysis time of the cryotrap to ~600 s for measurement of each sample.

Because of time constraints on each analysis, there is value in choosing which targets we analyze on each cryotrap analysis period from the flyby based on what was seen in the flyby data. To achieve this, the ten minutes of data around closest approach are aggregated into a single spectrum and sent to the spacecraft for priority downlink (the feedforward data). Once received, this composite spectrum is analyzed to determine the qualitative composition and a pseudo-quantitative estimate of the mixing fractions. This data is then analyzed, both automatically, and by the science team, to identify the most scientifically important measurements to be made on the forthcoming cryosample. The new analysis plan is up-linked and loaded into MASPEX prior to apojoove, thus completing the feedforward process. The same cycle is repeated using a summary spectrum from the cryosample and enabling the optimization of the flyby data collection for the next flyby.

## 4 Science Requirements

Table 2 summarizes requirements placed on the MASPEX investigation to successfully carry out the science measurements discussed above. Based on these requirements we selected a set of candidate chemical compounds whose detection will provide essential information about the composition of Europa's surface, its surface-ice-ocean exchange, and the chemistry of the ocean. This is based on a variety of sources, including current observational data on, and models of, Europa's chemistry, as well as Cassini/INMS observations at Titan and Enceladus (Waite Jr et al. 2004). Of particular importance for this selection of observables

**Table 2** Science measurement requirements and MASPEX capabilities

Science Measurement Requirement	MASPEX Performance Capability of Primary Importance for the Requirement
Characterize the presence of organic molecules from the ambient environment and also linked to life.	Mass range: 1 m/z to 500 m/z
Characterize organic molecules linked to oceanic redox state and hydrothermal activity.	Mass resolution: $\geq 4275$ (10% valley) up to 500 m/z
Ensuring that the sampling interval for sputtered materials must correspond to the spatial scale that distinguishes surface geological provinces at the altitude of closest approach.	Sampling interval: 5 seconds for a complete mass spectrum up to 250 m/z (restricted by the 5 s interval) obtained during a flyby. This is matched to the interval along track associated with the Lambertian emission of a point source within the geological feature.
Interpret ice grain data during flybys.	Ice grain mode measurements: Analyze at least 5 ice grains during a Europa Flyby Period to complement SUDA with high mass resolution.
Perform measurements of sputtered and plume materials with sensitivities approaching $10^6 \text{ cm}^{-3}$ .	Ion source sensitivity: Greater than or equal to $0.02 \text{ (counts s}^{-1}) / \text{(molecule cm}^{-3})$ .
Measure a density range from $10^9 \text{ cm}^{-3}$ to $1.7 \times 10^5 \text{ cm}^{-3}$ .	Dynamic range: $\geq 6000$ .
Measure the ratios of key species in aqueous systems that are diagnostic of the ocean's redox state.	Precision: 30% See example in Fig. 6.

(and for the critical question of chemosynthetic sources of metabolic energy) were theoretical and modeling studies of putative aqueous activity on icy moons as well as of terrestrial hydrothermal systems.

To demonstrate that MASPEX performance satisfies the science measurement requirements. Figures 7 and 8 show models of the composition of three European exospheric environments (Teolis et al. 2017c):

1. a sputter-induced exosphere with no plume (Model 1);
2. an exosphere that includes an active south polar plume (Model 2); and
3. an exosphere that includes sputtering of material remaining on the surface from the fall-out of a previously active plume (Model 3).

The exospheric models consider the composition, flux, and energy distribution of sputtered molecules; their in-flight trajectories under Europa's gravity neglecting intermolecular collisions; loss due to gravitational escape and impact/charge-exchange ionization; gravitational fallback and surface re-adsorption; and the subsequent desorption rate and Maxwell-Boltzmann velocity distribution of these molecules at the local time and latitude dependent surface temperature (Teolis et al. 2017a) (Fig. 2).

In Model 1 we used estimated sputtering fluxes of  $\text{H}_2$ ,  $\text{O}_2$  and  $\text{H}_2\text{O}$  from Europa's ice (Cassidy et al. 2013; Teolis et al. 2017b), together with compositional estimates of the 'non-ice' component of Europa's surface material as determined from remote-sensing observations (Carlson et al. 2009; Johnson et al. 2009; Dalton et al. 2012; Brown and Hand 2013). For the plumes (Models 2 and 3), we include in addition to water vapor a short list of candidate compounds ( $\text{CH}_4$ ,  $\text{C}_2\text{H}_2$ ,  $\text{C}_2\text{H}_6$ ,  $\text{C}_2\text{H}_4$ ,  $\text{C}_6\text{H}_6$ ,  $\text{H}_2\text{CO}$ ,  $\text{HCN}$ ,  $\text{CH}_3\text{OH}$ , and  $\text{CO}_2$ ) at mixing ratios ( $< 10^{-3}$ ) based on Johnson et al. (2009). This list is conservative and is consistent with Cassini/INMS measurements in the Saturn system (Waite et al. 2005a; Waite Jr et al.

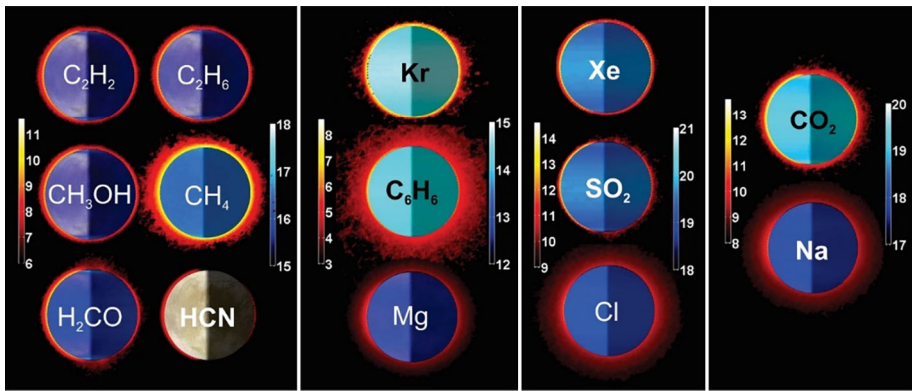


**Fig. 7** Modeled exospheres under sputter-only (Model 1) conditions showing examples of different types of exospheric structure that develop depending on the species. Red color: gas molecule number density cross section in log scale (scale bar: base ten logarithm of the density in molecules/m<sup>3</sup>). Blue colors: Adsorbate surface column density, including material adsorbed on the surface and diffused into the regolith (scale bar: base ten logarithm of surface column density in molecules/m<sup>3</sup>). Species with similar densities and column densities are grouped to share the same scale bar (Teolis et al. 2017c)

2006) and Enceladus' plume (Waite Jr et al. 2009), the only other known icy moon plume, providing a conservative basis for determining the degree of mass interference MASPEX may see at Europa.

In Model 2, plume sources ejecting hundreds of kg/s or more (Roth et al. 2014; Teolis et al. 2017c) are of sufficient intensity to dominate Europa's exosphere, supplying substantially more material to the global exosphere than the ~60 kg/s of material ejected by sputtering (Cassidy et al. 2013). Active plumes may also produce diurnal exospheric dynamics, as plume fallout sticks onto Europa's surface at night and then desorbs as the plume source crosses the dawn terminator.

In Model 3, patches of adsorbed surface material around recently active plumes are sputtered, acting as localized exospheric sources that may be identifiable by MASPEX during close flybys.

The densities and mixing fractions of molecules in the modeled exospheric environments were calculated along the spacecraft trajectory (Fig. 8), reflecting the longitudinal and solar local time structure and exospheric dynamics brought about by thermal desorption and sputtering. These results were used to synthesize anticipated mass spectra by calculating the mass and signal intensity of the fragment ions for all molecules, incorporating their isotopic substitution and molecular fragmentation in the ion source, and superimposing the MASPEX mass-peak shape on the data (see Sect. 6.3). The resolution required to separate each peak from its nearest neighbor was calculated allowing for differences in relative peak heights. While it is possible to perform measurements on overlapping peaks, the deconvolution process always reduces measurement precision, so MASPEX analysis uses fully resolved peaks wherever possible.

Knowledge of the composition of Europa's surface, the surface–ice–ocean exchange, and the chemistry of the ocean set the requirements for observations that in turn translate into requirements for the MASPEX investigation and instrument hardware. Operations, data, and software are essential to the investigation and are discussed in following sections.

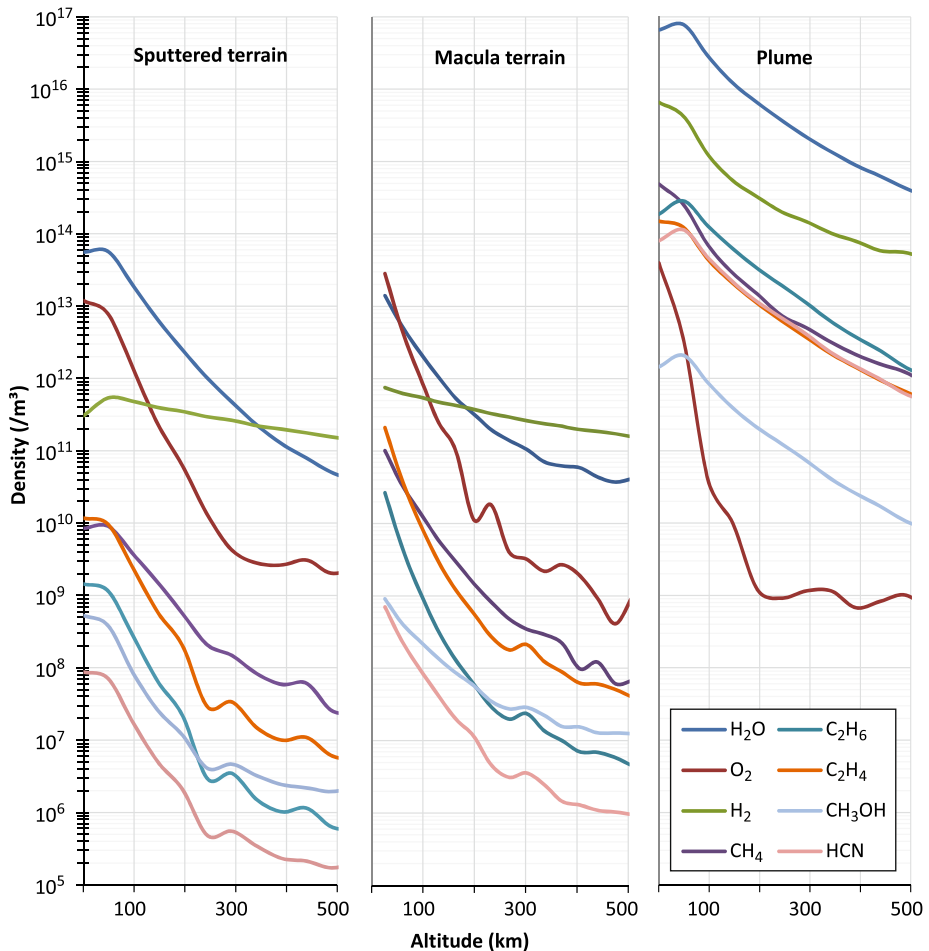


**Fig. 8** Modelled densities along the spacecraft trajectory for the three environments considered in Teolis et al. (2017c)

#### 4.1 MASPEX in the Context of the Europa Clipper Mission

The overall science objectives and implementation of the mission were described in Sect. 2. Determining how MASPEX contributes to the Europa Clipper mission is summarized in Table 3.

## 5 MASPEX Instrument Design

### 5.1 Overview

MASPEX is a state-of-the-art neutral gas mass spectrometer designed to measure the gas and ice grain environment surrounding Europa with exceptionally high resolution and sensitivity. At the heart of the instrument is a mass spectrometer (MS) based on multi-bounce time-of-flight (MBTOF) technology, together with supporting gas-handling systems and electronics

**Table 3** Europa Clipper Guiding Science Requirements

Name	Description	Rationale
Mass Range	When collecting atmospheric composition dataset ambient measurements and cryotrap samples, the molecular weight range of MASPEX shall be 2 u up to greater than or equal to 500 u.	Allows characterization of organic molecules linked to life, such as peptides, PAH's. The mass range from 300-500 u could permit analysis of nucleobase compounds such as ATP, CTP, and GTP.
Mass Resolution	When measuring the atmospheric composition dataset ambient and cryotrap samples, the mass resolution of MASPEX shall be $\geq 4275$ as measured by the 10% valley definition at masses less than 50 u (C2 hydrocarbons).	High mass resolution is required to characterize fully any organics linked to oceanic redox state and hydrothermal activity. This requires the determination of the nitrogen and oxygen content.
Association of Sputtered Materials with Geological Features	For the atmospheric composition dataset ambient measurements, the sampling interval of MASPEX for sputtered materials shall correspond to a surface spatial resolution equal to or smaller than the altitude of the flight system above Europa's surface at closest approach.	This spatial scale distinguishes between geological provinces, for example, the transition from chaotic to fractured terrains. The scale is conservative relative to what the investigation can achieve, based on current analysis, verified from modeling of Europa's sputtered atmosphere, assuming Lambertian emission from the surface.
Ice Grain Sampling	When collecting atmospheric composition dataset measurements for both the high and low altitude subsets, MASPEX shall be capable of analyzing at least 5 ice grains per Europa Flyby Period.	Occasionally ice particles will enter the sampling aperture (from Enceladus experience) and their compositions may differ from the incoming gas.
Closed Ion Source Sensitivity	When collecting atmospheric composition dataset measurements, the sensitivity of the closed ion source of MASPEX shall be greater than or equal to $0.02 \text{ (counts s}^{-1}) / \text{(molecule cm}^{-3})$ .	High sensitivity is required for continuous measurement sufficient to obtain spatial resolution on the ground of sputtered and plume materials, including major volatiles ( $\text{H}_2\text{O}$ , $\text{O}_2$ , $\text{H}_2$ , $\text{CH}_4$ , $\text{C}_2\text{H}_4$ , $\text{C}_2\text{H}_6$ , and HCN).
Atmospheric indicators of geological activity	For the atmospheric composition dataset, the sampling interval of MASPEX for active outgassing samples shall correspond to a surface source resolution equal to or smaller than 200 km.	This spatial scale is sufficient to locate the geographical region where activity may be occurring, e.g., plumes, chaos, or fracturing. The scale is based on current analysis, verified from modeling of Europa's sputtered atmosphere, assuming Lambertian emission from the surface.
Ambient Mode Dynamic Range	When collecting atmospheric composition dataset ambient measurements, the dynamic range of MASPEX shall be greater than or equal to 6000.	High dynamic range is needed to measure minor and trace species in the atmosphere.

(Brockwell et al. 2016). MASPEX is based on earlier MS designs begun in the early 2000s (Young 2002; Waite et al. 2005b; Young 2006; Young and Waite Jr 2007; Young et al. 2010). A total of five progressively more sophisticated prototypes were built with the support of Southwest Research Institute's Internal Research Program and NASA. Once selected for the Europa Clipper mission, Engineering and Flight Models (EM and FM, respectively) were built and calibrated. The high-fidelity EM will be used to gather additional calibration data during the mission.

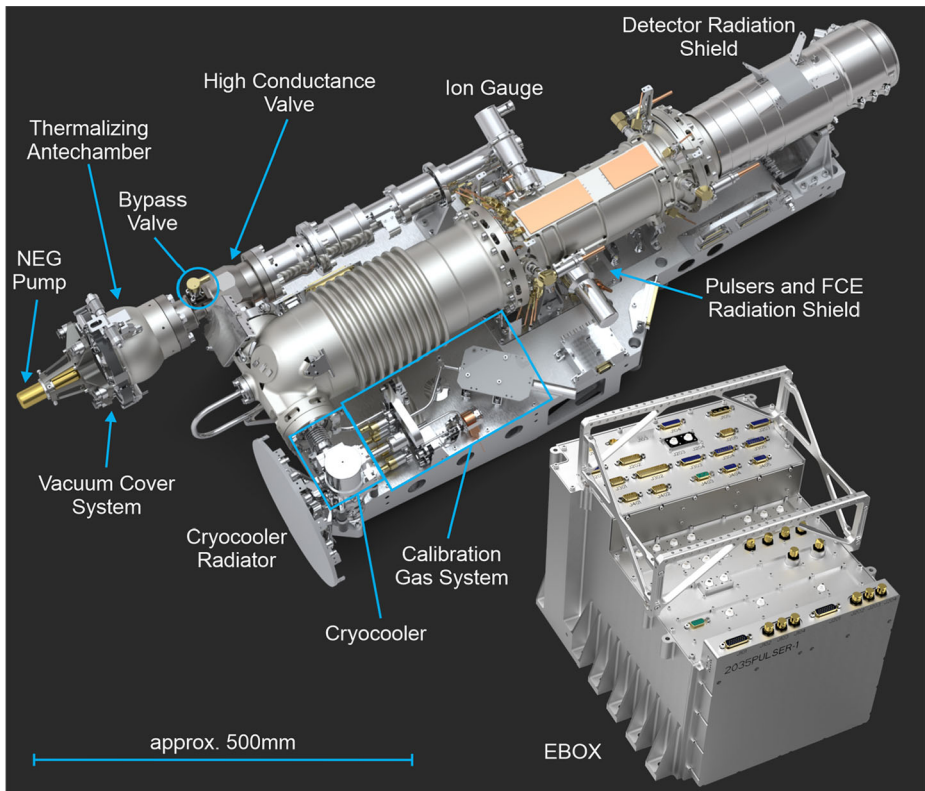


**Fig. 9** CAD drawing showing the MASPEX sensor and the EBOX. The intra-instrument cabling, and multi-layer insulation (MLI) are not shown for clarity. Labels in the figure correspond to major subsystems discussed in the text

During early development a high-throughput Gas Inlet System (GIS) including a cryotrap was added to the original MS; it will be needed for collecting samples during short duration Europa flybys at a velocity of  $\sim 5$  km/s. Because of Jupiter's intense radiation environment, after prototypes were built, the entire instrument was re-engineered to prevent damage to the detector and electronics. Other features were added to meet requirements for long-term accurate internal calibration during flight, and to ensure chemical cleanliness in the presence of the spacecraft outgassing environment.

MASPEX is comprised of three major subsystems. The first is the sensor, which houses the mass spectrometer and is mounted on the spacecraft with its aperture pointing in the  $+Z$  direction to provide a direct view of the incoming rammed gas during Europa flybys (Fig. 11). The second subsystem is the Electronics Box (EBOX, Fig. 9), which is mounted inside the spacecraft's radiation-shielded vault. The third subsystem is a heavily shielded cable assembly connecting the sensor and EBOX. Figure 9 is a CAD drawing of MASPEX identifying the main subsystems visible from outside the instrument. More detailed pictures of the interior are shown below.

Figure 10 is a photograph of the MASPEX Flight Model shortly after being mounted on the spacecraft. The instrument is located on the spacecraft's radiation vault with its aperture facing up along the  $+Z$  direction (the gas ram direction at closest approach during Europa flybys).



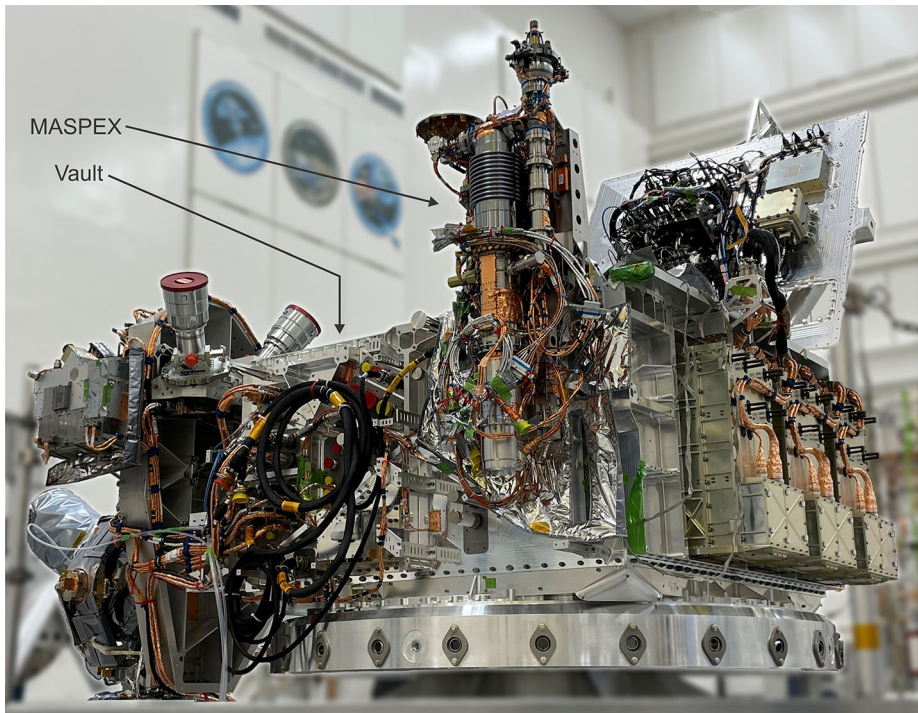


**Fig. 10** The MASPEX sensor, after mounting on the side wall of the vault. The coiled cables are awaiting connection through the vault wall to the EBOX mounted on the inside. The vault lid is at the right rear in the open position

Once the spacecraft is assembled it is covered with electrically conducting multi-layer insulation (MLI) (Fig. 11), which serves to prevent spacecraft charging and to control the thermal environment of the instruments and spacecraft.

During flybys, the spacecraft maintains nadir pointing of the observing instruments, so that the spacecraft +Y direction always points directly at Europa. This implies that the MASPEX inlet changes its angle relative to the ram direction of incoming gas throughout the  $\pm 2$  hours of flyby operations ( $\sim \pm 78^\circ$ ) and is only aligned with the +Z axis at the location of closest approach to the moon (Fig. 12).

## 5.2 System Design

Figure 13 is a high-level schematic diagram of the MASPEX instrument showing the major subsystem components and connecting harness. The sensor houses the Gas Inlet System (GIS) and all optical elements making up the mass spectrometer. Most of the electronics and electrical interfaces to the sensor and spacecraft are in the EBOX. The orange arrow connecting the sensor and EBOX represents the intra-instrument harness, which is about 2 m long and heavily shielded, making it a major subsystem in its own right.

Electronics that do not need to be co-located with the sensor are housed in the EBOX, located inside the spacecraft's radiation vault. The EBOX electronics are comprised of eight printed circuit boards that control instrument operations and interfaces, gather and format sensor data, and generate the high voltages that power the sensor.



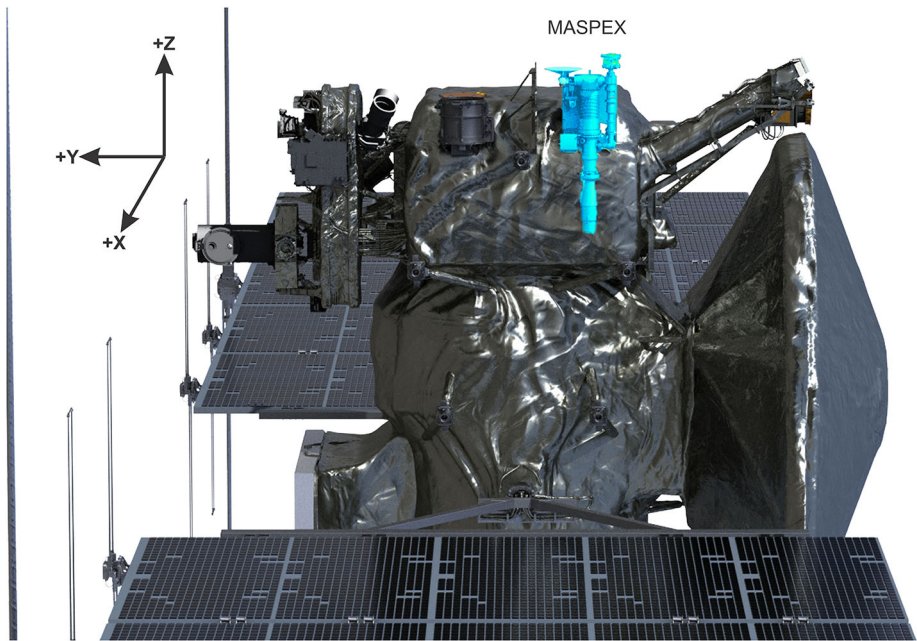


**Fig. 11** CAD rendering of the Europa Clipper spacecraft with MLI blankets installed. The figure is a cartoon showing the location of MASPEX (cyan) on the spacecraft (in this drawing MASPEX is shown without MLI blankets)

The sensor is comprised of two major subsystems (Fig. 14). The light brown section at the top of the diagram represents the GIS which includes the entrance aperture, gas handling system and associated pumps, and calibration gases and valves. The light-green section at the bottom of the diagram represents the mass spectrometer (MS) which includes the MBTOF optics with its storage ion source, Faraday cup for internal calibration, microchannel plate (MCP) detector, and high sensitivity front-end electronics. Each of the EBOX, GIS, and MS subsystems are discussed in detail below.

### 5.3 Gas Inlet System

The GIS (Fig. 14) thermalizes and then transfers rammed gases from the ambient Europa environment into the mass spectrometer ion source where they are ionized and extracted into the MBTOF for analysis. The GIS also includes calibration gas and a distribution network of capillaries and microvalves needed for in-flight calibration during operations at Europa.

#### 5.3.1 MASPEX Contamination

To meet its science requirements, MASPEX is extremely sensitive to the Europa gas environment ( $0.02 \text{ counts s}^{-1} / \text{molecule cm}^{-3}$ ). Unfortunately, this also makes it sensitive to contamination by trace quantities of materials outgassed from the Europa spacecraft. The Rosetta cometary mission carried two comparably sensitive mass spectrometers: the RTOF and DFMS (Balsiger et al. 2007), which showed that outgassing of spacecraft materials complicated analysis of target samples considerably (Graf et al. 2008; Schläppi et al. 2010; Hassig et al. 2011a,b; Schläppi et al. 2011).

**Fig. 12** Calculated data for a typical Europa flyby showing the effects of nadir pointing on the density of gas measured by MASPEX. The top panel shows the variation of ram angle and the resulting ram signal multiplication factor. The bottom panel shows the altitude of the spacecraft above Europa's surface, the modelled gas density at that altitude and the density of gas within the MASPEX antechamber. Calculations are for water (mass 18) and assume that the ambient gas temperature is 77 K, the MASPEX antechamber is at 288 K, spacecraft velocity is 4 km/s, and the density profile is from the model of Teolis et al. (2017a)

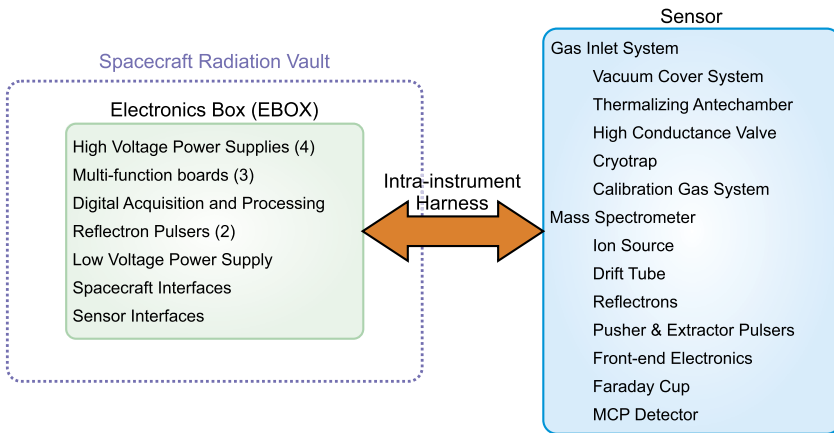
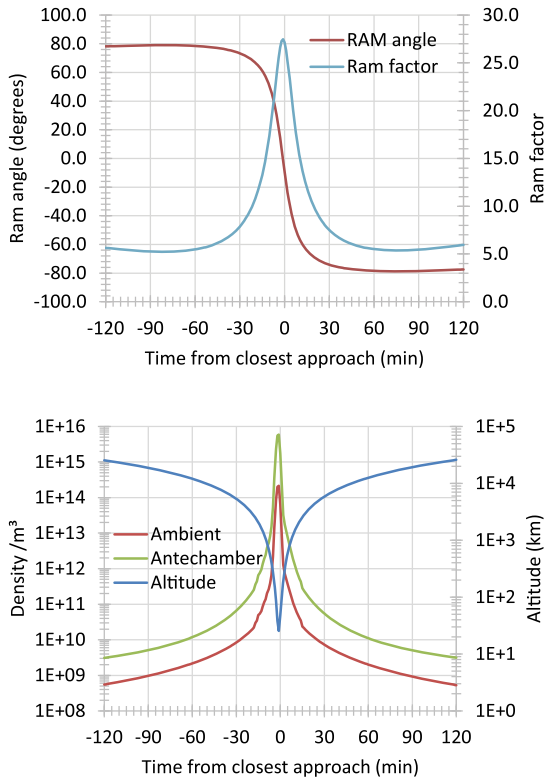


**Fig. 13** High-level MASPEX block diagram

In anticipation of outgassing problems, the MASPEX team worked closely with JPL contamination control experts to place the instrument in a location and orientation that would minimize the impact of spacecraft outgassing. In addition, the project set stringent standards for allowable outgassing of spacecraft equipment and materials and ensured that any venting of 'closed' volumes was directed to the aft end of the spacecraft, away from the GIS field of

**Fig. 14** Detailed schematic of the MASPEX sensor showing components of the Gas Inlet Subsystem (GIS), the vacuum cover system (VCS), thermalizing antechamber (TAC), High Conductance Valve (HCV), cryotrap and cooler, Mindrum microvalves, and Calibration Gas System (CGS). A microscopic particle screen is located in front of the MS but is not shown in the figure

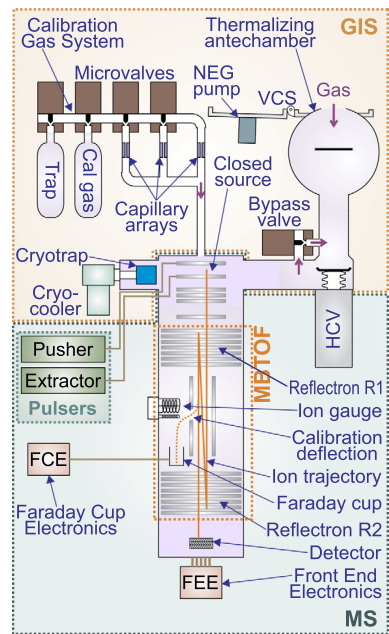


**Table 4** Table of outgassing flux requirements for MASPEX

Surface	Outgassing rate
Surfaces not covered with thermal blankets	$1 \times 10^{-14} \text{ g s cm}^{-2}$
Surfaces under thermal blankets	$5 \times 10^{-14} \text{ g s cm}^{-2}$
Surfaces within the vault	$1 \times 10^{-12} \text{ g s cm}^{-2}$

view. Table 4 shows the limiting outgassing rates from typical spacecraft surfaces. The rates apply to flight hardware at the time of delivery during spacecraft integration. The rates are expected to decrease during the five-year cruise to Jupiter.

After careful analysis, MASPEX was mounted on the side of the spacecraft vault with its entrance aperture facing the spacecraft +Z direction (Fig. 11). The entrance aperture is forward of all other parts of the spacecraft (except the Radar for Europa Assessment and Sounding: Ocean to Near-surface (REASON) High Frequency (HF) antennas) to prevent any spacecraft outgassing from directly entering the instrument. The REASON instrument is a radar with two small-diameter HF antennas (Fig. 15) that extend 8 m above and below the plane of the solar arrays. With the solar arrays in their flyby orientation at Europa, the HF antennas extend into the MASPEX field of view (FOV), providing a direct line-of-sight pathway for outgassed products to enter the GIS. However, their small surface areas pose a negligible threat to MASPEX objectives.

The Europa Clipper project extensively modelled the outgassing rates and their transfer to MASPEX (Soares et al. 2019a,b; Fugett et al. 2022) and provided estimates of three distinct mechanisms for outgassing materials to reach the instrument (Table 5). These results suggest that during sampling at Europa ~120 ppm of the measured gas will be due to spacecraft outgassing. Although it will be possible to deconvolve some of the contamination, it is possible that the outgassing rate will set the bottom level of the instrument’s dynamic range.

**Fig. 15** MASPEX (cyan) is mounted on the spacecraft with the solar arrays shown in the flyby configuration. MASPEX's inlet is forward (in the ram direction) of all other spacecraft components to minimize the quantity of outgassing that can enter the inlet, with the exception of the REASON HF antennas (green), which extend 8 m above and below the solar array

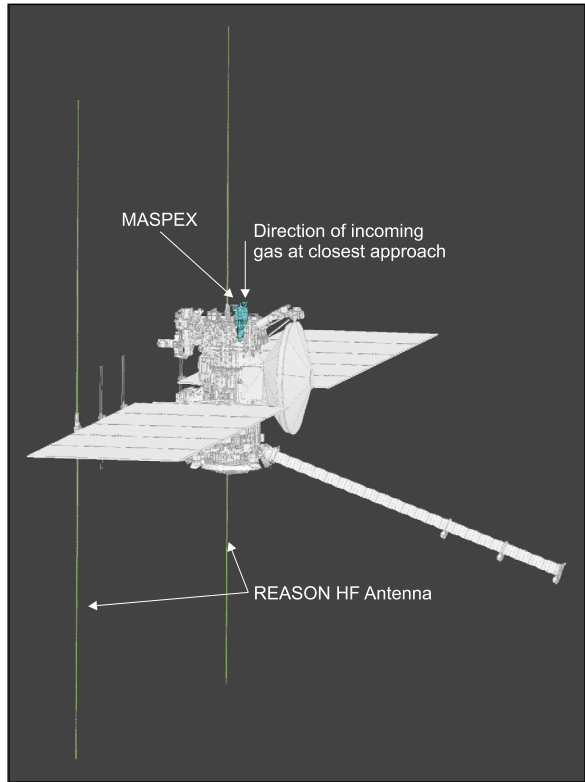


**Table 5** Table of estimated contamination fluxes at the GIS aperture

Flux Source	Rate (g s <sup>-1</sup> )	Description
Self-scatter	$3 \times 10^{-18}$	Outflowing outgassed molecules that strike each other causing them to return to MASPEX.
Direct / reflected	$1 \times 10^{-15}$	Outgassed molecules that land on a surface in front of MASPEX and desorb into the MASPEX inlet.
Return	$3 \times 10^{-13}$	Outgassed molecules that collide with molecules from Europa during the flyby and bounce back into the MASPEX inlet.

### 5.3.2 Vacuum Cover System

To ensure chemical and particulate cleanliness the Vacuum Cover System (VCS) seals the entire instrument prior to launch and is opened during cruise when the spacecraft is outbound to Jupiter (see Fig. 9 for external mechanical details).

The cover and its mechanism are attached near the entrance to the Thermalizing Antechamber (TAC). The vacuum cover is closed and sealed by a spring-loaded clamp band. The door is on a hinge that lifts it clear of the aperture to prevent any possible FOV obstruction after release. The door then rotates to its fully deployed state where it reaches a hard stop and latches into place. The VCS actuator fires when power is applied to one of two redundant heaters embedded in an integral High-output Paraffin Actuator (HOPA). The

door mechanism incorporates two microswitches. One indicates when the HOPA is fully extended while the other indicates that the cover is fully deployed.

The entrance aperture is encircled by a raised knife-edge ring machined into the TAC sphere's surface to interface tightly with the vacuum cover's proprietary copper H-seal<sup>1</sup>. A 2.75" diameter knife-edge ConFlat<sup>2</sup> flange was machined into the opposite end of the TAC to interface tightly with the High Conductance Valve (HCV). The GIS vacuum cover was sealed prior to launch. A Non-Evaporable Getter (NEG) pump is mounted on the interior of the cover and activated after the door is closed. The pump, in addition to pre-launch bakeout, helps maintain high vacuum during integration, test, launch, and cruise. Pumping ends once the vacuum cover is opened prior to reaching Jupiter.

### 5.3.3 Thermalizing Antechamber

The TAC is made of a high-strength stainless-steel sphere with an internal diameter of 90 mm and an entrance aperture measuring 21.29 mm in diameter. The chamber's interior is coated with a diffusion-bonded layer of tantalum 30 microns thick, forming a chemically neutral surface that does not react with atomic oxygen.

During a flyby, molecular flow at spacecraft velocity ( $\sim 5$  km/s) enters the GIS through an aperture with a  $\sim 2\pi$  steradian FOV. The gas sample then flows into the TAC where multiple collisions with chamber walls bring the hypersonic gas into thermal equilibrium before being transferred at a rate of  $12\ell\text{ s}^{-1}$  through the HCV to the ion source. The TAC incorporates an alumina-ceramic impact plate located halfway between the entrance aperture and the chamber exit. The TAC blocks gas and other material such as ice grains from directly entering the HCV without first colliding with multiple surfaces within the chamber.

During a flyby of Europa, gas samples are also adsorbed onto a cryotrap surface accessed via the antechamber-to-source conduit. This process collects a large volume of incoming gas that is analyzed following the flyby and before the next. After a flyby the HCV is closed. If the volume of trapped gas inside the sensor is too large, then a microvalve, that bypasses the HCV, adjusts the pressure autonomously prior to analysis (Sect. 8.5.3).

### 5.3.4 High Conductance Valve

The HCV isolates the mass spectrometer and GIS volume from the thermalizing antechamber. The HCV is opened during Europa flybys to concentrate incoming ambient gas by adsorption onto the cryotrap. After cryotrap analysis that occurs near apoapsis the HCV is re-opened to collect samples taken during the next flyby.

The HCV is a customized version of an off-the-shelf VAT<sup>3</sup> all-metal valve that incorporates several important features. It is opened and closed by an actuator comprising a high-temperature brushless motor with redundant windings and resolvers, connected to a precision low-backlash gearbox. A microswitch signals whether the HCV is open or closed. The VAT valve also features a low-outgassing coating (Silcolloy<sup>4</sup>) and a special port to a bypass microvalve (Mindrum Precision Inc., see Fig. 14). The microvalve is sealed to the valve body with metal seals to maintain an all-metal sealed vacuum envelope until the

---

<sup>1</sup>Bostec Engineering, Inc.

<sup>2</sup>Agilent Technologies, Inc.

<sup>3</sup>VAT Vakuumventile AG, Switzerland.

<sup>4</sup>SilcoTek Corporation.

cover is opened in cruise, for the lowest possible leak rate. The microvalve provides a low-conductance pathway past the VAT valve seal and enables the controlled release of excess pressure (see Sect. 8.5.3) from the cryotrap sample in the event that flyby densities exceed expectations or if a plume is present.

Metallic particles that can be produced by operation of the HCV's silver-plated metal seal have to be considered. During development tests these particles were found to range in size from 2 to 170  $\mu\text{m}$ . Almost 1200 metallic particles were identified after 100 cycles opening and closing the seal. Particle production rate and size both decreased with an increasing number of cycles. To reduce this potential problem, prior to launch the flight HCV was "run-in" by cycling and cleaning the seal 100 times. This process is not perfect, so a 38% transmissive screen with 26  $\mu\text{m}$  openings was placed in front of the mass spectrometer and the neighboring bypass valve to prevent particles larger than that size from entering tubing leading to the ion source. Smaller particles are not expected to move beyond the HCV because of electrostatic surface adhesion (Mikellides et al. 2020).

### 5.3.5 Cryotrap

The cryotrap, which is cooled to  $<75$  K by a high reliability Ricor<sup>5</sup> K508 Stirling-cycle cooler, boosts the amount of gas collected and trapped during a flyby, effectively increasing dynamic range relative to that available during a single flyby. Trapping time and gas density determine the amount of gas collected. After a flyby, the HCV is closed and the adsorber is allowed to warm up to ambient temperature, releasing the sample into the MS for analysis. If the volume of trapped gas is too large, then a microvalve that bypasses the HCV adjusts the pressure inside the sensor autonomously prior to analysis. (see Sect. 8.5.3). After analysis, the HCV is reopened to let any excess gas escape in preparation to admitting the next sample. Heaters are also attached to the adsorber head to drive off gas samples after analysis.

### 5.3.6 Calibration Gas System

The Calibration Gas System (CGS, Fig. 16) is used during calibration, which occurs prior to each flyby and after the analysis of the cryosample at apoJove. The CGS carries the reference standard calibrant compound FC-43 (heptacosane,  $\text{C}_{12}\text{F}_{27}\text{N}$ ), a liquid with a high vapor pressure that can be released at three selectable flowrates to support calibration of both the spectrometer's mass scale and the ion source sensitivity (a full discussion of calibration methods and results can be found in Sect. 6.5). The CGS includes a calibrant liquid reservoir that provides calibrant vapor to the source, a calibrant trap to evacuate the CGS between calibration operations, and a NEG pump to maintain vacuum within the CGS during cruise. Calibrant gas handling is controlled by a series of microvalves that are kept open during launch and cruise to prevent their deformation and creep into a position that might prevent their opening after reaching Jupiter.

The calibration gas volume and flow are controlled by the Calibration Gas Manifold. The manifold incorporates four microvalves (Mindrum Precision Inc.) and includes a serpentine coil that acts as an expansion volume (total length 0.5 m) to prevent calibrant gas pressure spikes. All manifold seals are metallic as are all tubes leading to the manifold. All internal surfaces are coated with an inert high purity silicon barrier to prevent chemical interactions with the calibrant gas.

---

<sup>5</sup>Ricor USA Inc.

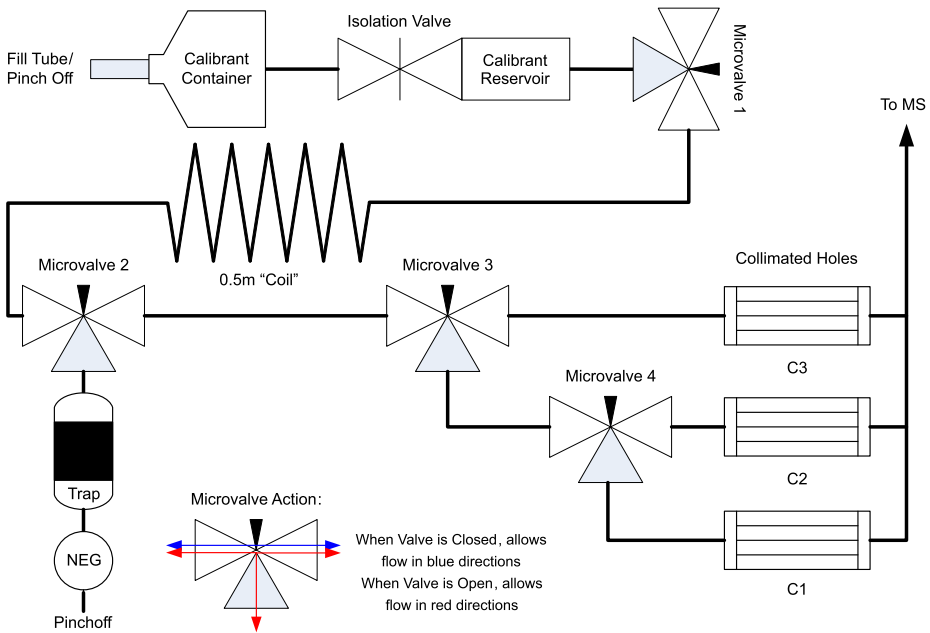


**Fig. 16** Schematic of the Calibration Gas System and Manifold

The calibrant reservoir holds 0.8 ml of FC-43 liquid that is injected via a tube into the reservoir. The tube was pinched-off and covered with a protective cap. Vapor is released from the calibrant reservoir into the CGS via an isolation valve (top of Fig. 16). The all-metal valve hermetically isolates the calibrant container from the gas manifold and the rest of the instrument during launch and cruise. The valve is opened only once, following Jupiter orbit insertion. Once open, the valve allows FC-43 calibrant gas to enter the manifold via a stainless-steel bellows that expands when the valve is opened.

The isolation valve incorporates a secondary sintered titanium calibrant reservoir, to accumulate liquid calibrant that thermally migrates from the primary container. A sintered-titanium metal filter at the manifold entrance prevents particles  $\geq 10 \mu\text{m}$  generated by the valve's actuation from interfering with downstream microvalves within the CGS. Calculations predict that the FC-43 surface tension will retain the liquid in the pores of the sintered titanium at all g-loads expected in flight. A carbon molecular sieve, with a trapping capacity that exceeds the supply of calibrant, purges the calibration gas module by absorbing and trapping the gas.

The calibrant trap also accommodates a NEG pump that is activated by an induction heater during ground preparation. The NEG pump maintains vacuum within the CGS prior to opening the isolation valve at Jupiter. The entire CGS was evacuated through a pinch-tube at one end of the trap. Once the CGS was evacuated during final ground operations, the NEG pump was activated, and the pinch-tube sealed off. The pinch-tube stub is protected from damage by a threaded cap staked in place.

Collimated holes (Fig. 16) limit gas conductance between the CGS and the MS. Three capillary arrays provide three selectable mass flow rates. Each collimated hole is comprised of a capillary array soldered to a titanium ring. The arrays are lead-alkali-silicate glass disks with multiple holes for redundancy. This material was selected because it has relatively high



**Table 6** Dimensions of holes in the capillary array

Capillary number	Diameter (μm)	Length (mm)	Length/Diameter
C1	10	2.92	292:1
C2	10	2.92	292:1
C3	5	1.00	200:1

**Fig. 17** Calibration data for the FM CGS using N<sub>2</sub> to measure throughput at 21 °C. The three lower series are the calibration values for the collimated holes prior to installation in the CGS. The upper three series show the calibration values after the CGS was fully assembled. Testing of the engineering model (which had similar issues) showed that the FC-43 pressures exceeded the safe operating pressure

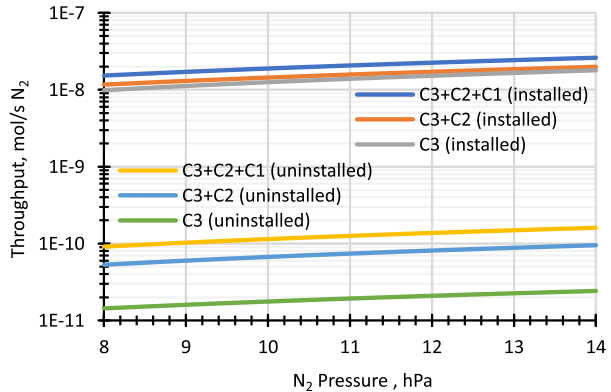


**Table 7** The as-designed and as-delivered pressures of FC-43 in MASPEX with each combination of collimated holes. The maximum safe working pressure limit is  $8 \times 10^{-6}$  hPa

Collimated holes	As-designed pressure (hPa)	As-delivered pressure (hPa)
C3	$9.6 \times 10^{-9}$	$8.9 \times 10^{-6}$
C3 + C2	$3.7 \times 10^{-8}$	$1.0 \times 10^{-5}$
C3 + C2 + C1	$6.0 \times 10^{-8}$	$1.3 \times 10^{-5}$

strength and similar thermal expansion characteristics needed to match the titanium ring. Each capillary array contains 3 tubes with dimensions given in Table 6.

The collimated holes were tested before and after press fit insertion into the flight mechanical manifold (see Fig. 17). Leaks around the press fits led to a much larger conductance than anticipated as shown by the upper set of traces in the figure. During nominal operation with microvalve 1 left open to allow continuous flow, the leaking press fits led to much higher pressures in the ion source and detector than are safe to operate the instrument (Table 7). The mitigation for this is to open and close microvalve 1 rapidly to reduce the quantity of FC-43 introduced to the CGS manifold. This creates pressures that make it safe to operate the ion source, but that decay during the calibration period and must be accommodated by the autotune process.

## 5.4 Mass Spectrometer

### 5.4.1 Overview

MASPEX is built around a compact, high-resolution, multi-bounce time-of-flight (MBTOF) MS (Fig. 18 and Fig. 19) capable of unprecedented mass resolution – no other mass spec-

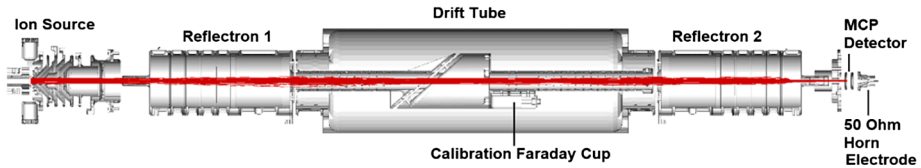


**Fig. 18** Cross section of the MS optics showing details of major subsystems and particle raytracing (red lines) with an overlay of external instrument features in gray. Ions leaving the ion source travel from left to right through Reflectron 1. With the reflectrons energized, ions bounce between Reflectrons 1 and 2 before being released through Reflectron 2 to the detector

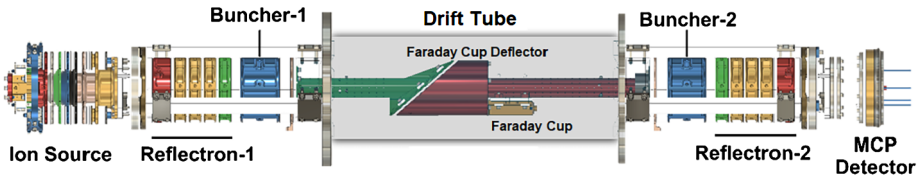


**Fig. 19** Details of internal optical components showing individual lens elements making up the ion source, reflectrons, bunchers, drift region, Faraday cup, and MCP detector

trometer with these capabilities has ever been flown in space. Its basic principle is that ions formed in a storage electron-bombardment ion source are focused and extracted into the MBTOF where they are trapped by carefully defined and timed switching electric fields. Once in the MBTOF, two “buncher” electrodes focus the ion beam radially towards the center of the spectrometer. This decreases angular and spatial dispersion of ions with the same  $m/z$  prior to releasing them into the drift tube. Beam perturbations are further reduced by drift tube fields driven by a very accurate, low-variability power supply.

Time-resolved ion packets enter a system of two opposing, coaxially aligned, electrostatic mirrors separated by a field-free drift tube. The two mirrors are isochronous (i.e., time-focusing) and referred to as “reflectrons.” The coaxial reflectrons trap ions extracted from the source and focus them spatially and temporally by folding the trajectories back on themselves. In this way flight paths ( $l$ ) as long as one kilometer are possible in an instrument just 50 cm long, leading to exceptionally high resolutions with  $l/2\Delta l = m/\Delta m > 17,000$  full-width half-maximum (FWHM), far in excess of mission requirements.

As ions bounce between the two reflectrons, they separate based on their velocities, which are proportional to their mass-to-charge ratios. An ion that completes a bounce off each reflectron in succession (i.e., from Reflectron 2 to Reflectron 1 and back to Reflectron 2) is said to have completed one “lap.” Mass resolution increases roughly in linear proportion to the number of laps (see Fig. 52), which can be as high as several hundred. After bouncing for a selected number of laps, Reflectron 2 voltage is dropped, and ions are released to the detector. Since the ion packets remain focused all the way to the detector surface, mass resolution can be made arbitrarily high by simply extending the amount of time ions are trapped between the reflectrons. Errors caused by the accumulation of electrical, mechanical, optical aberrations, and scattering affect resolution and are addressed in detail in Sect. 6.4.2.

In addition to the CGS, the MS includes several other components dedicated to laboratory and in-flight calibration (see Sect. 6.5 for a full discussion). An ion gauge inside the mass analyzer region measures gas density. Ion beam current is measured, without mass selection, by deflecting the entire ion beam off the main optical axis and into a Faraday cup

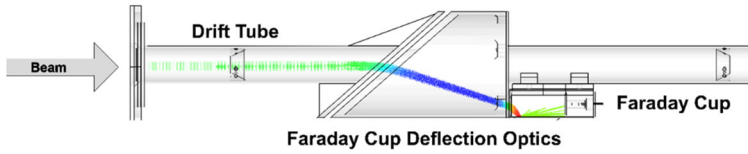


**Fig. 20** Optics of the FC used to calibrate the ion beam. Blue trajectories are deflected ions, and red trajectories are ions that strike the FC walls. Green trajectories represent paths of ions and secondary electrons knocked out of the FC wall that are trapped in the cup

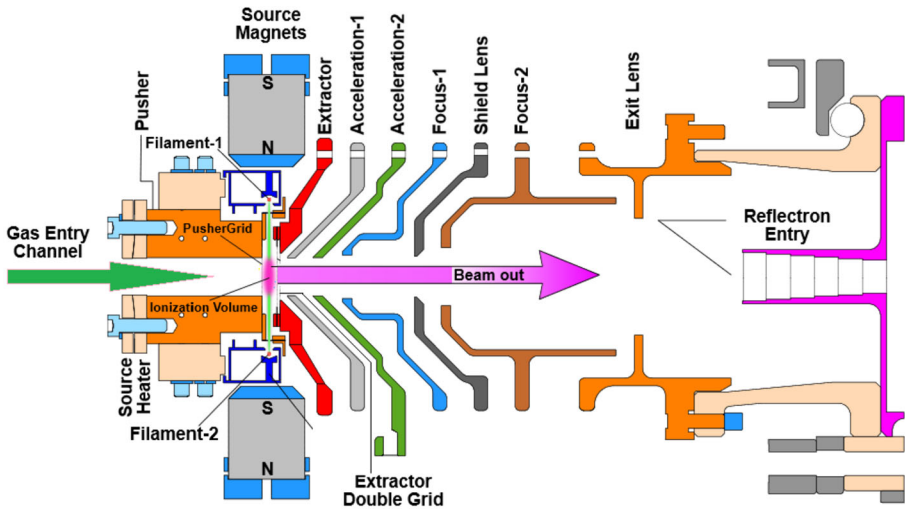


**Fig. 21** Ion storage source schematic cross-section showing the basic elements of the assembly up to the 5-mm diameter reflectron entry point at the far-right end of the figure

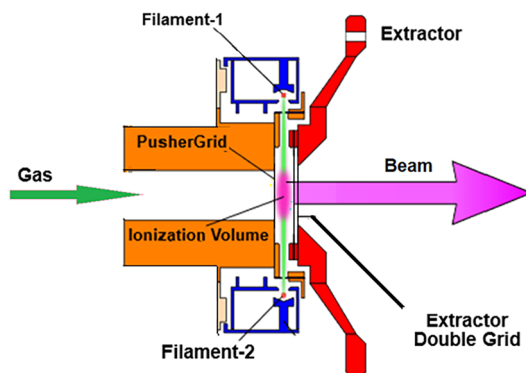
(FC) collector (see Fig. 20). The Faraday cup measures the total beam current using a high sensitivity electrometer whose signal is sent to the Digital Acquisition and Processing (DAP) board in the EBOX for processing. This technique enables absolute measurement of the ion beam, even as the gain of the detector MCPs changes over the lifetime of the instrument.

**5.4.2 Electron Ionization Source**

Gas enters the ionization source directly from the GIS through the HCV discussed earlier. The source contains two redundant filaments and matching collector plates (Fig. 21, Fig. 22 and Fig. 23). A constant current supply heats the operating filament, giving off electrons that are accelerated by a voltage applied between the filament and the ionization volume to energies selectable from 15 to 150 eV. Electrons interact with molecules and atoms in the ionization volume to create ions through the process:  $M + e^- \rightarrow M^+ + 2e^-$ . In this simple equation,  $M^+$  can represent not only ionized atoms and molecules, but also one or more ionized fragments of molecules. This is especially important for the many ionized fragments coming from the FC-43 compound used to calibrate MASPEX.

To increase the number of electron collisions, magnets are mounted immediately surrounding the source ionization region (Fig. 21 and Fig. 22). This creates a field of 200 G that forces electrons to spiral in a direction perpendicular to the ejected ion beam. The field

**Fig. 22** Enlargement of the ion storage source in Fig. 21 showing details of the ionization volume, pusher and double extractor grids, and extractor optical element



increases source sensitivity by a factor  $\sim 15$ . Three processes contribute to this improvement in sensitivity: 1) the electron gyroradius and helical pitch angle give the electrons a longer path length; 2) the longer path length leads to longer collisional interaction times; and 3) longer electron trapping times, and improved focusing, lead to space charge buildup that traps ions of 0.5 to  $\sim 1$  eV in a potential well located inside the ionization region (purple area in Fig. 22). The well “stores” equilibrated ions during the time between extraction pulses. The magnets are yoked with a high magnetic permeability material to contain the return magnetic flux. To reduce outgassing and remove any chemical contaminants, the source is also fitted with its own integral heater. Moreover, only ceramics and metals are used in source construction—there are no plastics.

During ionization, electrons are focused through two beam-defining slits immediately in front of the filaments, forming a narrow sheet across the ionization volume that is oriented perpendicular to the beam axis (Fig. 22). The filament emission current measured at the electron collector (blue element behind the filaments) can be varied by command between 15 and 200  $\mu\text{A}$ . A feedback circuit maintains constant emission current at the collector. A secondary redundant filament (2) mounted opposite to the primary filament (1) can replace the primary filament if it fails. Both primary and secondary filament assemblies are burned-in and fully characterized prior to installation in the MS.

The active ionization volume (purple “blob” in the center of the grids) is formed by grids positioned on either side of the volume. The “pusher” grid is located behind the closed source while the “extractor” double grid is in front. The grids are pulsed to accelerate the thermally equilibrated ions from the ionization volume into the extractor element and then into the acceleration and focusing optics of the MBTOF.

Between extractions, ions accumulate in the space charge created potential well. The negative potential depression stores equilibrated ions during the time between extraction pulses (Abplanalp et al. 2010; Fohn et al. 2021). The ionization volume’s fill time can be controlled by either the extraction frequency, or duration of the extraction pulse. The fill time between extractions is

$$\tau_{fill} = \frac{1}{\sigma \times \rho \times v_e} \quad (1)$$

where  $\tau_{fill}$  is the fill time,  $\sigma$  is the first ionization cross-section,  $\rho$  is the gas density, and  $v_e$  is the electron velocity at a given electron energy. The storage capability results in a sensitivity of  $>0.02$  (counts  $\text{s}^{-1}$ ) / (molecules  $\text{cm}^3$ ) when operating at 110  $\mu\text{A}$  emission current. A high duty cycle is possible because ions accumulated during the storage phase are not “wasted” during the time that the previous spectrum is being analyzed.

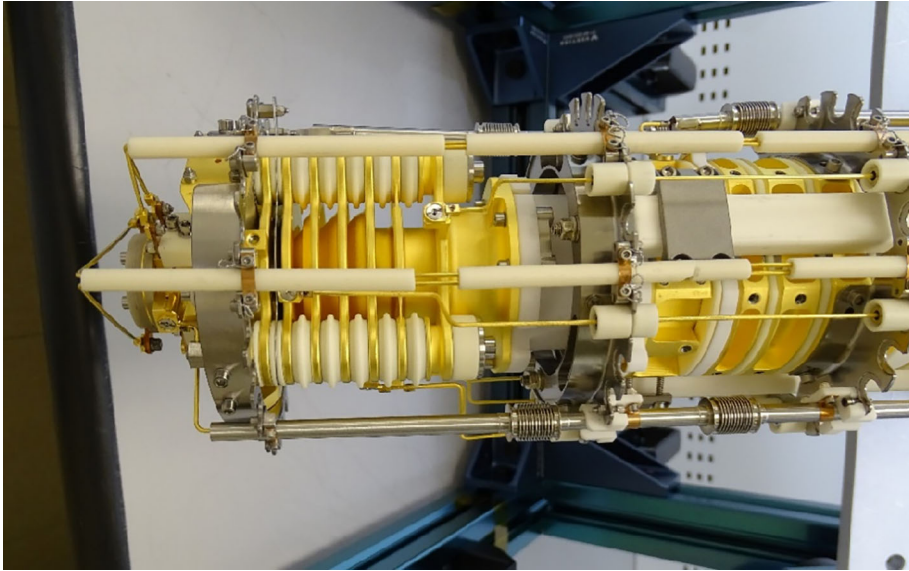


**Fig. 23** Photograph of the ion source showing the extraction, acceleration and focusing electrodes (compare with Fig. 21)

An important feature of the source is that during extraction, ions formed at the back of the ionization volume experience a pusher electric field for a longer duration than those close to the extraction grid (Fig. 22). Two accelerating stages generate narrow ion bunches at the beam's space-focus plane. The location of the focus plane can be shifted by changing the ratio of the pusher and extractor electric fields and the two accelerating electrodes. In multi-lap, high-resolution mode, the first time-space focus is shifted closer to the source and a final space focus plane is shifted to the detector plane by the isochronous reflectrons. For straight-through (i.e., without reflections) spectra, the space focus is shifted to the detector plane. Additional lenses are used to focus the beam radially to pass through a 5-mm diameter reflectron entrance aperture (Fig. 21). The exit end-cap aperture is 5 mm in diameter while the active microchannel plate diameter is 7 mm.

### 5.4.3 Ion Injection and Trapping

With reference to Fig. 24, ions are extracted from the source and injected into the MBTOF by two fast-switching ( $\Delta t \sim 5$  ns) high-voltage pulses that create high intensity electric fields ( $> 100$  V/mm) between the pusher and two extractor grids that define the ion source space charge trapping volume. The pusher electrode is given a positive potential and extractor electrode a negative potential. Fast switching of the voltages accelerates all ions to nearly identical energies. Ions leaving the ionization volume then fall through two additional accelerating stages (located at 60 mm and 210 mm from the source in Fig. 24), while two electrode lens elements focus the beam radially through the 5 mm reflectron end-cap electrode located 120 mm into the MBTOF.

The reflectrons are comprised of a set of four ring-shaped electrodes (Fig. 19) that reduce angular and spatial dispersion between ions with the same  $m/z$  ratio so that they arrive at the detector within a few nanoseconds of each other. Two buncher electrodes operate at

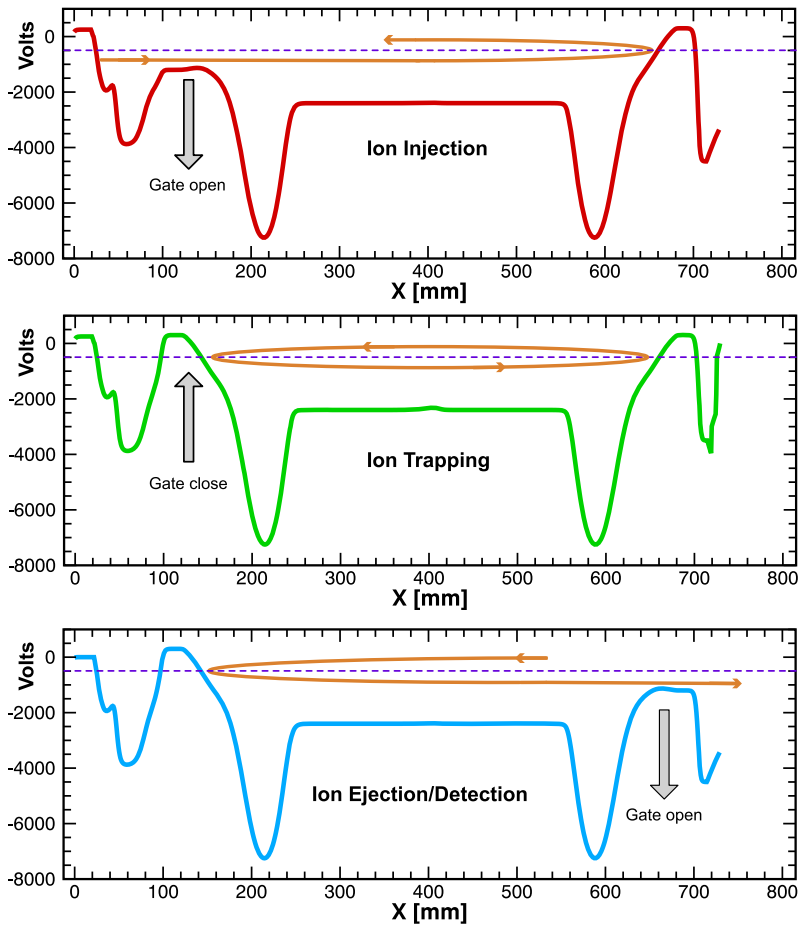


**Fig. 24** Schematic showing the operation of the MBTOF optics. The heavy red, green and blue lines show the distribution of voltages relative to position along the instrument length (Fig. 18 and Fig. 19). The dashed purple line represents the potential energy of the ion packet in the source ionization region (0 mm on the x-axis). The distance between the voltage line and the purple line is a measure of the ion packet velocity at that location. Heavy orange lines centered about the dashed line are a graphical representation of ion motion with reflectron gates opened (top and bottom panels) and closed (middle panel). The y-extent of the orange line is purely for clarity, it does not represent any change in energy of the ions

extremely high voltages and, as the name suggests, bunch the ion trajectories towards the center of the flight tube, thereby decreasing the beam's angular dispersion prior to their release into the drift tube. This action re-constitutes the beam after any trajectory perturbations caused by aberrations in the reflectron fields. The drift tube joins the two reflectrons optically, creating a static gradient-free electric potential that ions travel through at constant velocity. To prevent timing perturbations of the ion beam, drift tube optical elements are driven by a very accurate, highly stable power supply.

After entering the first reflectron (Fig. 24 top) the potentials on both reflectrons are raised, trapping the ions between them (Fig. 24 center). Because the ions are mono-energetic, they separate according to their velocities, and therefore  $m/z$ , by an amount proportional to the number of laps. Once ions execute a prescribed number of laps, they are released through



Reflectron 2 (Fig. 24 bottom). They then strike the front MCP of the detector where they generate a charge pulse that is amplified and buffered by high speed “front-end electronics” (FEE) before being transmitted to the DAP board in the EBOX.

The velocity difference between high and low mass ions means that light molecules such as hydrogen will have travelled to Reflectron 2, bounced, and returned to Reflectron 1, before the highest mass ions have passed Reflectron 1. This makes the measurement of both low and high masses with bouncing impractical, so the measurement of low mass ions is achieved by allowing them to travel directly through both reflectrons to the detector. Reflectron 2 potential is raised after ions up to approximately 12  $m/z$  have passed, and the higher masses are bounced as described earlier.

If desired, the highest masses in the spectrum can be removed by lowering the potential on Reflectron 1 once more, after the highest required mass has bounced, thus allowing the higher masses to pass through towards the source. The Reflectron 1 potential is then raised again, before the desired masses return from bouncing in Reflectron 2.

This process enables the selection of a specific range of ion masses, called a region of interest (ROI), which is then allowed to continue lapping the MBTOF until the desired mass resolution is achieved. The potential on Reflectron 2 is then lowered, releasing the ions to the detector. The selection of  $n$  or  $n + 1$  laps is achieved by adjusting the time at which the potential of Reflectron 2 is dropped to allow ions to reach the detector.

Thus, for every extraction, a low-mass sub-spectrum and a high-mass sub-spectrum are created. The low-mass sub-spectrum allows hydrogen to be measured in straight-through mode with every spectrum regardless of the number of laps other ions perform.

Mass resolution can be varied depending on the selected number of laps. Larger numbers of laps increase ion separation in time and space based on  $m/z$ . To achieve high mass resolution, the TOF can be made large, or the ion packet width  $\Delta t$  very small. However, there is a practical limit to how small the bunch width  $\Delta t$  can be made before peak broadening and asymmetry become important. Sources of these effects can be categorized as timing errors caused by aberrations arising from initial conditions in the ion source, and timing errors that occur when ions exit the flight tube after executing a chosen number of laps. The source and exit errors only occur once and hence do not accumulate over time. Errors that occur on every lap, for example those caused by aberrations within the reflectron fields, or scattering off neutral particles, accumulate over time and contribute the most to peak broadening. Section 6.4.2 gives a full discussion of factors that control peak broadening and resolution.

#### 5.4.4 Ion Ejection to Detector

Following the selected number of laps, the potential on Reflectron 2 is lowered, and ions are gated out to the detector. The beam is focused on the front MCP, generating an electrical pulse whose magnitude is proportional to the number of ions captured. A grid biased above the voltage of the first MCP (Fig. 27) prevents secondary electrons, which would otherwise have the detrimental effect of enhancing MCP response causing pulse height errors, from leaving the surface.

The detector is comprised of three microchannel plates arranged with a single plate facing the beam separated by several mm from the other two plates arranged in a chevron configuration (Fig. 25 and Fig. 26). The MCPs all have 3  $\mu\text{m}$  diameter pores on a 5  $\mu\text{m}$  pitch. The front MCP is biased at  $-3000$  V (Fig. 27) on the side facing the reflectron, ensuring that all ions strike the MCP with the same energy. The voltage across the MCP controls its gain. It is nominally 400 V but can be changed by varying the bias. The front MCP produces an electron cloud that is primarily proportional to the number of ions impacting the MCP surface and, to a lesser extent, is responsive to the ion mass. The latter effect will be calibrated

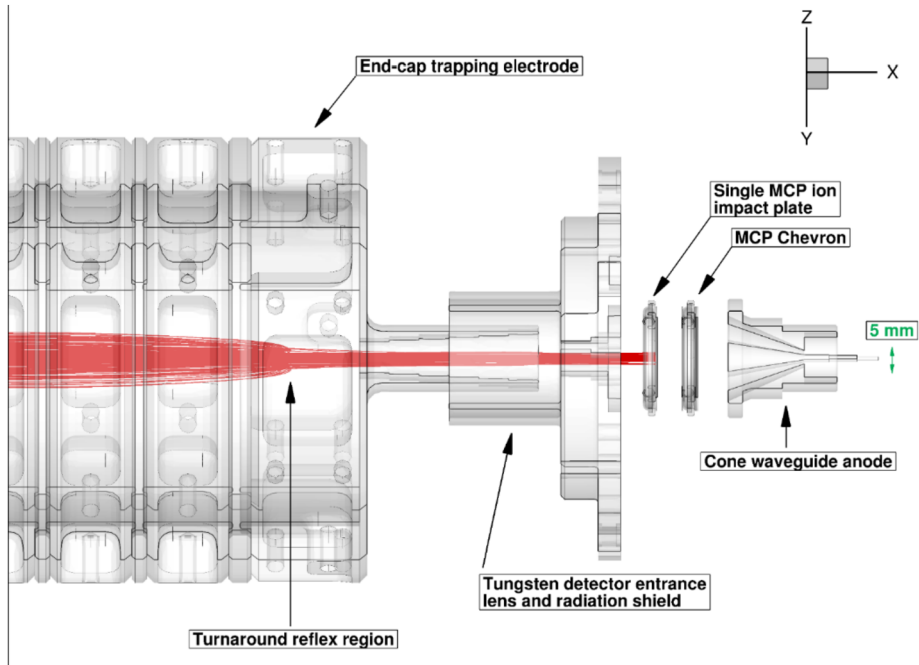
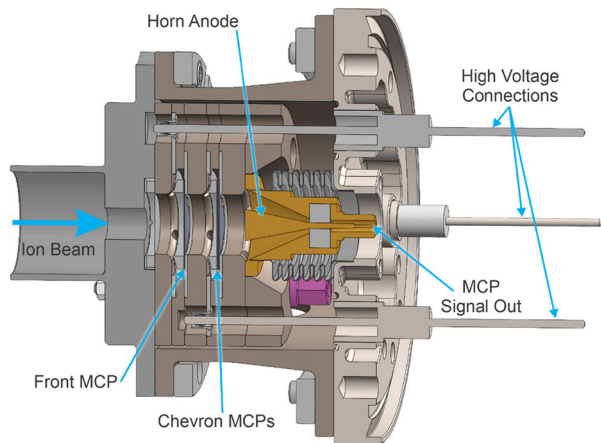


**Fig. 25** Cross section showing the endcap of Reflectron 2 and ion trajectories from there to the three microchannel plates and horn anode forming the detector. The diameter of the horn anode electron collection area is 5.0 mm. The conical horn anode is a solid piece of metal shaped and mounted coaxially within a solid metal enclosure to ensure 50 ohm impedance match between the MCP and the pre-amplifier (Wiza 1979; Wurz and Gubler 1996)

**Fig. 26** Three-dimensional CAD drawing of the detector showing details of the front and chevron MCPs and the horn anode



by laboratory measurements with the EM during the cruise phase to determine what, if any, correction needs to be applied to the FM data.

The chevron pair of MCPs further amplifies the electron signal. The chevrons are stacked with their 12° pore bias orientations opposed to prevent ion feedback. The front plate of the chevron pair is biased 500 V positively compared to the back of the top plate. This

**Fig. 27** Potential diagram for the MCP detector indicating the adjustable voltages and the resistor network that divides the adjustable voltages across the MCP plates

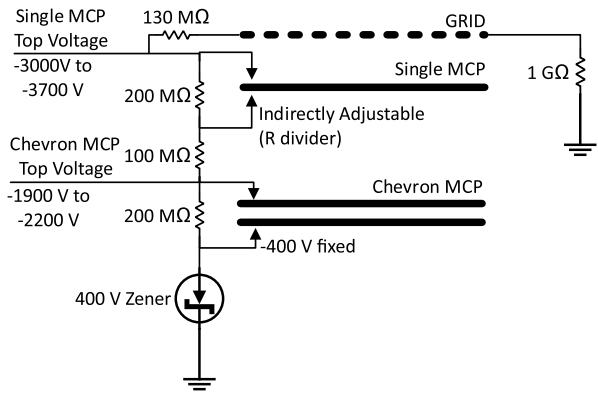
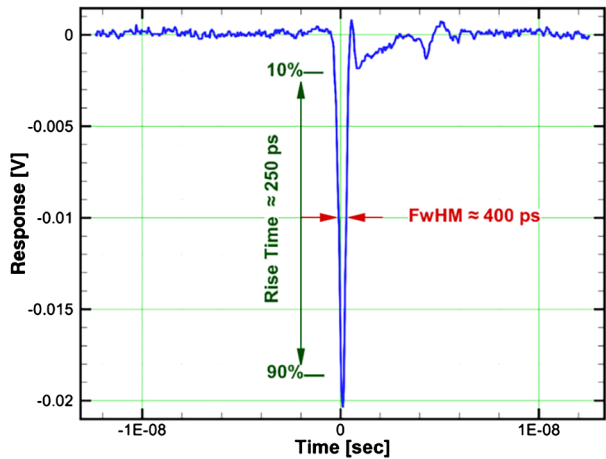


**Fig. 28** MCP response for a single ion-generated pulse measured at the exit of the horn anode



arrangement accelerates the electrons from the first to the second MCP. The chevron gain is then controlled by a total voltage drop of between 1100 V and 2000 V across the two MCPs. Finally, the back of the chevron stack is biased by Zener diodes at a fixed  $-400$  V relative to the anode, which itself is close to ground potential.

The charge cloud leaving the back of the chevron is collected by a horn-shaped anode designed to match the impedance of the output charge signal to the amplifier electronics mounted immediately adjacent to the anode. Typical MCP pulse signals are low voltage and very fast, on the order of 20 mV and sub-nanosecond (Fig. 28). The pulses are buffered and amplified by a high-bandwidth differential operational amplifier and then sent via 50-ohm matched cables to an analog-to-digital converter on the DAP board located in the EBOX.

A critical feature of the detector is that it is operated in a “modal” gain regime in which the amplitude of a pulse is proportional to the number of ions striking the detector (Fig. 28). The linear mode is used in high resolution TOF mass spectrometry because it allows spectra in which the peak amplitude is proportional to the number of incident ions and hence to the abundance of each species. (MCPs in spaceflight instruments are more normally operated in saturation in which case each event is only registered as a single count.)

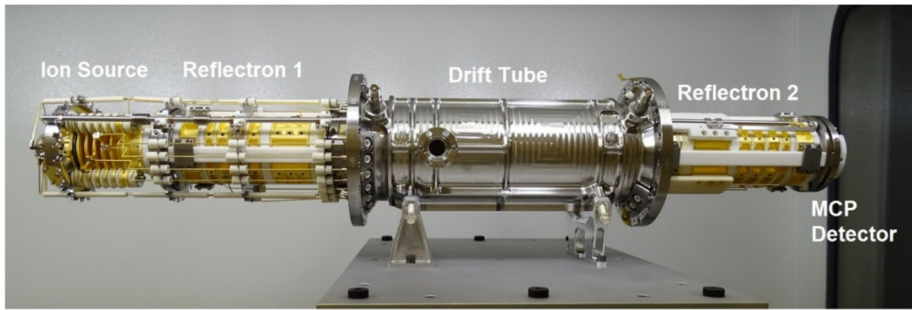


**Fig. 29** The completed FM mass spectrometer optics assembly is shown prior to final integration with the GIS and housing. The ion source on the far left is attached to Reflectron 1 followed (left to right) by the drift tube, Reflectron 2, and then the MCP detector assembly

### 5.4.5 Sensor-Mounted Electronics

The MCP amplifier and associated circuitry make up the highly sensitive front-end electronics (FEE, Fig. 30). The Faraday Cup Electrometer (FCE) used for onboard calibration depends on a second, highly sensitive circuit. Because the FEE and FCE read low-level signals they are noise-sensitive circuits that would be susceptible to electrical noise generated inside the EBOX, primarily by the extremely high-speed switching of high voltage and digital circuits. For this reason, the FEE and FCE are mounted inside the sensor housing in a radiation-shielded area to protect them from Jupiter's intense radiation environment. Locating the FEE and FCE in the sensor also allows its chassis to be used as the global electrical ground, further minimizing noise.

In addition, the pusher and extractor pulser control circuits are mounted on the GIS/MS deck because they switch at slew rates of  $25 \times 10^9 \text{ V s}^{-1}$ . If the supplies were placed inside the EBOX, the length of cables between them and the EBOX would distort the pulses whose shapes are critical for time-focusing the beam. The low-level signal electronics in the sensor and the digital electronics in the EBOX share a common ground which further aids in noise suppression.

One remaining consideration is thermal accommodation of the sensitive circuits and the precisely machined and fitted mechanical components (see Sect. 5.6). Heat from the ion source filament is conducted by the source structure to the instrument housing where it is radiated to space. The MBTOF assembly itself has rigorous thermal constraints designed to prevent changes in the length of ion flight paths that might perturb times of flight. Some idea of the mechanical limits necessary can be gained using the resolution equation  $m/\Delta m = l/2\Delta l$ . A resolution of 20,000 with the MBTOF length of 50 cm requires maintaining a precision of approximately 12 microns. During operations at apoapsis temperatures must be controlled to within  $\pm 10^\circ \text{C}$  of the nominal value to ensure accurate TOF measurements. The full flight assembly of the mass spectrometer is shown in Fig. 29.

### 5.4.6 Internal Calibration System

In conjunction with the calibration gas system in the GIS, the Faraday cup (Fig. 20) supports in-flight calibration by determining the source sensitivity in terms of detector counting rate as a function of the gas density.

Two vanes located in the drift tube deflect ions off the main beam path into the FC where the beam current is measured by a high impedance, high-gain electrometer amplifier.

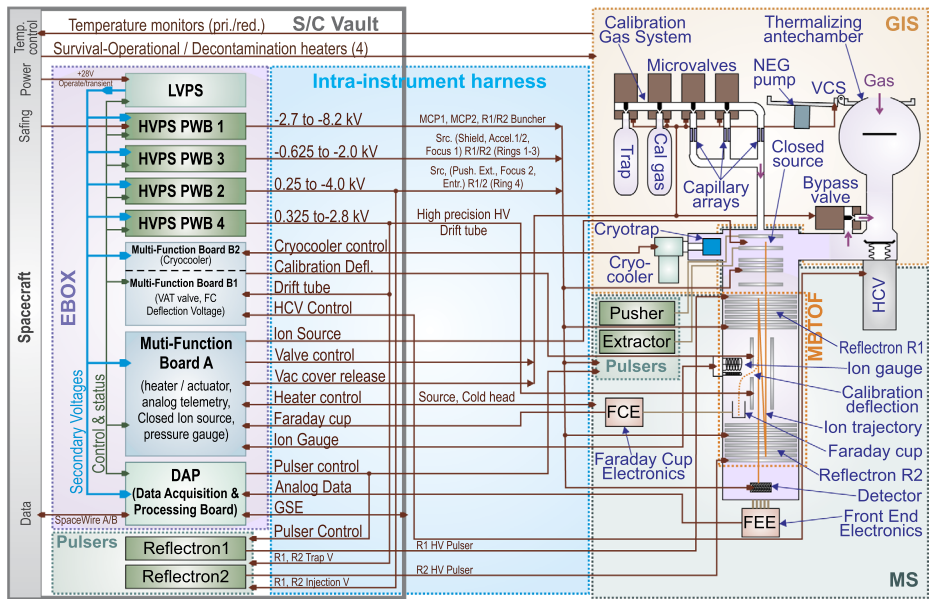


**Fig. 30** Block diagram of the EBOX and sensor (not all connections between the EBOX and sensor are shown)

Calibration then correlates the FC current with the gas density inside the MBTOF measured by the internal ion gauge. Before flight the FC is separately calibrated to give a known gain relationship proportional to the ion density. Calibration details are discussed in Sect. 6.

## 5.5 Electronics Box

### 5.5.1 Design Overview

The most sensitive electronics, the FEE and pulser supplies, are mounted on the sensor (Fig. 14 and Fig. 30). Electronics associated with the sensor are heavily shielded by the sensor deck and a detector radiation shield. The remaining electronics, primarily related to high voltages, data acquisition, instrument control and operation, and spacecraft communications are housed in the EBOX located inside the spacecraft radiation vault.

In addition to consideration of the usual mechanical and electrical interfaces to the spacecraft, the overall design of the MASPEX electronics was driven by the need for protection from the Jovian penetrating radiation environment. As a result the EBOX is mounted in the spacecraft radiation vault and connected to the sensor by a ~2 m intra-instrument harness containing a complex set of cables that themselves had to be shielded to reduce dielectric charging caused by the radiation (light blue shading in Fig. 30).

The EBOX interfaces directly with the Europa spacecraft via the Operational and Transient Power Bus, and a redundant SpaceWire link. EBOX circuits control the overall operation of the instrument, primarily by receiving and executing commands; collecting, formatting, and transferring data to the spacecraft telemetry bus; and powering and controlling the GIS, ion source, and reflectrons. Table 8 is a list of the printed circuit boards (PCBs) in the EBOX and their primary functions.

**Table 8** List of electronics boards in the EBOX

EBOX Board	Functions
Backplane	Voltage and signal distribution to all boards, structure mechanical support, and inter-board communication.
Low Voltage Power Supply (LVPS)	Condition and filter power to EBOX and sensor subsystems.
Digital Acquisition and Processing (DAP) Board	SpaceWire interface, experiment timing, spacecraft command receipt and execution, nominal science data processing, feedforward science data processing, telemetry collection and formatting.
Multi-Function Board A (MF-A)	Telemetry data acquisition and discrete control of ion source, GIS functions, digitize analog signals, local heaters.
Multi-Function Board B1 and B2 (MF-B1 and MF-B2)	MF-B1: HCV driver, FC deflection vanes. MF-B2: Cryocooler.
High Voltage Power Supply Boards (HVPS1)	MCP, Reflectron 1 and 2, buncher.
High Voltage Power Supply Boards (HVPS2)	Ion source lenses, reflectron lenses and source extraction.
High Voltage Power Supply Boards (HVPS3)	Ion source focus and acceleration, TOF reflectron lenses.
High Voltage Power Supply Boards (HVPS4)	TOF reflectron lenses, high accuracy drift tube.
Pulsers R1 and R2	High-speed switches for reflectron potentials from HVPS4.

While in general the MASPEX configuration meets all penetrating radiation and EMI constraints, the sensor design posed additional challenges. In addition to protecting sensitive signals from the FC and MCP, the high-voltage supplies, particularly for the drift tube, had to operate with high stability. These issues were resolved by careful system design and implementation that balanced current flow, provided a local secondary tie point at the sensor power supply input voltages, and isolated high-current actuation of GIS valves and doors from the primary power supply. High voltage stability (particularly in the high-voltage, high-transient-current pulser supplies) was resolved by onboard thermal control, careful signal filtering, and custom high-voltage triaxial cables that connect the EBOX electronics to the sensor.

### 5.5.2 Low-Voltage Power Supply

The LVPS filters and conditions power for each of the primary-referenced power feeds including the EBOX, instrument actuators such as the valve controls and cover release, and all sensor electronics. The supply also generates and distributes power to the floating voltages needed for the sensitive FEE and FCE electronics.

### 5.5.3 Data Acquisition and Processing (DAP) Board

The DAP board is the “brains” of MASPEX. It incorporates a FrontGrade Technologies’ GR712 SPARC V8 processor to manage communications with the spacecraft, control instrument settings, and provide overall instrument sequencing (software running on the SPARC V8 is discussed in Sect. 8.1). A power-switchable Xilinx V5 FPGA controls an ADC12D1620 12-bit analog-to-digital-converter (ADC) operating at a 1.6 GHz sampling



rate. The ADC converts analog pulses from the detector into digital values. The V5 then processes those values into science data products, which are stored in dynamic memory for later readout. An RTAX FPGA serves as the central distribution point on the DAP, providing interfaces to nearly everything on the DAP as well as to other instrument subcomponents. The DAP also provides redundant SpaceWire communication links with the spacecraft via a communications bus with a command bandwidth of 10 Mbps and data rate of 16 Mbps. As a safety feature, the DAP has a watchdog timer to monitor processor operation.

Additionally, the DAP provides both nonvolatile and volatile memory components to support instrument functions and data storage. Nonvolatile memory persists through power cycles while volatile memory does not. These components include 256 Kib of Programmable Read-Only Memory (PROM); 64 Mib nonvolatile Magnetoresistive Random Access Memory (MRAM); 160 Mib volatile Static Random Access Memory (SRAM); 64 Gib of nonvolatile flash memory for V5 configuration and science, engineering, and diagnostic data storage; and 6144 Mb of volatile Double Data Rate version 2 (DDR2) acquisition memory. PROM stores the software boot code, and a MRAM stores several images of the flight software.

Software running on the DAP most notably controls data extraction timing by controlling the phasing of the source pusher and extractor pulsers and both reflectron pulsers through a series of lookup tables. As science data are generated, a semi-autonomous data acquisition circuit accumulates spectra. These are packetized and formatted for spacecraft telemetry (Sect. 7). In addition to nominal operation, an ice grain mode (Sect. 8.5.1) is triggered when the hydrogen-ion TOF signal exceeds a certain threshold. After an ice grain cycle completes, normal science operation resumes.

#### 5.5.4 Multi-Function Boards (MF-A, MF-B1, MF-B2)

The DAP manages ancillary instrument operations primarily through three multi-function boards that control and collect data from the GIS and the MS. The MF-A provides control and readbacks for the ion source, Mindrum valve control, VCS release, instrument heater controls, Faraday cup signal measurement, and ion gauge control. MF-B2 is dedicated to the control of the cryocooler motor. MF-B1 controls the HCVA and the Faraday cup deflection voltage.

#### 5.5.5 High Voltages

Four HVPS located in the EBOX produce all MS optical voltages except for the Faraday cup diversion optics located on the MF-B1 board. An essential requirement of the HVPSs is that they maintain mass resolution and accuracy through low ripple and drift that would otherwise lead to TOF peak broadening and timing drift. This is in part accomplished through active autonomous temperature control for the most sensitive voltages that are used by reflectrons 1 and 2 and the drift tube. The requirements on drift are  $\leq 4$  ppm over 10 °C range.

In addition to providing voltages for the electron optics, the high voltage supplies generate the DC voltages used for the ion source and reflectron pulsers. The source pulsers are in a shielded enclosure embedded in the instrument deck below the MS and immediately above the vault. This gives the shielding against ionizing radiation needed for outside-the-vault electronics. The source pulsers comprise a pusher pulser that switches from 0 V to 300 V maximum, and an extractor pulser that switches from 0 V to  $-300$  V minimum. Both pulsers are programmable. The transition is triggered by LVDS timing pulses sourced from the EBOX DAP. The pulsers use heavily voltage-derated GaN Field Effect Transistors

(FETs) to switch between their extrema in  $<10$  ns. The input voltages are distributed from the HV supplies in the vault to the source pulsers via custom high-voltage triaxial cables that balance the DC current, preventing AC magnetic fields from radiating. The output signals are distributed on triax cables to triax feedthroughs on the source end of the MBTOF and thence to the pusher and extractor rings inside the source. The pulsers have significant input capacitance to ensure that the transient current generated by the output signal into the capacitive load of the ion optics is sourced from local capacitive storage and not from the HVPS.

The source and detector-end reflectron pulsers are located inside the vault. Each of the reflectrons is fed with two voltages from the HVPS: a very precise, thermally stabilized trap voltage of 300 V maximum and less precise  $-1200$  V minimum injection and ejection voltages, all of which are programmable. The voltages are distributed from the HVPS via custom triax connectors, and the inputs are heavily filtered for purposes of minimizing AC current flow. Each of the reflectron outputs switch between the trap voltage and the injection and ejection voltages in less than 100 ns with timing triggered by LVDS control pulses sourced from the EBOX DAP. The switching is accomplished by a series “stack” of six GaN FETs between each of the input voltages and the corresponding output signals. The switching control for this “stack” is designed such that the FETs switch sequentially from bottom to top. The output signal is distributed to triax feedthroughs on each end of the MBTOF through custom triax cables that balance the high-level transient current. The slower switching speed of the reflectron pulsers vs. the source pulsers (100 ns vs. 10 ns) allows the reflectron pulser circuitry to be in the more highly shielded vault rather than at the instrument, thus reducing shielding mass.

### 5.5.6 Engineering Status and Telemetry

Circuits in the EBOX transmit instrument health and status housekeeping data to the spacecraft at a maximum packet rate of 1 Hz. The data are collected from all boards in the EBOX together with several other voltage, current, and temperature monitors. These data are stored to a flash memory and can be retrieved via automated or commanded playback.

### 5.5.7 Cable Harness

MASPEX has 38 high-voltage cables and about 40 low-voltage cables, which are routed from the sensor to the EBOX. To ensure the two disjointed parts of the MASPEX instrument operate well together and meet stringent EMI/EMC test requirements, the harness assembly was controlled as a separate configuration item with its own specifications providing guidance on cable treatment and routing for the various types of signals.

- RS-644 (LVDS) protocol signals used to provide timing information and power supply synchronization for the source, reflectron, and pulsers.
- Low Voltage power to enable the FEE, FCE, and pulsers.
- Motor control interface signals for the cryocooler and high conductance valve (HCV) stepper motor actuator.
- Digital or switch feedback signals from the HCV position resolver and the motor open/close and instrument cover HOPA and door actuation sense.
- Solenoid control interface signals for the calibration gas system Mindrum valves and the HCV bypass valve.
- Calibration gas, electron source, and cryotrap heater drive signals.
- Calibration gas release valve (frangi-bolt style) and cover HOPA drive signals.

- Drive signals for the electron source and the ion gauge (vacuum tube-like interface).
- Low-level passive analog interface signals for the engineering temperature and cryocooler temperature (cryogenic sensor).
- Low-level active low frequency analog interface signals for the FCE.
- Low-level active high frequency analog interface signals for the FEE.
- High-voltage coaxial distribution for static ring bias and MCP drive signals.
- High-voltage triaxial distribution for pulser input and output voltage drive signals.

Each of the low-voltage cables has a minimum of two production breaks (connectorized breaks to make spacecraft assembly more efficient), severe EMC derived restrictions on cable shield impedance, and numerous restrictions on cable routing imposed to avoid interference with other spacecraft subsystems. This meant that an atypically high level of engineering effort was necessary to realize the harness design.

## 5.6 Thermal Design

Temperature affects MASPEX's operation in several ways and a necessary part of the design process was to identify and control those areas critical to instrument performance. We discuss each of these critical areas, their effect on MASPEX's performance, and how they are controlled.

### 5.6.1 Mechanical Effects

Measuring highly precise times of flight, MASPEX is sensitive to changes in the path length. If the instrument gets longer then the same mass peak will appear to have 'lost' mass. The greater the number of laps the ions take, the larger the apparent mass losses. MASPEX's optical construction is primarily titanium and ceramic, the expansion of the instrument is  $8.6 \mu\text{m/m } ^\circ\text{C}$ .

We made no attempt to address the temperature change as it is easier to ensure that we don't integrate spectra long enough for the peaks to smear in response to the thermal change of the sensor. We have temperature data in the Housekeeping and can correct for the effects of the change in data processing on the ground, tracking the peak shift with time and adjusting the mass calibration accordingly.

### 5.6.2 EBOX

The EBOX (see Sect. 5.2) relies on the performance of the heat redistribution system used by the spacecraft to remove heat from the vault electronics. During the flyby of Europa, all the instruments will be operating, and the heat is expected to increase the vault temperature as the flyby progresses. This implies that the temperature will increase in response. For most of the supplies in the EBOX, this causes no issues, but for the most precise high voltage power supplies (HVPS4), the expected  $15 \text{ } ^\circ\text{C}$  change in temperature is sufficient to change the voltages beyond the required stability. This will cause the peaks in the spectra to shift, thus invalidating the mass calibration. To compensate for the temperature change, the control circuit for the supplies is heated to the temperature expected at the end of the flyby. The temperature is then maintained across the flyby by steadily reducing the additional heat as the spacecraft warms up.

### 5.6.3 Source Heater

The ion source (see Sect. 5.4.2) operates at a high temperature because the incandescent filament generates heat. However, poor thermal coupling between the filament and the source implies that it takes hours for the temperature to stabilize. During this time the source is outgassing adsorbed material, which is visible to the mass spectrometer. For best results, we need a low and stable background pressure in the instrument. Since power is a limited commodity for the spacecraft, a 3.9 W heater is mounted directly to the rear of the source. The good thermal connection of the heater with the source enables it to be heated quickly to the operating temperature. This reduces the duration and power required for instrument startup.

### 5.6.4 Cryotrap

For the cryotrap (see Sect. 5.3.5) to reach its operating temperature of 65 K, it must remove heat from the adsorber body. The heat removed by the Ricor cryopump heats the body of the compressor, and if it becomes too hot, then heat leaking back to the cold head will limit the minimum temperature. To prevent this the Ricor body must be kept at  $-30^{\circ}\text{C}$  or lower. This is achieved by a passive radiator facing the ram direction. The temperature of the adsorber is monitored by a PRT and the speed of the cryopump adjusted to achieve the trapping temperature.

The cryotrap adsorber has a surface area far in excess of the rest of the instrument's interior. To drive the sample from the adsorber effectively, a 2.7 W heater mounted to the adsorber can be used to raise the temperature and drive off adsorbed species.

### 5.6.5 Calibration Gas System

The CGS (see Sect. 5.3.6) contains FC-43 calibrant that is used to perform in-flight calibration of MASPEX. If the pressure of the FC-43 were to change during these processes, it would result in an impaired tune or an incorrect gain calibration. The pressure is determined by the restriction of the capillary bundles and the pressure of FC-43 in the CGS body. In terms of temperature sensitivity, the change in the flow restriction with temperature provided by the capillary bundles (see Fig. 16) is negligible compared to the change in pressure of the FC-43 with temperature.

The FC-43 is a liquid with a significantly varying vapor pressure over the range of MASPEX operating temperatures. The FC-43 is stored in a reservoir in the CGS body and, to avoid losses over the long cruise to Jupiter, the reservoir outlet is sealed by the isolation valve assembly (IVA, see Fig. 16), an unbroken tube welded on the reservoir outlet. On reaching Jupiter the IVA is opened by a shape-memory actuator that fractures the tube at a score line to release the FC-43. Because the IVA protrudes from the CGS manifold it has a lower temperature that causes the FC-43 to distill from the CGS reservoir into the IVA body where it is retained on sintered stainless-steel discs. Since the liquid is in the IVA, it is the IVA that determines the vapor pressure that enters the CGS. The temperature of the IVA is monitored by a PRT so that the current vapor pressure can be determined. See Table 9 for predicted temperatures. The IVA is passively heated from the CGS. A 1.4 W heater on the CGS body allows it to be held at a constant temperature, ensuring stability of the FC-43 pressure in MASPEX.

**Table 9** Predicted temperatures in °C for the IVA and CGS body during the flyby and apojoive operating periods

Component	Apojoive	Flyby
IVA	3.8	22.7
Manifold	11.1	31.3

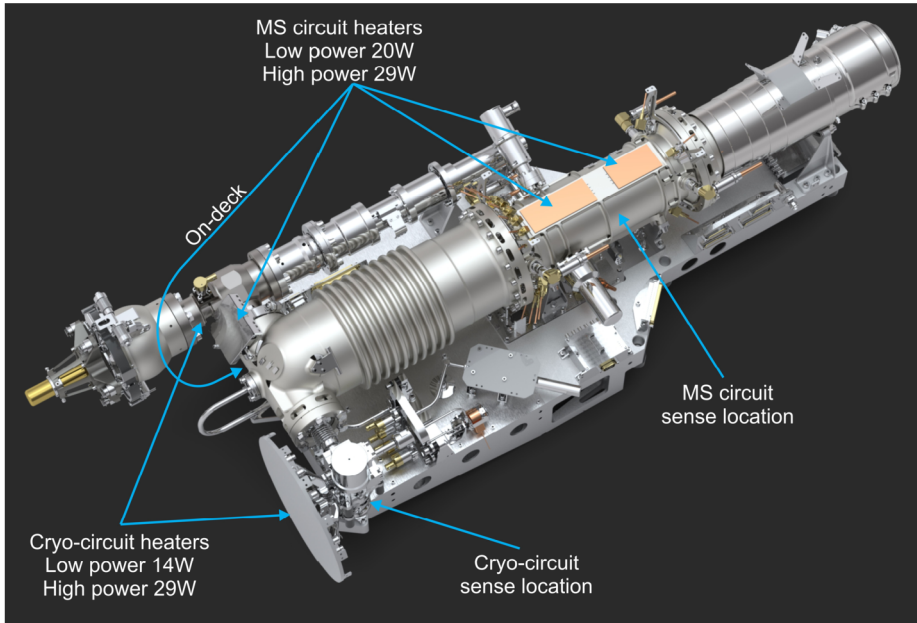


**Fig. 31** Heater and temperature sense locations on the MASPEX sensor for the spacecraft-controlled heaters. The heater labelled ‘On-deck’ is mounted on the surface of the deck that supports the whole of the sensor

### 5.6.6 Instrument Survival and Bakeout

The MASPEX instrument contains components that would be damaged if they got too cold. Additionally, MASPEX needs to be heated to reach a suitable operating temperature. MASPEX temperature control further functions to bake out the instrument in-flight. The bakeout function is important for MASPEX as it removes adsorbed material from the inside of the instrument. This might be from the previous sample, or it might be contamination from spacecraft outgassing. Heating the instrument drives those materials off the internal surfaces and allows the molecules to leave the instrument through the inlet.

To provide this thermal control, heaters are mounted in locations around the instrument (Fig. 31). The EBOX requires no survival heat as this is provided by the spacecraft through the cooling loop. The heaters are controlled by the spacecraft, not by MASPEX. Two locations are used to better match the heating requirements of the instrument. Furthermore, each location has two heaters of different power. Lower power is used for survival heat and to warm up the instrument for operation, while the higher-powered heaters are used for bakeout.

The spacecraft temperature control is a simple on/off switch that uses the temperature ranges shown in Table 10. Bakeout, which takes place following the analysis of the cryosam-

**Table 10** Heater circuit turn on/off temperatures based on operational mode

Circuit	Operational mode	Survival mode
	On/Off (°C)	On/Off (°C)
Cryocooler	-33/-30	-38/-35
Mass Spectrometer	22/25	-28/-25

**Table 11** Resource summary

Parameter	Subsystem	Value
Mass	Sensor	41.3 kg
	Harness	4.6 kg
	EBOX	18.9 kg
	Total	64.8 kg
Dimensions	Sensor	1046 × 435 × 292 mm
	EBOX	357 × 302 × 328 mm
Power (operating)	Sensor	14.9 W
	EBOX	73.3 W
	Total	88.2 W
Power (survival)	Sensor	5.5 W
Power (decontamination)	Sensor	49 W
Telemetry volume per orbit	Housekeeping	0.13 Gbit
	Science	5.06 Gbit

ple near apojove, is achieved by turning the heaters on for 14 hours after which the hottest part of the instrument will have reached a temperature of about 90 °C.

## 5.7 Resource and Consumables Summary

Table 11 is a summary of resources needed to implement the MASPEX design. Much of the instrument's mass is driven by the need for radiation shielding of the three major instrument components. The use of high-speed, high-voltage switching power supplies and the need for precision and high currents to power the closed ion source all require high precision power generation.

MASPEX contains components that have limited lifetimes. These are shown in Table 12 together with the usage planned by the end of the mission, demonstrating ample margin in their use.

## 5.8 Spacecraft Environment

The harsh radiation environment in the region around Europa's orbit, as well as instrument accommodation constraints imposed by the spacecraft design, heavily influenced MASPEX's mechanical architecture. Table 13 summarizes the effective Europa radiation environment, as it applies to MASPEX given its location on the spacecraft, and the mission's electrostatic discharge challenges. The inclusion of a HF/VHF radar, a low-energy plasma measurement instrument, and a sensitive magnetometer on the spacecraft, also presented significant challenges to controlling the MASPEX EMI/EMC environment that might affect other instruments.



**Table 12** Limited lifetime parts and estimated usage through the mission

Item	Units	Uses at delivery	Mission Planned use	Lifetime	% of lifetime
Cryocooler	Operating Hours	161.1	237	13,700	3%
Cryocooler	On/Off Cycles	25	80	8400	1.25%
HCV Valve	Open/Close cycles	244	46	1000	29%
HCV Motor <sup>1</sup>	Open/Close cycles	244	46	200	145%
Microvalve Vent Seal	Open/Close cycles	79	92	300	57%
Microvalve V1 Seal	Open/Close cycles	124	92	300	72%
Microvalve V2 Seal	Open/Close cycles	152	92	300	81%
Microvalve V3 Seal	Open/Close cycles	74	92	300	55%
Microvalve V4 Seal	Open/Close cycles	69	92	300	54%
Primary Source Filament	Operating hours	777.2	352	10,000	11%
Primary Source Filament	On/Off Cycles	206	306	5000	10%
Redundant Source Filament	Operating hours	15.6	0	10,000	0.2%
Redundant Source Filament	On/Off Cycles	27	0	5000	0.5%
Primary Ion Gauge Filament	Operating hours	179.8	76	n/a	n/a
Primary Ion Gauge Filament	On/Off Cycles	229	260	n/a	n/a
Redundant Ion Gauge Filament	Operating hours	11.3	0	n/a	n/a
Redundant Ion Gauge Filament	On/Off Cycles	30	0	n/a	n/a

<sup>1</sup>The counter for the number of uses increments whenever the motor changes direction overrepresenting the actual number of full open/close cycles.

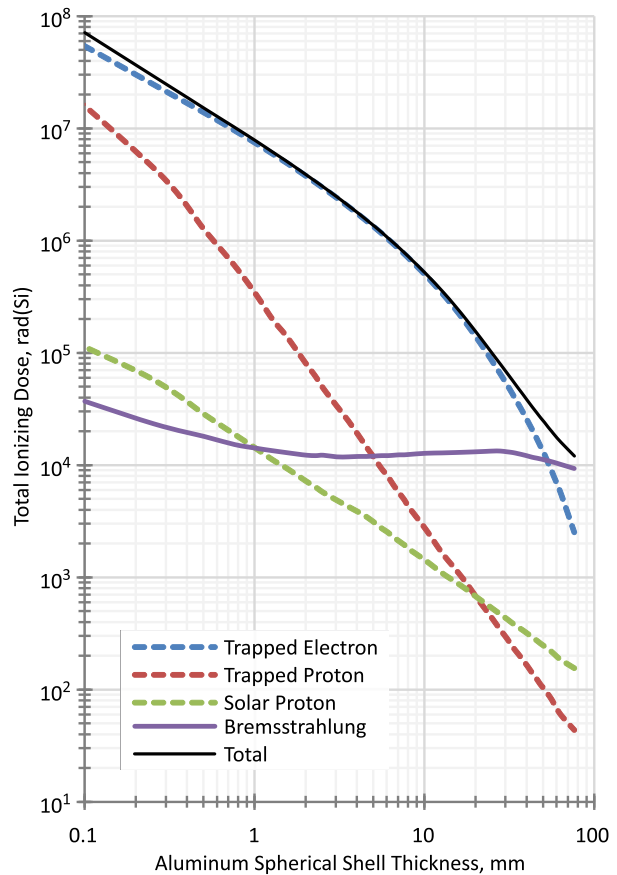
**Table 13** Penetrating radiation environment near Europa’s orbit

Distance (R <sub>J</sub> )	Time (hrs.)	Electron Flux (cm <sup>-2</sup> · s <sup>-1</sup> )			
		1 MeV	Peak flux 1 MeV	10 MeV	Peak flux 10 MeV
<13	40	>1.5 × 10 <sup>7</sup>	3.9 × 10 <sup>7</sup>	—	—
<18	80	>2.0 × 10 <sup>6</sup>	—	—	—
<10	<20	—	—	>1.6 × 10 <sup>6</sup>	4.0 × 10 <sup>6</sup>

While Europa Clipper’s highly elliptical orbit mitigates against some radiation effects, it does not entirely remove them. The extremely high energetic electron flux levels (in particular, along the trajectory within 40 hours of Europa closest approach) lead to a very high total penetrating dose, as well as a high probability of isolated conductor and insulator charging (with associated arcing). Figure 32 is a plot of total ionization dose for the Europa design reference mission, illustrating the challenges to electronics design. The figure shows the shielding provided by a spherical aluminum model (Rev. E of the Europa Environmental Requirements Document). The environment is such that 28 mm of aluminum shaped as a sphere is needed to reduce the total dose to 100 krad (Si) with no margin. The high radiation flux experienced on flybys will also result in significant charging of insulating materials and any ungrounded metal.

Both phenomena have significant impacts that had to be considered in the MASPEX design, primarily in the choice of electronic parts and their need for radiation shielding. This

**Fig. 32** Europa Clipper design reference mission total ionizing dose as a function of spherical shell aluminum thickness as derived by the trajectory analysis with the GIRE radiation model (Garrett et al. 2017) and the NOVICE<sup>6</sup> radiation transport code. Courtesy of Luz Maria Martinez Sierra (JPL)



led to creation and design of the EBOX and its location within the spacecraft radiation vault. However, circuits such as the FEE, FCE, and the MCP detector (which is very sensitive to penetrating radiation that creates signal background (Blase et al. (2015); Blase et al. (2017); Blase et al. (2018a); Blase et al. (2018b))) are located inside separate shielding attached to the sensor body (Fig. 9). The source pulsers and FCE are mounted beneath the sensor in a stainless-steel box. The MCP detector and FEE are shielded by a hollow stainless-steel tube with a tungsten alloy cap.

In addition to the impact of penetrating energetic particle radiation on the MASPEX design, the Europa Clipper spacecraft carries three instruments that impose constraints on electric and magnetic signals radiated by MASPEX. The REASON instrument imposed severe limitations on radiated E-field levels at high frequencies on instruments located outside the instrument vault. In addition, the PIMS and ECM instruments imposed severe limitations on DC and low-frequency B-field emissions. Attention to MASPEX circuit design and grounding allowed it to meet these very low limits in a frequency range where most high-speed digital circuits have numerous emissions.

<sup>6</sup>EMPC, Gaithersburg, MD.

## 6 MASPEX Calibration

Having described the design of MASPEX in the previous section, we turn to the process of calibration, which gathers the data needed to convert measurements made in flight into physical quantities. Calibration also demonstrates the mass spectrometer's ability to unambiguously meet mission and investigation science requirements. There are two performance categories that are essential to calibration. The first establishes the ability of MASPEX to detect target compounds above a given background. The second sets the parameters needed to identify those compounds. The performance requirements were listed earlier in Table 2.

Compound detection has two components. Dynamic range (DR) defines the ratio of the largest detectable mass peak to the smallest. The target set by science objectives is  $\geq 6000$ . The second factor is sensitivity, which is defined as the ratio of the rate of ion creation in the MS source (in ions/s) to gas density in the ion source (in molecules/cm<sup>3</sup>). The science goal is  $\geq 0.02$  counts s<sup>-1</sup> / molecule cm<sup>-3</sup>.

Compound identification has three aspects. The first is accurate mass, which is determined by accurately measuring ion TOF and then converting it to *m/z*. Calibration must establish those conversion factors over a range of 1 u to 500 u. This is performed using FC-43 (perfluorotributylamine, molecular weight 671 u), a calibrant widely used in mass spectrometry applications. The FC-43 breaks up in the ion source in a repeatable pattern to form fragments of specific, known masses. The most used fragments have mass/charge of 69 u, 131 u, 219 u, 414 u and 502 u, all of which appear in calibration data presented in this section. A second factor is that overlapping peaks must be resolved sufficiently well to make them identifiable over the same mass range. The science requirement for mass resolution is  $\geq 4275$  (10% valley) up to a mass of 500 u. The third factor in identification is establishing the ability of the MS to identify patterns of fragments produced by the ionization of an unknown compound (see Sect. 3.2.1).

Calibration of the FM and EM instruments was carried out at the Southwest Research Institute over the period that began approximately one year prior to delivery of the FM to JPL. During that time two different laboratory facilities were used to conduct three successful calibration campaigns of both instruments (Table 14). In this section, we describe the methods of acquiring calibration data, the data itself, how data were analyzed, and then discuss the results and their application to flight data analysis.

### 6.1 The COSMIC Calibration System

The COSMIC system (Comet Outgassing Simulator for MASPEX Instrument Calibration, Fig. 33) is critical to accurate calibration of both the EM and FM and will serve post-launch for further calibration activities as well as for verification of data returned from measurements made at Europa. COSMIC will be maintained as the primary post-flight calibration facility for the EM, which duplicates all FM functionality. A second chamber (CAPS), previously used for the Cassini Plasma Spectrometer (Young et al. 2004) was also used during the first part of calibration.

COSMIC supports two primary modes of operation: calibration with pure gases, and with gas mixtures. Pure gases may be supplied over a wide range of flow rates to the MS from a low-range flowmeter (Li et al. 2013). Gas mixtures are created from pure or pre-mixed gases. Creating calibrant gas mixtures is not a simple process but is essential because it is critical to calibrating MASPEX performance and, later, to analyzing data returned from Europa. Gases are pressure-reduced through a number of stages to the densities needed for calibration.

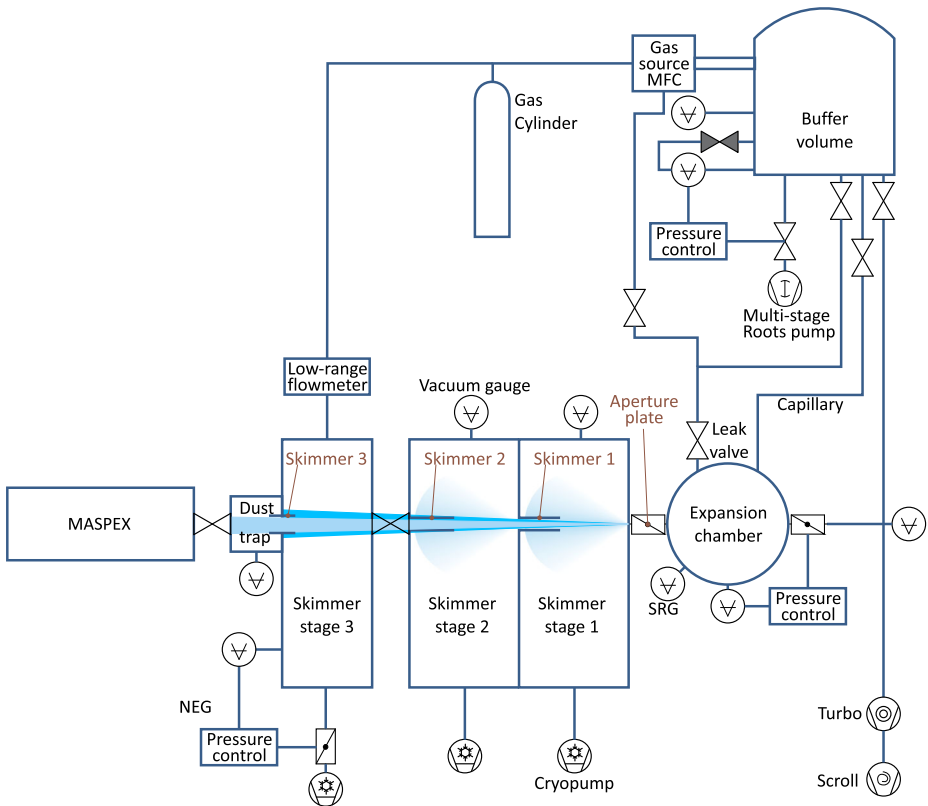


**Fig. 33** Simplified block diagram of the COSMIC calibration system

Figure 33 is a simplified block diagram of the COSMIC system. Pure un-mixed gases pass through a low-range flowmeter to the GIS through a laser-drilled orifice that is calibrated for conductance. The pressure of gas in the flowmeter determines the throughput to the instrument.

Gas mixtures are created from multiple cylinders using mass-flow controllers (MFCs). Gases then flow into the buffer volume where a pressure control system maintains the desired pressure by controlling flow to a waste pump via a proportional solenoid valve.

Gas from the buffer volume also flows through a capillary restriction into the expansion chamber. The pressure in the buffer volume is fully in the viscous flow regime, while the expansion chamber is always in the molecular flow regime. The pressure drop across the capillary causes fractionation of the gas mixture. However, flow through the buffer volume ensures that fractionation cannot build up and change the mixture composition.

The expansion chamber is designed to ensure an isotropic distribution and compositional homogeneity within the flowing gas. This avoids any fractionation of the gas leaving the chamber to either the spectrometer under calibration, or to the waste pump. A pressure controller adjusts the speed of the waste pump to achieve the desired chamber pressure. Gas leaving the chamber towards the instrument passes through an aperture plate with selectable hole sizes. The hole size, in combination with the chamber pressure, determines the intensity of the molecular beam formed from the gas. From there, gas flows through a series of three skimmers that were designed using Monte Carlo simulations of the gas flow.

The molecular beam expands from the hole aperture in a cosine distribution, travels through skimmer stage 1, and then exits through a small tube (the skimmer) on the far side. Gas that expands beyond the tube is pumped away by a cryopump attached to the chamber. The pressure falls in each successive skimmer stage while the molecular beam creates a higher pressure at the entrance to the mass spectrometer. The process repeats on the passage through skimmer stages 2 and 3, where additional cryopumps remove gas that does not pass through the skimmers. With each stage, the pressure in the chambers falls over a wide range that can vary somewhat but is typically  $\sim 10^{-7}$  hPa in skimmer stage 1,  $\sim 10^{-9}$  hPa in skimmer stage 2, finally falling to  $\sim 10^{-10}$  hPa in skimmer stage 3.

The molecular beam that arrives in the dust trap is converted back to an isotropic flow by a conical obstruction in the center of the dust trap. The gas travels from there to MASPEX as a molecular flow. The isotropic flow and molecular beam approach ensure that the gas mixture arriving in the dust trap has exactly the same composition as gas in the expansion chamber, but at much lower pressure. The advantage of this process is that the pressure in the expansion chamber is comfortably in the working range of the quadrupole mass spectrometer used to calibrate the precise composition of the fractionated gas mixture.

Accurate pressure measurements are the most important parameter recorded by COSMIC because they are key to calibrating source sensitivity. Measured pressures rely on high-accuracy gas capacitance manometers and spinning rotor gauges traceable to the U.S. National Institute of Standards and Technology (NIST) and to other international standards. The other critical component is a test volume used to calibrate the internal volumes of the low-range flowmeter.

COSMIC depends on EtherCAT<sup>®</sup> (Ethernet for Control Automation Technology), a fully automated commercial software that controls and monitors every aspect of system operation except the quadrupole mass spectrometers, which employ their own software. Data from all parts of the system are collected at least every second and then automatically stored in the same database used for MASPEX flight data. This ensures that a complete record of calibration activities is stored alongside flight data for the duration of the Europa Clipper mission.

All COSMIC vacuum chambers are designed for bake-out to 300 °C using a modular oven system that provides adequate space to bake the entire MASPEX instrument. The oven control is integrated with the EtherCAT<sup>®</sup> automation system to provide a simple ramp, dwell, and cool cycle. The bake temperature is adjustable, as are the ramp and cool rates. Permanently mounted thermocouples monitor the COSMIC chamber temperatures. There are an additional 24 thermocouple channels that may be temporarily affixed to the instrument exterior to monitor details of the temperature distribution on the test instrument. An alarm system with adjustable warning and alarm thresholds ensures safe operation. Reaching a warning level causes the system to reduce the temperature set point to maintain safe operating temperature. Exceeding an alarm threshold triggers the shutdown of the bake procedure and immediately puts the instrument into a cool-down phase. All alarms are reported to a list of selected team members by text message and email.

## 6.2 Calibration Campaigns

Three MASPEX calibration campaigns were carried out using the CAPS and COSMIC vacuum systems (Fig. 34) in three different configurations (Table 14). Data shown in this paper include results from all three campaigns. They represent only a portion of the full calibration dataset, which will be archived in the Planetary Data System.

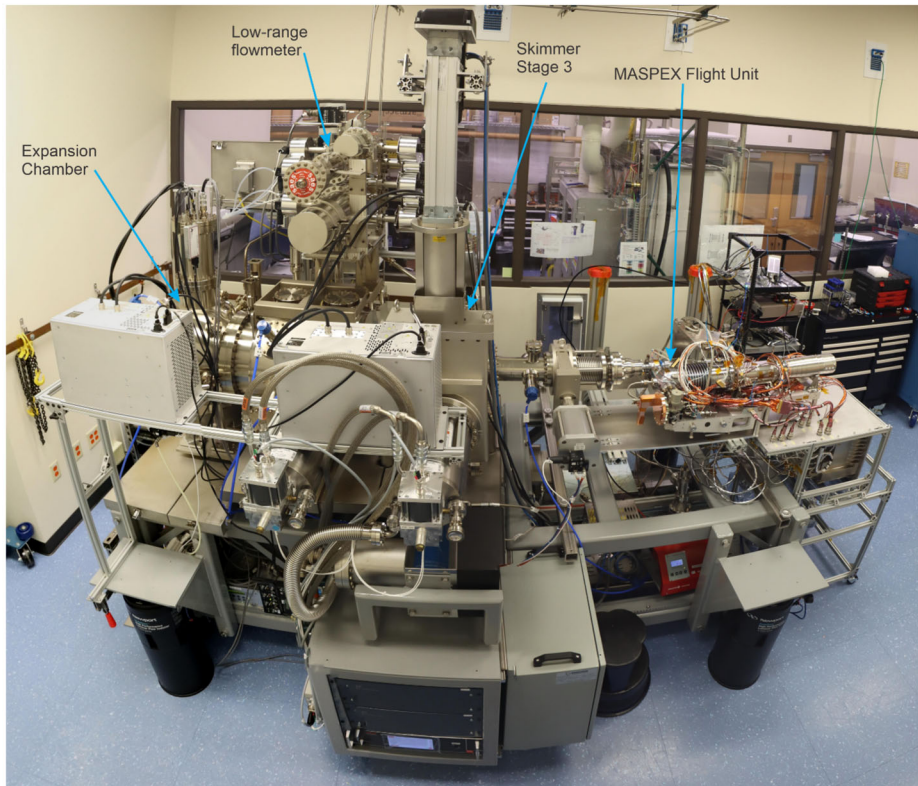


**Fig. 34** Panorama of the COSMIC chambers during MASPEX flight unit calibration

**Table 14** Summary of the three calibration campaigns

	Cal 1	Cal 2	Cal 3
Instruments	Engineering and Flight models	Flight	Flight
Chamber	CAPS	COSMIC	COSMIC
Configuration	No GIS, exposed source	GIS installed	GIS installed
Detector	EM detector	EM detector	FM detector
Calibrations performed	Mass resolution, fragmentation vs. electron energy, high mass range	Low mass range	Dynamic range, sensitivity, peak shape

**Cal 1.** Exercised both the EM and FM mass spectrometers including flight electronics, but without the GIS in place, and without the FM flight-selected detector. The data collected confirmed MASPEX mass resolution, characterized compound fragmentation as a function of the ion source's electron energy, and demonstrated the extent of the upper end of the mass range. During Cal 1, in addition to residual gas in the chamber,  $N_2$  and other gases were introduced through a variable leak valve. Gases derived from liquids (e.g., FC-43) were also introduced via a heated leak line.



The chamber gas composition was monitored with a residual gas analyzer, temperatures were carefully measured, and chamber pressure was monitored using two Anelva<sup>7</sup> miniature Bayard-Alpert gauges (Model M-431HG) chosen because of their similarity to the MASPEX internal ion gauge.

**Cal 2.** The second campaign, devoted to FM calibration, was carried out in the COSMIC facility. The GIS unit, including antechamber, HCV, CGS, and cryotrap, were added, but the EM detector was used rather than the FM.

**Cal 3.** The third campaign was also performed in COSMIC. This time, calibration was carried out on the FM in final flight configuration, including the flight detector. Major results from Cal 3 include calibration of the dynamic range, sensitivity, and TOF peak shape.

## 6.3 Compound Detection

Calibration of the factors that determine the limits of compound detection was carried out primarily during Cal 3. In this section we discuss how dynamic range and sensitivity were measured and the resulting conversion factors needed to detect compounds and determine their density. The results will also demonstrate that MASPEX meets its science requirements, particularly during challenging flybys near the surface of Europa.

### 6.3.1 Dynamic Range

Dynamic range is the largest measurable ratio of major to minor compounds. As noted above, the science requirement for DR during a low altitude flyby is 6000. Although the concept of DR is relatively simple, several other instrument parameters enter the calculation. We consider a single  $m/z$  peak extracted from the source and arriving at the detector as a peak broadened by passage through the ion optics into a roughly Gaussian shape. The signal from the detector is digitized at 1.6 gigasamples per second and converted to counts. The maximum number of counts is limited by the ADC input clamp to 3000. Numerically, the smallest possible count is 1 giving us a dynamic range of  $3000/1 = 3000$ , but this is for one sample of the ADC. If we consider a peak that is 20 ns wide at the base, then the ADC will sample the peak envelope  $20 \times 10^{-9} \times 1.6 \times 10^9 = 32$  times. But within all the samples the smallest count remains as 1 in a single sample, so that the DR becomes  $(32 \times 3000)/1 = 96,000$ . If we consider successive extractions of ions from the source at 1 kHz and sum the spectra for one second, we increase the maximum signal to  $96,000 \times 1000 = 96,000,000$ , but the smallest possible signal remains a value of 1 in a single ADC slice in a single spectrum. Thus, the dynamic range is a function of peak width and the summation (integration) period. In reality, there is noise in the system that increases the minimum count value. The total noise ( $N$ ) from all sources can be computed using

$$N = n\sigma_w^2 + n\lambda_d(a^2 + \sigma_a^2) + n\lambda_R(b^2 + \sigma_b^2) \quad (2)$$

where  $n$  is the number of extractions,  $\sigma_w$  is the standard deviation of the ADC noise,  $\lambda_D$  is the rate of stray ions hitting the detector,  $a$  is the amplitude of the detector response to a single ion and  $\sigma_a^2$  its variance,  $\lambda_R$  is the rate of radiation hits,  $b$  is the amplitude of detector pulses in response to radiation, and  $\sigma_b^2$  its variance. Below we consider each term on the right-hand side in further detail.

Term 1,  $n\sigma_w^2$  - ADC noise: The ADC noise model assumes that the cyclic noise is removed in ground processing. The cyclic noise comes from the different sub-converters in

<sup>7</sup>Canon Anelva Corporation.

**Table 15** Input parameters and results for the noise estimate during flybys at 25 and 100 km based on equation (2) and used to create Fig. 35

Flyby Altitude (km)	25	100
<sup>1</sup> Pressure (hPa)	$1.2 \times 10^{-7}$	$3.9 \times 10^{-8}$
ADC noise (%)	66.1	86.8
Diffuse noise (%)	33.7	13
Radiation noise (%)	0.2	0.3
Signal to noise	$1.5 \times 10^5$	$1.7 \times 10^5$
Dynamic range	$1.8 \times 10^4$	$2.0 \times 10^4$

<sup>1</sup>Pressure within the ion source.

the ADC and digital noise present in the ADC and FPGA at 200 MHz, 100 MHz, etc. There is an advantage in that these frequencies add coherently in the co-adding process. This enables us to remove them. If they added incoherently, they would increase the statistical noise of the co-added spectrum. The residual noise when the cyclic components are removed, and no ions are present is  $\sigma_w$ . This is the noise in the output of the ADC (after removing cyclics) if a DC value is present at the input. It has a standard deviation of approximately 0.9 to 1.1 counts of the ADC.

Term 2,  $n\lambda_d (a^2 + \sigma_a^2)$  - Ion leakage current: The  $\lambda_d$  part of the noise is from the diffuse ion background. This term represents how many non-peak ions there are in the vicinity of the peak we are looking at. The non-peak ions can come from ions leaking out of the source, and from ions scattering out of the ion packets by self-collision or collisions with residual neutral gas in the sensor during the lapping period. Scattering may be the dominant component. It can vary tremendously from one ROI to the next and within the same ROI. Two examples are relevant to illustrate this point: 1) On one hand, the H<sup>+</sup> peak of the dynamic range demonstration (see Fig. 36) shows very low ion noise for the H<sup>+</sup> peak because it is in straight-through mode and there is no time for heavier ions to traverse the instrument. 2) On the other hand, if there is a large peak with a long tail, and a small peak within that tail, then the tail ions make up the diffuse background for the small peak.

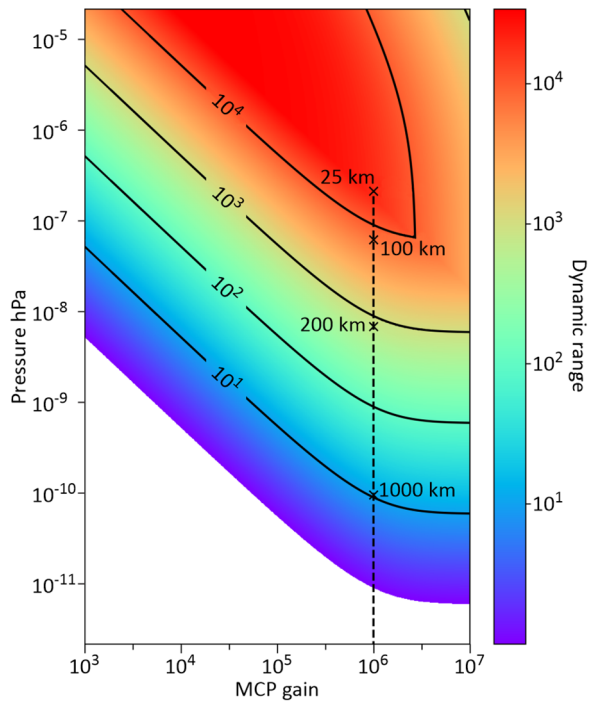
Term 3,  $n\lambda_R (b^2 + \sigma_b^2)$  - Radiation noise: This component is the smallest noise source, but with an uncertainty that can only be based on the mission tour experience. The values used here are from the MASPEX shielding design (Sect. 5.8).

Table 15 provides an estimate of the noise produced during flybys with closest approaches of 25 and 100 km, based on the Europa atmosphere environment model of Teolis et al. (2017c) (Sect. 3.2) utilizing our present understanding of the noise generation and our experience with the EM and the FM units. The following assumptions are used in the calculation: a) 1 second integration, b) 22 kHz radiation noise, c) 3 sigma false positive discrimination, and d) 2 sigma false negative discrimination. Signal-to-noise has been added to the chart calculated using maximum peak size.

Adding the effect of this noise reduces the DR at Europa closest approach. To increase the DR to meet science requirements we sum the spectra from successive extractions together for a period so that the uncorrelated noise terms (e.g., ion statistical noise) average out, increasing the noise at a slower rate ( $\sqrt{n}$ ) than the signal maximum, thus improving dynamic range. The maximum period of summation is limited by drift of the potentials in the instrument and by dimensional changes due to temperature changes across the flyby.

An additional constraint on the summation period during the flyby is the surface spatial resolution requirement, which is equal to the altitude. Taking the spacecraft ground speed

**Fig. 35** Modeled DR for a 1-second integration at closest approach as a function of MCP gain, ion source gas pressure (including ram effect and cryotrap pumping), and altitude above Europa's surface. The color scale corresponds to DR and the dashed line contains points indicating the altitude above Europa's surface for a standard Europa flyby. The complete simulation for the Flyby and Cryotrap dynamic range are based on models of the instrument and the atmosphere (Teolis et al. 2017c)



into account shows that, for all flybys, at least 5 s are available to meet the requirement (see Table 2). All necessary data must be taken in the 5 s period, which may comprise several spectral ROI (see Sect. 7.4.2).

As a practical demonstration of the dynamic range, we measured the ratio of the  $\text{H}^+$  and  $\text{CO}^+$  peaks in a residual gas spectrum. The  $\text{CO}^+$  was very near the maximum signal and the  $\text{H}^+$  only became measurable at the selected gain and sensitivity settings by increasing the summation time to 2 s.

Figure 35 illustrates how DR is projected to vary as a function of Europa's exospheric pressure and detector gain during an encounter. The figure is based on atmospheric model results from Sect. 3.2, and measured values taken from calibration. Representative closest approach altitudes are designated, and 1-s integrations are assumed. The figure illustrates the criticality of calibrating detector gain.

To demonstrate that the MS can meet requirements implied by this flyby simulation, the DR data were collected during Cal 3 by recording straight-through spectra of chamber residual gas at  $3 \times 10^{-7}$  hPa. This is equivalent to an altitude below 25 km according to our model of Europa's atmosphere. Straight-through spectra were recorded to capture the  $\text{H}^+$  and the  $\text{CO}^+$  peaks simultaneously in the same spectrum (Fig. 36). Twenty-nine spectra, each summed for 2 s (two-fifths of the flyby spectrum capture cadence), were collected at 1 kHz extraction rate (the same rate planned for flyby operations). Mass scale calibration was then performed to identify the TOF location of the  $m/z$  1 mass peak using the peaks associated with  $\text{H}_2^+$  and  $\text{DH}^+$ ,  $\text{C}^+$ ,  $\text{OH}^+$ ,  $\text{H}_2\text{O}^+$ ,  $\text{CO}^+$ ,  $\text{O}_2^+$ , and  $\text{CO}_2^+$ .

To obtain the DR for the  $\text{H}^+$  and  $\text{CO}^+$  peaks, we calculated the integrated peak area  $P$  following a procedure outlined in Gedcke (2001), which was modified for the MASPEX analog signal by including ADC noise. The regions sampled for signal and noise were identified using the average of 29 spectra. The background was taken symmetrically on either

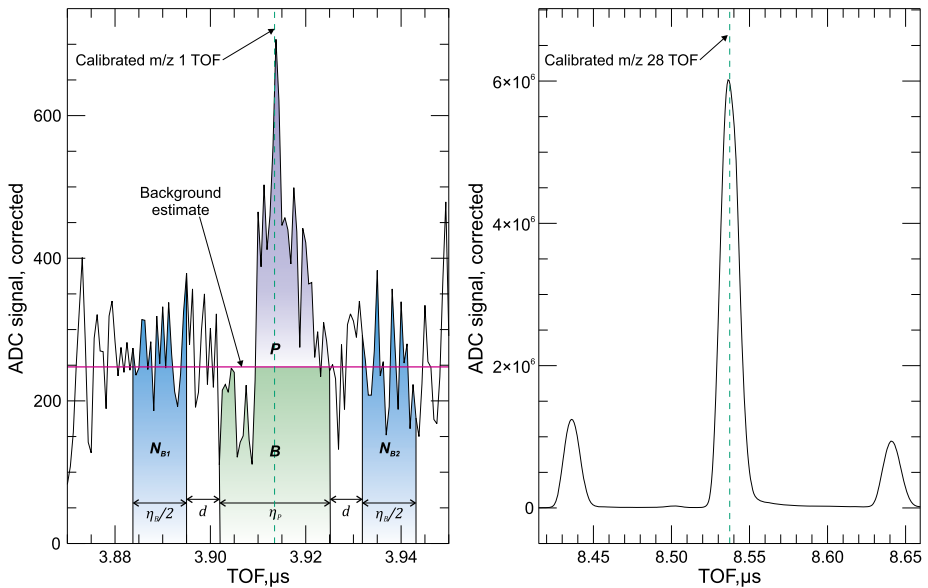


**Fig. 36** A representative 2-second spectrum showing the H<sup>+</sup> signal (left) and the CO<sup>+</sup> signal (right) from the DR measurement data set. The left panel identifies the regions of the spectrum used to establish the background signal, using the notation described in Gedcke (2001)

**Table 16** Summary of the results of the dynamic range analysis (data are rounded to the nearest thousand)

Average	51,000
Minimum	25,000
Maximum	100,000
Standard Deviation	20,000
Relative standard deviation	40%

side of the peak centroid (blue shaded regions in Fig. 36). We then calculated the signal for each spectrum as

$$B = \frac{\eta_P}{\eta_B} (N_{B1} + N_{B2}) \tag{3}$$

$$P = T - B \tag{4}$$

where  $B$  is the weighted background,  $N_{B1}$  is the integrated background signal to the left of the peak,  $N_{B2}$  is the integrated background signal to the right,  $\eta_B/2$  is the integration width for the background on a single side, and  $T$  is the total integrated signal over the region defined by  $\eta_P$ . The integrated peak area  $P$  was calculated for  $m/z$  1 and 28 in each spectrum and the DR calculated as

$$DR = \frac{P_{28}}{P_1} \tag{5}$$

The measured DR values (Table 16) show significant variability (SD = 20,000). As is expected, this is largely due to H<sup>+</sup> peak area variation. Even the smallest recorded value

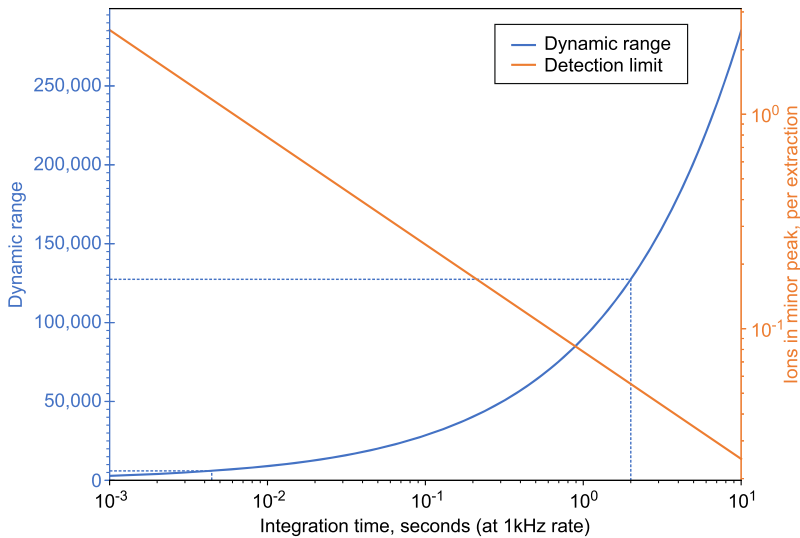


**Fig. 37** The calculated variation of dynamic range and detection limit based on equation (2). The two sets of dashed lines indicate the maximum performance for the experimental integration time of 2 seconds and the integration time necessary to achieve 6000 dynamic range (4.5 ms)

exceeds the requirement ( $>6000$ ) by a factor of four, providing a comfortable margin. Figure 37 shows the calculated variation of dynamic range using equation (2) with model parameters set for the  $H^+$  peak width and observed background noise. This shows that for a 2-s integration the dynamic range will be  $\sim 125,000$ . The difference between this and the results in Table 16 is to be expected as the  $H^+$  peak used in this work is greater than the detection limit. However, Fig. 37 enables us to predict the shortest integration period necessary to achieve the required 6000 dynamic range, which is 4.5 ms and far shorter than any of the planned ROI integration periods during flyby (Sect. 8.5.1).

### 6.3.2 Sensitivity and Gain

The calibration of gain and sensitivity depends on ionization of gases flowing from the GIS followed by their delivery to the MCP detector or the FC. This process can be affected by several factors shown in Fig. 38.

As the figure suggests, the ion source performance depends on several factors that must be carefully controlled and measured. Losses along the flight path result from ion scattering out of the beam, aberrations caused by fringing electric fields in the MBTOF, or by surface charging (which is mitigated by gold-plating optical surfaces). These losses are relatively constant and can be “calibrated out.” During internal MBTOF calibration the beam is deflected to the FC where its current is measured and then corrected for noise that arises in the very small signal. After the FC measurements, the beam is deflected back to the primary ion flight path, reaching the detector where the signal is amplified, digitized, and recorded.

Ion source sensitivity is defined by the rate of ion production at the source for a given pressure, which is proportional to the density of, and spacecraft velocity through, the Europa environment. The mass peak size in a spectrum is a function of the number of ions that reach the detector, so it follows that the total number of ions created at the source is the basis for compound quantitation.

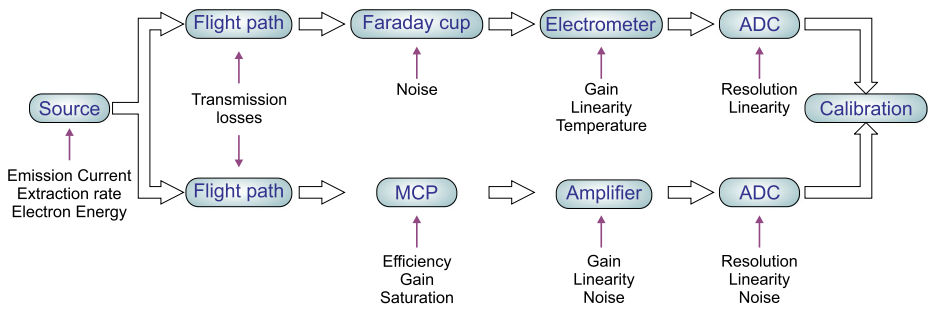


**Fig. 38** Factors affecting gain and sensitivity measurements

A second critical component of calibration is establishing the gain and efficiency of the detector and its signal chain in comparison to the FC signal chain, as the MCP gain will change over the lifetime of the instrument. The FC establishes the source sensitivity, which is then used to measure the MCP gain and its efficiency in converting ions into measurable pulses at the amplifier.

“Tuning” of the MBTOF optics is an important concept that is the basis for controlling the MS performance. The tuning process sets voltages that control the ion source and ion ejection process, together with the timing of voltage switching that determines mass spectral regions-of-interest (ROIs). Tuning can be done manually, or automatically using an auto-tune algorithm. The objective in both cases is to maximize peak height while minimizing peak width and asymmetry. In-flight operation will make use of auto-tuning tables determined by flight calibrations. Once voltages are tuned, the FC-43 spectrum will be used to adjust the timings for correct ROI mass ranges, and to determine a preliminary mass scale.

The sensitivity of the MS can be adjusted by changing the ion source emission current that determines the rate of ion production and the numbers of ions stored in the source (Sect. 5.4.2). Ion storage in the source is optimized through tuning and extraction-rate timing. The latter sets the length of the storage period (i.e., the duty cycle).

Sensitivity is measured by deflecting the ion beam leaving the source into the FC (Fig. 20). On arrival at the FC the beam must enter the cup completely. Ion trajectories that fall outside the entrance aperture will be lost from the measurement. The ion beam is routinely scanned across the FC, giving a flat-topped peak indicating that the entirety of the beam in the scan direction falls within the cup. This does not measure the extent of the beam perpendicular to the scan direction, but the deflectors and FC are carefully designed to prevent such losses (Fig. 20). Once the ion beam enters the FC, the impact of the ions with the surface of the cup results in the production of secondary ions that can create signal losses if they leave the cup. The strong positive electric field of the drift tube reduces the ion collision energy with the Faraday cup wall and minimizes any secondary emission. The acute angle of ions striking the wall also prevents losses before ions strike the bottom of cup and are recorded.

Ions striking the internal FC surfaces are neutralized, resulting in a very small net current flow. The current is then converted to a signal between 0 and  $-10$  V by an electrometer amplifier, chosen for its linearity and low noise. Its gain is determined by a  $20$  G $\Omega$  resistor with a  $\pm 100$  ppm/ $^{\circ}$ C temperature coefficient that must be calibrated since flight-operating temperatures differ from room temperature. The electrometer signal is sent to four differential amplifiers giving four gain channels (Hi, Mid-Hi, Mid-Lo, and Lo) that are read by a multiplexed 12-bit ADC located on the MF-A board. The differential amplifier outputs are

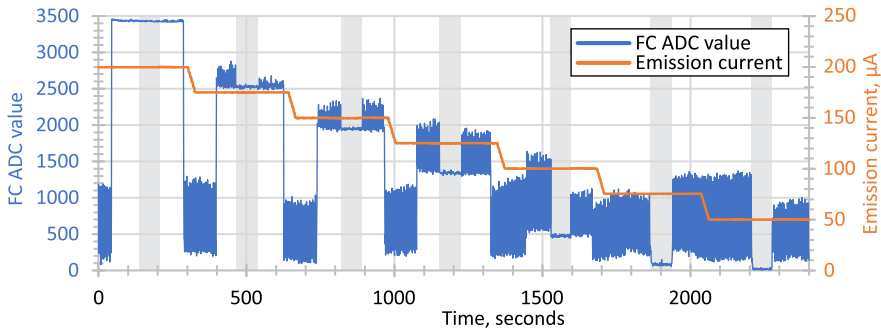


**Fig. 39** Source sensitivity data. The chart shows the FC Hi channel signal (blue) and the source emission current (orange). The sensitivity was calculated from data acquired during the grey-shaded intervals, which indicate the periods when the COSMIC cryopumps were turned off to remove the microphonic noise source

clamped at the upper end of the signal range to ensure the ADCs are not overloaded. The clamps reduce the signals to the ADCs once their threshold has been met, resulting in non-linearity at the high end of the gain curve. The 12-bit dynamic range of the ADC is defined by the onset of clamping at the high end, and by background signal levels at the low end.

The FC electrometer’s gain and linearity, and the differential amplifier’s ADC gain and linearity, were calibrated, as was the voltage needed for FC beam deflection. All other error sources were minimized through system design; however, a few FC-related parameters will be measured on the identical EM unit during the cruise to Jupiter.

To measure source sensitivity, the source filament emission current was varied, and the resulting ion flux was measured by the FC. The measurements were made using the residual gas in the chamber. Early in calibration, it was discovered that the FC had significant microphonic noise excited by COSMIC’s cryopumps. To overcome this problem, at each five-minute-long emission current step, a roughly one-minute segment of data was collected with the cryopumps turned off (Fig. 39). These ‘quiet’ periods, together with the Anelva gauge pressures and thermocouple temperatures, were used to calculate the source sensitivity as a function of source emission current. The effect of the microphonic noise on mission operations has been considered. The FC will be used only during calibration prior to each flyby and after the cryosample analysis at apojoive, when spacecraft activities will not excite the FC. This will be confirmed by testing during cruise.

The chamber residual gas is comprised predominantly of water (18 u), nitrogen/carbon monoxide (28 u) and carbon dioxide (44 u). As each of these species produces a different signal on the ion gauge, the recorded pressure must be corrected by a gauge factor ( $G_w$ ), weighted for the gas composition.

The proportion of each species ( $f_i$ , where  $i = [H_2O, N_2, CO_2]$ ) is estimated by scaling measured peak heights ( $p_i$ ) with gauge factors ( $G_i$ ) provided by the gauge manufacturer before using the estimated  $f_i$  to calculate the weighted gauge factor ( $G_w$ ) (Table 17). The product of  $G_w$  and the recorded pressure gives the actual pressure.

$$f_i = \frac{p_i / G_i}{\sum_{i=1}^n p_i / G_i} \tag{6}$$

$$G_w = \frac{\sum_{i=1}^n f_i}{\sum_{i=1}^n f_i G_i} \tag{7}$$



**Table 17** Calculation of the Weighted Gauge Correction Showing Factors and Results

Compound ( <i>i</i> )	Mass used (u)	Peak height ( $p_i$ )	Gauge ( $G_i$ )	Proportion ( $f_i$ )	$G_w$
Water, H <sub>2</sub> O	18	624.8	1	52.0%	
Nitrogen, N <sub>2</sub>	28	464.1	1	26.6%	
Carbon dioxide, CO <sub>2</sub>	44	420.8	1.42	21.4%	
Weighted Gauge Correction Factor					0.92

The beam of electrons in the source ionizes molecules according to,  $M + e^- \rightarrow M^+ + 2e^-$ . Source sensitivity ( $s$ ) is the ratio of the rate of ion creation ( $\dot{M}^+$ , ions/s) and the gas density ( $\rho$ , molecules/cm<sup>3</sup>). This value, in ions/s per molecule/cm<sup>3</sup>, was determined from the measured ion current and pressure using the equations below:

$$s = \frac{\dot{M}^+}{\rho} \quad (8)$$

The ion beam current ( $I$ , A) is measured by the Faraday cup, digitized, and then calculated from the number of counts reported by the ADC ( $n$ , count), and the conversion factors ( $F_s$ , nA/count;  $F_i$ , nA) from Table 18.

$$I = n \cdot F_s + F_i \quad (9)$$

Which is converted to the rate of ion creation ( $\dot{M}^+$ , ions/s) by dividing by the charge on an electron ( $e$ , C).

$$\dot{M}^+ = \frac{I}{e} \quad (10)$$

The gas density ( $\rho$ , molecules/cm<sup>3</sup>) is calculated from the observed pressure during the measurement ( $P$ , hPa).

$$\rho = \frac{PNa}{1000RT} \quad (11)$$

Where:  $Na$  is Avogadro's number in mol<sup>-1</sup>,  $R$  is the gas constant in  $\ell \cdot \text{hPa} \cdot \text{K}^{-1} \cdot \text{mol}^{-1}$ , 83.14472, and  $T$  is the gas temperature in K.

Combining the terms, we get:

$$s = \frac{n \cdot F_s + F_i}{e} / \left( \frac{P \cdot Na}{1000 \cdot R \cdot T} \right) \quad (12)$$

Simplifying, we get:

$$s = \frac{(n \cdot F_s + F_i) \cdot 8.62 \times 10^{-10}}{P} \quad (13)$$

The source sensitivities were calculated for each filament current based on the signal from each of the four channels reading the ion current from the FC and are plotted in Fig. 40.

Immediately following the acquisition of sensitivity data, the source tuning directing the ion beam to the detector was loaded and the cycle of emission current variations repeated to measure the detector gain (Fig. 41). Measurements were performed on the residual chamber

**Table 18** Conversion factors for the Faraday cup

Channel	Low	Mid-Low	Mid-Hi	High
Slope $F_s$ (A/count)	$1.503 \times 10^{-13}$	$2.003 \times 10^{-14}$	$6.031 \times 10^{-15}$	$1.213 \times 10^{-15}$
Intercept $F_i$ (A)	$7.720 \times 10^{-13}$	$2.546 \times 10^{-13}$	$1.835 \times 10^{-13}$	$1.417 \times 10^{-13}$

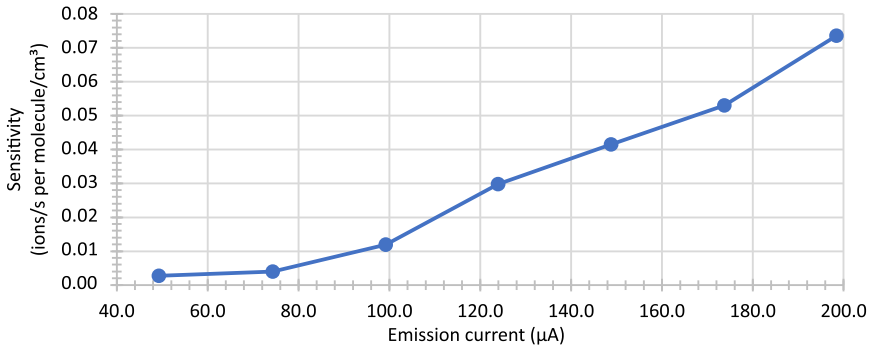


**Fig. 40** Source sensitivity of the FM instrument as a function of source emission current based on the FC gain channel signals in the segments shown in Fig. 39

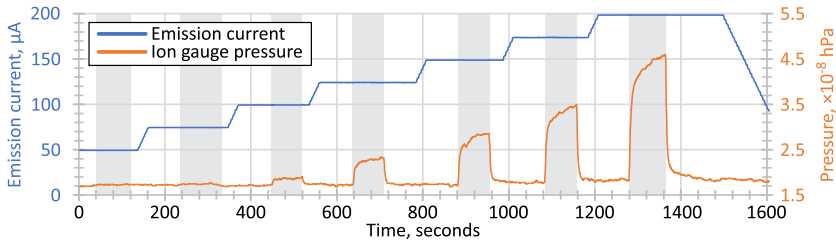


**Fig. 41** Source emission current and pressure during acquisition of the residual gas MCP detector gain measurement data, taken immediately following the data in Fig. 39. The grey blocks indicate the periods when the ion beam was applied to the MCP detector

gas and at two higher pressures achieved through the addition of nitrogen gas from COSMIC.

The gain of the detector ( $g$ ) is the rate of electrons produced by the detector ( $\dot{Q}_d$ , electrons/s) over the rate of incident ions ( $M_i^+$ , ions/s):

$$g = \frac{\dot{Q}_d}{M_i^+} \tag{14}$$

We know the rate of incident ions from the Faraday cup measurements, so from Eq. (8) we get:

$$g = \frac{\dot{Q}_d}{s \cdot \rho} \tag{15}$$

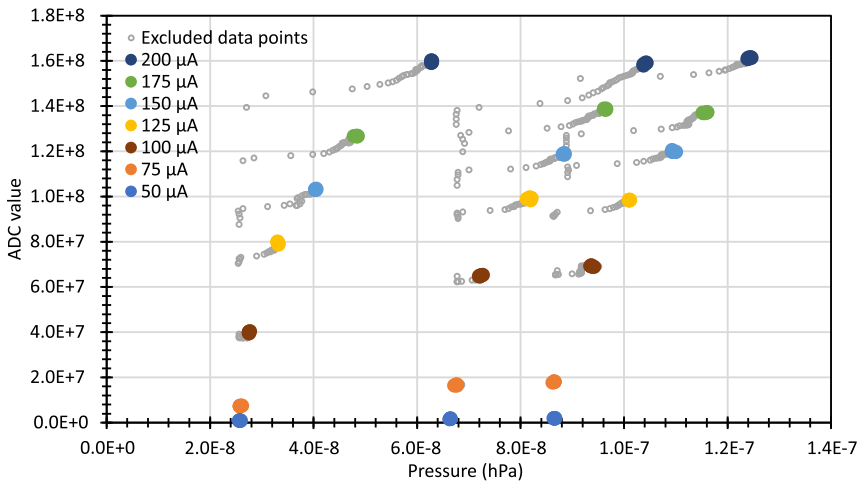


**Fig. 42** The MCP ADC signal versus the ion gauge pressure. Data for all three overall instrument pressures are shown for each of the emission currents. The last five data points (where the pressure is most stable) of each individual measurement are shown in color. The data points for the remainder of each measurement are shown as small grey circles and demonstrate the time evolution of the signal

The data indicate that the application of the ion beam to the MCP releases gas into the chamber. To investigate the relationship, the number of counts produced by the MCP was plotted against the ion gauge pressure (Fig. 42). This shows that the change in pressure is related to the MCP counts, though the relationship is not a simple one. The plot also shows that the three different pressures of the experiments resulted in smaller changes in MCP counts than any single step in the emission current. At the lowest emission currents the points all appear to overlay because the amount of gas released was negligible compared to the background pressure (see Fig. 41). By 100  $\mu\text{A}$  emission current the data points are beginning to show spread in the reported counts, especially for the higher-pressure experiments, and the peak due to evolved gas is becoming apparent in Fig. 41.

The MCP gain was calculated according to equation (15) using the pressure measured at the time the data were recorded to compensate for the pressure peaks. The gain produced by the detector was plotted against the emission current and is shown in Fig. 43. If the MCP was behaving ideally then the data should be a horizontal line indicating the gain of the detector. What we observe instead is a rise to higher gains with increasing emission up to 100  $\mu\text{A}$ ; beyond this point the gain falls again and does not plateau within the data collected.

When the ion beam is applied to the detector a rise in the pressure recorded by the ion gauge is seen. When the ion beam is removed, the pressure falls once again to the initial value. The size of the pressure increase is proportional to the ion beam intensity, even after the addition of nitrogen gas to increase the intensity further (and changing the composition of the gas mixture). The spectrum of the residual gas has three significant peaks, 18  $m/z$  the largest, followed in size order by 28  $m/z$  and 44  $m/z$ . This is interpreted as the majority species present being water, which is converted to carbon monoxide and carbon dioxide on the hot filaments of the source and the ion gauge.

We conclude from these observations that the change in gain can be explained by the presence of adsorbed water on the MCP, sourced from the outgassing of the PEEK (polyether ether ketone) body of the detector. The water is adsorbed onto the large surface area of the MCP where it changes the electron production from the MCP resulting in a varying gain.

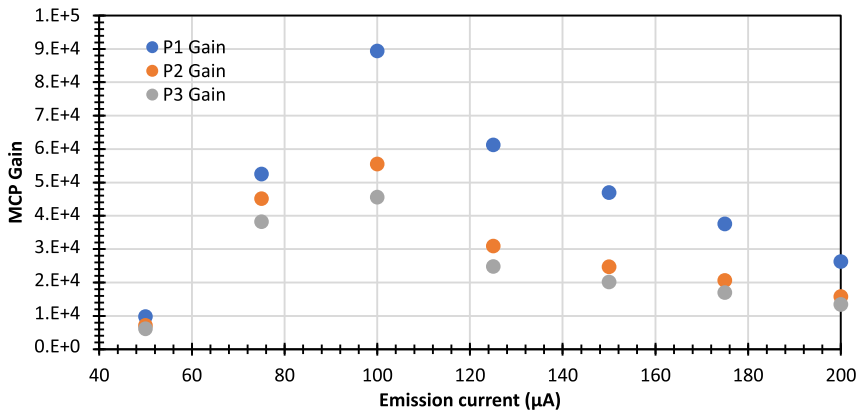


**Fig. 43** Gain calibration showing detector gain as a function of emission current for the measurements at three pressures (P1, P2, & P3 – ascending order)

The impingement of the ion beam and the subsequent electron cascade cause stimulated desorption of the water from the surface of the MCP, giving rise to the pressure peaks, and reducing the amount of water available to change the gain. The data indicate that as the surface coverage is decreased the gain increases for a period (up to 100  $\mu\text{A}$  emission), and that beyond this point the gain is on a decreasing trend that appears to be moving towards a constant value of roughly 10,000. Because of the high residual gas pressure, the voltages on the MCP were set conservatively to avoid possible damage. Based on the gains measured during detector burn-in, the low value of 10,000 is not unexpected. The use of higher voltages will produce higher gains. Despite the issues of adsorbed water on the MCP, the data presented here serve to demonstrate the utility of the in-flight calibration procedure (Sect. 6.5) in determining the source sensitivity and MCP gain. Outgassing of the PEEK detector body will diminish during the cruise to Jupiter so that future gain measurements will reflect the true detector gain un-enhanced by the adsorbed water.

### 6.3.3 Projected Performance

Using the performance characteristics of the instrument combined with the predicted density profiles across a flyby (Fig. 8) performance envelopes were calculated for two putative environments – a purely sputter-generated atmosphere (Fig. 44 and Table 19) and an Enceladus-like plume (Fig. 45 and Table 20) (Teolis et al. 2017c). The envelopes for performance through the flyby, for the cryotrap measurement, and for an enhanced (high gain) cryotrap measurement where the detector gain is set so high that the major components would saturate the detector are shown in Fig. 44. This “high gain” mode enables the rarest species to be detected in the shortest integration time.

The performance envelopes on the charts (Fig. 44, Fig. 45) are indicated by a colored boundary line. The upper boundary is the largest signal that the ADC can measure, the lower boundary is the limit of detection and may be limited by ADC noise or ion statistical noise depending on the conditions. The left limit is a single source extraction while the right limit is somewhat arbitrary but encompasses the duration of the flyby and the maximum cryosample analysis time. The colored outlines bound the limits of instrument performance for three separate operating cases. In the flyby case (orange) the performance for ambient gases is displayed, the detection limit is due to the ADC noise, and the right limit shape

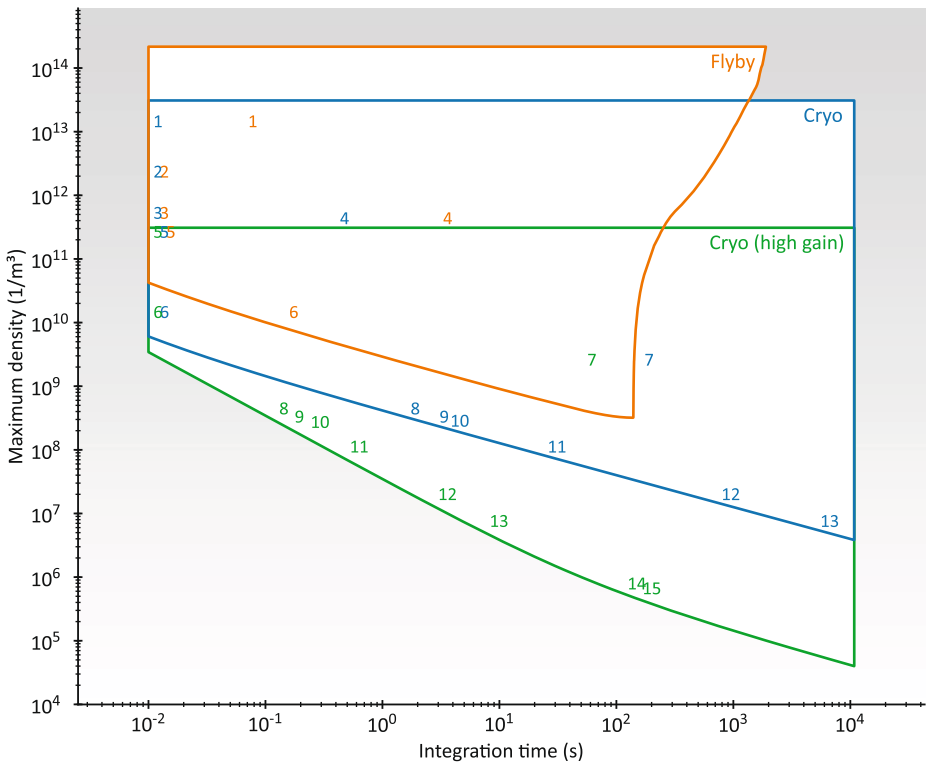


**Fig. 44** The predicted performance envelopes for MASPEX at Europa in a purely sputtered atmosphere. The x-axis denotes the integration time necessary for the measurement of numbered compounds as listed in Table 19. The y-axis is the maximum density across the flyby (at closest approach). See Sect. 6.3.3 for a full description of the performance envelopes

**Table 19** Average composition of the sputtered atmosphere from the model of Teolis et al. (2017c). The numbering and mixing ratio of the compounds corresponds to the values shown in Fig. 44

#	Formula	Mixing ratio	#	Formula	Mixing ratio
1	H <sub>2</sub> O	8.00E-01	9	C <sub>2</sub> H <sub>6</sub>	1.80E-05
2	O <sub>2</sub>	1.30E-01	10	C <sub>2</sub> H <sub>2</sub>	1.80E-05
3	SO <sub>2</sub>	2.90E-02	11	CH <sub>4</sub> O	6.20E-06
4	CO <sub>2</sub>	1.90E-02	12	HCN	1.10E-06
5	H	1.60E-02	13	Kr	4.20E-07
6	<sup>40</sup> Ar	8.00E-04	14	Xe	4.30E-08
7	CH <sub>4</sub>	1.40E-04	15	C <sub>6</sub> H <sub>6</sub>	3.80E-08
8	CH <sub>2</sub> O	2.40E-05			

is caused by the density profiles of different species, which rise above the detection limit for different durations about the closest approach. The cryo case is for the analysis of the cryosample. The maximum density is lower in this case since we can adjust the sample pressure to the optimum value, while with the flyby sample we must leave some headroom

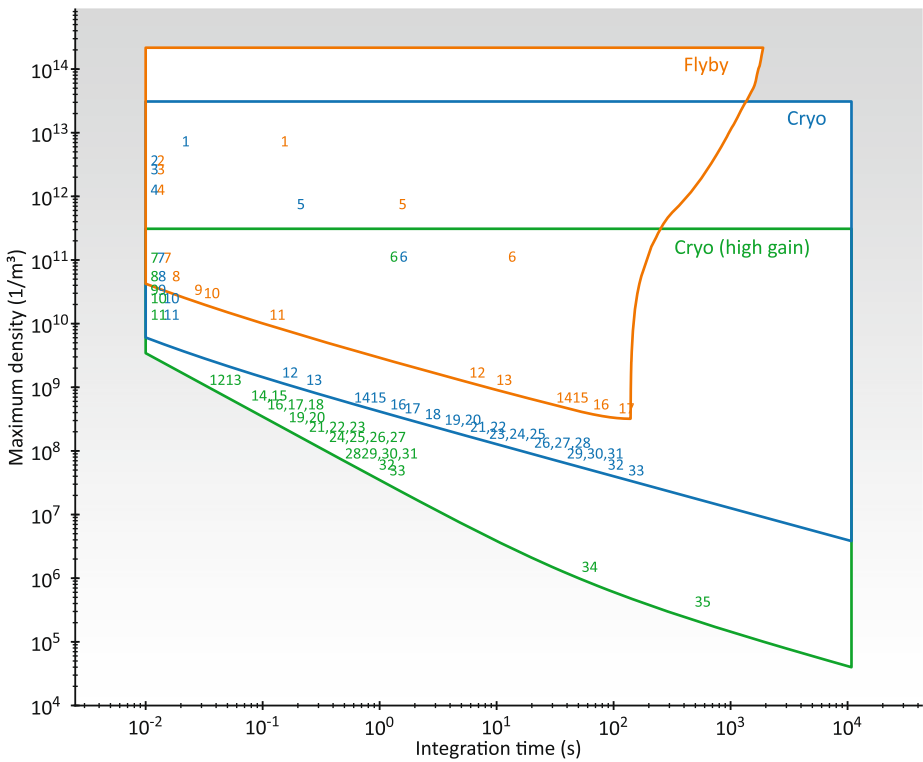


**Fig. 45** The predicted performance envelopes for MASPEX at Europa with an Enceladus like plume. The x-axis denotes the integration time necessary for the measurement of numbered compounds as listed in Table 20. The y-axis is the maximum density across the flyby (at closest approach). See Sect. 6.3.3 for a full description of the performance envelopes

**Table 20** Average composition of the modeled Europa atmosphere with an Enceladus-like plume from the model of Teolis et al. (2017c). The numbering and mixing ratio of the compounds corresponds to the values shown in Fig. 45

#	Formula	Mixing ratio	#	Formula	Mixing ratio	#	Formula	Mixing ratio
1	H <sub>2</sub> O	4.00E-01	13	C <sub>2</sub> H <sub>4</sub> O	7.10E-05	25	H <sub>2</sub> S	8.50E-06
2	CO <sub>2</sub>	2.00E-01	14	C <sub>3</sub> H <sub>8</sub>	4.00E-05	26	C <sub>4</sub> H <sub>10</sub> O	8.40E-06
3	N <sub>2</sub>	1.60E-01	15	C <sub>2</sub> H <sub>2</sub> O	3.90E-05	27	C <sub>8</sub> H <sub>18</sub>	7.70E-06
4	H <sub>2</sub>	6.90E-02	16	C <sub>3</sub> H <sub>6</sub>	2.90E-05	28	C <sub>3</sub> H <sub>6</sub> O	6.40E-06
5	CH <sub>4</sub>	4.10E-02	17	C <sub>3</sub> H <sub>4</sub>	2.50E-05	29	C <sub>4</sub> H <sub>10</sub>	5.00E-06
6	CO <sub>2</sub>	6.10E-03	18	C <sub>2</sub> H <sub>7</sub> N	2.10E-05	30	C <sub>5</sub> H <sub>12</sub>	4.90E-06
7	NH <sub>3</sub>	5.90E-03	19	C <sub>2</sub> H <sub>6</sub> N <sub>2</sub>	1.70E-05	31	Kr	4.80E-06
8	C <sub>2</sub> H <sub>2</sub>	3.00E-03	20	C <sub>2</sub> H <sub>4</sub> O <sub>2</sub>	1.50E-05	32	O	3.30E-06
9	C <sub>2</sub> H <sub>4</sub>	1.90E-03	21	CH <sub>4</sub> O	1.30E-05	33	C <sub>4</sub> H <sub>8</sub>	2.70E-06
10	C <sub>2</sub> H <sub>6</sub>	1.60E-03	22	C <sub>3</sub> H <sub>8</sub> O	1.20E-05	34	Xe	8.20E-08
11	CHN	7.50E-04	23	C <sub>2</sub> H <sub>3</sub> N	1.00E-05	35	Ar	2.30E-08
12	CH <sub>2</sub> O	9.30E-05	24	CH <sub>5</sub> N	9.40E-06			

to allow for density variations. The detection limit is still driven by ADC noise. For the cryo (high gain) case the detection limit is driven by ion statistical noise at integration times up to  $\sim 100$  seconds where the ADC noise dominates. The color-coded numbers correspond to the integration time necessary to reach the measurement precision required by the science objective or 25%, whichever is more constraining.

## 6.4 Compound Identification

Identification of compounds by mass spectrometry relies on three pieces of information: the exact molecular mass, mass resolution and peak shape, and fragmentation patterns of the unknown compound. Identifying the molecular ion mass provides elemental composition. Determination of elemental composition in this way is known as “accurate mass determination.” Accurate mass in turn depends on the ability of the MS to resolve neighboring mass peaks and on the conversion of measured TOF to  $m/z$ . Accurate mass determination is needed, particularly to identify organic compounds that are singly substituted by oxygen and nitrogen (Fig. 49).

Mass fragmentation patterns resulting from electron impact dissociative fragmentation are used to supplement accurate mass determination. The MS uses 70 eV electrons to create fragmentation patterns that form a ‘fingerprint’ characteristic of the parent molecule (70 eV is a widely used value for which a number of libraries of spectra are available). Each ion source has a slightly different fingerprint that must be measured in the laboratory for maximum instrument performance. Comparison of fragment ions with a library of known products provides additional information that is used to identify compounds.

At the high mass resolutions achievable with MASPEX, and the mass accuracy needed to identify near-isobaric ions, we account for the electrons missing from ions by calculating the exact mass of known reference ions,

$$\frac{m}{z} = \frac{m_{mol}}{z} - z \times m_e \quad (16)$$

where  $m_{mol}$  is the exact molecular mass (sum of atomic mass of all atoms in molecule or fragment ion),  $m_e$  is the mass of a single electron, and  $z$  is the number of electrons stripped off the ion leading to the ion charge state (e.g.,  $z = 1$  corresponds to a singly charged ion with one electron missing,  $z = 2$  is a doubly-charged ion).

### 6.4.1 Accurate Mass Measurements

The MS measures detector signals as a function of elapsed time starting when ions are extracted from the ion source to the time when they are detected. The time-of-flight of an ion peak is proportional to the elapsed time multiplied by the square root of its mass. By accurately measuring the time-of-flight, the mass of ions can be calculated, and thus the elemental composition of the parent ion or its fragments can be determined. Assuming a Gaussian peak, the mass uncertainty ( $\Delta m/m$ ) varies with resolution  $R$ , and the number of ions in the mass peak  $C$ , and its theoretical limit is given by

$$\frac{\Delta m}{m} = \frac{1}{2.355 R_{FWHM} \sqrt{C}} \quad (17)$$

The accuracy of mass measurements by the FM was determined during Cal 3 through the measurement of the residual gas spectrum. Three TOF peaks were used for the analysis: water, carbon monoxide, and carbon dioxide. The ions of interest (“target ions” in a particular ROI) are tracked between successive TOF spectra by setting the MBTOF reflectron



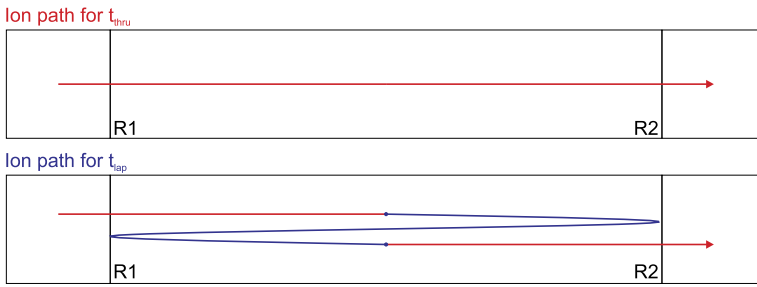


**Fig. 46** Schematic representation of the trajectories and associated time parameters used for calculating ion TOF. The top panel shows the ion path for straight-through trajectories, whose elapsed time is  $t_{thru}$ . The bottom panel shows the ion path for one lap with ion trajectories reflecting off reflectrons R1 and R2 and the representative timing components of  $t_{thru}$  (in red) and  $t_{lap}$  (in blue). The bottom panel trajectory is shown offset from the central ray axis for clarity. The two blue dots indicate the beginning and end of the lap portion of the trajectory with elapsed time  $t_{lap}$

opening times to the number of laps. Figure 46 shows a schematic of the ion trajectories and their relation to timing of the signal peaks (Fig. 24 shows the timing of voltages that control reflectron gating).

“Tuning” operations are carried out during flight to account for small changes in the applied voltages to maintain consistency with calibration data. Changing voltages, especially those in multi-lap mode, generally change the ion location in TOF spectra, sometimes by microseconds or more before peak shapes are affected. Because of this, ROI timing also needs to be adjusted in flight during tuning to capture the desired mass range with the desired number of laps. Additionally, although tuning can be adjusted using the FC-43 calibrant, applying results to ROI mass selection (or to a different number of laps) requires adjusting the timing for non-calibrant masses.

To test the consistency between manual tunes during calibration, and to get data needed for the auto-tuning algorithm, two tunings were tested, one for 10 laps and one for 50 laps. In each case, the tune aimed to maximize peak height while minimizing peak width and asymmetry. For each tuning in turn, starting with a single lap, single extraction spectra were collected at an extraction rate of 100 Hz and then 256 individual spectra were summed together. The opening time for Reflectron 2 was increased steadily so that spectra were taken of each peak on every lap. Data were taken for  $n$  and  $n + 1$  laps to identify any peaks in the spectrum remaining from a different lap. The tuning voltages for the 10-lap-tune and 50-lap-tune were held constant throughout calibration.

For accurate mass analysis the detector signal of each spectrum was smoothed using a Savitsky-Golay filter (The Savitsky-Golay filter is a signal smoothing technique widely used in analytical chemistry (Savitzky and Golay 1964).), with degree of 3 and width equivalent to 5 ADC time steps ( $t_{step} = 6.2 \times 10^{-4} \mu s$ ). The exact TOF of a target peak was calculated as the centroid of each peak shape using the relation,

$$t(m', n) = \left( \sum_{t_i \in [t_l, t_r]} t_i \times y_i \right) / \sum_{t_i \in [t_l, t_r]} y_i \tag{18}$$

where  $m'$  is the known target ion mass ( $m/z$ ),  $n$  is the known number of laps the target ions have completed,  $t_i$  and  $y_i$  are the TOF ( $\mu s$ ) and signal amplitude (in arbitrary units), respectively, at sample index  $i$ . The immediately preceding  $t$  values set the continuous region

bracketed by  $[t_l, t_r]$  that forms left and right bounds of the local maximum such that each  $y_i > 0.25 \times \max(y_i)$ .

For thousands of spectra, this analysis proved to be the most reliable method to determine the accurate mass from TOF data. Results were visually inspected to ensure that the signal peaks were assigned to the correct target ion, and that the signal peaks were well-behaved and not altered by instrument artifacts or overlapping signals from other ions (such as those having completed a different number of laps). Only ion peaks that met these criteria were used in the analysis.

For each set of fixed tuning voltages, the collected  $t(m', n)$  values were assumed to fit the following model relationship between  $m/z$  and TOF,

$$t(m', n) = t_0 + (\tilde{t}_{thru} + n \times \tilde{t}_{lap}) \times \sqrt{m'} \tag{19}$$

where  $\tilde{t}_{thru}$  and  $\tilde{t}_{lap}$  (Fig. 46) represent time constants proportional to the square root of an ion's mass to charge,  $m'$ , and  $t_0$  represents a mass-independent time constant. The quantity  $\tilde{t}_{thru} \times \sqrt{m'}$  is the time needed to traverse the distance between the ion source and the detector for an ion of mass  $m/z$  when neither reflectron is engaged (Fig. 46, top panel). The quantity  $\tilde{t}_{lap} \times \sqrt{m'}$  represents the additional time needed for an ion of mass  $m/z$  to traverse a single lap within the drift tube when both reflectrons are engaged (Fig. 46, bottom panel). Multiplying this quantity by  $n$  gives the time for the ion to traverse  $n$  full laps. While the path represented by  $\tilde{t}_{thru}$  is discontinuous in the case of one or more laps, the full path is still executed. This is schematically represented in Fig. 46 by the blue dots, which indicate where in the flight path the  $\tilde{t}_{lap}$  segment begins and ends. The mass-independent parameter  $t_0$  accounts for the injection time caused by ramping ion source voltages. The model parameters are dependent upon the specific tuning voltages of the 10-lap-tune and 50-lap-tunes chosen for this analysis.

Uncertainties for the model parameters  $t_0$ ,  $\tilde{t}_{thru}$ , and  $\tilde{t}_{lap}$  lead to the overall uncertainty in  $t(m', n)$  by the following relation,

$$\sigma_{t(m',n)} = \sqrt{\sigma_{t_0}^2 + \left(\sigma_{\tilde{t}_{thru}}^2 + n^2 \times \sigma_{\tilde{t}_{lap}}^2\right) \times m'} \tag{20}$$

where the contribution of  $\sigma_{t_0}$  provides a constant source of uncertainty, the contribution of  $\sigma_{\tilde{t}_{thru}}$  is mass dependent, and the contribution of  $\sigma_{\tilde{t}_{lap}}$  depends on both mass and lap number.

Fitting directly to the above model provided poor results because this approach was dependent upon initial estimates of the parameters and was not robust to outliers. The following methodology was used instead. To estimate the parameters of the model relation above, we first determine mass-dependent parameters by fitting the  $t(m', n)$  values for each target ion to the following linear equation,

$$t(m', n) = t_{thru}(m') + n \times t_{lap}(m') \tag{21}$$

from which a set of  $t_{thru}(m')$  and  $t_{lap}(m')$  may be estimated along with their uncertainties  $\sigma_{t_{thru}(m')}$  and  $\sigma_{t_{lap}(m')}$ . Fits were performed iteratively, removing the largest outlier,  $abs(t(m', n) - t_{fit}(m', n)) > 5 \times t_{step}$ , until no outliers remained outside this threshold. Then the set of  $t_{thru}(m')$  values were fit to the equation:

$$t_{thru}(m') = t_0 + \tilde{t}_{thru} \times \sqrt{m'} \tag{22}$$

from which  $t_0$  and  $\tilde{t}_{thru}$  can be estimated together with their uncertainties. The final model parameters and uncertainty estimates were obtained from the equations:

$$\tilde{t}_{lap} = mean \left( \frac{t_{lap}(m')}{\sqrt{m'}} \right) \tag{23}$$

$$\sigma_{\tilde{t}_{lap}} = stdev \left( \frac{t_{lap}(m')}{\sqrt{m'}} \right) \tag{24}$$

While this may not be the exact methodology by which TOF spectra will be calibrated to a mass scale in flight, it provides a robust and accurate way to estimate the model parameters relating ion mass to TOF for data analysis during calibration.

Mass accuracy is the difference between the known ion mass and the mass calculated from its measured TOF ( $m_{t(m',n)}$ ) in parts per million (ppm). The measured ion mass and its measurement accuracy is given by,

$$m_{t(m',n)} = ((t(m',n) - t_0) / (\tilde{t}_{thru} + n \times \tilde{t}_{lap}))^2 \tag{25}$$

$$m/z \text{ diff. (ppm)} = 10^6 \times (m_{t(m',n)} - m) / m \tag{26}$$

where  $m/z$  diff. (ppm) is a relative difference (diff.) between the known mass  $m$  and measured mass  $m_{t(m',n)}$  based on its TOF.

Analysis of  $t(m',n)$  calibration data demonstrates that the fixed tuning voltages for both the 10-lap tune and 50-lap tune perform best within a limited TOF range. This relationship is shown in the left-side panels of Fig. 47, where it is apparent that all target ions ( $H_2O^+$ ,  $CO^+$ , and  $CO_2^+$ ) achieve a consistent lap-to-lap mass accuracy at nearly identical TOF values and exhibit an inconsistent lap-to-lap mass accuracy for TOF times prior to this inflection point. This suggests that the ions are focused as a function of time rather than at a set number of laps, and that the assumed mass vs. TOF model relationship (with constant parameter estimates) is only applicable for a given TOF time range. This highlights the need for appropriate use of any single set of tuning operation scenarios (e.g., the 50-lap-tune would be suitable for a targeted isotopic analysis with ion TOFs around 600  $\mu s$ , whereas the 10-lap-tune would be more suitable for construction of a survey spectrum with TOFs in the range of 100 to 140  $\mu s$ , see Sect. 8.3.2).

Because one goal of calibration is to establish accurate absolute mass determination, we estimated model parameters (Table 21) using the analysis methodology described above with only  $t(m',n)$  data beyond the time-focus inflection points determined for each of the 10-lap-tune and 50-lap-tune data (99  $\mu s$  and 236  $\mu s$ , respectively). Likewise, we consider the mass accuracy of only the same  $t(m',n)$  data points to be representative of the MASPEX performance for these sets of tuning voltages. The relevant (consistent) TOF ranges are shown as gray areas on the left-side panels of Fig. 47 while the resulting distributions of mass accuracy are shown in the right panels. The ion mass accuracies were within  $\pm 20$  ppm for all ions in both the 10-lap-tune and 50-lap-tune data, with most data accurate to within  $\pm 10$  ppm. The 50-lap-tune data show that nearly all data points are concentrated within  $\pm 10$  ppm accuracy. This is due in part to a significantly larger data set, as well as the TOF-to-mass accuracy relationship described below. These results demonstrate the capability of MASPEX to determine the accurate mass of ions found in TOF spectra. The final model parameters and uncertainty estimates are used in calculation of the measured mass accuracies shown in Table 21.

**Fig. 47** Relationship between TOF (in  $\mu\text{s}$ ) and the calculated mass (in  $m/z$  diff. (ppm)) for the three chosen target ions. The three upper panels represent the 10-lap-tune spectra. The three lower panels represent the 50-lap-tune spectra. Blue numbers and vertical dashed lines indicate lap numbers for each ion at the corresponding TOF, while light gray areas indicate the TOF region for which the adjusted ion peak time-focus was consistent. Right-side panels show histograms of the  $m/z$  diff. (ppm) distribution for the ions from these TOF ‘gray’ regions

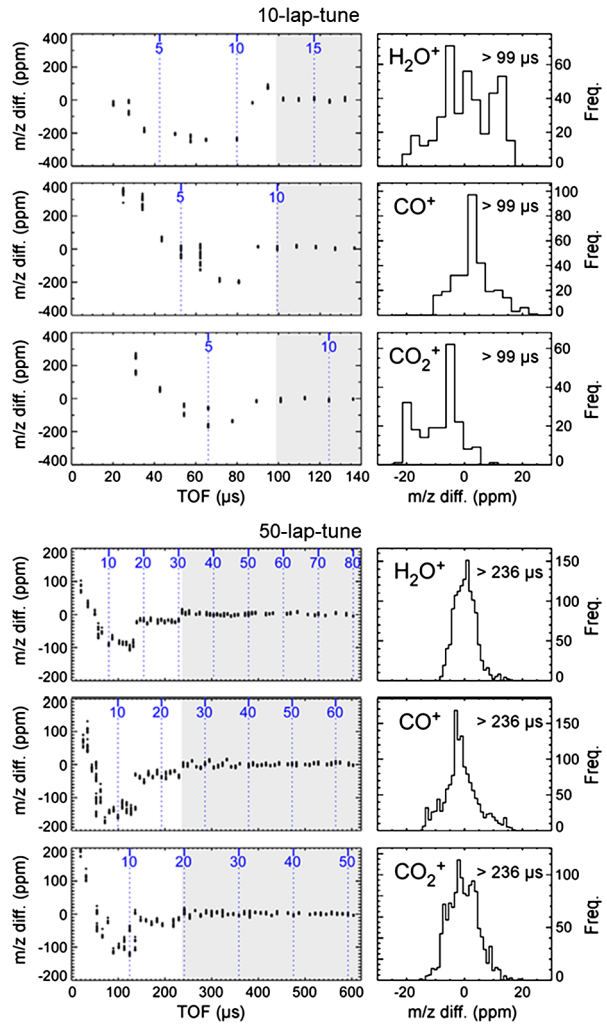


**Table 21** Final model parameters and uncertainty estimates calculated for the 10-lap-tune and 50-lap-tune data. The parameter  $t_0$  has the greatest uncertainty, as  $\sigma_{t_0}$  is equal to approximately  $60 \times t_{step}$ . Table values are only applicable for spectra obtained during this calibration activity with their specific sets of tuning voltages

Model parameter	10-lap-tune ( $\mu\text{s}$ )	50-lap-tune ( $\mu\text{s}$ )
$t_0$	0.33195	0.33172
$\tilde{t}_{thru}$	1.11017	1.10903
$\tilde{t}_{lap}$	1.75982	1.76165
$\sigma_{t_0}$	0.003763	0.003734
$\sigma_{\tilde{t}_{thru}}$	0.0006871	0.0006818
$\sigma_{\tilde{t}_{lap}}$	0.00000974	0.000003336
$\tilde{t}_{thru}/\tilde{t}_{lap}$	0.63084	0.62954

**Fig. 48** The modeled relationship between calculated mass accuracy and TOF after ions complete 1 to 100 laps using the model parameters of the 50-lap-tune data, assuming a constant error in the ion's TOF position of  $t_{step}$  (1 ADC sample). Table 22 shows experimental data used to estimate uncertainties

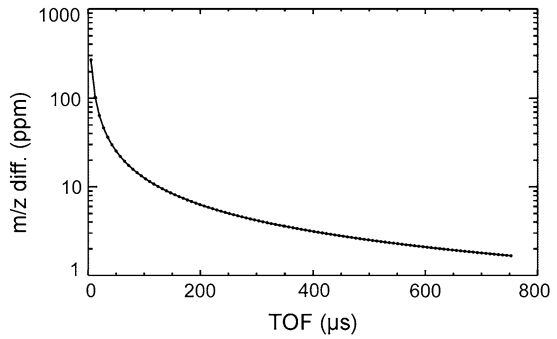


**Table 22** Mass-dependent parameter and uncertainty estimates calculated for the 10-lap-tune and 50-lap-tune data presented in this section

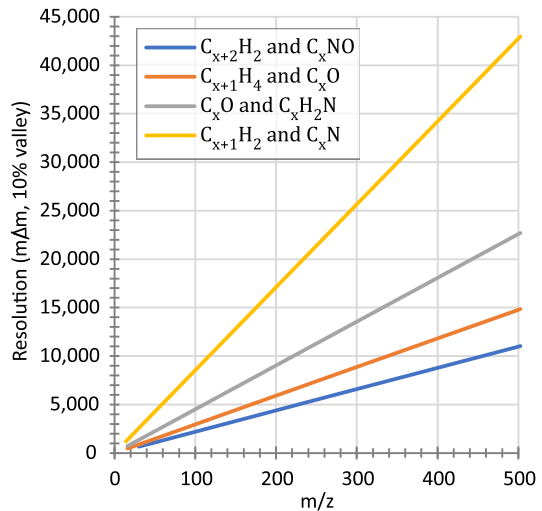
	10-lap-tune ( $\mu\text{s}$ )			50-lap-tune ( $\mu\text{s}$ )		
Species	$\text{H}_2\text{O}^+$	$\text{CO}^+$	$\text{CO}_2^+$	$\text{H}_2\text{O}^+$	$\text{CO}^+$	$\text{CO}_2^+$
$t_{thru}$ (m)	5.04281	6.20677	7.69467	5.03875	6.19859	7.68767
$t_{lap}$ (m)	7.46841	9.31111	11.67191	7.47610	9.32084	11.68400
$\sigma_{t_{thru}}$ (m)	0.0003089	0.0001794	0.0002428	0.0000718	0.0000981	0.0000834
$\sigma_{t_{lap}}$ (m)	0.0000197	0.0000145	0.0000250	0.0000014	0.000022	0.00000241

Neither of the datasets collected for the 10-lap and 50-lap tune spectra were measured at TOFs where the mass accuracy began to degrade; although it may be assumed that the time-focus will not continue to retain this consistency regardless of increased ion flight time. There is, however, a clearly demonstrated relationship between the accuracy in estimating or measuring an ion peak's TOF and the resulting accuracy in calculated ion mass as a function of TOF itself. This relationship is shown in Fig. 48, for which we assume a consistent TOF inaccuracy for the  $\text{H}_2\text{O}^+$  ion of  $t_{step} = 6.25 \times 10^{-4} \mu\text{s}$  (1 ADC sample interval), and plot the associated ion mass inaccuracy after ions complete 1 to 100 laps using the model parameters of the 50-lap-tune data. We demonstrate this relationship using  $t_{step}$  as a reference because ADC sampling itself is one inherent source of error in estimating an ion signal peak's center TOF position. The resulting curve is independent of mass, so the relationship holds for all ion species. At a lower number of laps, and therefore shorter TOFs, the value of  $t_{step}$  is larger relative to the ion TOF, meaning that the same uncertainty in estimation of an ion peak's TOF results in poorer accuracy of the calculated ion mass than at a higher number of laps. This relationship helps to contextualize the mass accuracy achieved during calibration.

The mass-dependent parameter and uncertainty estimates derived from data in this part of calibration are shown in Table 22 for each target ion. The relation between TOF and mass is dependent on the specific tuning voltages. This demonstrates that tuning affects not only the ion peak shapes observed at the detector, but also the ion velocity and thus TOF.

In-flight operation of MASPEX will make use of pre-defined sets of tuning voltages paired with timing tables that define ROIs in the mass spectra. Based on ground calibration, a unique set of TOF-to-mass relation model parameters will be applied to each set of tuning voltages and estimates for these parameters will be paired to all spectra collected in flight. Tuning operations and in-flight calibration will also be performed prior to Europa flybys. The in-flight calibration procedures are discussed in Sect. 6.5 below. The values presented

**Fig. 49** Model showing the mass resolution ( $m/\Delta m$ ), as a function of ion mass, required to separate nearly isobaric ions. The model shows the effect of a single substitution, in a hydrocarbon, by O, N or NO to provide a small but constant mass difference, while increasing the number of carbons in the molecule. The formulae for the relationships are shown in the legend. By increasing  $x$ , the effect of molecular mass on the resolution is explored



in Table 22 demonstrate accurate mass calibration for sets of spectra taken during ground calibration.

## 6.4.2 Mass Resolution

Common functional groups in geochemical mixtures can be nearly isobaric, so high mass resolution is needed to separate ion fragments from one another and correctly identify the ion stoichiometry (Fig. 49). For example, the exact mass of  $CH_2$  is 14.016 u, while  $^{14}N$  is 14.003 u. To resolve them would therefore require a resolution of approximately  $(14.016 + 14.003)/(2 \times (14.016 - 14.003)) = 1078$ . As discussed above, MASPEX mass resolution is controlled by the number of laps that the ions complete before detection, since completion of a longer flight path (in both time and distance) will lead to larger separation for small mass differences. Here, we describe data demonstrating mass resolution capabilities.

Mass resolution can be increased by increasing the number of laps, but is ultimately limited by the mass peak shape, primarily by peak broadening. There are two types of contributors to broadening. The first is caused primarily by the ion source and by mechanical and electrical “errors” built into the ion injection and exit processes. Ions complete these processes only once. The second type of errors, caused for example by ion scattering caused by neutral atoms in the drift region, stack up as the number of laps increases. Two other possible contributors, the sampling time of the ADC (0.625 ns) and the width of the MCP pulse (0.4 ns, Fig. 28), are negligibly small compared to the width of the TOF peaks. For example, Fig. 53 shows two peaks at highest resolution that are 135 ns at FWHM and are separated by 227 ns. Thus, the two effects together contribute <1% to broadening.

Errors that occur only once and do not accumulate are:

1.  $t_{thru}$  is the TOF from the source straight through the MBTOF to the detector without laps between the reflectrons (Fig. 46). Its associated variance  $\Delta t_{thru}$  results from thermal spread and grid effects in the source, as well as errors associated with MCP and source mounting, optical element parallelism, and electronics.
2.  $t_0$  accounts for electronic insertion delays and  $\Delta t_0$  is time spread resulting from insertion delays and electronic timing errors.

3.  $\Delta t_{iat}$  is the thermal spread due to the ion turnaround time in the source.

Errors that accumulate with every lap are:

1.  $t_{lap}$  is the time for a single lap (Fig. 46). Its spread  $\Delta t_{lap}$  is caused by electrical, mechanical, and optical errors.
2.  $\Delta t_{gas}$  is a component of ion scattering that increases with pressure in the MBTOF.

The time-of-flight in the simplest straight-through case, from the ion source to the detector, for ions accelerated by a potential  $U_a$  is:

$$t = \frac{L}{v} = L \sqrt{\frac{m}{2zeU_a}} \tag{27}$$

where  $t$  is the time-of-flight (ns),  $L$  is the flight distance between the source and detector (cm),  $\frac{m}{z}$  is the ion mass to charge ratio and  $eU_a$  is the accelerating energy (eV). Mass to charge is given by:

$$\frac{m}{z} = \frac{2eU_a}{L^2} \cdot t^2 = a \cdot t^2 \tag{28}$$

Substituting for unit values gives the time taken by ions to cross the field-free region (ns):

$$t = k_1 \cdot L \cdot \left(\frac{m}{U_a}\right)^{\frac{1}{2}} \tag{29}$$

where  $k_1$  is a constant equal to 22.85 ns. The theoretical mass resolving power for a time-of-flight spectrometer is given by simple differentiation:

$$R_{FWHM} = \frac{m}{\Delta m} = \frac{t}{2\Delta t} \tag{30}$$

Errors that do not accumulate can be neglected as the number of laps ( $n$ ) increases. In the limit that  $n$  is very large and gas pressure is within operational limits then:

$$R_{FWHM} = \text{Lim} (n \rightarrow \infty) = \frac{t_{lap}}{2\Delta t_{lap}} \tag{31}$$

Assuming that these errors are independent then the total error is

$$\Delta t = \left(\sum (\Delta t_i)^2\right)^{1/2} \tag{32}$$

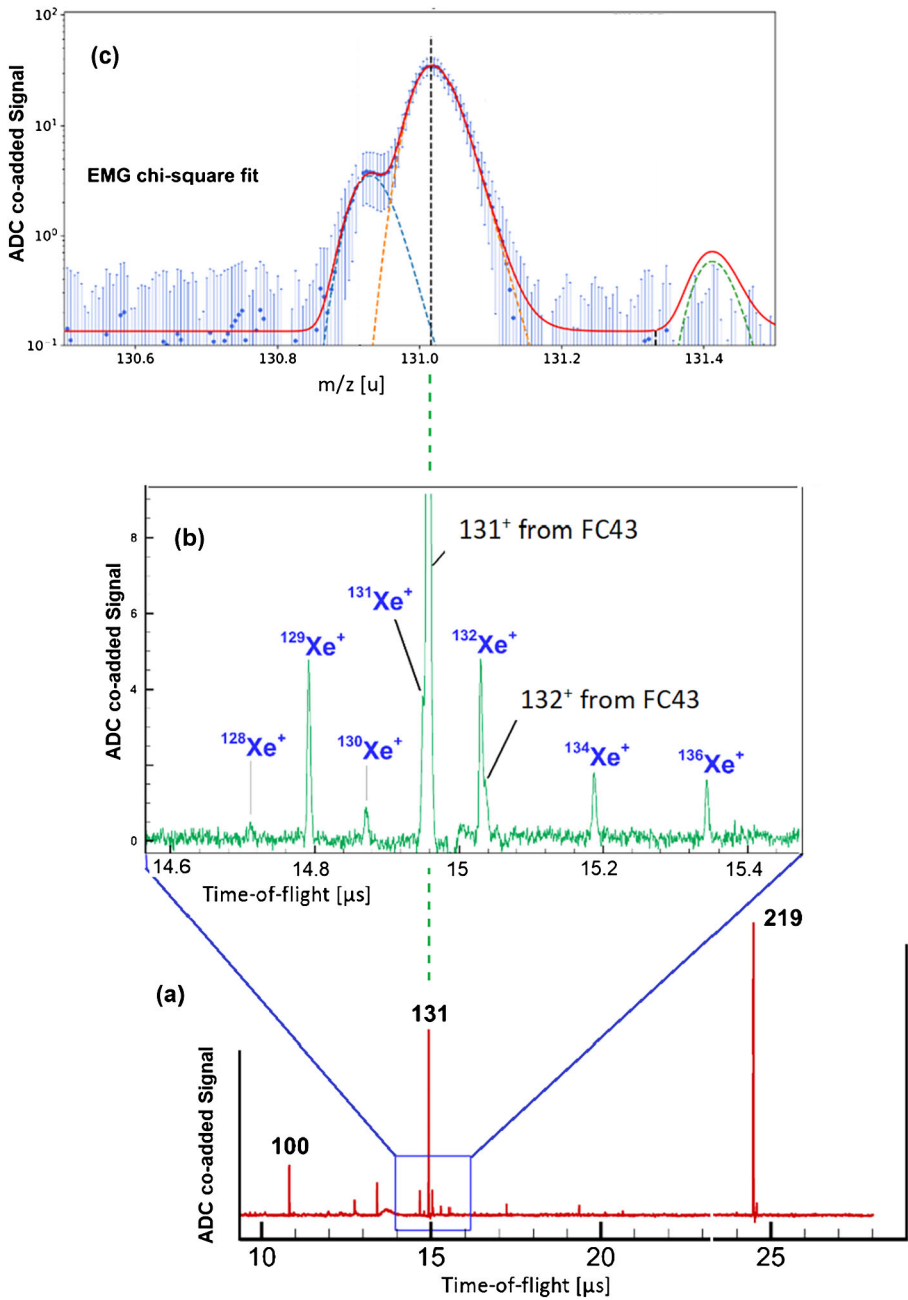
Given the basic resolution equation (30), the total peak broadening is given by:

$$R_{FWHM} = \frac{t_{thru} + t_0 + n \cdot t_{lap}}{2\sqrt{\Delta t_{iat}^2 + \Delta t_{thru}^2 + \Delta t_0^2 + \Delta t_{gas}^2 + ((n + 1) \cdot \Delta t_{lap})^2}} \tag{33}$$

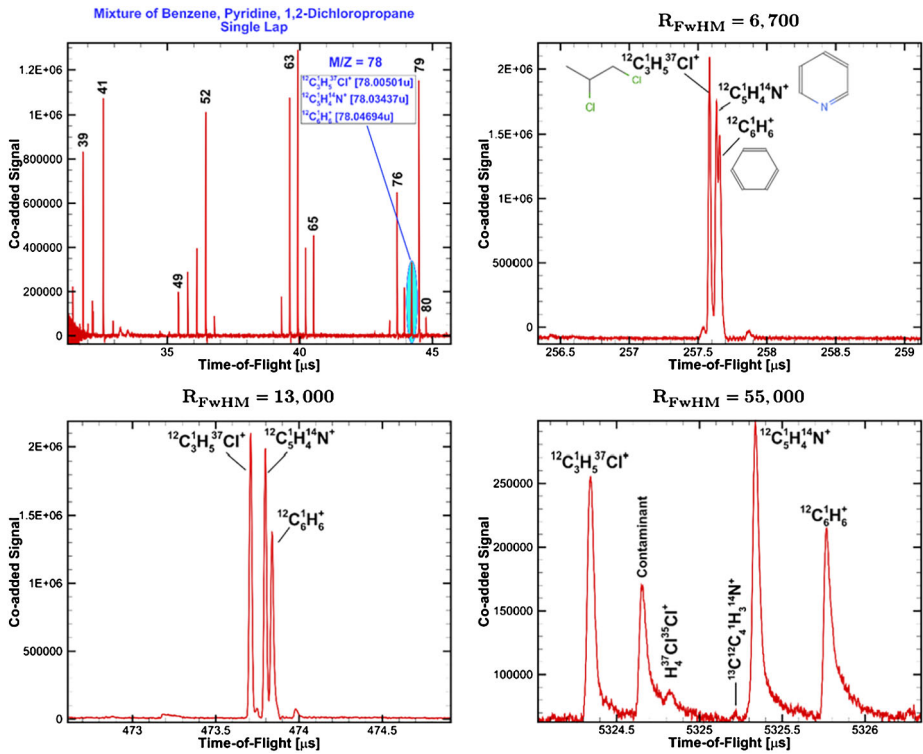
Table 22 illustrates the improvement not only in mass-dependent parameters and uncertainty estimates, but also in resolution with the increase in the number of laps from 10 to 50.

Figure 50 shows three progressively stretched TOF spectra of the FC-43 gas sample and fragments mixed with a small sample of xenon gas. All three spectra were taken with the





**Fig. 50** TOF spectrum of residual Xe and leaked FC-43 gas shown at three different TOF scale expansions. In this spectrum, ions travel directly from the source to the detector without lapping. See text below for a full description



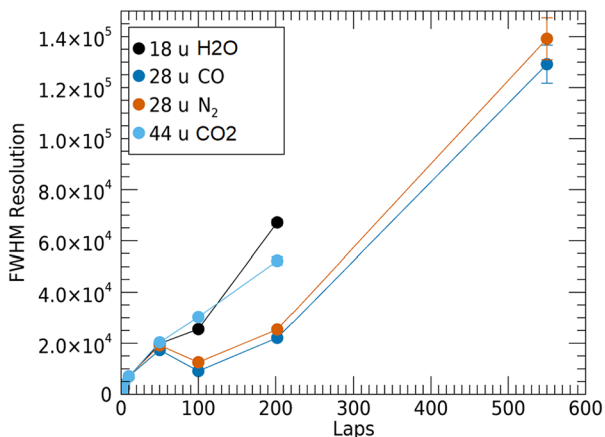
**Fig. 51** Demonstration of MASPEX resolving power in separating a mixture of benzene, pyridine, and 1,2-dichloropropane. The panels show the number of laps and corresponding flight times. Clockwise from the upper left panel: single lap (~44 μs), 15 laps (257.5 μs), 29 laps (473.8 μs), 346 laps (5325 μs)

FM instrument using a single lap, i.e., Reflectron 2 to 1 back to 2 and then to the detector resulting in TOF resolution  $t/2\Delta t = 640$  FWHM. Spectrum (a) shows the complete TOF range of a heavy ion spectrum covering approximately 30 μs. Spectrum (b) is an expansion of spectrum (a) covering 1 μs capturing all Xe isotopes in this TOF range, as well as two of the many FC-43 fragments at approximately 131<sup>+</sup> ( $^{12}\text{C}_3\text{F}_5^+$ ) and approximately 132<sup>+</sup> ( $^{13}\text{C}^{12}\text{C}_2\text{F}_5^+$ ) m/z. Spectrum (c) expands the axis still further but the units have been changed to m/z rather than TOF to demonstrate peak shape and the separation of  $^{131}\text{Xe}^+$  from  $^{12}\text{C}_3\text{F}_5^+$  using an exponentially modified Gaussian fitting routine (see below).

Spectra in Fig. 51 were obtained with the EM unit in the CAPS chamber. These data demonstrate the MS capabilities for resolving high-mass ions separated by as little as 0.0126 m/z. The growth of long tails to the high-TOF side of peaks is discussed below (see Fig. 53).

To demonstrate that the increase of resolution with number of laps is independent of mass, measurements of mass resolution as a function of laps for single ion peaks ( $\text{H}_2\text{O}^+$  at mass 18, and  $\text{CO}_2^+$  at mass 44) and for peaks with close masses (CO at mass 28 and  $\text{N}_2$  at mass 28) were performed on residual chamber gas (Fig. 52). Measurements of resolution (FWHM) were made at 1, 2, 4, 10, 50, 100, 202, and 550 laps. The number of laps was increased systematically by adjusting Reflectron 2 opening times. At each measurement step, voltages were tuned to optimize peak shapes. The same tuning method was used for all masses. Because of the complications in manually tracking all the peaks at a high number

**Fig. 52** Mass resolution as a function of laps completed for singlet (18 u, 44 u) and doublet (28 u) peaks



of laps, only the mass 28 peaks were tracked up to 550 laps. Each data point in Fig. 52 represents the average FWHM value for individual Gaussian fits to approximately 10 spectra, each of which has 256 extractions taken at a frequency of 100 Hz.

The data for H<sub>2</sub>O and CO<sub>2</sub> show a similar trend with the resolution increasing linearly with laps over the range considered. The CO and N<sub>2</sub> peaks also start along the same trend but by 100 laps have moved to a new line, with a similar slope, but at lower resolution. It is suspected that this is due to coalescence of the CO and N<sub>2</sub> peaks, creating asymmetry in the peaks and reducing the resolution (Grinfeld et al. 2014; Kaufmann and Walker 2018).

Even with this issue the data show that the resolutions required by the model in Fig. 49 are readily achievable, and that the rate of increase in resolution is similar over a nearly 60% change in mass, as predicted by theory (Guilhaus 2005; Ayet San Andrés et al. 2019).

Data for mass resolution calibration were collected during the Cal 1 campaign with the FM instrument installed in the CAPS chamber (Table 14). Toluene and <sup>13</sup>C-labeled o-xylene were introduced in roughly similar amounts into the vacuum chamber. The compounds were first measured in straight-through spectra, and the fragmentation patterns were used to verify the two molecules.

Once the ion peaks were selected, Reflectron 2 opening times were adjusted to increase the number of laps executed by the ions until the C<sub>6</sub>H<sub>4</sub><sup>13</sup>CH<sub>3</sub><sup>+</sup> and the C<sub>6</sub>H<sub>5</sub>CH<sub>3</sub><sup>+</sup> peaks were separated. During this process, voltages were tuned periodically to improve ion peak shapes and separation resulting in the spectrum shown in Fig. 53. In addition, the extraction frequency, which can be as high as 1 kHz, was reduced to 100 Hz to allow the total flight times of ~10 ms shown in the figure.

The peaks in Fig. 53 were smoothed and fit with an exponentially modified Gaussian (EMG) with the same peak shape for both (shown in orange). The mass resolution was calculated using the EMG fits, demonstrating TOF resolution of approximately 35,000 FWHM. This equates to a 10% valley resolution of 10,400, providing a comfortable margin above the requirement of 4275.

The shapes of the doublet peaks of C<sub>6</sub>H<sub>4</sub><sup>13</sup>CH<sub>3</sub><sup>+</sup> and C<sub>6</sub>H<sub>5</sub>CH<sub>3</sub><sup>+</sup> in Fig. 53 show broadening and asymmetry caused by the convolution of several factors intrinsic to TOF mass spectrometers operated at very high resolution. In particular, scattering and stray electric fields in the reflectrons tend to slow down a small portion of the ion distribution, creating longer TOFs and tails on the “slow” side of peaks. These effects tend to become larger as flight times become longer. For example, the peak tails in Fig. 51 appear after 5375 μs,

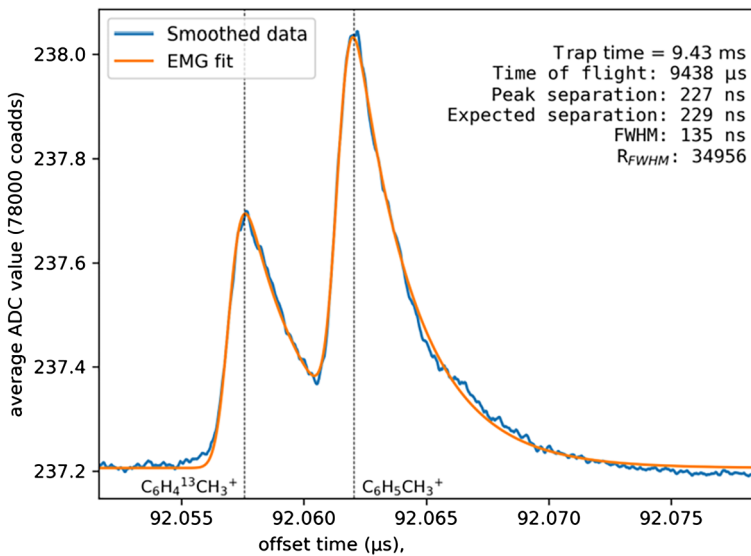


**Fig. 53** Mass spectrum of o-xylene showing peak separation of 227 ns out of a total flight time of 9438  $\mu\text{s}$  covering 564 laps. The source storage time was less than 10 ms making a repetition rate of over 100 Hz possible. The figure demonstrates resolution of approximately 35,000 FWHM

resulting in a resolution of 55,000 FWHM. Peaks in Fig. 53 develop relatively larger tails at 9438  $\mu\text{s}$ , dropping resolution to 35,000 FWHM. Differences in the relative size of the tails and mass resolution depend on details of the masses selected, the setup of the MBTOF, vacuum conditions, etc.

### 6.4.3 Mass Range

The mass range defines the limits of the heaviest and lightest compounds that can be detected. The mass of organic compounds increases rapidly with growing molecular complexity, with  $\text{C}_7$  compounds already reaching masses greater than 100 u. While it is possible that fragments from compounds larger than the upper mass limit can be measured in a mass spectrum, positive identification of the parent compound may not be achieved. On the other end of the scale, measurement of  $\text{H}_2$  requires that the mass range extend lower than 2 u. While the mass range of TOF mass spectrometers is theoretically unlimited, detection of peaks at either end of the mass scale requires the correct time-focus for ions reaching the detector. All data used for mass range calibration were collected as straight-through spectra with electron energy set at 70 eV and filament emission current at 100  $\mu\text{A}$ .

The low mass range (Fig. 54) was calibrated using the ions listed in Table 23.  $\text{He}^+$  was present in the vacuum system because of its use as a purge gas during loading of the CGS, while  $\text{H}_2^+$  is present as a fragment of water molecules. The other calibration ions are associated with the residual gas mixture present in the calibration chambers. The vertical lines in Fig. 54 show the position of the exact masses for  $\text{H}_2^+$  and  $\text{He}^+$ . Data shown earlier in Fig. 36 show the spectrometer's ability to reach a lower mass limit of atomic hydrogen ( $^1\text{H}^+$ ), demonstrating an effective mass range that extends below 2 m/z. Since the  $\text{H}_2^+$  and  $\text{He}^+$  peaks were outside the mass range used for calibration, the larger mass error (due to extrapolation) shown in Table 23 when compared to peaks within the calibrated range is not unexpected.

**Fig. 54** A straight-through spectrum of the lowest mass region

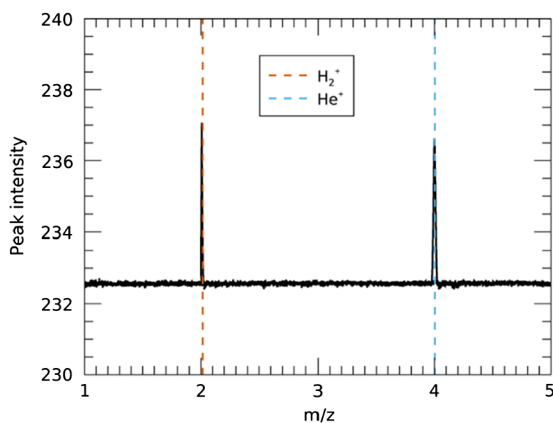


**Table 23** Results from the analysis of the low mass range spectrum. The ‘In mass cal.’ column indicates the peaks used to define the mass calibration. The mass calibration was then used to calculate the  $\text{H}_2^+$  and  $\text{He}^+$  masses

Ion fragment	In mass cal.	Centroid time $\mu\text{s}$	Exact mass $m/z$	Calculated mass $m/z$	% Mass error
$\text{H}_2^+$	No	4.37533	2.0151	2.00857	-0.32%
$\text{He}^+$	No	5.0095	4.0021	3.99889	-0.08%
$^{14}\text{N}^+$	Yes	6.90424	14.0025	13.9983	-0.03%
$^{16}\text{O}^+$	Yes	7.18684	15.9944	16.0086	0.09%
$^{16}\text{O}^1\text{H}^+$	Yes	7.31968	17.0022	16.9979	-0.03%
$^1\text{H}_2^{16}\text{O}^+$	Yes	7.45007	18.0100	18.0023	-0.04%
$^{12}\text{C}^{16}\text{O}^+$	Yes	8.59034	27.9944	27.9975	0.01%

Calibration of the high mass range was performed using the masses and centroid times listed in Table 24 and shown in Fig. 55. Centroid times were defined based on Gaussian fits to the peaks within TOF windows that were manually selected to exclude adjacent peaks. Black dots represent the entirety of collected data out to 620  $m/z$ . Points over-plotted in color are derived from the NIST spectra for water, nitrogen, oxygen, propane, and FC-43. For each integer mass identified in the NIST spectra as a fragment ion for these parent compounds, the data points within  $\pm 0.5$   $m/z$  were over-plotted in the corresponding color i.e., for 18  $m/z$ , data from 17.5 to 18.5  $m/z$  are colored. The inset in Fig. 55 shows an example at  $m/z$  264 at the calculated position of the ion mass (vertical dashed line) versus the measured peak. Like the low mass range, the mass error rapidly increases for peaks above the calibrated range, but is still reasonable given that we are extending the calibration by 112  $m/z$ .

This high-mass-range data (Fig. 56) includes a fragment of the FC-43 peak near 502  $m/z$  using mass calibration data from Table 24. This result demonstrates ion focusing to at least 500  $m/z$ , which meets the required mass range performance. The data shown in Fig. 54, Fig. 55, and Fig. 56 taken together demonstrate that MASPEX will be able to identify the accurate mass of compounds over the required mass range.

#### 6.4.4 Fragmentation Patterns

The electron ionization process creates molecular ions with excess energies. The ions achieve a lower energy state by rearrangement and/or fragmenting into smaller compounds.

**Table 24** Results from the analysis of the high mass range spectrum. The ‘In mass cal.’ column indicates the peaks used to define the mass calibration. The mass calibration was then used to calculate the  $C_{12}F_{22}N^+$  and  $C_{12}F_{24}N^+$  masses

Ion fragment	In mass cal.	Centroid time $\mu s$	Exact mass $m/z$	Calculated mass $m/z$	% Mass error
$^{16}O^+$	Yes	4.71867	15.9944	15.9856	-0.06%
$OH^+$	Yes	4.85473	17.0022	16.9929	-0.05%
$H_2O^+$	Yes	4.98675	18.0100	17.9971	-0.07%
$CO^+$	Yes	6.13877	28.0056	27.9939	-0.04%
$O_2^+$	Yes	6.53896	31.9893	31.9798	-0.03%
$CF_3^+$	Yes	9.45179	68.9947	69.0076	0.02%
$C_3F_5^+$	Yes	12.901	130.9910	131.04	0.04%
$C_4F_9^+$	Yes	16.5864	218.9850	219.099	0.05%
$NC_5F_{10}^+$	Yes	18.1798	263.9870	264.156	0.06%
$NC_8F_{16}^+$	Yes	22.6834	413.9770	414.219	0.06%
$NC_9F_{18}^+$	Yes	23.9904	463.9740	464.087	0.02%
$C_9F_{20}N^+$	Yes	24.9218	501.9710	501.333	-0.13%
$C_{12}F_{22}N^+$	No	26.5364	575.9670	569.306	-1.16%
$C_{12}F_{24}N^+$	No	27.2325	613.9640	599.955	-2.28%

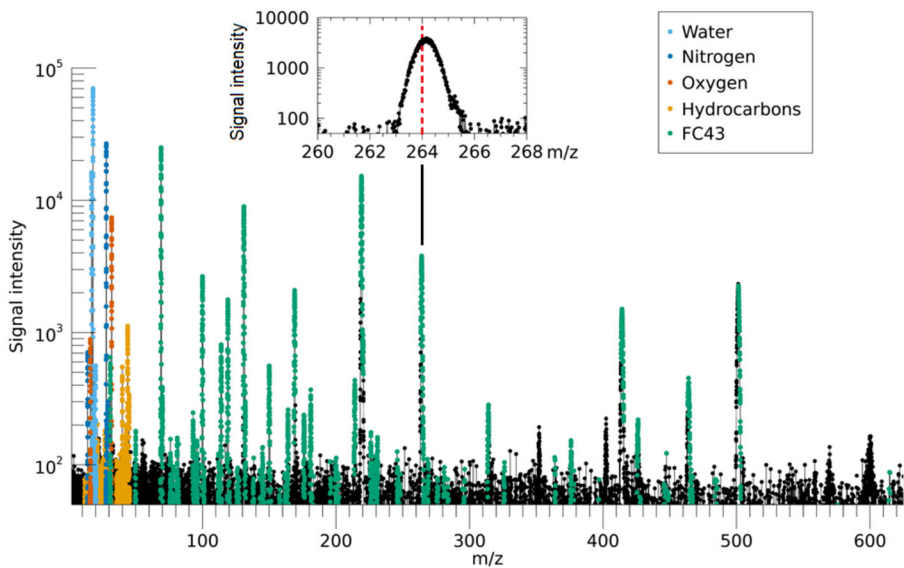


**Fig. 55** Spectrum demonstrating the entire MASPEX mass range, particularly its ability to reach over 600  $m/z$ . The multiple green peaks are fragments from the ionization of FC-43. The inset shows the match between the peak centroid and exact mass for the 264  $m/z$  fragment of FC-43 (dashed vertical line)

The nature of the rearrangement and the locations of the fragmentation are largely dependent on the structure and composition of the parent molecule and the ion source’s electron energy, resulting in a recognizable pattern of abundances for the ion masses. This enables comparison of fragmentation patterns from MASPEX, particularly those taken at 70 eV

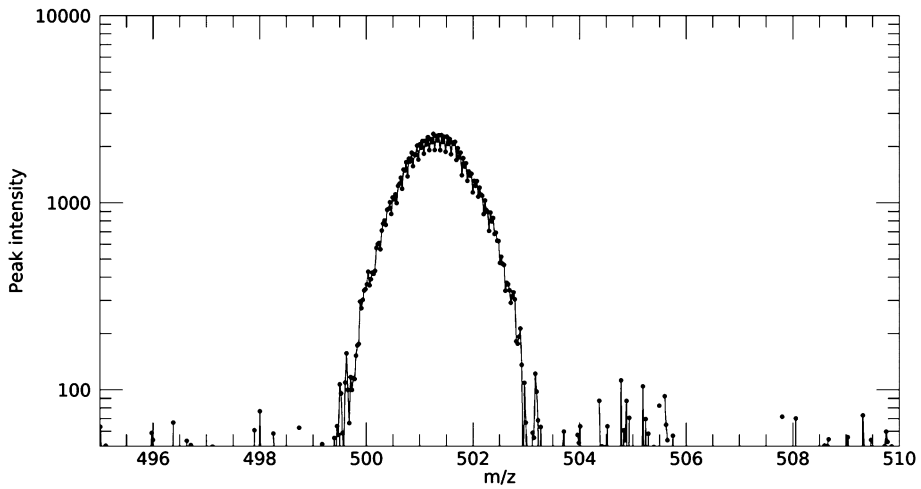


**Fig. 56** Shape of the high mass range peak near 502 m/z

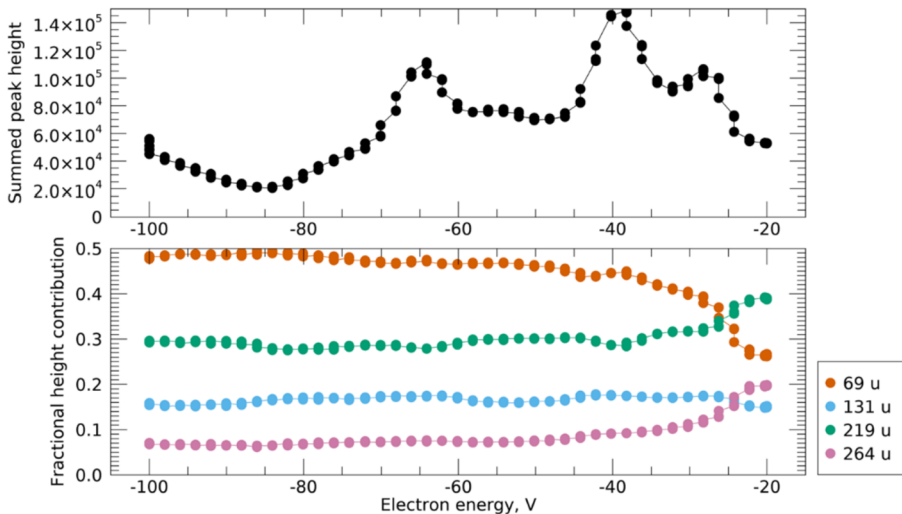


**Fig. 57** Fragmentation of FC-43 in MASPEX was characterized as a function of electron energy. The top panel shows the summed production of ions at 69 u, 131 u, 219 u, and 264 u, taken to represent the total ionization efficiency. The bottom panel shows the fraction of the total signal (in the top panel) attributed to each of the individual ions

electron energy, with widely available databases including those maintained by Wiley and NIST. However, the design geometry of the ion source can also influence fragmentation, so our calibration data were compared to the NIST library to determine the utility of library spectra in the analysis of MASPEX data that will be taken at Europa (Fig. 58).

Data characterizing the effects of electron energy on mass spectra were collected during Cal 1. The FC-43 was introduced manually via syringe injection and vaporized through a heated line into the calibration chamber. Total pressure was virtually constant ( $7.25 \times 10^{-7}$  to  $7.31 \times 10^{-7}$  hPa) over the course of the data collection period. Electron energy was



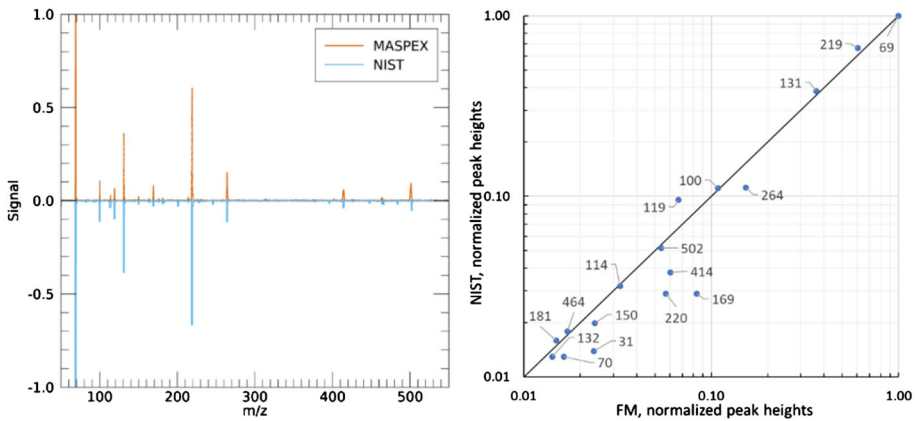


**Fig. 58** Comparison of NIST and MASPEX spectra for FC-43 fragments at an electron energy of 70 eV and source emission current of 100  $\mu$ A. The left figure shows ion fragment masses. The peak amplitudes are slightly different because of differences in source efficiencies at particular masses. The right figure shows a different visualization of the differences between the peak heights in the same spectra (normalized to the 69 m/z peak for heights  $\geq 1\%$ )

stepped every 20 seconds in 2 V steps starting from an initial value of  $-100$  V to a final value of  $-20$  V. Straight-through spectra with a mass range that included the four main fragment ions (69 u, 131 u, 219 u, and 264 u) were taken at an extraction rate of 100 Hz. All other operating parameters were left unchanged throughout the measurements, including the source emission current of 100  $\mu$ A.

The four largest peaks from FC-43 (Fig. 57) were identified using the NIST spectrum, and corresponding time windows were manually selected from spectra taken with an electron energy of 70 eV. The maximum signal within each time window was recorded as the peak height for the corresponding mass fragment. Total signal values were approximated by summing peak heights of the four FC-43 calibrant peaks. While some fluctuation in total ionization as a function of electron energy is observed (Fig. 57, top panel), the relative heights of the main four peaks are virtually unchanged until  $-40$  V (Fig. 57, bottom panel).

The fragmentation pattern for FC-43 on MASPEX at 70 eV is directly compared with the NIST pattern in Fig. 58. It is evident that larger fragment peaks below  $\sim 300$  u are similar in amplitude to those in the NIST spectrum (Fig. 58, left panel). The smaller peaks show larger deviations from the NIST spectrum. The right panel is a comparison of the MASPEX and NIST peak heights at 70 eV for the largest peaks normalized to 69 u.

The similarity of the MASPEX data to the NIST library for larger peaks means that it will be possible to use the library for qualitative analysis of mission data to identify candidate compounds. Accurate quantitative analysis of unanticipated compounds will require collection of fragmentation and sensitivity data from the EM instrument during the cruise to Jupiter or after arrival in the Jovian system.

## 6.5 In-Flight Calibration

All mass spectrometers require adjustment of voltages and currents controlling performance throughout their lives to compensate for aging electronics, contamination build-up on optical elements (particularly those nearest the ion source), changes in filament emission characteristics, and detector gain degradation. These adjustments, made during flight (Sect. 8.5.4),

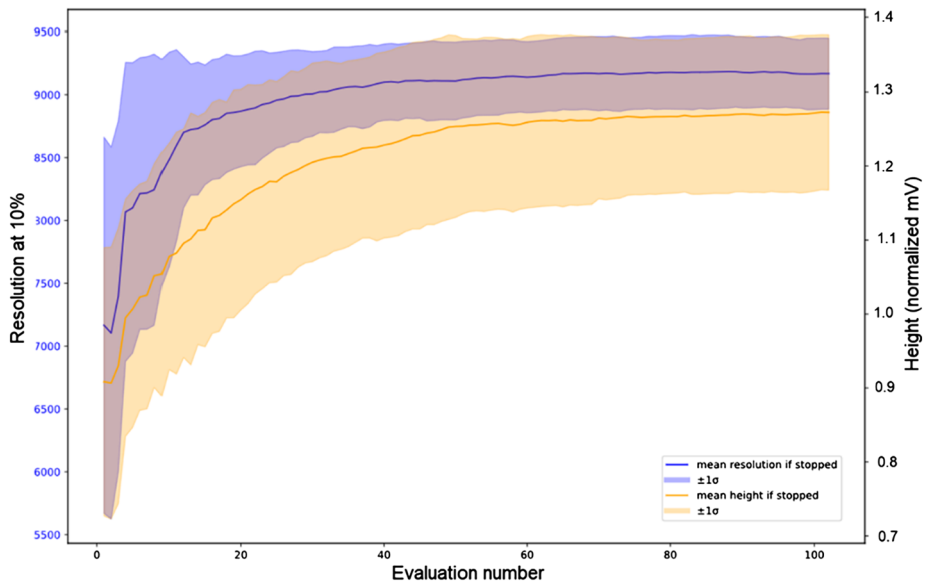


**Fig. 59** The x-axis is the number of evaluations of the auto-tuning algorithm. The blue line (with left scale) shows the average resolution of the 86 trials, with the shaded area showing the  $\pm 1\sigma$  spread of the distribution over the evaluations. The orange line (with right scale) gives the normalized peak height, with shaded area again showing the  $\pm 1\sigma$  spread of the distribution over the trials. This plot shows that the search converges after roughly 50 evaluations

require a means of reestablishing calibration of the mass scale, the detector gain, and the ion source sensitivity. The CGS and FC together allow recalibration prior to every flyby of Europa and, as necessary, at any point during the mission. In-flight calibrations can be validated through cross-calibration with data from the EM using the COSMIC ground system.

During the mission, MASPEX will be calibrated before each flyby and after each cryosample has been analyzed (Sect. 8.5.4). During each orbit, MASPEX will operate at two different temperatures: the first during the flyby, and the second during cryo-sample analysis, making separate calibrations essential. After each measurement, a reduced set of “feedforward data” is created and priority downlinked (Sect. 8.4). Feedforward data are analyzed on the ground and used to revise current ROIs to adapt to, and prepare for, the next sample. The data are also used to account for any variation in performance. The refined ROIs are then uplinked before the next orbit. This cycle is repeated on every flyby to maintain characteristics needed for optimum performance during the next sampling period.

Auto-tuning (Sect. 8.5.4) will utilize flight data to optimize the optical element voltages and timing. In-flight operation will then make use of pre-defined sets of tunes paired with timing tables that define ROIs for the mass spectra. Once tuned, the FC-43 spectrum will be the basis for checks of the mass scale and ROIs.

Source sensitivity will be measured for the new tuning by measuring detector counting rate and then deflecting ions out of the beamline and into the Faraday cup where the beam current is measured. Comparison of the two provides the necessary calibration of detector gain allowing adjustments to be made (Sect. 6.3.2).

Tests with the tuning algorithm produced the results shown in Fig. 59. Eighty-six trials were performed with voltages detuned by  $\pm 1\%$  rms from the nominal baseline values based on a combination of calibrant FC-43 gas and residual gas (75% calibrant, 25% residual gas).

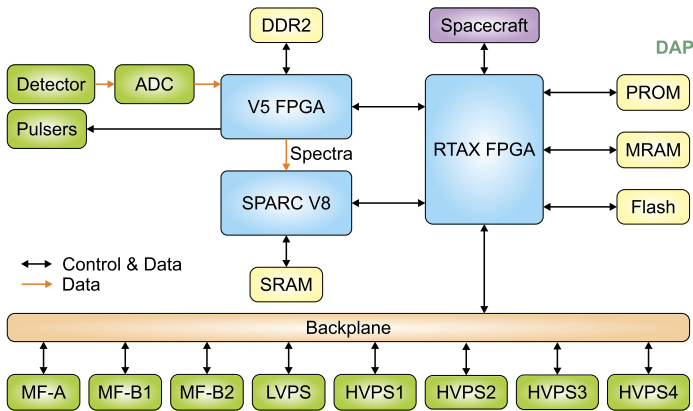


**Fig. 60** Simplified block diagram identifying the features relevant to the FSW control of MASPEX. Blue boxes are microprocessors, yellow boxes are memory, green boxes are other boards or hardware controlled by the software. The FSW code is executed by the SPARC microprocessor

Simulations were terminated after  $n$  evaluations of peak height and resolution convergence beginning with  $\pm 1\%$  rms de-tunings.

## 7 Flight Software

MASPEX is a complex instrument operating in a harsh radiation environment and its command-and-control system reflects those aspects. This section describes how the control of MASPEX is managed by the Flight Software (FSW) and the features introduced to provide resilience against environmental conditions. We begin by discussing the command-and-control architecture (Sect. 7.1) followed by the bootstrap process (Sect. 7.2), detailing the steps necessary to get MASPEX operational. This is followed by a discussion of the layered approach to commanding (Sect. 7.3), building from individual commands, through to multiple complex operations. This approach is further expanded with autonomous operation (Sect. 7.4) where MASPEX is able to sequence its own operations autonomously, based on timer information that makes possible the science mission flyby and cryosample analysis activities, at the heart of which lies the ROI cycle (Sect. 7.4.2) that performs the core function of mass spectral data acquisition. Finally, the packaging of data generated by MASPEX for downlink is considered in Sect. 7.5.

### 7.1 Command and Control Architecture

The FSW that controls all the operations of MASPEX, runs on the DAP board within the EBOX (Sect. 5.5). This section gives a general overview of the DAP and control architecture and will aid understanding of the system. A simplified block diagram is shown in Fig. 60.

The DAP contains three microprocessors, each handles a different part of the command and control depending on their characteristics:

1. The radiation hardened SPARC V8 processor runs the FSW.
2. The RTAX<sup>®</sup> FPGA is a radiation tolerant, one-time programmable processor, programmed before launch. It serves as the central distribution point for nearly all components and subsystems including the spacecraft interface, and instrument memory and

hardware. It is responsible for starting the bootstrap process and enables the FSW to communicate with and control all MASPEX's features.

3. The V5 FPGA processor is radiation hardened and is responsible for data acquisition including the precise timing control and setting of necessary MBTOF potentials.

The DAP uses five different types of memory, each selected to meet the requirements of their uses and to provide tolerance to radiation effects:

1. The non-volatile Magnetorestrictive Random-Access Memory (MRAM) stores a redundant copy of the bootstrap as well as copies of the science FSW and all its configuration data. Its ability to be rewritten frequently with random access makes it suitable for use with the FSW.
2. The nonvolatile Programmable Read-Only Memory (PROM) stores the primary bootstrap software responsible for the initialization of hardware and loading of the science FSW that controls MASPEX. The physically discrete, nonwritable component provides resiliency to a physical failure of the MRAM.
3. The volatile Static Random Access Memory (SRAM) is the working memory for the SPARC V8 into which is loaded the bootstrap and science FSW code. The FSW mitigates the effects of radiation in this memory by automatically correcting for single-bit errors, it can also detect multi-bit errors, in which case it raises an error flag and halts operation.
4. The nonvolatile Flash memory is partitioned into separate regions for storage of V5 images, science data, engineering data, and diagnostic data. It is used for the storage of large blocks of data since its block based read/write makes it less suitable for random access data.
5. The volatile, high-speed Double Data Rate 2 (DDR2) synchronous dynamic random-access memory is used by the V5 to store integrated spectra from data acquisition. Error Correction Code (ECC) memory is used to protect against the effects of radiation. The memory is double-buffered, allowing the finished integrated spectra to be transferred directly to the SPARC for further processing by the FSW.

The FSW runs on the SPARC microprocessor using the SRAM. It communicates to the rest of MASPEX through the RTAX FPGA. The V5 FPGA performs timing-critical data acquisition tasks when instructed by the FSW. It sets all the operating potentials, provides the highly precise nanosecond-level timing for the pulsers, gathers the data from the detector and integrates it into spectra that are stored in the DDR2 memory. The finished integrated spectra are transferred directly to the SPARC where they are further processed according to the currently active aggregation scheme.

## 7.2 Bootstrap Activities

This section discusses the actions MASPEX takes to become operational and highlights the design features employed to ensure that the instrument will either operate or be recoverable from errors or damage caused by radiation. The major steps are shown in Fig. 61 and are described as instrument modes. When MASPEX is powered on, it immediately enters **Boot Mode**. The RTAX FPGA begins the boot by loading the bootstrap software into SRAM. Out of concern for faults that could be caused by the high radiation environment, there are two copies of the bootstrap software, one in PROM and one in MRAM. This approach of storing redundant copies is continued throughout the software and configuration data, and the boot process is designed to provide multiple opportunities to recover from corrupted software.

The RTAX is responsible for the selection of which version of the bootstrap software is used. Should MASPEX fail to boot, the version can be changed using a Remote Memory

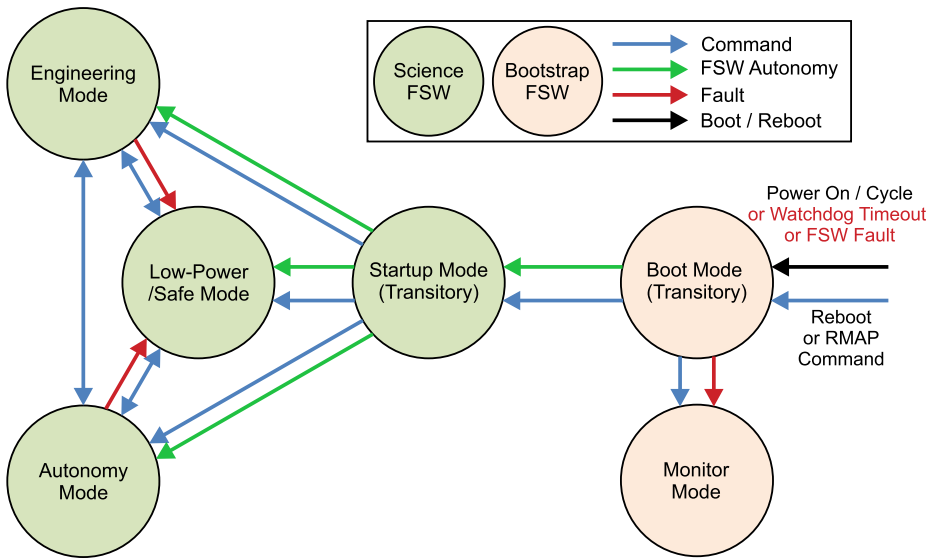


**Fig. 61** FSW operating mode flow chart

Access Protocol (RMAP) command from the spacecraft. The bootstrap is executed by the SPARC and is responsible for initializing the hardware and performing several tests before waiting for 10 seconds to allow for the receipt of an RMAP command to change the boot selection. Should a command be received, the software is rebooted, and the specified version is run. If no command is received, then the science FSW and configuration table are checksummed before loading them from MRAM into SRAM. If the checksum is incorrect, then the redundant copy is loaded instead. Should both checksums, or any of the tests fail, then the bootstrap remains running, processing commands from, and sending status packets to the spacecraft. This condition, called **Monitor Mode**, enables new software to be uploaded to recover MASPEX operation on the next power on.

### 7.2.1 Flight Software Modes

Once execution of the science FSW begins (called **Startup Mode**, Fig. 61) the FSW waits a further 10 seconds to allow a command to be received from the spacecraft that will override the programmed mode selection, enabling recovery should MASPEX become ‘locked’ in an operational mode. Once the delay has elapsed the software calculates checksums for all the configuration files, and if at least one of the redundant copies passes, loads them into SRAM. The FSW then moves into the prescribed operating mode using records of the last mode that was in operation and how long ago that occurred.

The operating mode selection uses the following rules:

1. If there is no previous mode, then move to Low-power / Safe Mode (LPSAFE)
2. If the previous mode was Engineering Mode less than 90 seconds ago, then move to Engineering Mode. If greater than 90 seconds, then move to LPSAFE.
3. If the previous mode was LPSAFE or Autonomy Mode, the spacecraft clock is synced, an Activity sequence table (AST, see Sect. 7.4.1) is active, and the Real Time Sequence (RTS, see Sect. 7.3.3) library is valid, then move to Autonomy Mode.

Each operating mode fulfils a specific role for MASPEX as follows.

**Low-power / Safe Mode** - in this mode all the MASPEX peripheral systems are turned off, resulting in the lowest possible power consumption. In the event of errors occurring in Engineering or Autonomy modes the FSW transitions to LPSAFE through a configurable process that ramps-down all the HVPSs and filaments before disabling them. The Mindrum valves (Sect. 5.3.4 and 5.3.6) are closed and the V5 FPGA, MFB1 and MFB2 are turned off.

**Engineering Mode** – in this mode, full control of MASPEX is possible. All peripheral systems can be powered and controlled. Control is affected through commands sent from the spacecraft. This is expected to be the nominal operational mode during cruise.

**Autonomy Mode** – this mode embodies all the features of Engineering Mode, while also running the sequencer (see Sect. 7.4), which enables MASPEX to perform functions autonomously based on the time of the spacecraft clock. It requires no instructions from the spacecraft. This is expected to be the nominal operational mode during the tour.

## 7.3 Commanding

The simplest form of commanding for MASPEX is a single command. A command instructs MASPEX to perform anything from simple operations such as turning on a power supply, through to extremely complex operations such as performing an ROI sequence (see Sect. 7.4.2). There are nine commands supported by the bootstrap FSW in Monitor Mode. These provide the tools necessary to upload new software to the MRAM to recover from corruption of the software. The science FSW supports 151 commands that control every aspect of MASPEX operations. Commands are only valid in certain operating modes. For example, LPSAFE has a subset of only 76 out of the 151 commands, Engineering Mode has 149, and Autonomy Mode has 142. The spacecraft directly supports only 29 of the commands to enable operations that the spacecraft must perform, such as loading configuration files, reading diagnostic data, and operating the vacuum cover release. Commands not directly supported by the spacecraft are sent via CCSDS<sup>8</sup> command packets.

### 7.3.1 Command Parameters

Most commands require additional information to direct their actions. This information is provided in parameters appended to the command. The simple commands can have the parameters appended directly to the command. For example, the command to operate the switchable outputs of the low voltage power supply has the form `MASPEX_LVPS_Control(<Switch>, <State>)` and requires the parameters `<Switch>` to identify which switch to operate, and `<State>` to indicate the desired position, on or off.

### 7.3.2 Parameter Tables

Complex operations also require parameters, but because of the amount of work that the command does, the parameter list would be unwieldy. To provide a solution to this problem, tables of parameters were created to group together all the necessary values. Libraries provide multiple copies of the tables (with different values) to support multiple sets of parameters. To give additional flexibility, the tables were defined at a low level to provide functionally related groups of parameters. Tables can also contain pointers to tables in other libraries. This allows a branched hierarchy of tables that build up to a single top-level table

<sup>8</sup>Consultative Committee for Space Data Systems.

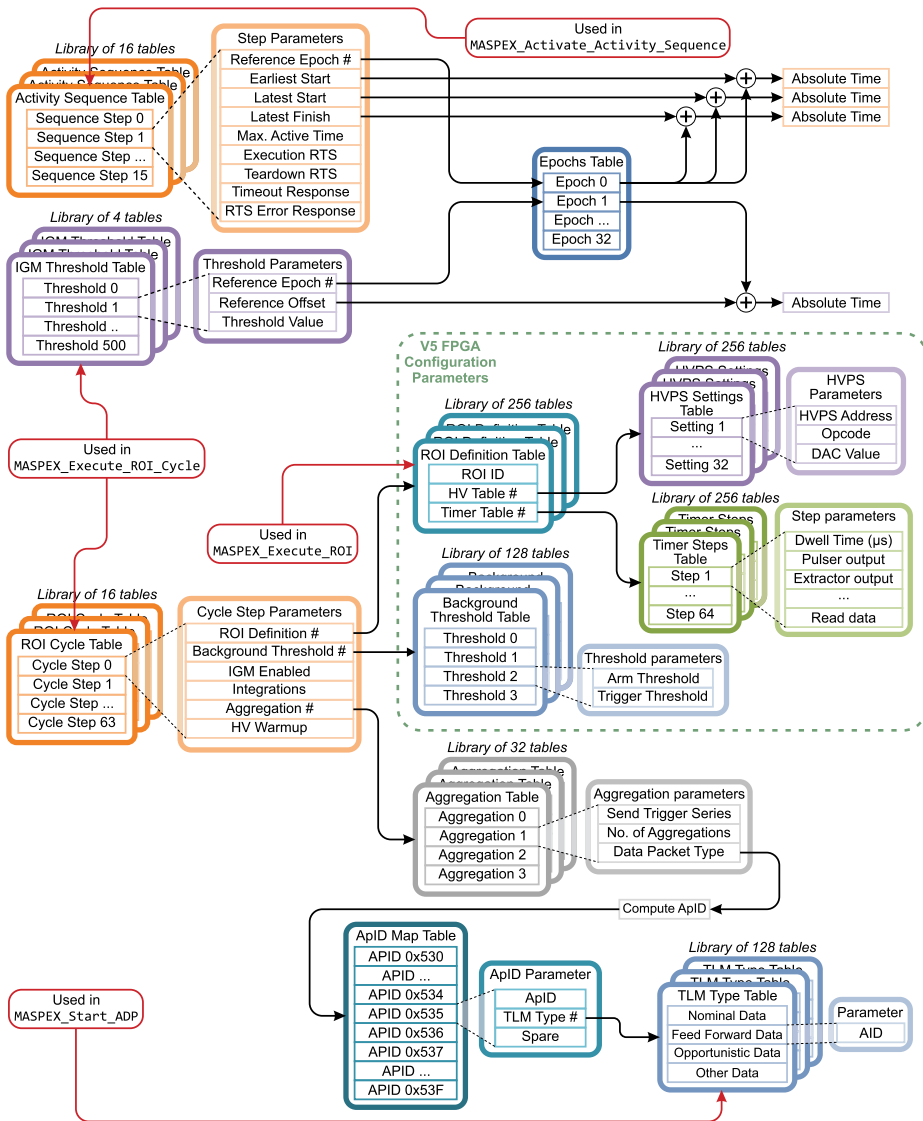


**Fig. 62** The parameter table hierarchy showing how a single entry in a parameter table provides all the parameters required for the operations detailed in Table 25, and how the multiple operating conditions required to analyze the European atmosphere are stored within the structure

(Fig. 62) that can then be referenced in the command. There are only four commands that use tables as parameters, and these are shown in Table 25.

The desired set of tables is unlinked and stored in non-volatile memory so that they can be used repeatedly. Throughout the mission (and as frequently as twice per orbit during the tour), operations tables will be updated based on science measurement goals and instrument performance (Sect. 8.4).



**Table 25** The MASPEX commands that support table-based parameters. Bold parameters are the table references. See Fig. 62 for details of the table contents. Figure 63 gives an example of how parameters are used in command logic

Command	Function
MASPEX_Execute_ROI_Cycle (<ROI Cycle Table #>, <Iterations>, <Enable IGM>, <IGM Thresholds Table #>, <ROI Cycle Table # for IGM>)	Executes a cycle of ROI acquisitions (see Sect. 7.4.2)
MASPEX_Execute_ROI (<ROI Definition Table #>, <Integrations>, <Iterations>)	Executes a single ROI acquisition
MASPEX_Start_ADP (<Use_Default>, <TLM Type Table>)	Selects the telemetry type identifiers to be used for the current data acquisition
MASPEX_Activate_Activity_Sequence (<Sequence Table #>)	Once activated the sequencer will perform the actions at the times defined in the sequence (see Sect. 7.4.1)

### 7.3.3 Real Time Sequences

Even with 151 commands, most MASPEX operations require multiple commands to perform them. The FSW supports this through RTSs, which are just lists of commands to be executed from the first command to the last in the sequence. Additional RTSs can be called from within an RTS, enabling branching. The additional RTS is run in parallel to the first. Up to 16 RTSs can be running simultaneously. Sequential operation of RTSs can be achieved by waiting until the additional RTS has completed. Conditional waits are also supported, to enable a variable delay while monitoring a parameter until it falls within a desired range.

Each RTS can contain a maximum of 85 commands. RTSs are stored in duplicate libraries in the MRAM. Both libraries are checksummed during FSW boot to ensure they are not corrupted.

RTS execution can be started by several processes:

1. A command from the spacecraft to start an RTS.
2. An active AST (see Sect. 7.4.1), which starts RTSs at scheduled times.
3. A transition to LPSAFE, which can use an RTS to perform safing operations.
4. Abort and Shutdown commands, which can use an RTS to perform operations.
5. Fault detection and correction rules to manage fault actions.

Each entry into an RTS includes the following:

1. How many seconds to wait before executing the command or, in the case of a conditional wait, the timeout.
2. What action to take if the command is rejected or a conditional wait times-out (issue warning and continue or terminate the RTS).
3. The command to execute.

## 7.4 Autonomous Operation

The complexity of MASPEX operations and their timing requirements would place a heavy burden on the spacecraft were it to provide direct control. To lessen this workload and to provide a level of resiliency in response to spacecraft issues that may be caused by the harsh environment, MASPEX can be preprogrammed to perform operations within defined windows of time. This means that the spacecraft only needs to turn MASPEX on and provide the spacecraft clock time signal to enable MASPEX to schedule all the operations involved in a flyby or a cryosample analysis. In case the spacecraft clock is no longer received, or the spacecraft stops receiving data, MASPEX can continue data acquisition as planned, storing the data until the spacecraft responds again. At this point the stored data are transmitted.

MASPEX autonomy is provided by the sequencer, which runs when MASPEX is in Autonomy Mode (Sect. 7.2.1). This mode is primarily used to perform the flyby and cryosample analysis operations during science operations (see Sect. 8.1), although it could be used for any of MASPEX's operations.

The sequencer takes no action until an Activity Sequence Table (AST, Sect. 7.4.1) is activated through a command. Only one AST can be active at a time. Details of the currently executing AST are stored in MRAM so that the instrument can be power-cycled or rebooted, and the sequencer will continue executing the AST where it left off. If the instrument experiences a FSW or Watchdog reset event, then the sequencer will continue operation, skipping any AST steps that have already been marked as complete. If the instrument is power-cycled, then the sequencer will start over at the first AST step (since the assumption is that all hardware has been reverted to its initial power on state).

### 7.4.1 Activity Sequence Tables

An AST defines the internal automated activity sequencing (Fig. 62). With MASPEX in Autonomy Mode, once a table is activated, the FSW will execute the sequence steps at their scheduled times. Each sequence step in this table defines a window of time within which the step can be started and identifies the latest time that the step must be completed by.

To reduce the number of changes necessary from flyby to flyby, times are stored in the AST as values relative to an epoch. An additional field in the step identifies which epoch should be used to calculate the absolute time that will be used by the sequencer. This tactic means that, for example, the flyby operations can be defined relative to closest approach. Now it is only necessary to update the epoch with the time of the next orbit's closest approach and the same operations can be repeated.

Sequence steps are performed by executing an RTS that is identified in the step parameters of the AST. The selection and operation of any ROI cycle is performed by the parameters stored in the RTS. Once the execution is complete there is another RTS identified that can be used to close-down the operations. MASPEX stores 16 ASTs in MRAM memory, each with 16 steps (Fig. 62).

### 7.4.2 Region of Interest Cycles

The ion optical design of MASPEX yields an inverse relationship between mass resolution and range (Sect. 5.4.3). Low resolution gives a wide mass range and vice versa. This means that we are unable to operate MASPEX to answer all science questions in one set of conditions. Adequate, mass-resolved data are needed for quantitation of a mixture of compounds, this requires analysis of different mass ranges measured with different resolutions. To do

this, multiple ROIs are used to build up a full mass range picture of the spectrum (Sect. 5.4.3 and Fig. 4). Finally, in order to provide localization of materials leaving from Europa's surface, the ROI cycle will be performed repeatedly throughout the flyby completing the series of measurements within a maximum of five seconds.

From a hardware and software perspective, an ROI is a set of instrument parameters that produce the desired science data. There are three main classes of parameters that are involved: potentials that are applied to the various electrodes, timing of the source extraction and reflectron operations, and data processing requirements that define how the data are processed and labeled for transmission to the ground.

The speed of the ions flying through the MASPEX optics requires nanosecond timing precision that the FSW on the SPARC cannot provide. Instead MASPEX relies on the V5 FPGA to perform time-critical functions of data acquisition for each ROI. Figure 62 shows the tables containing the V5 configuration data (within the dashed green outline). The tables contain the voltages controlling the HVPS (HVPS Settings Table), the timings that define the mass range and resolution (Timer Steps Table), and the configuration of the thresholds that identify background counts caused primarily by the radiation environment (Background Threshold Table). The FSW then controls the ROI cycle by queuing the ROI configurations to the V5 (Fig. 63).

Each ROI is operated for a pre-determined number of integrations. All the spectra collected in this interval are added into a single location in the DDR2 memory. At the completion of the number of integrations, the V5 moves on to the next ROI in the cycle. The new ROI data are sent to a different memory location allowing the FSW time to download the acquired spectrum to the SPARC for further processing.

The FSW uses information in the Aggregation Table to perform additional processing according to as many as four schemas defined in the table. The incoming spectra may be added together for defined periods before it is packetized and labeled with a defined Application IDentification (AID). The spectra are then sent to the spacecraft for storage in the Bulk Data Storage (BDS) prior to downlink. This series of operations is illustrated as a flow chart in Fig. 63 showing the partitioning between the FSW and the V5.

The following sections describe the parameters stored in the tables defining the ROI cycle operation. The relationships of the tables to one another are shown in Fig. 62. The partitioning of ROI acquisition processing between the FSW and the V5 FPGA during ROI Data Cycle operation is shown in Fig. 63.

**ROI Cycle Table.** This is used to define groups of ROIs to run in a cycle, set the Background Thresholds Table to be utilized, enable Ice Grain Mode, and provide acquisition parameters that are not included as part of an ROI definition (e.g., number of integrations, aggregation configuration, warmup iterations). Sixteen cycle tables are stored in memory, each with 64 entries for including ROIs in the cycle. The fields of a single cycle entry are described in Table 26.

For a particular ROI in the ROI Cycle Table, the V5 will iterate through the Timer Steps Table the number of times specified in the 'HV Warmup Iterations' field (further described below in the HVPS Settings Table description) and in the 'Integrations' field of the ROI Cycle Table. Each iteration through the Timer Steps Table results in a single TOF spectrum of 12-bit values from the 1.6 GSample/s science ADC. Once all iterations have been completed and spectra have been collected and integrated by the V5, it will store a single Integrated Spectrum data product to the DDR2 memory and move on to the next ROI in the ROI Cycle Table. The referenced Aggregation Table then provides instructions as to any further co-adding that is required to produce aggregated spectra and provides references to the telemetry routing tables.

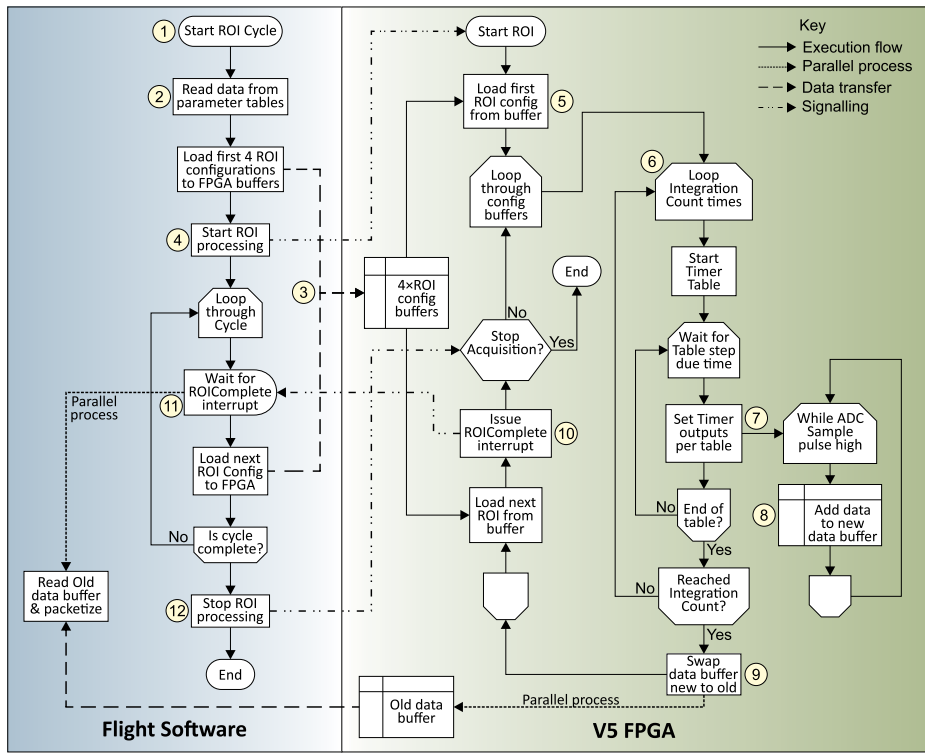


**Fig. 63** The partitioning of ROI acquisition processing between the FSW and the V5 FPGA during ROI Data Cycle operation. Operation starts at (1), top left, with a MASPEX\_EXECUTE\_ROI\_CYCLE command. (2) Reads from the parameter table (Fig. 62). (3) The V5 configuration buffer is loaded, initially with four parameter sets, and then with individual sets as the ROI's are processed. (4) Signals the V5 to start acquiring spectra. (5) Reads the first configuration from the buffer and sets the HVPS voltages. (6) Starts the cycle to collect the required number of spectra. (7) The Timer Table signals when spectral data should be collected. (8) Data is written into one of a pair of data buffers. (9) Once the spectra are collected the data buffer is swapped for the other one. (10) The V5 signals the FSW that the ROI has been completed. (11) Triggering the FSW to load the next configuration to the V5 and to start the parallel data transfer from the old buffer. (12) Once the cycle is complete the FSW signals the V5 to stop, ending the acquisition process

**ROI Definition Table.** This provides a unique ID (used for ground processing and configuration management) and selects the HVPS and Timer Steps Tables that physically define an ROI. Each row in the ROI Definition Table defines a single physical ROI configuration. The ROI Definition Table has provisions for 256 ROI configurations.

**Background Threshold Table.** Backgrounds are measured and reported by the V5 as a count of ADC signals that exceed a threshold value. There are four counters with independent thresholds that can be used to categorize signals of different sizes. Each counter has two states, Armed and Triggered, and two thresholds, Trigger Threshold and Arm Threshold. The thresholds are stored in the Background Threshold Table. At the start of an ROI the counters are all in the Armed state. When a signal exceeds the Trigger Threshold, the counter is incremented, and the state moves to Triggered. The signal must fall below the Arm Threshold to return the counter to the Armed state before another count is possible. This approach ensures that broad signals are only counted as a single signal. The thresholds are checked against blocks of four consecutive ADC datum points to reduce overhead in

**Table 26** ROI Cycle Table Fields

Field name	Description
ROI	An index into the ROI table to specify which ROI configuration to run
Background Thresholds Table	An index into the Background Thresholds table to specify which set of thresholds to use when running the ROI
Ice Grain Mode Enabled	Whether or not to allow the ROI to be interrupted by an Ice Grain Event
Integrations	How many integrations to perform for the ROI each time it is run in the cycle
Aggregation Table	An index into the Aggregation table to specify the aggregation and priority routing of the ROI
HV Warmup Iterations	How many Timer Steps Table iterations to run through before beginning to acquire data. This is used to allow for power supply settling time when the HVPS or Timer configuration changes between ROIs

the V5, so any single value in the block can trigger a count or re-arm the counter, but not simultaneously. This means that it is technically possible to ‘miss’ a second event within a block, but the pulse width from the detector is wide enough to make this unlikely.

Asserting the Background Radiation Enable output in the Timer Steps Table will enable the four counters. The counters are reset at the beginning of each ROI, maintained throughout the duration of the ROI, and stored to DDR2 memory along with the metadata and integrated spectra. A library of 128 Background Threshold tables is stored in memory, each with threshold parameters for the four counters. The ROI Cycle table (Table 26) selects a Background Threshold Table to use for each ROI in the cycle.

Background radiation data are acquired during periods when no ions arrive at the detector, e.g., while ions are lapping between the reflectrons or in the interval between the end of one spectrum and the start of the next.

**HVPS Settings Table.** This provides the HVPS potential settings to configure the supplies for a specific ROI. Each entry in the table includes a voltage to command one or more of the four HV boards. Commands in the selected table are provided to the V5 so that it can apply the configuration when the V5 starts processing the ROI. As one ROI is running, HVPS commands with voltage settings for the next ROI are sent from the V5 to the four HVPS boards. These commands load the new values into registers but do not affect the currently operating voltages. Once the previous ROI finishes and the next ROI begins processing, a final HVPS command is sent to apply the new values to the outputs. It may take from milliseconds to seconds for the HV outputs to stabilize at the new voltages, depending on the supply and direction of voltage change. While this occurs, the V5 performs a configured number of warmup iterations (as provided in the ROI Cycle Table) in which pulsers are operated but no spectra are recorded. The pulsers must be operated during this warmup phase so that the output current of the pulsed supplies does not change when the integrations begin.

In total, 256 HVPS Settings Tables are stored in instrument memory. This allows for a 1:1 mapping between ROI table entries and HVPS Settings Tables, although multiple ROIs could point to the same HVPS Settings Table. Each HVPS Settings Table has 32 HVPS Command entries. Each row in the table describes a single HVPS command that the V5 will send when configuring the system to collect data for an ROI.

**Timer Steps Table.** This contains the timer settings used by the V5 for an ROI configuration. Each entry in the table specifies a duration as a 20-bit value (duration is how long the associated outputs are applied, with 10-ns resolution), and a single bit for each V5 timer

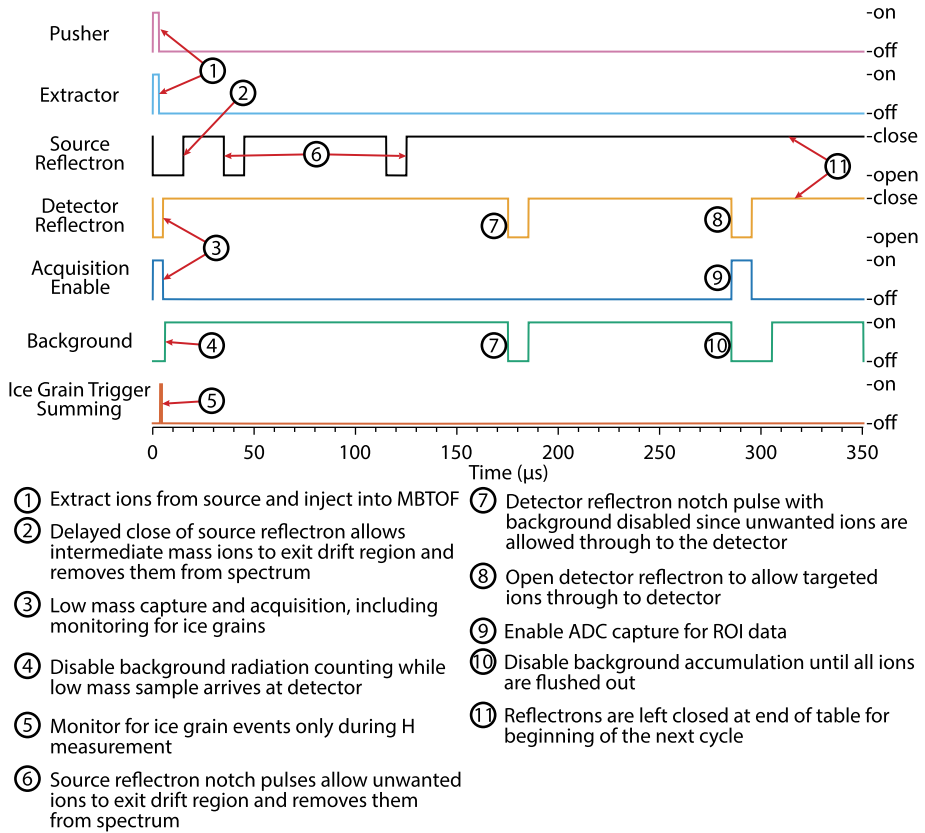


**Fig. 64** Sample Timer Steps Table Output

output (described in Table 27) to specify whether that output should be high (enabled) or low (disabled) for the step duration.

The FSW provides this table to the V5 FPGA, which configures the ROI and drives the timing of ROI data collection. The table controls all the pulsed HVPS outputs (the Pusher, Extractor, Source Reflectron, and Detector Reflectron supplies), determines when ADC data are sampled, when Ice Grain Trigger data are collected, and when background radiation data are collected.

Figure 64 is a schematic of a sample timing sequence output from a single iteration of the Timer Steps Table.

The 256 Timer Steps Tables allow for a 1:1 mapping between ROI table entries and Timer Steps Tables, although multiple ROIs could point to the same Timer Steps Table. Each Timer Steps Table has 64 timer output entries. Each row in the table is comprised of fields that describe a single timer output state that the V5 will apply while executing an ROI capture sequence. Table 27 describes the Timer Steps Table fields (not all fields are shown in the box in Fig. 62).

**Aggregation Table.** This table type specifies how integrated spectra from the V5 should be aggregated and routed. Each entry in the ROI Cycle table points to one of the aggregation tables to specify how a particular ROI should be processed. There are 32 Aggregation Tables stored in memory, each with four entries. Each entry in the table specifies how many aggre-

**Table 27** Timer Steps Table fields

Field name	Description
Dwell Time ( $\mu\text{s}$ )	Duration, in microseconds, over which the output state should be applied. Note that the hardware supports 10 ns resolution, so this value is specified with 0.01 $\mu\text{s}$ resolution.
Ice Grain Trigger	All ADC samples collected while this signal is high are summed together into a single 32-bit value and used as input to the Ice Grain trigger algorithm (this value is compared to the thresholds provided in the Ice Grain Mode Thresholds table). In addition to driving the trigger algorithm, the value is provided as part of the output data product. These values are reported in the MASPEX_SCI_TRIGGER_SERIES packet (Sect. 7.5.1) when the “Send Trigger Series” field of an Aggregation table entry is set. It is expected that this signal will typically follow the first Acquisition Enable output pulse that is used to capture the Hydrogen ROI that is included as part of every ROI configuration. It is provided as a standalone signal so it can be controlled independently if the need arises.
Enable Background	Asserting the Background Radiation Enable output in the Timer Steps Table will enable 4 background radiation counters.
Pusher	Timer output that drives the MBTOF Pusher pulse. When the timer output is high the Pusher HVPS output is active, and when the timer output is low the HVPS output is inactive.
Extractor	Timer output that drives the Extractor pulse. When the timer output is high the Extractor HVPS output is active, and when the timer output is low the HVPS output is inactive.
Source Reflectron	Timer output that drives the Source Reflectron HVPS output. When this timer output is high ions are reflected. When the output is low ions are allowed to pass.
Detector Reflectron	Timer output that drives the Detector Reflectron HVPS output. When this timer output is high ions are reflected. When the output is low ions are allowed to pass.
Acquisition Enable	When this output is high, samples are read from the ADC and collected into the TOF spectrum. When this output is low, data are not stored into the spectrum. This signal may be pulsed multiple times to capture different regions of data during the overall Timer Steps Table iteration. The planned use is that there will be a short pulse at the beginning of the Timer Steps Table to capture straight-through (i.e., no bouncing) low mass ions during every ROI, and then a longer pulse will follow to capture the ROI-specific region after the ions have bounced as configured for mass resolution separation.

gations to perform and what Application Process Identifier (APID) to use for the generated data product.

The four table entries allow multiple aggregation and routing configurations for a single ROI. For example, one could specify an aggregation of one to be routed to the nominal data priority bin, and an aggregation of 100 to be routed to the feedforward priority bin (Sect. 8.4).

In addition, this table includes a setting to specify which of the integrated spectra the Ice Grain Trigger series data should be generated for. If the Send Trigger Series bit is set, then the Ice Grain trigger series data (Table 27) for each individual spectrum that feeds into the aggregate data product will be sent (trigger series data itself is not aggregated).

**Ice Grain Mode Threshold Table.** This provides the thresholds used by the V5 FPGA to determine when to trigger the Ice Grain Mode (IGM). During each iteration of a Timer Steps Table, ADC values are summed together while the Ice Grain Trigger timer output is enabled (see Table 27), and the resulting value is compared to the configured threshold. If the value is greater than the threshold and IGM processing is enabled, the V5 will terminate the current ROI and switch to a set of ROIs designed to characterize ice grain events.

Due to variations in atmospheric density with altitude, the threshold value may need to be changed throughout the flyby. FSW selects the entry based on the current time and writes



**Table 28** List of MASPEX Telemetry packets grouped according to function

Required	Science	Engineering/Housekeeping	Diagnostic
Health & Status	SCI_SPECTRUM_0	RTS Status	DIAG_AXFPGA
ADP Metadata	SCI_SPECTRUM_1	EVENT_MESSAGE	DIAG_V5FPGA
	SCI_SPECTRUM_2	MEM_DUMP	DIAG_HV1
	SCI_SPECTRUM_3	SHK	DIAG_HV2
	SCI_TRIGGER_SERIES_0	FSW	DIAG_HV3
	SCI_TRIGGER_SERIES_1	THERMAL	DIAG_HV4
	SCI_TRIGGER_SERIES_2	PTA	DIAG_MFA
	SCI_TRIGGER_SERIES_3	HV-DAC	DIAG_MFB1
	SCI_TUNE_REPORT	CRYO	DIAG_MFB2
	SCI_THERMAL_COMP	HCV	DIAG_FSW
	SCI_CAL	MFA	DIAG_ASM
		MISC_ADC	
		DAP	
		FCDV	

it to a V5 FPGA register. The V5 will latch the threshold value when it starts processing the next ROI and the threshold will remain in effect for all ROI until FSW provides a new value.

IGM Threshold Tables, consisting of 500 entries each, allow the threshold to be updated every 5 s for about 40 minutes around the closest approach.

## 7.5 Telemetry

During its operation, MASPEX creates an enormous amount of data. In addition to high-resolution mass spectra, a large amount of Health and Status (H&S) information is reported from all parts of MASPEX subsystems. MASPEX produces 38 different types of telemetry packets that can be organized in four groups (see Table 28).

The *Required* packets are sent to the spacecraft. The *Science* packets contain the recorded mass spectra from the ROI cycles and from the IGM (see Sect. 8.5.1), as well as the results from the calibration and tuning of the instrument (see Sect. 8.5.4). *Engineering/Housekeeping* packets contain information about the condition of every part of MASPEX. The *Diagnostic* packets go even further and record all possible information about MASPEX subsystems.

All telemetry packets contain an APID value that identifies the data as being created by MASPEX and identifies the packet type. There are two reserved values to identify the *Required* packets, the remaining 62 possible values are assigned by the MASPEX team to identify packets as necessary.

The *Science* packets in addition contain a 32-bit Accountability Identifier (AID) that is assigned by the MASPEX team. The lowest three bits define the routing of the packet to one of the four BDS bins (see below). The remaining bits identify the specific activity being performed, e.g., data from flyby E15.

All except the *Required* packets are stored by MASPEX in the Flash Memory (Fig. 60). *Science* and *Engineering/Housekeeping* packets are sent to the spacecraft BDS for storage and downlink. Packets are only created when the appropriate subsystem or process is active. The rate of creation varies amongst the packets but is generally no faster than one packet

per second (science packet intervals are controlled by the ROI Cycle). The destination of telemetry packets determines their further processing as follows.

1. **Spacecraft FSW:** The spacecraft uses the H&S packet for onboard autonomy and can be configured to select and subsample specific fields for downlink in the real-time telemetry stream. The Accountable Data Product (ADP) metadata packets provide information to the ground data system about how much data of each APID is being stored in the BDS.
2. **Spacecraft BDS:** Data is routed to the BDS, where it is stored for later downlink. Each instrument has eight bins that can be used. MASPEX has defined four bins for use with science data, feedforward data (Sect. 8.4), opportunistic data, and other data (as defined by the project). The bins each have a different downlink priority, with feedforward being the highest. Engineering packets are normally routed to the BDS nominal data bin.
3. **MASPEX Onboard Flash:** This destination is used as backup storage for data sent to the BDS, and for storage of *Diagnostic* telemetry. Flash routing is further broken into three separate partitions for *Engineering*, *Diagnostic*, and *Science* data; these partitions are circular buffers capable of storing approximately 18, 9, and 11 orbits of data, respectively. When required, data from the flash memory can be transferred to the spacecraft for downlink, e.g., for troubleshooting.

### 7.5.1 Science Packets

MASPEX's primary function is to measure mass spectra, which are stored in SCI\_SPECTRUM\_n packets ( $n = 0$  to 3). Each TOF spectrum is comprised of 12-bit samples from the 1.6 GSample/s science ADC. In normal operations MASPEX acquires TOF spectra in two parts. As described in Sect. 5.4.3, the low mass ions are recorded first, followed by an interval in which the remaining ions lap between the reflectrons to reach the desired resolution before being released to the detector to record the high mass ions.

When enabled in the Timer Steps Table (Sect. 7.4.2), single acquisition spectra are acquired at a rate that would rapidly exceed downlink data volumes. To constrain the data volume, successive acquisitions of the same ROI are coadded (i.e., signals with the same TOF are added together) to produce an integrated spectrum (see Fig. 65). To provide additional flexibility and further reduce data volume, an additional process of coaddition is performed by the FSW to create an aggregated spectrum. The Aggregation Table (see Sect. 7.4.2 and Fig. 62) supports four aggregation schemes simultaneously that can be used to populate the four possible SCI\_SPECTRUM\_n packets. As an example, consider flyby data where SCI\_SPECTRUM\_0 is used to record the integrated spectra without further aggregation; SCI\_SPECTRUM\_1 is used for feedforward data, which coadds data taken ten minutes either side of closest approach to create a single spectrum; and SCI\_SPECTRUM\_2 is used to report any Ice Grain Mode data that may be created during the flyby. Each spectrum is encoded with a different APID and AID and then delivered to different locations in the BDS.

In addition to the TOF data, the following are required for processing each TOF spectrum and are downlinked:

1. The HVPS Settings Table and Timer Steps Tables that define the tuned instrument configuration.
2. Spacecraft clock times for the start and end of each integration and/or aggregation period.
3. The integration and aggregation parameters used in onboard processing.

When Ice Grain Trigger data are enabled, signals in the low mass portion of each spectrum are added together to create a single value representative of the total signal (Fig. 65).

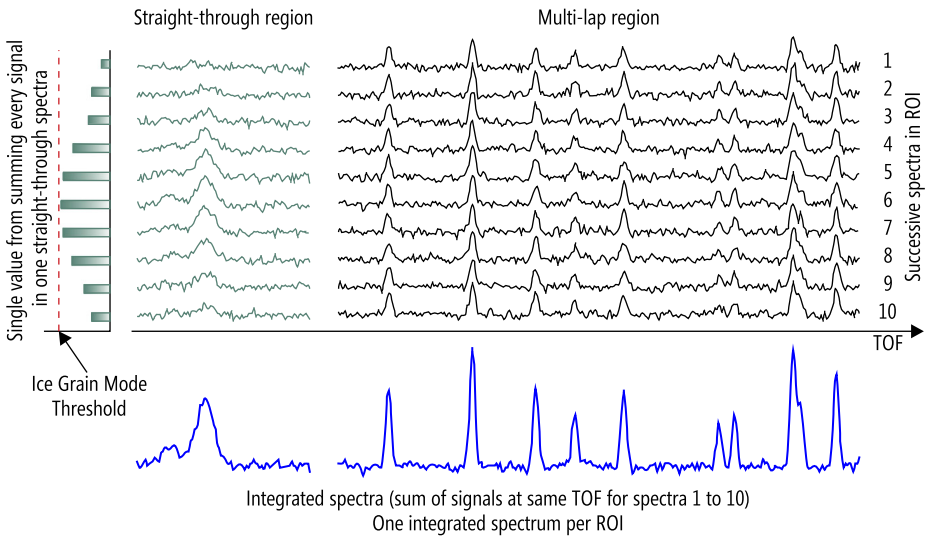


**Fig. 65** How MASPEX calculates integrated spectra and trigger values for Ice Grain Mode

These values are stored as a time series with high temporal resolution in `SCI_TRIGGER_SERIES_n` ( $n = 0$  to 3) packets. The summed values are expected to generally match the increase and decrease in pressure associated with closest approach, but if an ice grain arrives in the inlet, a sudden increase is expected. It is this increase that will trigger the Ice Grain Mode if it exceeds the defined threshold. As with the `SCI_SPECTRUM_n` packets, four APIDs are available to enable routing to different BDS bins. `SCI_TRIGGER_SERIES_n` packets will be generated and routed to a feedforward bin (Sect. 8.4) for twenty minutes around closest approach.

The remaining *Science* telemetry packets (`TUNE_PEAK`, `TUNE_STEP`, `TUNE_DONE`, and `SCI_CAL`) are generated during autotuning and calibration (Sect. 8.5.4).

## 7.5.2 Engineering and Diagnostic Packets

FSW collects engineering information from all instrument components (including hardware, processors, FPGAs, and FSW status) at least once per second. Collected information includes voltage, current, and temperature sensors; mechanism and valve status; ion pressure gauge readings; heater, door, and isolation valve control status; HCV position; HCV and door monitor switch statuses; error reporting; and internal FSW state. Whether or not a specific engineering packet is generated depends on the instrument components that are operating at a given point in time.

1. Engineering/Housekeeping telemetry comprises several packets that each provide insight into one aspect of the overall health and status of the instrument (e.g., HVPS ADC telemetry). Fields here represent a curated subset of all internal status data that are useful for overall trending and monitoring of the instrument and fit within the housekeeping storage and bandwidth allocation.
2. Diagnostic telemetry comprises larger packets that provide detailed insight into system components (e.g., all FPGA register values are reported). These packets are stored in flash memory and are only downlinked on request (e.g., during an anomaly investigation).

## 8 Instrument Operations

### 8.1 Operations Overview

MASPEX operations comprise three main tasks: 1) command the instrument to collect data (Sect. 8.1.1), 2) analyze the data to produce science results and modify future operations (Sect. 8.1.2), and 3) archive the data (Sect. 8.1.3). Figure 66 illustrates the interplay of the operations tasks schematically along with the data flow and its distribution within the MASPEX instrument science data system (Europa Operation Network, EON), the mission ground data system (Europa Clipper GDS), the spacecraft, and the NASA Planetary Data System (PDS) node.

Mission operations follow a cycle beginning with a project level science planning process that results in a Reference Activity Plan (RAP). The MASPEX science and operations teams use the RAP as a guide for the creation of commands and tables for uplink prior to specific operations. This is followed by downlink and analysis of data resulting from the operations, and then by creation of archival products and distribution of data to the feedforward process and the science team. Because the downlink, data analysis and creation of archival products take some time, multiple overlapping cycles occur throughout the mission. There are faster (occurring twice per orbit), closed cycles, that are used to react to new information contained in the latest data. These are called feedforward operations and are discussed in Sect. 8.4.

The cycle of operations varies across the mission. Operations during cruise are less frequent and comprise mainly maintenance operations (Sect. 8.2). The most intense period of operations occurs during the tour (Sect. 8.3) where each orbit requires the generation of new commands for flyby activities and for cryosample analysis.

#### 8.1.1 Commanding Operations

Commanding begins with inputs from the RAP (mission objectives and plans for instrument operations), previous measurements of the European environment, and the science team. EON tools enable the creation of ROI Cycle Tables (Fig. 62) used to command measurements of key gases of interest as well as a wide mass-range survey spectrum to look for the

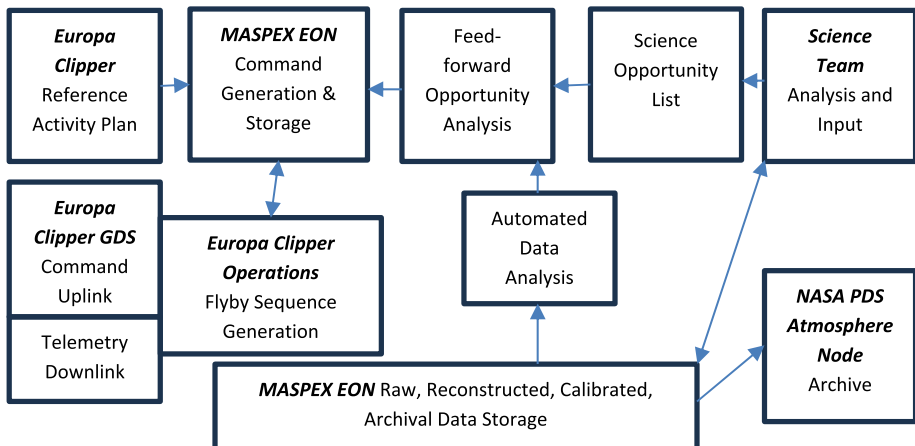


Fig. 66 Schematic depiction of the organization and interplay of the operational tasks for MASPEX

unexpected. Using operations timing information from the Europa Clipper GDS, updates are made to the Epoch Table (Fig. 62) and AST (Sect. 7.4.1) to allow MASPEX to operate new ROI Cycles (see Sect. 7.4.2).

The spacecraft is controlled via Spacecraft Command Sequence files, which enable three forms of control over MASPEX.

1. Maintaining MASPEX at either its survival temperature (when not operating) or operating temperature; this control is exercised solely by the spacecraft (Sect. 5.6.6).
2. The spacecraft FSW can issue a subset of MASPEXs commands (Sect. 7.3) to perform the high-level operations functions of the instrument such as setting the operating mode, running an RTS, activating an AST, or opening the cover.
3. The spacecraft FSW can be commanded to send Instrument Command Files to MASPEX; these are MASPEX commands encoded as CCSDS command packets that can be used to send sequences of MASPEX commands, parameter and table uploads, and RTF file uploads. These files enable the use of the full set of MASPEX commands.

### 8.1.2 Data Analysis

Because of the large volume of data as well as limited downlink rates and connection opportunities, delivery of newly acquired data can take some time. The exception to this is a small quantity of feedforward data (Sect. 8.4), which is downlinked soon after the operation. This enables rapid analysis and a team response to maximize the information gained from new discoveries.

EON processes data once the downlink is completed (Sect. 9.1.2). Initially, data analysis produces raw data products (Sect. 9.1.1), that include TOF spectra and time series data. Once all the data for a particular operation is returned, the Europa Clipper GDS will produce reconstructed SPICE<sup>9</sup> kernels defining the actual spacecraft position and trajectory during the operation. These data are used to recalculate the raw products with the updated spacecraft position information.

Raw products are further processed by applying the instrument calibration data from both ground and in-flight calibration. This creates mass spectra (Sect. 9.1.2) that are the basis for production of gas composition measurements along the trajectory.

Preliminary processing produces QuickLook collaborative data products (Fig. 66, Sect. 9.2) that provide information to the Mission Science Team to aid operational planning.

### 8.1.3 Archiving Operations

The raw TOF spectra, the resulting calibrated spectra, and the derived products such as density, are all delivered to the PDS Atmospheres node for future use by the community. Timescales for the deliveries are detailed in Sect. 9.1.

## 8.2 Cruise Activities

Following launch, MASPEX will perform a test at reduced voltages to ensure the instrument is healthy. Later in the cruise, after the Earth gravity assist maneuver, once the spacecraft

---

<sup>9</sup>Spacecraft, Planet, Instrument, C-matrix, Events – Coined by Dr. Hugh Kieffer, USGS Astrogeology Branch, Flagstaff AZ, circa 1985.

is beyond 2.2 AU outbound to Jupiter, the cover will be opened. The cover was originally planned to be opened after Jupiter Orbit Insertion, but the high outgassing rate of the PEEK detector body (Sect. 6.3.2) makes it necessary to open the cover earlier to allow it to outgas and enable a full test of instrument functionality. Regularly, every three months throughout cruise, the cryotrap will be operated to keep lubricant distributed around the bearings. Concurrent with this operation, a residual gas spectrum will be collected to monitor the cleanliness and progress of the PEEK outgassing.

### 8.3 Tour Activities

Nominal MASPEX orbital operations comprise two science activities and one engineering activity:

1. Flyby Activity: Science measurements aimed at sampling Europa's ambient atmosphere are executed during an encounter. Flyby Activity and expected data products are discussed in Sect. 8.3.1.
2. Cryosample Analysis Activity: Science measurements executed at or near apoapsis when the radiation background is lower than near Europa. Data are acquired from an analysis of gases cryotrapped during the Europa flyby. Cryosample Analysis Activity and expected data products are provided in Sect. 8.3.2.
3. Decontamination Activity: Engineering process that is executed at a point along the trajectory between the Cryosample Analysis and Flyby Activities. Decontamination heaters warm up the instrument, removing contaminants and previously measured species from the mass spectrometer prior to the next flyby.

The detailed steps that comprise each of these activities are shown in the Orbit in the Life diagram (Fig. 67). Expected telemetry for each step is provided in Table 29 and Table 31, and planned archival data products are listed in Table 35.

In addition to the orbital activities, there are two other types of planned activities:

1. Torus Activities: Science measurements aimed at acquisition of data from Europa's ambient torus by cryotrapping torus samples and analyzing them (Sect. 8.3.3).
2. Contamination Characterization Activities: Engineering measurements aimed at characterizing instrument contamination caused by spacecraft outgassing (Sect. 6.5). Data are collected by cryotrapping ambient gas over a 20-hour period while in a similar radiation environment to what is observed during a Europa flyby, but far from any atmosphere.

The Flyby, Cryosample Analysis, Torus, and Contamination Characterization activities are commanded by spacecraft FSW, which warms up MASPEX to operating temperature and then turns its power on before activating the AST file that controls MASPEX throughout the activity.

The Decontamination Activity uses spacecraft FSW to turn on the MASPEX decontamination heaters for a fixed interval before turning all heaters off while MASPEX cools down. At the end of cooldown, the heaters are set to survival temperature setpoints. MASPEX remains off throughout the whole process.

Any other engineering activities that are deemed necessary in flight (e.g., anomaly response) are commanded using one of the following methods:

1. Spacecraft FSW turns on the spacecraft-controlled heaters and warms up MASPEX to operational temperature, powers up MASPEX and issues a MASPEX command(s) to execute the necessary operations. This can include executing an RTS.
2. Spacecraft FSW warms up MASPEX to operational temperature, powers up MASPEX and loads an Instrument Command File.

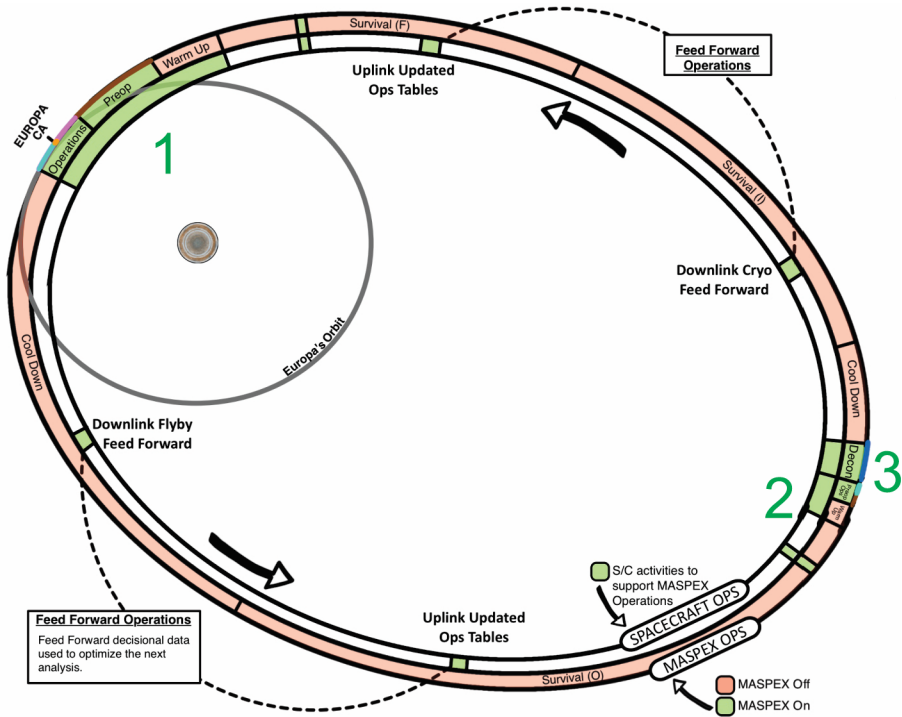


Fig. 67 MASPEX Orbit-in-the-Life Diagram. Green numbers identify activities listed in Sect. 8.3

### 8.3.1 Flyby Activity

The Flyby Activity (Fig. 67) consists of a series of steps (Table 29) that prepare the instrument for science data acquisition, background measurements, auto-tuning to refine high voltage settings and measurement timing, and acquisition of calibration spectra. These steps are followed by three periods of ambient science acquisition, each of which has a corresponding set of ROIs and a set of integration and aggregation parameters that control temporal resolution of data products and data volume:

1. Ambient In-Run Science
2. Ambient Closest Approach Science
3. Ambient Out-Run Science

The Flyby science acquisition is an *in-situ* measurement designed to provide spatial information on the quantity and distribution of atmospheric gases on a maximum geographic scale equal to the lowest flyby altitude (25 km). The timing of the required scale is based on a maximum flyby of 5 km/s resulting in a need to collect data on a 5 s cycle near closest approach (CA) over a total period of ~600 s. The flyby period is defined to be 4 hours long (roughly ±2 hours around periapsis) but the density of gas available outside the central period of the flyby is very small. As such, during the more distant parts of the flyby (In-Run and Out-Run), either the integration periods will be longer, or the integrated spectra produced during those periods will be aggregated for downlink. The maximum integration duration will never be more than 600 s.



**Table 29** Flyby Activity steps and descriptions

Step(s)	<sup>1</sup> Start Time (hh:mm)	Duration (min)	Description
Open HCV	CA-08:25	4	Open HCV to allow ambient gas to enter the instrument
Preop	CA-08:21	277	Prepare instrument for science operations by checking pressure and ramping source filament, HV outputs, and MCPs
Optimize (Tune) / Calibration	CA-03:45	30	Perform autotuning (Sect. 6.5) followed by calibration
Background Measurement	CA-02:45	30	Perform science acquisition prior to entering atmosphere to acquire a background measurement
Ambient + Cryo Trap In-Run	CA-02:00	115	Perform ambient science acquisitions (Table 30) at 30-second resolution and perform cryotrapping prior to closest approach
Ambient + Cryo Trap	CA-00:05	10	Perform ambient science acquisitions (Table 30) at 5-second resolution and perform cryotrapping around closest approach
Closest Approach (CA)			
Ambient + Cryo Trap Out-Run	CA+00:05	115	Perform ambient science acquisitions (Table 30) at 30-second resolution and perform cryotrapping following closest approach
Close HCV	CA+02:00	4	Close HCV to prevent the cryotrapped gas from leaving the instrument once the cryocooler is disabled
Process Data	CA+02:04	8	Process any remaining data prior to shutting down and then execute Shutdown RTS

<sup>1</sup>Start time is relative to the closest approach of Europa.

**Table 30** Flyby Activity ambient science acquisition from the measurement plan

Analysis	Laps	Driving resolution	ROI Start mass	ROI end mass
H <sub>2</sub> and HD concurrent analysis	0	37	0.000	13.000
H <sub>2</sub> O & CH <sub>4</sub> analysis	4	1464	12.000	18.193
Survey region	4		18.000	27.289
C <sub>2</sub> H <sub>4</sub> , C <sub>2</sub> H <sub>6</sub> & HCN analysis	15	7194	26.900	30.106
O <sub>2</sub> analysis	6	3042	30.000	39.660
Survey region	1		39.000	199.066
C <sub>3</sub> H <sub>8</sub> and C <sub>2</sub> H <sub>7</sub> N isobar analysis	19	11120	42.600	46.566

Table 30 shows the baselined measurements for the flyby activity ambient science acquisition. These inputs are used to generate ROI configuration tables (Sect. 7.3.2). ROI tables are configurable in flight and will change throughout the mission as detailed science planning and analysis.

In addition to the baseline ROIs, an additional set of ROIs are generated for the same mass range but designed such that the ions travel one additional lap, referred to as “n + 1” laps. By comparing the output from the n and n + 1 ROIs (Sect. 5.4.3), peaks that have travelled a different number of laps through the instrument can be identified in ground processing.

**Table 31** Cryosample Analysis Activity steps and descriptions

Step(s)	Start Time (hh:mm)	Duration (min)	Description
Preop & Measure/Reduce Pressure	Start near Apoapsis	276	Prepare instrument for science operations by checking/reducing pressure and ramping source filament, HV outputs, and MCPs
Science Data Acquisition	START+04:36	66	Perform cryosample analysis acquisition of survey (Table 32) and targeted (Table 33) ROIs
Open HCV	START+05:42	4	Open HCV to allow any remaining gas to leave the instrument
Pressure Reduction	START+05:46	30	Allow time for gas to continue to leave the instrument
Background Measurement	START+06:16	30	Perform science data acquisition of any remaining or outgassing material
Leak Cal Gas	START+06:46	30	Exercise Mindrum valves to leak calibrant gas into the instrument for use in autotuning and calibration
Optimize (Tune) / Calibration	START+07:16	30	Perform autotuning followed by calibration
Process Data	START+07:46	8	Process any remaining data prior to shutting down and then execute Shutdown RTS

### 8.3.2 Cryosample Analysis Activity

The Cryosample Analysis Activity performed near apoapsis is comprised of a series of steps (Fig. 67 and Table 31) to: check the internal instrument pressure before science acquisition, acquire the data, open the HCV to release the trapped sample, check background, and then tune the instrument.

ROI ranges governing the baselined measurement plan for the Survey and Targeted ROIs are listed in Table 32 and Table 33, respectively. The initial compounds targeted for measurement during the Cryosample Analysis Activity are indicated in Table 33. Prior to the Cryosample Analysis Activity, the feedforward process (Sect. 8.4) will allow this table to be updated throughout the mission to maximize science return.

### 8.3.3 Torus Measurements

During the Torus Activity, MASPEX samples the ring of material distributed along Europa's orbit to further understand the relation between endogenic and exogenic materials in Europa's atmosphere (see Sect. 2.2 for details). To allow sampling of the torus, the instrument boresight is pointed within 25° of the spacecraft velocity direction (gas is thermalized inside the MASPEX inlet so the actual pointing direction does not have to be exact). The activity duration is dependent on the amount of time needed for the spacecraft to traverse the torus and is expected to be 1 to 9 hours long. Three of these activities are planned during the tour, all on orbits where there is either no Europa flyby or where the closest approach altitude for a flyby is greater than 1000 km. Like Europa flybys, this activity includes ambient measurements while also cryotrapping a sample of the torus. Once near apoapsis, a Cryosample Analysis Activity is performed to analyze the cryotrapped sample.

**Table 32** Cryosample Analysis Activity survey measurement plan (mass resolution  $\sim 10,000$ )

ROI	m/z low	m/z high	ROI	m/z low	m/z high	ROI	m/z low	m/z high
1	11.8	12.4	23	33.33	35.67	45	124.77	135.12
2	12.28	12.92	24	35.2	37.7	46	133.05	144.09
3	12.79	13.47	25	37.2	39.87	47	141.88	153.65
4	13.33	14.05	26	39.34	42.19	48	151.3	163.85
5	13.9	14.66	27	41.62	44.66	49	161.34	174.72
6	14.51	15.32	28	44.06	47.31	50	172.04	186.32
7	15.16	16.01	29	46.66	50.14	51	183.46	198.68
8	15.84	16.75	30	49.44	53.17	52	195.64	211.87
9	16.57	17.54	31	52.42	56.41	53	208.62	225.93
10	17.34	18.37	32	55.61	59.87	54	222.46	240.92
11	18.16	19.26	33	59.02	63.58	55	237.23	256.91
12	19.04	20.2	34	62.67	67.55	56	252.97	273.95
13	19.97	21.2	35	66.57	71.8	57	269.76	292.14
14	20.96	22.27	36	70.76	76.36	58	287.66	311.52
15	22.01	23.41	37	75.24	81.24	59	306.75	332.2
16	23.13	24.62	38	80.04	86.46	60	327.11	354.24
17	24.32	25.91	39	85.18	92.07	61	348.81	377.75
18	25.59	27.29	40	90.69	98.07	62	371.96	402.82
19	26.95	28.76	41	96.6	104.52	63	396.65	429.55
20	28.39	30.32	42	102.93	111.42	64	422.97	458.06
21	29.94	31.99	43	109.73	118.83	65	451.04	488.45
22	31.58	33.77	44	117.01	126.71	66	480.97	520.87

### 8.3.4 Contamination Characterization Observations

The accommodation of the payload and the design and building of the instruments and spacecraft resulted in significantly higher contamination deposition in MASPEX's inlet than given in the original MASPEX requirement (Sect. 5.3.1). Contamination modeling and simulation by JPL and the MASPEX team suggested that spacecraft contamination gases, when backscattered from the atmosphere during the flyby, would reach levels that might interfere with characterization of some minor and trace chemical compounds of importance to the MASPEX science investigation. This concern is mitigated operationally by adding three 20-hour activities to acquire cryotrap samples when the spacecraft is at the orbit of Europa, but Europa itself is far away. This sampling scenario will replicate the attitude, illumination, and radiation conditions of the flyby. The long sampling time requested is required to obtain analyzable amounts of contamination when atmospheric backscattering is not operative. The three activities are planned to take place near the beginning, middle, and end of the mission. This spacing of the observations enables monitoring of the modification of the contamination composition by radiation-induced processes.

**Table 33** Cryosample Analysis Activity targeted measurement plan

ROI	Integration time (s)	Analyte	Mass (u)	<sup>1</sup> Resolution (m/ $\Delta$ m)
1	26.2	CO( <sup>13</sup> C)	29	35,800*
1	26.2	N <sub>2</sub> ( <sup>15</sup> N)	29	73,805*
1	26.2	C <sub>2</sub> H <sub>6</sub> ( <sup>2</sup> H)	31.05	25,158*
2	4.67	C <sub>3</sub> H <sub>8</sub> ( <sup>13</sup> C)	45.07	11,699
2	4.67	C <sub>3</sub> H <sub>8</sub> ( <sup>2</sup> H)	45.07	37,120*
2	4.67	C <sub>2</sub> H <sub>6</sub> O	46.04	10,539
3	27.26	CO( <sup>18</sup> O)	30	33,113*
4	8.13	C <sub>2</sub> H <sub>2</sub> ( <sup>2</sup> H)	27.02	23,822
5	57.4	NH <sub>3</sub>	17.03	1154
5	57.4	CH <sub>4</sub> ( <sup>13</sup> C)	17.03	4351
5	57.4	CH <sub>4</sub> ( <sup>2</sup> H)	17.04	11,811
6	5.35	H <sub>2</sub> O	18.01	91
6	5.35	NH <sub>3</sub> ( <sup>15</sup> N)	18.02	2283
6	5.35	NH <sub>3</sub> ( <sup>2</sup> H)	18.03	12,882
7	27.42	H <sub>2</sub> O( <sup>17</sup> O)	19.01	9851
7	27.42	H <sub>2</sub> O( <sup>2</sup> H)	19.02	13,228
8	28.99	C <sub>4</sub> H <sub>8</sub>	56.06	13,048
8	28.99	C <sub>2</sub> H <sub>4</sub> O <sub>2</sub>	60.02	2167
8	28.99	C <sub>5</sub> H <sub>10</sub>	70.08	4630
8	28.99	C <sub>5</sub> H <sub>12</sub>	72.09	16,988
9	22.9	C <sub>3</sub> H <sub>6</sub>	42.05	10,061
9	22.9	CO <sub>2</sub>	43.99	143
9	22.9	C <sub>3</sub> H <sub>8</sub>	44.06	10,996
9	22.9	C <sub>2</sub> H <sub>7</sub> N	45.06	10,424
9	22.9	C <sub>4</sub> H <sub>10</sub>	58.08	10,305
9	22.9	C <sub>8</sub> H <sub>18</sub>	114.14	690
10	1756.9	Ar( <sup>40</sup> Ar)	39.96	2312
10	1756.9	C <sub>3</sub> H <sub>4</sub>	40.03	9392
11	7.95	C <sub>2</sub> H <sub>2</sub>	26.02	110
11	7.95	CO	27.99	2846
11	7.95	N <sub>2</sub>	28.01	2846
11	7.95	C <sub>2</sub> H <sub>4</sub>	28.03	6948
11	7.95	C <sub>2</sub> H <sub>6</sub>	30.05	6948
12	1.56	CH <sub>4</sub> O	32.03	7427
13	53.01	CH <sub>4</sub>	16.03	1464
13	53.01	H <sub>2</sub> O( <sup>18</sup> O)	20.01	96

\*Determined using peak deconvolution

<sup>1</sup>Each row gives the required resolution (10% valley definition) for the analyte, the largest resolution in each ROI determines the resolution of the ROI.

## 8.4 Feedforward Data and Operations

### 8.4.1 Feedforward Operations

The feedforward operations process is to be performed over the span of three days and will be repeated twice per orbit, once between the Flyby Activity and the associated Cryoscience Activity, and again between the Cryoscience Activity and subsequent Flyby Activity (Fig. 67).

During the first day of operation after the flyby, EON automatically imports feedforward data from the Europa Clipper GDS. The data are processed by the data analysis pipeline to identify observed mass peaks and associated species. The science decision-making tool (Sect. 3.2) uses a database of geochemical tracers (Sect. 3.1.1), and biosignature fragments (Sect. 3.1.2), to identify which of the tracers and biosignature fragments may be present.

On the second day of feedforward operations, the output of the science decision-making tool is reviewed by the MASPEX Science Team. The task of the team is to prioritize possible measurements based on guidance from the mission's Thematic Working Groups to create a short-list that can be accommodated during the next flyby or cryotrap operation.

For the third day of the process, the science data analysis tool will create a list of the target compounds and calculate the optimum ROI cycles. This analysis will take account of the contamination information, so that heavily contaminated fragment masses are avoided. The uplink products are then prepared for the new analysis. The MASPEX Operations Team generates, reviews, and tests updated operations tables and associated commanding files and then delivers them to the Europa Clipper Mission Operations System for uplink.

Feedforward operations are intended to optimize the data return from the next data collection period, so the data from the flyby is used to optimize the analysis of the cryosample, and vice versa. However, the characteristics of the two activities are very different. The flyby data, due to its higher temporal/spatial cadence, has a limited mass range and dynamic range so that only the major species will be visible. On the other hand, the cryosample data covers the full instrument mass range at medium resolution (Table 32) and therefore contains information for many more species. Thus, the objective of the post-flyby and post-cryo feedforward analysis is different. Feedforward data from a flyby will require the identification of only major species that are then linked through the feedforward library to related compounds that are obscured by lack of mass resolution or signal to noise but are required for determination of macro-observables such as formation temperature, pH, oxidation state, and possible biomarkers. Feedforward data from a cryosample might involve the re-measurement of major species at higher resolution on the next flyby due to their possible scientific significance.

### 8.4.2 Feedforward Data

The reduced set comprised of feedforward data (see Sect. 6.5) is intended to provide a timely overview of recently acquired data following flyby and apoapsis measurements. Once downlinked, this information will be analyzed in the feedforward operations process to inform updates to measurement settings for subsequent sample analyses. Table 34 provides a summary of the expected feedforward data set and associated downlink data volume.

## 8.5 Operational Functions

There are instrument functions that must be performed to ensure safe and effective operation. Other functions include gathering science data and performance information such as autotune parameters or in-flight calibration required for data analysis.

**Table 34** Feedforward data descriptions and data volumes

	Type of Data	Description	Spectra per Orbit	Repeat for n + 1 laps	Data Volume (Gbit)
Flyby	Aggregated Background Spectra	Background data aggregated over 30 minutes used to classify peaks in the Aggregated Closest Approach Spectra as ambient or background.	1	Y	0.13
Flyby	Tuning/Mass Scale Determination	Tuning and Mass Scale Determination information used to convert data from a mass to a TOF scale.	1	Y	0.07
Flyby	Aggregated Closest Approach Spectra	A single summary spectrum that is the product of aggregating data acquired while the spacecraft is passing through Europa's atmosphere (CA $\pm 5$ minutes). This data provides a first look at compositional information on Europa's atmosphere, but it is not spatially resolved.	1	Y	0.01
Flyby	Ice Grain Trigger Time Series Data	Time series data acquired each extraction for CA $\pm 10$ min during the Flyby Sequence which provides a first look at the spatial distribution of Europa's atmosphere, including information that could be indicative of a plume.	-	-	0.04
Flyby	Ice Grain Mode Spectra	A single summary spectrum that is the product of aggregating data acquired while the instrument is operating in Ice Grain Mode which is enabled when the Ice Grain Trigger Time Series Data increases above a threshold level, indicative of measuring an ice grain.	1	Y	0.01
	Flyby Feedforward Subtotal:				0.26
Cryo	Aggregated Background Spectra	Background data aggregated over 30 minutes used to classify peaks in the Aggregated Cryo Survey Spectra as ambient or background.	1	Y	0.13
Cryo	Tuning/ Mass Scale Determination	Tuning and Mass Scale Determination information used to convert data from a mass to a TOF scale.	1	Y	0.05
Cryo	Aggregated Cryo Survey Spectra	A single summary spectrum that is the aggregation of the Cryosample Analysis Activity's observed survey spectra.	1	Y	0.12
	Cryo Feedforward Subtotal:				0.30
	Feedforward Total:				0.55

### 8.5.1 Ambient Science Acquisition

Ambient science data acquisition is performed with the HCV open, allowing Europa's atmosphere to enter and be measured. While in this mode, a set of ROIs are cycled through every

five seconds, providing spatial resolution of at least 25 km of spacecraft ground track. Ambient science data are acquired simultaneously with cryotrapping of a sample for analysis at apojoove.

While performing ambient science acquisitions, Ice Grain Mode, a special sub-mode, can be enabled to respond to a high gas density ice grain event. The ice grain will be detected over the low-mass region ( $<12$  u) collected with each ROI spectrum. This low mass region is summed and compared to a set of thresholds in the operations tables to determine if the Ice Grain Mode should be triggered (Fig. 65). A separate set of ROIs, organized into an Ice Grain ROI Cycle Table (Sect. 7.4.2), is configured for Ice Grain Mode. These ROIs are designed to capture the volatile decay products found in the ice. Ice Grain Mode, when triggered, works by terminating and discarding the current integration cycle and executing the Ice Grain ROI Cycle. After the Ice Grain ROI Cycle completes, the previous integration is resumed.

### 8.5.2 Cryosample Analysis Acquisition

At the end of the cryocooler operation during ambient science acquisition, the HCV is closed and the cryocooler is disabled, releasing the trapped gas into the MBTOF. At a future time (e.g., near apoapsis where radiation noise is less), MBTOF generates spectra that are analyzed to determine the composition of the trapped sample.

### 8.5.3 Automated Pressure Check and Reduction

To apply high voltages safely without risk of arcing and potential damage to the instrument, the pressure within the instrument must be below  $1.3 \times 10^{-6}$  hPa. The FSW includes an internal algorithm that iteratively checks the pressure and releases stored gas as necessary to obtain a safe operating pressure (see Fig. 68). This function is executed prior to ramping up high voltage. Any RTS that includes the command to execute the pressure algorithm also includes a conditional wait that will halt sending subsequent commands until successful completion of this algorithm.

### 8.5.4 Auto-tuning and Calibration

MASPEX is extremely sensitive to changes in potentials that affect ion TOF, peak widths, and intensities of analyte species. Given that power supplies and detectors are known to change with age and operating temperature, coupled with the Jovian radiation environment that exacerbates those effects, it was necessary to design the instrument with the ability to optimize its own performance. Optimization via auto-tuning (Sect. 6.5) will be performed immediately prior to measurements made before a flyby and following cryosample analysis acquisition (calibration must necessarily occur after the measurement to avoid destroying the trapped sample).

Performance optimization is achieved through tuning and calibration, which together optimize the operating potentials of the instrument, adjust the timings of the ROI windows to re-align with the desired mass ranges, and adjust the gain on the detector to ensure that the correct dynamic range can be reached.

Once auto-tuning has been completed, in-flight calibration takes place. MCP operation is particularly critical because the detector can be damaged by high beam currents. Under these circumstances it is desirable to lower the detector gain so that the most intense signals remain on scale. The opposite is true for the cryotrap sample where we are trying to measure trace species such as argon and gain must be increased.



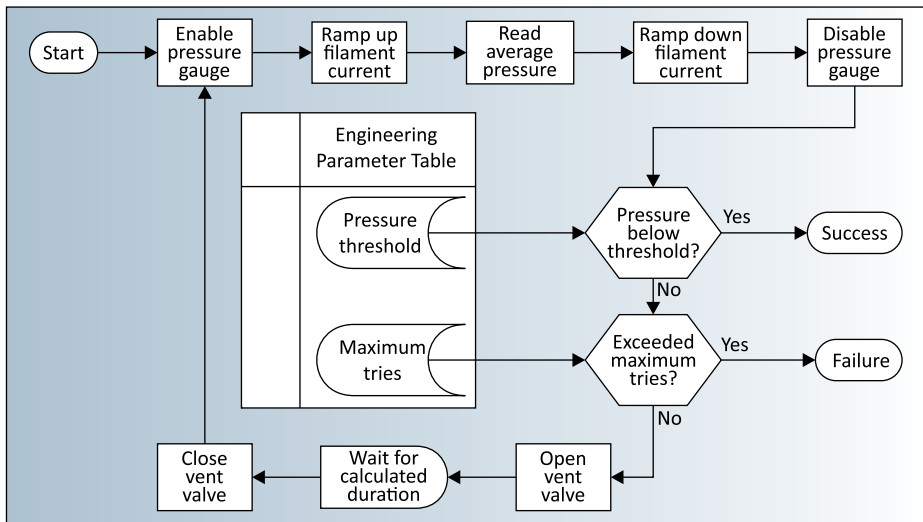


**Fig. 68** MASPEX Automated Pressure Check and Reduction Algorithm

**Table 35** PDS Archival Data Products

PDS4 Level	Description	Processing Duration	Estimated Mission Archive Volume (Gbits)
Raw	Coadded TOF Spectra, Time Series Data	1 week	10,000
Calibrated	Calibrated Composite Mass Spectra	6 months	10,000
Derived	Compound Abundances	6 months	3125
Raw	Engineering Data	1 week	

## 9 Data Products

The data acquired during instrument flight operations (Sects. 8.3 and 8.4) are downlinked and processed by EON, which generates raw coadded TOF spectra, raw ice grain trigger timeseries data, calibrated composite mass spectra, and derived compound abundances. Other products include raw engineering data used for health and safety monitoring. All of these data products are submitted to the Planetary Data System (PDS). Additionally, EON generates QuickLook collaborative data products for the Europa Clipper Science Team, which are not archived at the PDS because they are ultimately superseded by higher quality archival data products.

### 9.1 PDS Archival Data Products

MASPEX data are organized by PDS-defined data processing levels. Data products include raw TOF spectra and time series, calibrated mass spectra, and derived compound abundances. Instrument engineering data are also included with the raw data archive. Table 35 is a summary of these data products.

The raw and calibrated data products will be delivered to the Europa Clipper GDS and to the PDS Atmosphere’s node within 6 months of receiving the downlinked data.

### 9.1.1 Raw Data Products

Raw data products are generated by extracting the information from the binary CCSDS science and engineering packets and organizing it, along with ancillary position and attitude information from SPICE kernels, into comma-separated values files.

Coadded TOF Spectra received in `SCI_SPECTRUM` packets provide the primary science data product for MASPEX. These packets contain integrated and aggregated (including feedforward) spectra that are produced independently of whether the instrument is performing in-flight calibration, nominal gas acquisition, or ice grain analysis.

In addition to the TOF spectra, the following are downlinked, included in the raw data product, and used for processing each TOF spectrum.

1. The tuned ROI HV and Timer Steps Tables that define the instrument configuration.
2. Spacecraft clock times for the start and end of each integration and/or aggregation period.
3. Integration and aggregation parameters used in onboard processing.

**Time Series Data.** The Ice Grain Trigger data (Sect. 7.5.1) will be generated for closest approach  $\pm 10$  minutes at a rate of 1 kHz. Once downlinked, these timeseries data are organized into PDS raw archive files, each covering a 5-minute period.

**Engineering Data.** Diagnostic data, if downlinked (Sect. 7.5.2), are also processed into raw data products via EON and archived in PDS along with the science data within six months of downlink. These data are used to provide context for the instrument's health, performance, and activities throughout the mission.

### 9.1.2 Calibrated and Derived Products

Once raw archive products are produced, the automated data analysis pipeline in EON then incorporates both ground calibration data (also stored in EON) and flight calibration data (raw archive product) into the processing that converts TOF spectra to mass spectra. The calibrated spectra are then used to identify chemical species and their abundances. The processing steps performed by the data analysis pipeline are detailed in Fig. 69.

In-flight calibration data resulting from auto-tuning along with ROI-specific ancillary data tables will be utilized by the pipeline on a per-spectrum basis to set parameters related to the expected ion peak shape and TOF-to- $m/z$  scale. Ground calibration data will be used by the pipeline as the reference for potential ions, ion presence likelihood, and the EI spectra library of compounds from which to search and fit.

The first task of the pipeline is signal processing of the raw product TOF spectra. This task prepares the TOF spectra signal for further analysis by setting the baseline signal level, determining noise characteristics, smoothing the signal, detecting and analyzing spectral features (e.g., ion peaks), and diagnosing artifacts. This task is necessary for summarizing the TOF spectra's signal quality and filtering its spectrum into a set of ion signal peaks that can be passed forward in the pipeline for reliable analyses.

The second task is to calibrate the  $m/z$  scale of the TOF spectra. Initial parameters for this conversion from TOF (see Sect. 6.4.1) will be utilized to set a preliminary  $m/z$  scale. Under suitable conditions, a refined  $m/z$  scale can be determined by estimating updated TOF-to- $m/z$  model parameters using the ion signal peaks detected from this and related TOF spectra. The list of detected ion signal peaks will be filtered into a subset of "calibration quality" peaks (high signal-to-noise, isolated peaks conforming well to the expected shape for a unique ion species). These will then be compared to known ions that are reliably present in the sampled environment to assign any of these ions to the observed signal peaks. If enough

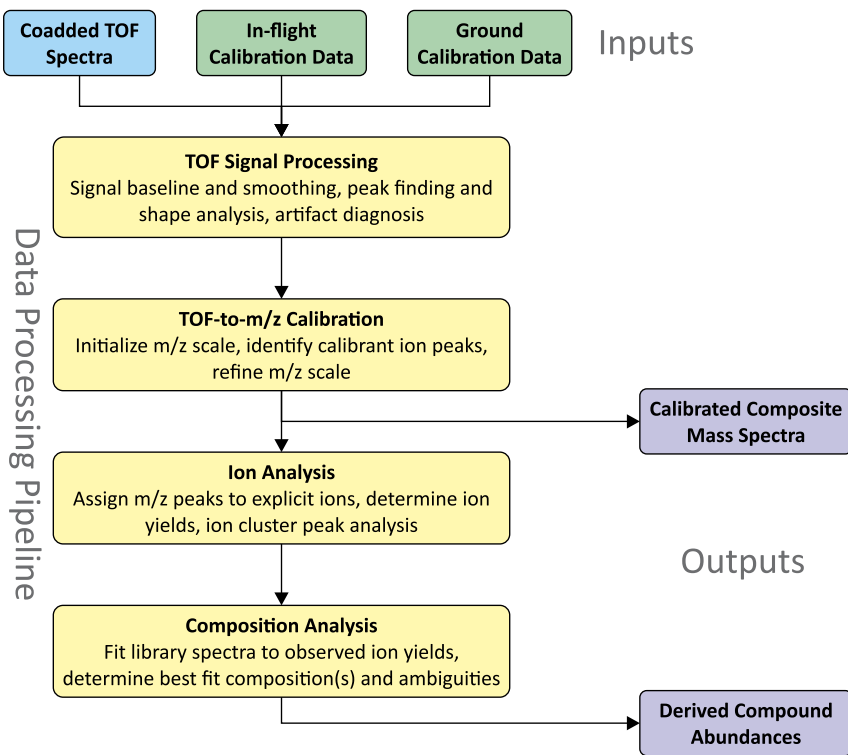


**Fig. 69** MASPEX Data Processing Pipeline from Raw TOF Spectra to Calibrated Mass Spectra and Derived Data Products

ion assignments can be made, then an updated set of TOF-to- $m/z$  model parameters will be estimated, and the performance will be determined by comparing the calculated exact  $m/z$  to the known ion  $m/z$ . This task ultimately results in spectra from which the Calibrated Composite Mass Spectra data products are produced.

The third task in the pipeline is an analysis of the mass spectra. This task performs ion assignment and ion yield determination across the full  $m/z$  spectrum, making use of the detected ion signal peaks, expected ion peak shape, and uncertainty in the  $m/z$  scale. Ground calibration data will provide reference information in the form of the potential ion list (from which to search and assign to signal peaks) and ion presence likelihood (e.g.,  $\text{CH}_4^+$  is more likely than  $\text{CH}_2\text{D}^+$ , which is relevant when the mass resolution of a spectrum would not separate these two ions). This task will report which signal peaks may be attributed to well-separated unique ions and which signal peaks may be attributed to an unseparated cluster of different ions. Upper limit ion yields will also be set for any unassigned ions of interest based on the signal background, noise, and potential interference with other signal features (e.g., artifacts). The result of this ion analysis is a set of ions, and their ion intensity along with metrics relating their detection and assignment confidence, uncertainty in intensity, and signal interference. Proper data handling in this task is crucial to determining the presence of individual compounds in the next task.

The fourth task in the pipeline is composition analysis of the mass spectra. This task will utilize the results of the ion analysis in the previous task and the reference library of compound EI spectra from ground calibration to determine the chemical composition of

**Table 36** MASPEX QuickLook Collaborative Data Products

Description	Requesting Thematic Working Group	Processing Duration
Approximate composition of flyby ambient gas	Geology	1 week
Approximate composition of cold-trapped sample	Geology	1 week
Time series of H <sub>2</sub> O/O <sub>2</sub> ratio	Composition	1 week

the mass spectra in the form of detected and likely compounds and their abundances. All relevant compounds will be fit to the ion analysis results and absolute upper limit abundances will be deduced along with fit metrics. These compounds will be filtered into a subset of potentially present compounds which have suitable fit characteristics (i.e., can contribute significantly to detected ion yields, important fragment ions not missing from spectrum data). This subset of potentially present compounds will then be fit as groups to the ion analysis results of the full spectrum to compare and determine the best fit composition(s) of compounds, their abundances, and abundance uncertainties. Information on composition ambiguity will be derived as well as ion abundances unexplained by fits to the reference library spectra. Multivariate techniques such as factor analysis may be used for related series of spectra (e.g., from a Europa flyby) to determine the most likely present compounds and their abundances. The results of this task will feed into the Derived Compound Abundances data product.

## 9.2 QuickLook Collaborative Data Products

In addition to PDS archival data products, EON will generate QuickLook Collaborative Data Products for the Europa Clipper Thematic Working Groups within two weeks of receiving the relevant data. Information about composition or ratios of compounds requires the full flyby or cryosample analysis data set. These preliminary products, summarized in Table 36, are delivered to the Europa Clipper GDS for use by the science team but will not be archived in the PDS.

## 10 Conclusion

This paper serves as an introduction to the science motivation, measurement objectives, instrument design, and measured performance of the MASPEX investigation as a tool for exploring the habitability of Europa. The novel instrument used to carry out these goals is a high-performance time-of-flight mass spectrometer that of necessity is complex and was equally demanding to build, test, and calibrate. In this paper we have described the spectrometer in a way that lets the informed reader understand the principles behind the design and how they were implemented. We have described the instrument's optical design, discussed its functions as an integrated system, and its operation in flight. Finally, we included examples of calibration data to show that MASPEX performance exceeds mission requirements and to introduce future users to expectations for data returned from Europa.

### Glossary

AC	Alternating Current
ADC	Analog to Digital Converter

AID	Accountability Identifier
APID	Application Process Identifier
AST	Activity Sequence Table
ATP	Adenosine TriPhosphate
BDS	Bulk Data Storage
CA	Closest Approach
CAD	Computer Aided Design
CAPS	CAssini Plasma Spectrometer
CCSDS	Consultative Committee for Space Data Systems
CGS	Calibration Gas System
CHNOPS	Carbon, Hydrogen, Nitrogen, Oxygen, Phosphorus, Sulphur
COSMIC	Comet Outgassing Simulator for MASPEX Instrument Calibration
CTP	Cytidine TriPhosphate
DAP	Data Acquisition and Processing
DC	Direct Current
DDR2	Double Data Rate Version 2
DFMS	Double Focusing Mass Spectrometer
DNA	DeoxyriboNucleic Acid
DR	Dynamic Range
EBOX	Electronics BOX
ECC	Error Correction Code
ECM	Europa Clipper Magnetometer
EI	Electron Ionization
EM	Engineering Model
EMG	Exponentially Modified Gaussian
EMI/EMC	ElectroMagnetic Interference/ ElectroMagnetic Compatibility
EON	Europa Operation Network
FC	Faraday Cup
FCE	Faraday Cup Electrometer
FEE	Front End Electronics
FET	Field Effect Transistor
FM	Flight Model
FOV	Field Of View
FPGA	Field-Programmable Gate Array
FSW	Flight SoftWare
FWHM	Full-Width Half-Maximum
GDS	Ground Data System
GIRE	Galileo Interim Radiation Electron
GIS	Gas Inlet System
GSE	Ground Support Equipment
GTP	Guanosine TriPhosphate
H&S	Health & Status
HCV	High-Conductance Valve
HCVA	High Conductance Valve Actuator
HF	High Frequency
HOPA	High-output Paraffin Actuator
HV	High Voltage
HVPS	High Voltage Power Supply
IGM	Ice Grain Mode

INMS	Ion Neutral Mass Spectrometer
IVA	Isolation Valve Assembly
JPL	Jet Propulsion Laboratory
LPSAFE	Low-Power / Safe Mode
LVDS	Low Voltage Differential Signaling
LVPS	Low Voltage Power Supply
MASPEX	MASS Spectrometer for Planetary Exploration
MBTOF	Multi-Bounce Time-Of-Flight
MCP	MicroChannel Plate
MF-A	Multi-Function board-A
MF-B1	Multi-Function Board B1
MF-B2	Multi-Function Board B2
MFC	Mass Flow Controller
MISE	Mapping Imaging Spectrometer for Europa
MLI	Multi-Layer Insulation
MO1	MASPEX Objective 1
MO2	MASPEX Objective 2
MRAM	Magnetoresistive Random Access Memory
MS	Mass Spectrometer
NASA	National Aeronautics and Space Administration
NEG	Non-Evaporable Getter
NIST	National Institute of Standards and Technology
PAH	PolyAromatic Hydrocarbons
PCB	Printed Circuit Board
PDS	Planetary Data System
PEEK	PolyEther Ether Ketone
PIMS	Plasma Instrument for Magnetic Sounding
PPM	Pyrrhotite-Pyrite-Magnetite
PROM	Programmable Read-Only Memory
PRT	Platinum Resistance Thermometer
PWB	Printed Wiring Board
RAP	Reference Activity Plan
REASON	Radar for Europa Assessment and Sounding: Ocean to Near-surface
RMAP	Remote Memory Access Protocol
ROI	Region Of Interest
RTOF	Reflectron Time-Of-Flight
RTS	Real Time Sequence
SD	Standard Deviation
SPARC	Scalable Processor ARChitecture
SPICE	Spacecraft, Planet, Instrument, C-matrix, Events
SRAM	Static Random Access Memory
SUDA	Surface Dust Analyzer
TAC	Thermalizing AnteChamber
TOF	Time-Of-Flight
UVS	UltraViolet Spectrograph
V5	Xilinx V5 FPGA
VCS	Vacuum Cover System
VHF	Very-High Frequency

**Acknowledgements** The MASPEX high-resolution mass spectrometer was developed in response to the needs of NASA's planetary science programs. Beginning in 2003 our work on the design and prototyping of MASPEX was supported by grants totaling over \$2.8 M from Southwest Research Institute's Internal Research Program, and by its Center for Excellence in Analytical Mass Spectrometry (CEAMS). Development efforts were also aided by Discovery Program, phase A and technology development funding; the Instrument Concepts for Europa Exploration program; by Clipper's first Project Manager Barry Goldstein; and the Jet Propulsion Laboratory. Our participation in the Cassini- Huygens Ion Neutral Mass Spectrometer, led by Hasso Niemann at NASA Goddard Space Flight Center, was critically important to the science development of MASPEX. We also acknowledge contributions made by the many scientists and engineers who assisted in the development of this very complex instrument including John Roberts, Robert Bolanos, Charlie Nunez, David Ruggles, Anthony Botting, Robert Rendon, and Jacob Grimes. Finally, we thank the European institutions Aix-Marseille Université, Origins Institute, Marseille, France, and Imperial College London, Department of Earth Science and Engineering, London, UK for their continued support. This work was supported by NASA through the Europa Clipper Project via the Jet Propulsion Laboratory, California Institute of Technology, under NASA-JPL subcontract 1531256.

## Declarations

**Competing Interests** The authors declare that they have no conflict of interest.

**Open Access** This article is licensed under a Creative Commons Attribution 4.0 International License, which permits use, sharing, adaptation, distribution and reproduction in any medium or format, as long as you give appropriate credit to the original author(s) and the source, provide a link to the Creative Commons licence, and indicate if changes were made. The images or other third party material in this article are included in the article's Creative Commons licence, unless indicated otherwise in a credit line to the material. If material is not included in the article's Creative Commons licence and your intended use is not permitted by statutory regulation or exceeds the permitted use, you will need to obtain permission directly from the copyright holder. To view a copy of this licence, visit <http://creativecommons.org/licenses/by/4.0/>.

## References

- Abplanalp D et al (2010) An optimised compact electron impact ion storage source for a time-of-flight mass spectrometer. *Int J Mass Spectrom* 294(1):33–39. <https://doi.org/10.1016/j.ijms.2010.05.001>
- Alexander CMOD et al (2012) The provenances of asteroids, and their contributions to the volatile inventories of the terrestrial planets. *Science* 337(6095):721–723. <https://doi.org/10.1126/science.1223474>
- Altwegg K et al (2017) Organics in comet 67P - a first comparative analysis of mass spectra from ROSINA-DFMS, COSAC and Ptolemy. *Mon Not R Astron Soc* 469:S130–S141. <https://doi.org/10.1093/mnras/stx1415>
- Amend JP et al (2011) Catabolic and anabolic energy for chemolithoautotrophs in deep-sea hydrothermal systems hosted in different rock types. *Geochim Cosmochim Acta* 75(19):5736–5748. <https://doi.org/10.1016/j.gca.2011.07.041>
- Ayet San Andrés S et al (2019) High-resolution, accurate multiple-reflection time-of-flight mass spectrometry for short-lived, exotic nuclei of a few events in their ground and low-lying isomeric states. *Phys Rev C* 99(6):064313. <https://doi.org/10.1103/PhysRevC.99.064313>
- Balsiger H et al (2007) Rosina - Rosetta orbiter spectrometer for ion and neutral analysis. *Space Sci Rev* 128(1–4):745–801. <https://doi.org/10.1007/s11214-006-8335-3>
- Běhounková M et al (2021) Tidally induced magmatic pulses on the oceanic floor of Jupiter's moon Europa. *Geophys Res Lett* 48(3):e2020GL090077. <https://doi.org/10.1029/2020GL090077>
- Bierson CJ, Nimmo F (2020) Explaining the Galilean satellites' density gradient by hydrodynamic escape. *Astrophys J Lett* 897(2):L43. <https://doi.org/10.3847/2041-8213/aba11a>
- Blase RC et al (2015) Microchannel plate detector detection efficiency to monoenergetic electrons between 0.4 and 2.6 MeV. *IEEE Trans Nucl Sci* 62(6):3339–3345. <https://doi.org/10.1109/TNS.2015.2488481>
- Blase RC et al (2017) Microchannel plate detector detection efficiency to monoenergetic electrons between 3 and 28 keV. *Rev Sci Instrum* 88(5):053302. <https://doi.org/10.1063/1.4983338>
- Blase RC et al (2018a) Review of measured photon detection efficiencies of microchannel plates. *IEEE Trans Nucl Sci* 65(12):2839–2851. <https://doi.org/10.1109/TNS.2018.2877356>
- Blase RC et al (2018b) Microchannel plate detector efficiency to monoenergetic photons between 0.66 and 20 MeV. *IEEE Trans Nucl Sci* 65(4):980–988. <https://doi.org/10.1109/TNS.2018.2806319>



- Bockisch C et al (2018) Kinetics and mechanisms of dehydration of secondary alcohols under hydrothermal conditions. *ACS Earth Space Chem* 2(8):821–832. <https://doi.org/10.1021/acsearthspacechem.8b00030>
- Bouquet A et al (2015) Possible evidence for a methane source in Enceladus' ocean. *Geophys Res Lett* 42(5):1334–1339. <https://doi.org/10.1002/2014GL063013>
- Bouquet A et al (2019) The role of clathrate formation in Europa's ocean composition. *Astrophys J* 885(1):14. <https://doi.org/10.3847/1538-4357/ab40b0>
- Bowden SA et al (2009) Survival of organic compounds in ejecta from hypervelocity impacts on ice. *Int J Astrobiol* 8(1):19–25. <https://doi.org/10.1017/S147355040900442X>
- Brockwell TG et al (2016) The mass spectrometer for planetary exploration (MASPEX). In: IEEE aerospace conference proceedings. <https://doi.org/10.1109/AERO.2016.7500777>
- Brown ME (2001) Potassium in Europa's atmosphere. *Icarus* 151(2):190–195. <https://doi.org/10.1006/icar.2001.6612>
- Brown ME, Hand KP (2013) Salts and radiation products on the surface of Europa. *Astron J* 145(4):110. <https://doi.org/10.1088/0004-6256/145/4/110>
- Carlson RW et al (2009) Europa's surface composition. In: Pappalardo RT, McKinnon WB, Khurana KK (eds) *Europa*. University of Arizona Press, Tucson, pp 283–328. <https://doi.org/10.2307/j.ctt1xp3wdw.18>
- Cassidy TA et al (2009) Trace constituents of Europa's atmosphere. *Icarus* 201(1):182–190
- Cassidy TA et al (2013) Magnetospheric ion sputtering and water ice grain size at Europa. *Planet Space Sci* 77:64–73. <https://doi.org/10.1016/j.pss.2012.07.008>
- Chiavari G, Galletti GC (1992) Pyrolysis—gas chromatography/mass spectrometry of amino acids. *J Anal Appl Pyrolysis* 24(2):123–137. [https://doi.org/10.1016/0165-2370\(92\)85024-F](https://doi.org/10.1016/0165-2370(92)85024-F)
- Chiavari G et al (1998) Characterisation of standard tempera painting layers containing proteinaceous binders by pyrolysis (/methylation)-gas chromatography-mass spectrometry. *Chromatographia* 47(7):420–426. <https://doi.org/10.1007/BF02466473>
- Cleeves LI et al (2014) The ancient heritage of water ice in the solar system. *Science* 345(6204):1590–1593. <https://doi.org/10.1126/science.1258055>
- Collins G, Nimmo F (2009) Chaotic terrain on Europa. In: Pappalardo RT, McKinnon WB, Khurana KK (eds) *Europa*. University of Arizona Press, Tucson, pp 259–282. <https://doi.org/10.2307/j.ctt1xp3wdw.17>
- Court RW et al (2006) The alteration of organic matter in response to ionising irradiation: chemical trends and implications for extraterrestrial sample analysis. *Geochim Cosmochim Acta* 70(4):1020–1039. <https://doi.org/10.1016/j.gca.2005.10.017>
- Cruse AM, Seewald JS (2006) Geochemistry of low-molecular weight hydrocarbons in hydrothermal fluids from Middle Valley, northern Juan de Fuca Ridge. *Geochim Cosmochim Acta* 70(8):2073–2092. <https://doi.org/10.1016/j.gca.2006.01.015>
- Dalton JB et al (2012) Europa's icy bright plains and dark linea: exogenic and endogenic contributions to composition and surface properties. *J Geophys Res, Planets* 117(3):E03003. <https://doi.org/10.1029/2011JE003909>
- Daswani MM et al (2021) A metamorphic origin for Europa's ocean. *Geophys Res Lett* 48(18):e2021GL094143. <https://doi.org/10.1029/2021GL094143>
- Daubar IJ et al (2024) Planned geological investigations of the Europa clipper mission. *Space Sci Rev* 220(1):18. <https://doi.org/10.1007/s11214-023-01036-z>
- DeLuca S et al (1990) Direct analysis of bacterial fatty acids by Curie-point pyrolysis tandem mass spectrometry. *Anal Chem* 62(14):1465–1472. <https://doi.org/10.1021/ac00213a022>
- Fabbri D et al (2012) Analytical pyrolysis of dipeptides containing proline and amino acids with polar side chains. Novel 2, 5-diketopiperazine markers in the pyrolysates of proteins. *J Anal Appl Pyrolysis* 95:145–155. <https://doi.org/10.1016/j.jaap.2012.02.001>
- Fohn M et al (2021) Description of the mass spectrometer for the Jupiter icy moons explorer mission. In: IEEE aerospace conference proceedings. <https://doi.org/10.1109/AERO50100.2021.9438344>
- Fugett D et al (2022) Contamination control approach to mitigating radiation induced outgassing on Europa clipper. In: IEEE aerospace conference proceedings. <https://doi.org/10.1109/AERO53065.2022.9843223>
- Garrett H et al (2017) The latest Jovian-trapped proton and heavy ion models. *IEEE Trans Nucl Sci* 64(11):2802–2813. <https://doi.org/10.1109/TNS.2017.2755618>
- Gedcke D (2001) How counting statistics controls detection limits and peak precision. ORTEC Application Notes AN59
- Glein CR (2023) N<sub>2</sub> accretion, metamorphism of organic nitrogen, or both processes likely contributed to the origin of Pluto's N<sub>2</sub>. *Icarus* 404:115651. <https://doi.org/10.1016/j.icarus.2023.115651>
- Glein CR, Waite JH (2020) The carbonate geochemistry of Enceladus' ocean. *Geophys Res Lett* 47(3):e2019GL085885. <https://doi.org/10.1029/2019GL085885>
- Glein CR et al (2008) The oxidation state of hydrothermal systems on early Enceladus. *Icarus* 197(1):157–163. <https://doi.org/10.1016/j.icarus.2008.03.021>

- Glein CR et al (2015) The pH of Enceladus' ocean. *Geochim Cosmochim Acta* 162:202–219. <https://doi.org/10.1016/j.gca.2015.04.017>
- Goesmann F et al (2015) Organic compounds on comet 67P/Churyumov-Gerasimenko revealed by COSAC mass spectrometry. *Science* 349(6247):aab0689. <https://doi.org/10.1126/science.aab0689>
- Graf S et al (2008) Thruster plumes: sources for high pressure and contamination at the payload location. *J Spacecr Rockets* 45(1):57–64. <https://doi.org/10.2514/1.30600>
- Greeley R et al (2004) Geology of Europa. In: Bagenal F, Dowling TE, McKinnon WB, McKinnon W (eds) *Jupiter: the planet, satellites and magnetosphere*. Cambridge University Press, Cambridge
- Grinfeld D et al (2014) Space-charge effects in an electrostatic multireflection ion trap. *Eur Mass Spectrom* 20(2):131–142. <https://doi.org/10.1255/ejms.1265>
- Guilhaus M (2005) Mass spectrometry | time-of-flight. In: Worsfold P, Townshend A, Poole C (eds) *Encyclopedia of analytical science*, 2nd edn. Elsevier, Oxford, pp 412–423. <https://doi.org/10.1016/B0-12-369397-7/00347-2>
- Hand KP et al (2007) Energy, chemical disequilibrium, and geological constraints on Europa. *Astrobiology* 7(6):1006–1022. <https://doi.org/10.1089/ast.2007.0156>
- Hand KP et al (2009) Astrobiology and the potential for life on Europa. In: Pappalardo RT, McKinnon WB, Khurana K (eds) *Europa*. University of Arizona Press, Tucson, pp 589–629
- Hand KP et al (2022) Science goals and mission architecture of the Europa lander mission concept. *Planet Sci J* 3(1):22. <https://doi.org/10.3847/PSJ/ac4493>
- Hansen GB, McCord TB (2008) Widespread CO<sub>2</sub> and other non-ice compounds on the anti-Jovian and trailing sides of Europa from Galileo/NIMS observations. *Geophys Res Lett* 35(1):L01202. <https://doi.org/10.1029/2007GL031748>
- Hao J et al (2022) Abundant phosphorus expected for possible life in Enceladus's ocean. *Proc Natl Acad Sci USA* 119(39):e2201388119. <https://doi.org/10.1073/pnas.2201388119>
- Hassig M et al (2011a) Spacecraft outgassing, a largely underestimated phenomenon. In: 2nd international conference on space technology, ICST 2011
- Hassig M et al (2011b) Investigation of spacecraft outgassing by sensitive mass spectrometry. *Spectrosc Europe* 2:20–23
- Helgeson HC et al (1993) Petroleum, oil field waters, and authigenic mineral assemblages are they in metastable equilibrium in hydrocarbon reservoirs. *Geochim Cosmochim Acta* 57(14):3295–3339. [https://doi.org/10.1016/0016-7037\(93\)90541-4](https://doi.org/10.1016/0016-7037(93)90541-4)
- Ionov N, Mamyrin B (1953) Mass spectrometer with a pulse ion source. *Zh Tekh Fiz* 23:2101
- Jakosky BM, Shock EL (1998) The biological potential of Mars, the early Earth, and Europa. *J Geophys Res, Planets* 103(E8):19359–19364. <https://doi.org/10.1029/98JE01892>
- Jaramillo-Botero A et al (2012) Hypervelocity impact effect of molecules from Enceladus' plume and Titan's upper atmosphere on NASA's Cassini spectrometer from reactive dynamics simulation. *Phys Rev Lett* 109(21):213201
- Jia X et al (2018) Evidence of a plume on Europa from Galileo magnetic and plasma wave signatures. *Nat Astron* 2(6):459–464. <https://doi.org/10.1038/s41550-018-0450-z>
- Johnson RE et al (1984) Sputtering processes: erosion and chemical change. *Adv Space Res* 4(9):41–51. [https://doi.org/10.1016/0273-1177\(84\)90007-3](https://doi.org/10.1016/0273-1177(84)90007-3)
- Johnson JW et al (1992) SUPCRT92: a software package for calculating the standard molal thermodynamic properties of minerals, gases, aqueous species, and reactions from 1 to 5000 bar and 0 to 1000 °C. *Comput Geosci* 18(7):899–947. [https://doi.org/10.1016/0098-3004\(92\)90029-Q](https://doi.org/10.1016/0098-3004(92)90029-Q)
- Johnson RE et al (2002) Energy distributions for desorption of sodium and potassium from ice: the Na/K ratio at Europa. *Icarus* 156(1):136–142. <https://doi.org/10.1006/icar.2001.6763>
- Johnson RE et al (2009) Composition and detection of Europa's sputter-induced atmosphere. In: Pappalardo RT, McKinnon WB, Khurana KK (eds) *Europa*. University of Arizona Press, Tucson, pp 507–528. <https://doi.org/10.2307/j.ctt1xp3wdw.27>
- Kattenhorn SA, Prockter LM (2014) Evidence for subduction in the ice shell of Europa. *Nat Geosci* 7(10):762–767. <https://doi.org/10.1038/ngeo2245>
- Kaufmann A, Walker S (2018) Coalescence and self-bunching observed in commercial high-resolution mass spectrometry instrumentation. *Rapid Commun Mass Spectrom* 32(6):503–515. <https://doi.org/10.1002/rcm.8054>
- Kebelmann K et al (2013) Intermediate pyrolysis and product identification by TGA and Py-GC/MS of green microalgae and their extracted protein and lipid components. *Biomass Bioenergy* 49:38–48. <https://doi.org/10.1016/j.biombioe.2012.12.006>
- Khawaja N et al (2019) Low-mass nitrogen-, oxygen-bearing, and aromatic compounds in Enceladean ice grains. *Mon Not R Astron Soc* 489(4):5231–5243. <https://doi.org/10.1093/mnras/stz2280>
- Kieffer SW et al (2006) A clathrate reservoir hypothesis for Enceladus south polar plume. *Science* 314(5806):1764–1766. <https://doi.org/10.1126/science.1133519>

- Kissel J et al (1986) Composition of comet Halley dust particles from Giotto observations. *Nature* 321(6067):336–337. <https://doi.org/10.1038/321336a0>
- Li D et al (2013) Very low gas flow measurements for UHV/XHV and leak calibration. *Metrologia* 50(1):15–19. <https://doi.org/10.1088/0026-1394/50/1/15>
- Lowell RP, DuBose M (2005) Hydrothermal systems on Europa. *Geophys Res Lett* 32(5):L05202. <https://doi.org/10.1029/2005GL022375>
- Lu GS et al (2021) Bioenergetic potentials in terrestrial, shallow-sea and deep-sea hydrothermal systems. *Chem Geol* 583:120449. <https://doi.org/10.1016/j.chemgeo.2021.120449>
- Lyons TW et al (2014) The rise of oxygen in Earth's early ocean and atmosphere. *Nature* 506(7488):307–315. <https://doi.org/10.1038/nature13068>
- Magee B, Waite JH Jr (2017) Neutral gas composition of Enceladus' plume – model parameter insights from Cassini-INMS. In: 48th lunar and planetary science conference, The Woodlands, Texas, Lunar And Planetary Institute
- Mahaffy PR et al (2013) Abundance and isotopic composition of gases in the Martian atmosphere from the Curiosity rover. *Science* 341(6143):263–266. <https://doi.org/10.1126/science.1237966>
- Mamyrin BA et al (1973) The mass-reflectron, a new nonmagnetic time-of-flight mass spectrometer with high resolution. *Soviet Phys JETP* 37:45
- Matson DL et al (2007) Enceladus' plume: compositional evidence for a hot interior. *Icarus* 187(2):569–573. <https://doi.org/10.1016/j.icarus.2006.10.016>
- McCullom TM (1999) Methanogenesis as a potential source of chemical energy for primary biomass production by autotrophic organisms in hydrothermal systems on Europa. *J Geophys Res, Planets* 104(E12):30729–30742. <https://doi.org/10.1029/1999JE001126>
- McCullom TM, Shock EL (1997) Geochemical constraints on chemolithoautotrophic metabolism by microorganisms in seafloor hydrothermal systems. *Geochim Cosmochim Acta* 61(20):4375–4391. [https://doi.org/10.1016/S0016-7037\(97\)00241-X](https://doi.org/10.1016/S0016-7037(97)00241-X)
- McDermott JM et al (2015) Pathways for abiotic organic synthesis at submarine hydrothermal fields. *Proc Natl Acad Sci USA* 112(25):7668–7672. <https://doi.org/10.1073/pnas.1506295112>
- McKeegan KD et al (2011) The oxygen isotopic composition of the sun inferred from captured solar wind. *Science* 332(6037):1528–1532. <https://doi.org/10.1126/science.1204636>
- Mikellides I et al (2020) Modelling and simulations of particle resuspension and transport for the assessment of terrestrial-borne biological contamination of the samples on the Mars 2020 mission. *Planet Space Sci* 181:104792. <https://doi.org/10.1016/j.pss.2019.104792>
- Miller KE et al (2019) Contributions from accreted organics to Titan's atmosphere: new insights from cometary and chondritic data. *Astrophys J* 871(1):59. <https://doi.org/10.3847/1538-4357/aaf561>
- Moore WB, Hussmann H (2009) Thermal evolution of Europa's silicate interior. In: Pappalardo RT, McKinnon WB, Khurana KK (eds) *Europa*. University of Arizona Press, Tucson, pp 369–380. <https://doi.org/10.2307/j.ctt1xp3wdw.21>
- Mousis O, Gautier D (2004) Constraints on the presence of volatiles in Ganymede and Callisto from an evolutionary turbulent model of the Jovian subnebula. *Planet Space Sci* 52(5–6):361–370. <https://doi.org/10.1016/j.pss.2003.06.004>
- Mousis O et al (2023) Early stages of Galilean moon formation in a water-depleted environment. *Astrophys J Lett* 944(2):L37. <https://doi.org/10.3847/2041-8213/acb5a4>
- Mumma MJ, Charnley SB (2011) The chemical composition of comets—emerging taxonomies and natal heritage. *Annu Rev Astron Astrophys* 49(1):471–524. <https://doi.org/10.1146/annurev-astro-081309-130811>
- Nealson KH (1997) The limits of life on Earth and searching for life on Mars. *J Geophys Res, Planets* 102(E10):23675–23686. <https://doi.org/10.1029/97JE01996>
- New JS et al (2021) Quantitative evaluation of the feasibility of sampling the ice plumes at Enceladus for biomarkers of extraterrestrial life. *Proc Natl Acad Sci USA* 118(37):e2106197118. <https://doi.org/10.1073/pnas.2106197118>
- Niemann HB et al (2010) Composition of Titan's lower atmosphere and simple surface volatiles as measured by the Cassini-Huygens probe gas chromatograph mass spectrometer experiment. *J Geophys Res, Planets* 115(E12):E12006. <https://doi.org/10.1029/2010JE003659>
- Paganini L et al (2020) A measurement of water vapour amid a largely quiescent environment on Europa. *Nat Astron* 4(3):266–272. <https://doi.org/10.1038/s41550-019-0933-6>
- Paranicas C et al (2000) Energetic charged particles near Europa. *J Geophys Res Space Phys* 105(A7):16005–16015. <https://doi.org/10.1029/1999JA000350>
- Peters KE et al (2004) *The biomarker guide: volume 1: biomarkers and isotopes in the environment and human history*. Cambridge University Press, Cambridge. <https://doi.org/10.1017/CBO9780511524868>
- Plainaki C et al (2012) The role of sputtering and radiolysis in the generation of Europa exosphere. *Icarus* 218(2):956–966. <https://doi.org/10.1016/j.icarus.2012.01.023>

- Plyasunov AV, Shock EL (2001) Correlation strategy for determining the parameters of the revised Helgeson-Kirkham-Flowers model for aqueous nonelectrolytes. *Geochim Cosmochim Acta* 65(21):3879–3900. [https://doi.org/10.1016/S0016-7037\(01\)00678-0](https://doi.org/10.1016/S0016-7037(01)00678-0)
- Postberg F et al (2009) Sodium salts in E-ring ice grains from an ocean below the surface of Enceladus. *Nature* 459(7250):1098–1101. <https://doi.org/10.1038/nature08046>
- Postberg F et al (2011) A salt-water reservoir as the source of a compositionally stratified plume on Enceladus. *Nature* 474(7353):620–622. <https://doi.org/10.1038/nature10175>
- Postberg F et al (2018) Macromolecular organic compounds from the depths of Enceladus. *Nature* 558(7711):564–568. <https://doi.org/10.1038/s41586-018-0246-4>
- Prockter LM, Patterson GW (2009) Morphology and evolution of Europa's ridges and bands. In: Pappalardo RT, McKinnon WB, Khurana KK (eds) *Europa*. University of Arizona Press, Tucson, pp 237–258. <https://doi.org/10.2307/j.ctt1xp3wdw.16>
- Prockter LM et al (2010) Characteristics of icy surfaces. *Space Sci Rev* 153(1–4):63–111. <https://doi.org/10.1007/s11214-010-9649-8>
- Ray C et al (2021) Oxidation processes diversify the metabolic menu on Enceladus. *Icarus* 364:114248. <https://doi.org/10.1016/j.icarus.2020.114248>
- Reynard B, Sotin C (2023) Carbon-rich icy moons and dwarf planets. *Earth Planet Sci Lett* 612:118172. <https://doi.org/10.1016/j.epsl.2023.118172>
- Roberts JH et al (2023) Exploring the interior of Europa with the Europa clipper. *Space Sci Rev* 219(6):46. <https://doi.org/10.1007/s11214-023-00990-y>
- Robinson KJ et al (2020) Metastable equilibrium of substitution reactions among oxygen- and nitrogen-bearing organic compounds at hydrothermal conditions. *Geochim Cosmochim Acta* 272:93–104. <https://doi.org/10.1016/j.gca.2019.12.030>
- Robinson KJ et al (2023) Ethene-ethanol ratios as potential indicators of hydrothermal activity at Enceladus, Europa, and other icy ocean worlds. *Icarus* 406:115765. <https://doi.org/10.1016/j.icarus.2023.115765>
- Ronnet T, Johansen A (2020) Formation of moon systems around giant planets: capture and ablation of planetesimals as foundation for a pebble accretion scenario. *Astron Astrophys* 633:A93. <https://doi.org/10.1051/0004-6361/201936804>
- Ronnet T et al (2017) Pebble accretion at the origin of water in Europa. *Astrophys J* 845(2):92. <https://doi.org/10.3847/1538-4357/aa80e6>
- Ronnet T et al (2018) Saturn's formation and early evolution at the origin of Jupiter's massive moons. *Astron J* 155(5):224. <https://doi.org/10.3847/1538-3881/aabcc7>
- Roth L et al (2014) Transient water vapor at Europa's south pole. *Science* 343(6167):171–174. <https://doi.org/10.1126/science.1247051>
- Salter TL et al (2022) Mass spectrometric fingerprints of bacteria and archaea for life detection on icy moons. *Astrobiology* 22(2):143–157. <https://doi.org/10.1089/ast.2020.2394>
- Savitzky A, Golay MJE (1964) Smoothing and differentiation of data by simplified least squares procedures. *Anal Chem* 36(8):1627–1639. <https://doi.org/10.1021/ac60214a047>
- Schenk PM et al (2018) Enceladus and the icy moons of Saturn. University of Arizona Press, Tucson
- Schläppli B et al (2010) Influence of spacecraft outgassing on the exploration of tenuous atmospheres with in situ mass spectrometry. *J Geophys Res Space Phys* 115(12):A12313
- Schläppli B et al (2011) Characterization of the gaseous spacecraft environment of Rosetta by ROSINA. In: 3rd AIAA atmospheric space environments conference
- Schmidt BE et al (2011) Active formation of 'chaos terrain' over shallow subsurface water on Europa. *Nature* 479(7374):502–505. <https://doi.org/10.1038/nature10608>
- Schrödter R, Baltes W (1991) Pyrolysis of various furan model compounds. *J Anal Appl Pyrolysis* 19:131–137. [https://doi.org/10.1016/0165-2370\(91\)80039-B](https://doi.org/10.1016/0165-2370(91)80039-B)
- Schwarzbauer J, Jovančićević B (2020) Introduction to analytical methods in organic geochemistry. Springer, Cham. <https://doi.org/10.1007/978-3-030-38592-7>
- Seewald JS (1994) Evidence for metastable equilibrium between hydrocarbons under hydrothermal conditions. *Nature* 370(6487):285–287. <https://doi.org/10.1038/370285a0>
- Seewald JS (2001) Aqueous geochemistry of low molecular weight hydrocarbons at elevated temperatures and pressures: constraints from mineral buffered laboratory experiments. *Geochim Cosmochim Acta* 65(10):1641–1664. [https://doi.org/10.1016/S0016-7037\(01\)00544-0](https://doi.org/10.1016/S0016-7037(01)00544-0)
- Sephton MA (2002) Organic compounds in carbonaceous meteorites. *Nat Prod Rep* 19(3):292–311. <https://doi.org/10.1039/b103775g>
- Sephton MA (2014) 12.1 - organic geochemistry of meteorites. In: Holland HD, Turekian KK (eds) *Treatise on geochemistry*, 2nd edn. Elsevier, Oxford, pp 1–31. <https://doi.org/10.1016/B978-0-08-095975-7.01002-0>
- Sephton MA et al (2018) Searching for life with mass spectrometry. *Astron Geophys* 59(3):3.23–3.24. <https://doi.org/10.1093/astrogeo/aty146>


- Shock EL (1990) Geochemical constraints on the origin of organic compounds in hydrothermal systems. *Orig Life Evol Biosph* 20(3–4):331–367. <https://doi.org/10.1007/BF01808115>
- Shock EL, Helgeson HC (1990) Calculation of the thermodynamic and transport properties of aqueous species at high pressures and temperatures: standard partial molal properties of organic species. *Geochim Cosmochim Acta* 54(4):915–945. [https://doi.org/10.1016/0016-7037\(90\)90429-O](https://doi.org/10.1016/0016-7037(90)90429-O)
- Shock EL, McKinnon WB (1993) Hydrothermal processing of cometary volatiles-applications to Triton. *Icarus* 106(2):464–477. <https://doi.org/10.1006/icar.1993.1185>
- Shock EL, Schulte MD (1998) Organic synthesis during fluid mixing in hydrothermal systems. *J Geophys Res, Planets* 103(E12):28513–28527. <https://doi.org/10.1029/98JE02142>
- Shock EL et al (2013) Thermodynamics of organic transformations in hydrothermal fluids. *Rev Mineral Geochem* 76:311–350. <https://doi.org/10.2138/rmg.2013.76.9>
- Smith GG et al (1988) Gas chromatographic–mass spectrometric analysis of the Curie-point pyrolysis products of some dipeptides and their diketopiperazine. *J Chem Soc, Perkin Trans 2* 2:203–211. <https://doi.org/10.1039/P29880000203>
- Soares CE et al (2019a) Spacecraft return flux considerations for missions targeting detection of organics with mass spectrometers. In: Proceedings of the international astronomical congress, IAC
- Soares CE et al (2019b) High-energy radiation testing and effects on spacecraft materials outgassing. In: Proceedings of the international astronomical congress, IAC
- Sohl F et al (2010) Subsurface water oceans on icy satellites: chemical composition and exchange processes. *Space Sci Rev* 153(1–4):485–510. <https://doi.org/10.1007/s11214-010-9646-y>
- Sparks WB et al (2017) Active cryovolcanism on Europa? *Astrophys J Lett* 839(2):L18. <https://doi.org/10.3847/2041-8213/aa67f8>
- Stankiewicz BA et al (1997) Assessment of bog-body tissue preservation by pyrolysis-gas chromatography/mass spectrometry. *Rapid Commun Mass Spectrom* 11(17):1884–1890. [https://doi.org/10.1002/\(SICI\)1097-0231\(199711\)11:17<1884::AID-RCM62>3.0.CO;2-5](https://doi.org/10.1002/(SICI)1097-0231(199711)11:17<1884::AID-RCM62>3.0.CO;2-5)
- Summons RE et al (2008) Molecular biosignatures. *Space Sci Rev* 135(1–4):133–159. <https://doi.org/10.1007/s11214-007-9256-5>
- Teolis BD, Waite JH (2016) Dione and Rhea seasonal exospheres revealed by Cassini CAPS and INMS. *Icarus* 272:277–289. <https://doi.org/10.1016/j.icarus.2016.02.031>
- Teolis BD et al (2010) Cassini finds an oxygen-carbon dioxide atmosphere at Saturn’s icy moon Rhea. *Science* 330(6012):1813–1815. <https://doi.org/10.1126/science.1198366>
- Teolis BD et al (2017a) Enceladus plume structure and time variability: comparison of Cassini observations. *Astrobiology* 17(9):926–940. <https://doi.org/10.1089/ast.2017.1647>
- Teolis BD et al (2017b) Water ice radiolytic O<sub>2</sub>, H<sub>2</sub>, and H<sub>2</sub>O<sub>2</sub> yields for any projectile species, energy, or temperature: a model for icy astrophysical bodies. *J Geophys Res, Planets* 122(10):1996–2012. <https://doi.org/10.1002/2017JE005285>
- Teolis BD et al (2017c) Plume and surface feature structure and compositional effects on Europa’s global exosphere: preliminary Europa mission predictions. *Icarus* 284:18–29. <https://doi.org/10.1016/j.icarus.2016.10.027>
- Tobie G et al (2010) Surface, subsurface and atmosphere exchanges on the satellites of the outer solar system. *Space Sci Rev* 153(1–4):375–410. <https://doi.org/10.1007/s11214-010-9641-3>
- Trumbo SK et al (2019) Sodium chloride on the surface of Europa. *Sci Adv* 5(6):eaaw7123. <https://doi.org/10.1126/sciadv.aaw7123>
- van Der Kaaden A et al (1983) Analytical pyrolysis of carbohydrates: I. Chemical interpretation of matrix influences on pyrolysis-mass spectra of amylose using pyrolysis-gas chromatography-mass spectrometry. *J Anal Appl Pyrolysis* 5(3):199–220. [https://doi.org/10.1016/0165-2370\(83\)80028-X](https://doi.org/10.1016/0165-2370(83)80028-X)
- Vance S et al (2007) Hydrothermal systems in small ocean planets. *Astrobiology* 7(6):987–1005. <https://doi.org/10.1089/ast.2007.0075>
- Vance SD et al (2023) Investigating Europa’s habitability with the Europa clipper. *Space Sci Rev* 219(8):81. <https://doi.org/10.1007/s11214-023-01025-2>
- Villanueva GL et al (2023) Endogenous CO<sub>2</sub> ice mixture on the surface of Europa and no detection of plume activity. *Science* 381(6664):1305–1308. <https://doi.org/10.1126/science.adg4270>
- Vorburger A, Wurz P (2018) Europa’s ice-related atmosphere: the sputter contribution. *Icarus* 311:135–145. <https://doi.org/10.1016/j.icarus.2018.03.022>
- Vorburger A, Wurz P (2021) Modeling of possible plume mechanisms on Europa. *J Geophys Res Space Phys* 126(9):e2021JA029690. <https://doi.org/10.1029/2021JA029690>
- Waite JH Jr et al (2004) The Cassini ion and neutral mass spectrometer (INMS) investigation. *Space Sci Rev* 114(1–4):113–231. <https://doi.org/10.1007/s11214-004-1408-2>
- Waite JH Jr et al (2006) Cassini ion and neutral mass spectrometer: Enceladus plume composition and structure. *Science* 311(5766):1419–1422. <https://doi.org/10.1126/science.1121290>



- Waite JH Jr et al (2009) Liquid water on Enceladus from observations of ammonia and  $^{40}\text{Ar}$  in the plume. *Nature* 460(7254):487–490. <https://doi.org/10.1038/nature08153>
- Waite JH et al (2005a) Ion neutral mass spectrometer results from the first flyby of Titan. *Science* 308(5724):982–986. <https://doi.org/10.1126/science.1110652>
- Waite JH et al (2005b) The Mars analytical chemistry experiment. In: 2005 IEEE aerospace conference. <https://doi.org/10.1109/AERO.2005.1559352>
- Waite JH et al (2017) Cassini finds molecular hydrogen in the Enceladus plume: evidence for hydrothermal processes. *Science* 356(6334):155–159. <https://doi.org/10.1126/science.aai8703>
- Wiza LJ (1979) Microchannel plate detectors. *Nucl Instrum Methods* 162(1–3):587–601. [https://doi.org/10.1016/0029-554X\(79\)90734-1](https://doi.org/10.1016/0029-554X(79)90734-1)
- Wurz P, Gubler L (1996) Fast microchannel plate detector for particles. *Rev Sci Instrum* 67(5):1790–1793. <https://doi.org/10.1063/1.1146975>
- Xu X et al (1991) Mechanism and kinetics of the acid-catalyzed formation of ethene and diethyl ether from ethanol in supercritical water. *Ind Eng Chem Res* 30(7):1478–1485. <https://doi.org/10.1021/ie00055a012>
- Yoshida K et al (2021)  $^{14}\text{N}$ NMR evidence for initial production of  $\text{NH}_3$  accompanied by alcohol from the hydrolysis of ethylamine and butylamine in supercritical water. *Chem Lett* 50(2):316–319. <https://doi.org/10.1246/CL.200783>
- Yoshida K et al (2023) Nuclear magnetic resonance analysis of hydrothermal reactions of ethyl- and octylamine in sub- and supercritical water. *J Phys Chem A* 127(17):3848–3861. <https://doi.org/10.1021/acs.jpca.3c01213>
- Young DT (2002) Mass spectrometry for planetary science. In: Mendillo M, Nagy A, Waite JH (eds) *Atmospheres in the solar system: comparative aeronomy*, pp 353–365. <https://doi.org/10.1029/130GM24>
- Young DT (2006) Mass spectrometry for planetary missions: future state-of-the-art. In: 3rd annual Asia Oceania geosciences society meeting, Singapore. Invited paper 59-PS-A0544
- Young DT, Waite JH Jr (2007) Ultra-high resolution mass spectrometry for planetary probes. In: 5th international planetary probe workshop, Bordeaux, France
- Young DT et al (2004) Cassini plasma spectrometer investigation. *Space Sci Rev* 114(1–4):1–112. <https://doi.org/10.1007/s11214-004-1406-4>
- Young DT et al (2010) The role of high-resolution mass spectrometry in the future exploration of Titan. In: *European planetary science congress 2010, Rome, Italy. EPSC abstracts, Vol. 5, EPSC2010-312*
- Zhu R et al (2016) Detection of microbial biomass in seafloor sediment by pyrolysis GC/MS. *J Anal Appl Pyrolysis* 118:175–180. <https://doi.org/10.1016/j.jaap.2016.02.002>
- Zolotov MY (2008) Oceanic composition on Europa: constraints from mineral solubilities. In: 39th lunar and planetary science conference, League City, Texas
- Zolotov MY, Fegley B Jr (2000) Eruption conditions of Pele volcano on Io inferred from chemistry of its volcanic plume. *Geophys Res Lett* 27(17):2789–2792. <https://doi.org/10.1029/2000GL011608>
- Zolotov MY, Kargel JS (2009) On the chemical composition of Europa's icy shell, ocean, and underlying rocks. In: Pappalardo RT, McKinnon WB, Khurana KK (eds) *Europa*. University of Arizona Press, Tucson, pp 431–458. <https://doi.org/10.2307/j.ctt1xp3wdw.24>
- Zolotov MY, Shock EL (2004) A model for low-temperature biogeochemistry of sulfur, carbon, and iron on Europa. *J Geophys Res, Planets* 109(E6):06001. <https://doi.org/10.1029/2003JE002194>

**Publisher's Note** Springer Nature remains neutral with regard to jurisdictional claims in published maps and institutional affiliations.

## Authors and Affiliations

J.H. Waite Jr.<sup>1,2</sup>  · J.L. Burch<sup>3</sup> · T.G. Brockwell<sup>3</sup> · D.T. Young<sup>3</sup> · G.P. Miller<sup>3</sup> · S.C. Persyn<sup>3</sup> · J.M. Stone<sup>3</sup> · P. Wilson IV<sup>3</sup> · K.E. Miller<sup>3</sup> · C.R. Glein<sup>3</sup> · R.S. Perryman<sup>3</sup> · M.A. McGrath<sup>4</sup> · S.J. Bolton<sup>3</sup> · W.B. McKinnon<sup>5</sup> · O. Mousis<sup>6</sup> · M.A. Sephton<sup>7</sup> · E.L. Shock<sup>8</sup> · M. Choukroun<sup>9</sup> · B.D. Teolis<sup>3</sup> · D.Y. Wyrick<sup>3</sup> · M.Y. Zolotov<sup>8</sup> · C. Ray<sup>3,10</sup> · A.L. Magoncelli<sup>11</sup> · R.R. Raffanti<sup>12</sup> · R.L. Thorpe<sup>3</sup> · A. Bouquet<sup>6</sup> · T.L. Salter<sup>7</sup> · K.J. Robinson<sup>8</sup> · C. Urdiales<sup>3</sup> · Y.D. Tyler<sup>3</sup> · G.J. Dirks<sup>3</sup> · C.R. Beebe<sup>3</sup> · D.A. Fugett<sup>9</sup> · J.A. Alexander<sup>3</sup> · J.J. Hanley<sup>3</sup> · Z.A. Moorhead-Rosenberg<sup>3</sup> · K.A. Franke<sup>3</sup> · K.S. Pickens<sup>3</sup> · R.J. Focia<sup>3</sup> · B.A. Magee<sup>3</sup> · P.J. Hoeper<sup>3</sup> · D.P. Aaron<sup>3</sup> · S.L. Thompson<sup>3</sup> · K.B. Persson<sup>3</sup> · R.C. Blase<sup>3</sup> · G.F. Dunn<sup>3</sup> · R.L. Killough<sup>3</sup> · A. De Los Santos<sup>3</sup> · R.J. Rickerson<sup>3</sup> · O.H.W. Siegmund<sup>13</sup>

✉ J.H. Waite Jr.

- 1 Waite Science LLC, Pensacola, FL, USA
- 2 University of Alabama, Physics Department, Tuscaloosa, AL, USA
- 3 Southwest Research Institute, Space Sector, San Antonio, TX, USA
- 4 SETI Institute, Mountain View, CA, USA
- 5 Washington University, Dept. of Earth and Planetary Sciences, St. Louis, MO, USA
- 6 Aix-Marseille Université, Origins Institute, Marseille, France
- 7 Imperial College London, Department of Earth Science & Engineering, London, UK
- 8 Arizona State University, School of Earth and Space Exploration, Tempe, AZ, USA
- 9 Jet Propulsion Laboratory, California Institute of Technology, Pasadena, CA, USA
- 10 American Geosciences Institute, Alexandria, VA, USA
- 11 Lockheed Martin, Advanced Technology Center, Palo Alto, CA, USA
- 12 Techne Instruments, Berkeley, CA, USA
- 13 Sensor Sciences LLC, Pleasant Hill, CA, USA